

**Droplet-Based Approaches to Probe Complex Behavior in
Colloidal Fluids with High Composition Resolution**

Submitted in partial fulfillment of the requirements for
the degree of
Doctor of Philosophy
in
Chemical Engineering

Blake J. Bleier

B.S., Chemical and Biomolecular Engineering, University of Pennsylvania

Carnegie Mellon University
Pittsburgh, PA

May, 2018

© [Blake J. Bleier], [2018]

All Rights Reserved

Acknowledgements

This work would not have been possible without the support and guidance from many friends, family, coworkers, and mentors during my time here in Pittsburgh. First and foremost, I would like to thank advisors, Lynn Walker and Shelley Anna, for their incredible guidance and mentorship over the past five years. With their continued direction and constant involvement, I felt like my work was always valued and strove to reach the lofty goals set for me. They have taken me under their wing and with care and support and have molded me into the researcher I am today, something for which I will be forever grateful. I'd like to thank my funding source, Dow Chemical, along with three outstanding researchers at Dow, Ben Freireich, Adam Grzesiak, and Karl Jacob, for their insightful discussions and oversight of my project. I'd also like to thank my thesis committee, Aditya Khair, Alan McGaughey, and Dennis Preive.

I would like to thank current and past members of the Complex Fluids office for helping me both in my work and in staying sane during my time on the 3rd floor lab. Michael Davidson, for your help and joint suffering during our neutron scattering trips together. Chris Nelson and Benjamin Yezer for your guidance and friendship when I was but a wide-eyed first year. Some additional members I would like to thank include Junchi Ma, Rajarshi Sengupta, Stephanie Kirby, Melissa Dao, and Javier Lanauze. You are all the best co-workers/friends I could have asked for and am immensely glad for our time together.

Alex Bertuccio, I've enjoyed our years together living in Squirrel Hill and the house. You've helped me both professionally with my interview prep and as a friend by being there when I needed someone. I'll miss our trips to Tom, our MMA conversions, but most importantly I'll miss your constant quoting and expect many random texts about Dom. Pass on your wisdom to the young ones, professor.

Travis, my other (male) half, thank you for all the fun times we've shared in Pittsburgh. From the renaissance faire, to guys night, to singing Karaoke at Lynn's, your friendship and bromance has kept me going through the good times and the bad. I wish you and Sarah the best, and have only one thing left to say: "Pooooour me another one"

Sarah, Travis's actual other half, I'm so glad I was able to meet you during my first weeks here and that our friendship has blossomed into what it is today. Thank you for putting up with Travis and me through the years. You're such a kind, heartfelt (yet incredible strong) woman and I plan on seeing a lot of you and Travis in New York.

Yuan Chen, my eternal housemate, I'm so lucky that Alyssa had some cool friends in college. I can't imagine having lived with anyone else during my time here and will dearly miss our Netflix and football binges. I'm sorry we're all leaving you behind at the house, but you'll be a billionaire soon enough.

Khalid Hajj and Chris "Handsome" Hanselman, I'm going to cherish our time spent as part of the old Skibo crew. We bonded over our time spent suffering under Alex's tutelage and I consider you some of my closest friends in Pittsburgh. Thanks for being such great gym buddies and remember to never skip leg day.

Toni Bechtel, my birthday buddy, Emily Wallitsch, my unofficial housemate, and Nick Lamson, the curling connoisseur, I'm going to miss our fun times out. As much as we've all matured during our time here, it's really nice to be able to relax and have a little fun. May your future be filled with delicious, but reasonably priced IPA's.

Bruce Yan and Jennifer Zhang, I've enjoyed our time spent at the ChemE house together.

You've both helped me significantly during the thesis writing process and I truly value the study

breaks you've helped me take over the last few months. You let me know I always have a home at the ChemE house and will certainly be back to visit (mostly for Melo).

Frank, my locker room friend, our morning conversations have always made my day a little brighter and brought a smile to my face. I'll miss seeing you every day, but will think of you whenever I step foot in a steam room.

Divij Damodhar, Brian Hsia, and Jason Dickhaut, my closest college friends, thank you for having my back through the years and giving me a place to regroup and unwind. Whether we're meeting up in DC or taking over Japan (Sugoi!), I'm always able to have a great time and be myself with you guys. Thank you for being such amazing friends, and I can't wait to make our mark on Europe this summer.

And last but certainly not least, I would like to especially thank Heejin Jeong and my parents for being the most kind, wonderful, support network I could have ever asked for. Heejin, you've helped me more than I thought possible over the last few years. You've been there for me during the best and worst of times and I honestly don't know if I could have made it through the PhD without you. Thank you for being the selfless, caring person you are, and I hope to return the favor even half as well when it's your turn to defend.

Mom and Dad, your ever-present encouragement and support has meant the world to me, and I certainly could not have made it through this process without you behind me. Knowing I have your unconditional support regardless of the outcome gave me the confidence and drive needed to get my degree. I love you both and I hope to make you proud.

Abstract

In this work, microfluidic and millifluidic droplets are utilized to study and control complex fluid behavior with high composition resolution. Different techniques are used on two length scales to create unique approaches towards the same goal of merging droplet-based experiments with classical colloidal characterization experiments. First, a microfluidic dehydrating droplet device is characterized and a procedure established by concentrating a phase separating organic-inorganic system on chip and using geometric calculations to determine composition. The device is then expanded to a more complex, particle-polymer system to investigate suspension stability and interparticle behavior. A model system containing silica particles and PEO polymer is found to transition from a bridging flocculation mechanism to polymer-coated particle jamming based on the mass ratio of polymer to particle. Lastly, a phase separating particle-polymer system consisting of polystyrene particles and hydroxyethyl cellulose is concentrated on-chip. Interparticle interactions are controlled by varying particle size, polymer size, and polymer type and the effects on phase behavior are examined.

Droplet experiments are scaled-up to millifluidic droplets and concentration gradients are used to produce high composition resolution in place of time, used in the dehydrating microfluidic experiments. A novel, millifluidic containment device is created to study aggregation and sedimentation in droplets containing carbon black and OLOA surfactant suspended in dodecane. A slow increase in stabilization behavior is observed as opposed to the previously observed sharp “on-off” effect. The droplet production technique is then improved to achieve more complex composition paths and the device is expanded for a small angle neutron scattering (SANS) application. SANS is performed on flowing droplets with varying concentration to map interparticle interactions and phase behavior of complex particulate

systems. Feasibility of device is demonstrated and preliminary model systems of silica particles and polymer, salt, and surfactant are analyzed and characterized.

Table of Contents

Abstract	v
Table of Contents	v
List of Tables	xi
List of Figures	xii
Chapter 1. Introduction	1
Chapter 2. Background	9
2.1 Droplets	9
2.1.1 Droplet production.....	9
2.1.2 Microfluidic versus millifluidic droplets.....	11
2.2 Colloidal Suspensions	12
2.2.1 Stability of particulate suspensions	12
2.2.2 Phase changes	13
2.3 References	15
Chapter 3. Materials and Methods	17
3.1 Materials.....	17
3.2 Microfluidic Device Fabrication	17
3.2.1 Mold fabrication	17
3.2.2 Device fabrication.....	18
3.3 Millifluidic Device Fabrication.....	19
3.4 Microfluidic Droplet Production.....	20
3.5 Millifluidic Droplet Production.....	21
3.5.1 UV-Vis experiments with 2 inlet syringe pumps	21
3.5.2 UV-Vis experiments with 3 inlet syringe pumps	28
3.6 References	32
Chapter 4. Microfluidic Droplet-Based Tool to Determine Phase Behavior of a Fluid System with High Composition Resolution	34
4.1 Introduction	34
4.2 Materials and Methods	36
4.2.1 Device fabrication.....	37

4.2.2 Analysis of droplet concentration	39
4.2.3 Microscopy	40
4.3 Results	40
4.4 Discussion	55
4.5 Conclusions	57
4.6 References	58
Chapter 5. Dehydrating Particle-Polymer Droplets to Investigate Jamming at High Particle Concentrations	64
5.1 Introduction	64
5.2 Materials and Methods	67
5.3 Results	68
5.3.1 Verification of volume measurement	68
5.3.2 Valid range of technique.....	72
5.3.3 Particle-polymer mixtures	76
5.4 Discussion	82
5.5 Conclusions	91
5.6 References	93
Chapter 6. Controlling Colloid-Polymer Phase Separation in Dehydrating Microfluidic Droplets	98
6.1 Introduction	98
6.2 Background	100
6.3 Materials and Methods	103
6.4 Results	106
6.4.1 Observation of phase separation.....	106
6.4.2 Controlling phase behavior by controlling interparticle interactions	111
6.5 Discussion	122
6.5.1 Demonstration of depletion induced aggregation.....	122
6.5.2 Varying interparticle potential.....	124
6.6 Conclusions	126
6.7 References	128
Chapter 7: Droplet-Based Characterization of Surfactant Efficacy in Colloidal Stabilization of Carbon Black in Nonpolar Solvents	132
7.1 Introduction	132

7.2 Experimental	135
7.2.1 Materials	135
7.2.2 Sample Preparation	135
7.2.3 Droplet production.....	136
7.2.4 Millifluidic droplet array	139
7.2.5 Conductivity measurements	139
7.2.6 Image analysis	140
7.3 Results	141
7.4 Discussion	151
7.5 Conclusions	155
7.6 References	157
Chapter 8. Small Angle Neutron Scattering on Millifluidic Droplets (SANSDrop) to Characterize Fluid Structure over Large Composition Space.....	162
8.1 Introduction	162
8.2 Materials and Methods	164
8.2.1 Sample preparation.....	164
8.2.2 Neutron scattering conditions.....	164
8.2.3 Device setup	165
8.2.4 Contrast match experiment.....	166
8.2.5 Gauntlet experiment	167
8.2.6 Droplet-spacer detection.....	170
8.2.7 Macroscopic phase behavior	174
8.3 Results	175
8.3.1 Contrast matching of silica nanoparticles in H ₂ O/D ₂ O mixtures	175
8.3.2 Phase separating silica nanoparticle systems.....	181
8.4 Discussion	198
8.4.1 Ludox TMA and C ₄ E ₁	199
8.4.2 Ludox TMA and NaCl.....	200
8.4.3 Ludox TMA and 600 g/mol PEO	201
8.5 Design Implications.....	203
8.5.1 Concentration dependence.....	203
8.5.2 Contrast matching.....	204
8.5.3 Fluid properties.....	205

8.5.4 Adsorption to interface	206
8.5.5 Wetting	207
8.5.6 Flow rates and exposure time	208
8.5.7 Alternative designs	209
8.6 Conclusions	210
8.7 References	212
Chapter 9. Conclusions	216
Appendix A. Phase Behavior of Concentrating Particle-Polymer-Salt Systems	219

List of Tables

Table 2.1: Characteristic dimensionless groups and droplet information for comparison between microfluidic and millifluidic droplets	12
Table 3.1: Dispersed phase flow rate conditions for all 3 inlet syringe pumps during spiral gradient experiment. Flow rates vary linearly along each line.	31
Table 6.1: Molecular weight results from GPC measurements performed on all HEC samples	105
Table 7.1: Sedimentation times of macroscopic 7mL carbon black and OLOA 11000 suspensions as a function of surfactant concentration in pph. Example images of 4 pph, 5 pph, and 6 pph samples taken after 9 months are shown on the right.	142
Table 8.1: Scattering length density parameters for components in the silica particle and PEO system.	202

List of Figures

Figure 3.1: Images of millifluidic containment device containing Teflon tubing inside of a lasercut Plexiglas sheet. Droplets are contained in the device indefinitely with order 50-100 droplets per device. Devices are held vertically to detect phase separation in sedimenting droplets..... 19

Figure 3.2: Time sequenced images of the droplet pinching mechanism for microfluidic droplet production in hydrodynamic traps. The continuous phase in mineral oil with 2 wt% Span-80 and the dispersed droplet phase is water. Scale bar in shown in top left image and corresponds to 200 μm . Images courtesy of Chris Nelson..... 20

Figure 3.3: Schematic diagram and images of the experimental set up for production of droplets with a gradient in concentration. Two inlet suspensions are mixed (low and high concentrations) at an upstream Y-junction. Droplets of dispersed suspension are produced at the T-junction in a continuous phase of fluorinated oil. Quantitative values of flow rates during gradient production are shown in the inset. 21

Figure 3.4: Absorbance measurements to determine the concentration accuracy of droplet production. In each graph, the solid black lines are the absorbance data as a function of time. The green line demonstrates the calculated expected absorbance of each droplet starting at the beginning of the droplet gradient. The red points plot the average absorbance of each measured droplet. The graphs have a maximum flow rate ratio of (a) 4, (b) 6, (c) 8, and (d) infinite. 25

Figure 3.5: Droplet absorbance and size measurements of aqueous droplets produced in a continuous outer phase oil (silicone oil or fluorinated oil) using co-flow droplet production. Gradients are formed by combining pure H_2O and 1 mM KMnO_4 . The legend containing dispersed and continuous phase flow conditions is shown in the top left. (a) Droplet absorbance during as a function of time for 10 and 20 minute gradients. Black lines show predicted absorbance values and data points show measured values with the shape and color depicting flow conditions. (b-c) Droplet time spend in-beam (droplet size) for gradient experiments with a silicone oil and fluorinated oil continuous phase respectively. 27

Figure 3.6: Absorbance measurements of droplets during a ternary millifluidic experiment. (a) Schematic of the flow rate composition paths starting and node 1 and progressing sequentially to node 8. (b-d) Absorbance measurements of individual droplets containing mixtures of pure water and 1 mM KMnO_4 . Data points correspond to droplet measurements, solid black lines correspond to predicted absorbance values, and dotted black lines correspond to locations where a node is reached and a new gradient begins. 29

Figure 4.1: Schematic diagram of full microfluidic droplet device and a single droplet trap. Droplets are produced and stored in the 575 μm circular droplet trap. All channels are

approximately 100 μm in height, the exact value is determined for each device after an experiment. The schematic depicts the microfluidic device when no droplets are present. 38

Figure 4.2: Images of a single droplet containing ammonium sulfate and 600 g/mol PEO during dehydration ($\xi = 9.3$, $\phi_o = 0.079$ g/mL). The droplet is a single-phase fluid in images (i-iii), two liquid phases in (iv) and two phases with solid crystals in (v). Scale bar is 200 μm 41

Figure 4.3: The phase diagram for ammonium sulfate and PEO of two different molecular weights developed through the microfluidic experiments provided on (a) a volume basis and (b) a weight basis. The points correspond to the phase boundary for 600 g/mol PEO (■) and 7500 g/mol PEO (●). Solid lines denote the phase boundary and are drawn to guide the eye. Dotted lines are lines of constant mass ratio of the two solutes. The dashed line is the upper limit that can be reached in the experiment. 43

Figure 4.4: Temporal progression of experiment and measured parameters. The blue points are the measured diameter for a single droplet as a function of time. The black points are the combined salt/polymer concentration in the droplet. The dotted red line indicates the first frame where phase separation is observed. Note that the phase separation is not detectable in the volume change of the droplet. 44

Figure 4.5: Phase diagram for two different continuous phase oils. (a) Phase separation points for (○) 100cSt silicone oil with no surfactant and (●) mineral oil with 2% Span-80. (b) Data replotted in θ - ξ space. Error bars correspond to volume calculations from images taken one frame before and after phase separation. 47

Figure 4.6: Comparison between microfluidic and macroscopic phase separation experiments for an ammonium sulfate and 600 g/mol PEO system. The closed points are the microfluidic phase boundary points from Figure 4.3a. The open points are results from macroscopic experiments for (square) one phase and (triangle) two phase solutions. The inset shows the clear visual difference between a macroscopic 1-phase and 2-phase system. 49

Figure 4.7: Images of phase separating droplets at various polymer:salt mass ratios and at 3 different time points. The first row of images shows representative droplets 1 frame after noticeable phase separation, the second row shows droplets 20 minutes after phase separation, and the third row of shows droplets 5 days after droplet production. Scale bars are equivalent to 100 μm 51

Figure 4.8: (a) Schematic of the dehydrating and rehydrating cycle performed in experiments. ($\xi = 36$) (b) Images of droplets at different time points during the rehydration cycle and the second dehydration cycle. Images in the top row progress in time from left to right as the droplet dehydrates. Images in the second row progress in time from right to left as the droplet rehydrates. Images in the third row progress left to right as the droplet dehydrates a second time. Scale bar is equivalent to 100 μm 54

Figure 5.1: (a) Images of a sucrose droplet drying refractive index match experiment. Time goes from left to right along images with a refractive index match between the droplet and the oil

at $t = 1142$ min. (b) Scaled volume refractive index verification of sucrose droplets in mineral oil as a function of initial droplet concentration. Solid black line is the predicted value and closed circles are experiment results. The hashed red line depicts the pancake to sphere transition at $95 \pm 5 \mu\text{m}$. (c) Scaled volume measurements replotted as an error percentage. Partial results courtesy of Deyu Yang. 70

Figure 5.2: Analysis of characteristic ring formation during final stages of droplet drying. (a) Images of observable ring as a function of time. Images times with respect to ring formation correspond to 0 min, 18 min, 40 min, and 64 min. (b) Droplet diameter as a function of time during the dehydration process. 73

Figure 5.3: Final particle volume fraction of Ludox TM-40 silica nanoparticles as a function of final aspect ratio for 5 initial concentrations. Each data point is the average of 8 droplets with error bars displaying the standard deviation. Corresponding initial droplet concentrations are shown in the legend. The hashed red line is the pancake to sphere transition at $95 \pm 5 \mu\text{m}$. Images show characteristic droplet shapes based on aspect ratio. 74

Figure 5.4: Phase diagram of Ludox TMA particles and 7500 g/mol PEO mapped using microfluidic droplet drying. (a) The red circles denote initial droplet concentrations, open circles denote the final droplet concentration, and the single closed black circle denotes the only system that displays phase separation. The thin dotted black lines depict the composition paths of each experiment, the thick dotted black lines represent maximum concentration of particles and polymer, and the solid black line shows the system composition when no water remains in the droplet. The dotted red line denotes the saturation line (1.2 mg/m^2 , $\xi = 0.17$).⁵⁵ (b) Images of droplet behavior at the final stages of the drying experiment. First row of images is characteristic of droplets above the saturation limit and the second row is characteristic of droplets below the saturation limit. 78

Figure 5.5: Final droplet particle concentration as a function of polymer-particle mass ratio. (a) Solid black circles show final concentrations for the Ludox TMA and 7500 g/mol PEO system. Dotted black line demonstrates final particle concentration with no polymer. Solid black line shows the particle volume fraction at which no water remains in the system (only particles and polymer). (b) Similar results with two additional tested systems, labeled in the legend. The dashed black line demonstrates the final particle volume fraction for Ludox TMA particles and the dot-dash black line for Ludox TM-40 particles. 80

Figure 5.6: Cartoon describing the proposed system behavior at different polymer-particle mass ratios. Large droplets in the first row are representative droplets at dilute concentrations and the small droplets in the second row are of the same droplets after dehydration. Proposed mechanism is shown below each droplet. Note the increase in size of the dehydrated bridging flocculation droplet with respect to the higher mass ratio mechanisms. 84

Figure 5.7: Results from droplet dehydration experiments rescaled to overlay. Final volume fraction for 7500 g/mol PEO systems is normalized by final volume fraction of the polymer free case. Final volume fraction of Ludox TM-40 and 100k g/mol PEO is normalized maximum volume fraction of that system. Mass ratio is shifted in the horizontal direction by the difference

between the maximum mass ratio and the maximum mass ratio of the Ludox TMA and 7500 g/mol PEO system. To the left of the dotted line is the bridging flocculation regime and to the right is the polymer filled spaces regime. System components are described in the legend. 87

Figure 5.8: Predicted calculations of Laplace pressure and compressive yield stress based on initial droplet concentration. (a) The solid black line shows the compressive yield stress of a zirconia oxide particulate system as concentration increases.⁶⁸ The dotted lines denote Laplace pressure of droplets initially 575 μm in diameter and 100 μm in height with initial concentrations of 0.05 wt%, 0.5 wt%, and 5 wt% denoted as the dashed blue, dot-dash red, and dot-dot-dash black lines respectively. (b) Compressive yield stress normalized by the Laplace pressure for each initial concentration as a function of particle concentration. The thin dotted lines display the particle concentrations at which the stresses are equal. 89

Figure 6.1: Combined van der Waals, steric, electrostatic, and depletion pair potential forces with varying particle size for illustrative purposes. Chosen parameters are $\Psi_0 = -10$ mV, $\epsilon_r = 80$, $R_g = 10$ nm, $\kappa^{-1} = 50$ nm, $A_{121} = 3 \times 10^{-20}$ J, $T = 298$ K, and $\chi = 0.35$, and $\Phi_2^a = 0.1$. Particle size is denoted in the legend. 102

Figure 6.2: Molecular weight distributions of all HEC material measured with GPC. 100 μL samples of 1 wt% polymer solution in 0.05 M Na_2SO_4 are injected into the GPC instrument. Manufacturer reported molecular weights are shown in the legend in the top right. 105

Figure 6.3: (a) Images of droplets containing 20 nm PS particles and 90k g/mol HEC at different polymer-particle mass ratios (ξ) as droplet dehydration and phase separation occurs. Time progresses from left to right along images. Total solute mass is shown in the upper left corner of each image in which droplet size could be accurately measured. $\xi = 0.11$ shows no phase separation while $\xi = 1.00$ and 9.03 display optical darkening. (b) Average droplet intensity as a function of particle volume fraction for several mass ratios. Black curves are exponential decay fits to droplet intensity with time and the red squares denote the midpoints, taken to be a characteristic time of the phenomenon. Mass ratio of each droplet is displayed in the legend. 107

Figure 6.4: Phase behavior results for 20 nm PS and 90k g/mol HEC system. (a) Macroscopic and microfluidic results in polymer-particle phase space. Closed circles denote measured microfluidic phase separation points determined from Figure 6.3. Open points denote tested macroscopic concentrations with squares denoting no observed phase separation and triangles denoting phase separation. Dotted black lines depict the composition paths for each droplet-based experiment. Dashed red line shows the adsorption limit of HEC on PS (1 mg/m^2).^{40,41} (b) Data replotted in θ - ξ coordinates. 110

Figure 6.5: Phase behavior results for 20 nm PS particles and 2 different HEC polymer sources. (a) Microfluidic results in polymer-particle phase space. The closed points show measured microfluidic phase separation points for both 90k g/mol HEC samples with the open circles

corresponding to 90k-A and the closed squares corresponding to 90k-B. Dotted black lines depict composition paths for each droplet-based experiment. Dashed red line shows the adsorption limit of HEC on PS (1 mg/m²). Inset shows experiments with 90k-B HEC at $\xi = 1.00$ with preadsorbed Triton X-405 with concentrations of circle = 0.04 mg Triton/m², triangle = 0.22 mg Triton/m², and diamond = 1.53 mg Triton/m². (b) Data replotted in θ - ξ coordinates. 113

Figure 6.6: (a) Intensity average size and (b) zeta potential measurements of 20 nm PS particles as a function of preadsorbed Triton X-405 concentration. Error bars are standard deviation of triplicate runs. 115

Figure 6.7: (a) Droplet intensity measurements as a function of particle volume fraction with a mass ratio $\xi = 1.00$ for 20 nm PS particles and 3 different molecular weight HEC polymers. Open circles correspond to 90k g/mol HEC, open hexagons to 260k g/mol HEC, and open squares to 380k g/mol HEC. Phase separation is determined by a cut-off boundary value of 10 times the standard deviation of the flat average pixel intensity regions for each experiment. Cut-off values for each experiment is shown by the dotted lines corresponding to the color of the data set. (b) Phase separation particle concentration as a function of molecular weight. The closed circles denote droplets where concentration is measured and the open square denotes a droplet where concentration is inferred from a dehydration calibration. 116

Figure 6.8: (a) Initial image of all droplets in device demonstrating initial sizes and number density (34 traps out of 40 traps filled). Black rectangle denotes inner droplets and white dotted rectangles denote outer, edge droplets. (b) Droplet dehydration time until phase separation is observed as a function of initial droplet size. Solid black circles correspond to inner droplets and open circles denote outer droplets. Solid line and dotted line are least squared linear fits through inner and outer droplet results respectively. 119

Figure 6.9: Images of various polystyrene particles and polymer combinations during the dehydration process. Time progresses from left to right along images. First three rows show systems of PS particles increasing in particle size with 90k g/mol HEC polymer source. Last two rows show images for 20 nm PS particles and 100k g/mol PEO at different polymer-particle mass ratios. 120

Figure 7.1: Schematic diagram and images of the experimental set up for production of droplets with a gradient in surfactant concentration. (a) Two bulk suspensions are mixed (low and high surfactant concentrations) at a starting volumetric ratio of 6:1. Droplets of dispersed suspension are produced at the T-junction in a continuous phase of fluorinated oil. Quantitative values of flow rates are shown in the inset. (b) Schematic diagram of the OLOA 11000 concentration gradient in droplets in device, colors to clarify the formation of a concentration gradient. (c) Image of device taken seven months after droplet production. 137

Figure 7.2: (a) Images of a single carbon black droplet (6.4pph OLOA 11000) at various time points (days) up to 37 days after initial droplet production with the sediment area (A_i) in pixels and normalized droplet area (A_i^*) displayed beneath. (b) Images of droplets at 3 different surfactant concentrations taken 7 months after droplet production. 143

Figure 7.3: Evolution of suspension stability as a function of time and surfactant concentration. Normalized area is plotted as a function of surfactant concentration. Each color represents a different time after droplet generation up to 30 days. The open square points depict the sediment heights at 5 days which is observed to be the steady state value. The horizontal dashed red line is the densely packed lower limit that corresponds to the normalized area for a fully sedimented carbon black pellet at the bottom of a droplet. The vertical dashed black lines show the two bulk inlet sample concentrations. The inaccessible region marked at the left corresponds to sample concentrations too unstable to produce homogeneous droplets. The color scale is not linear. .. 144

Figure 7.4: Comparison of macroscopic and millifluidic sedimentation results. Normalized droplet area is plotted versus surfactant concentration in pph. The filled symbols (circle, triangle, and square) correspond to three separate devices imaged 5 days after droplets were produced. The open points correspond to macroscopic long term results (months). The dashed horizontal red line corresponds to the densely packed lower limit and the vertical dashed black lines correspond to the bulk sample inlet concentrations. 146

Figure 7.5: Conductivity experiments to determine OLOA 11000 adsorption onto carbon black particles. (a) Horizontal axis is the initial concentration of OLOA 11000 in wt% and the vertical axis is the conductivity of the suspension measured using EIS. The particle free samples (open points) contain dodecane and OLOA 11000 before carbon black is added to the solution. The filtered samples (closed points) contain the same amount of OLOA 11000 initially and 3.33 g/L carbon black. These samples are sonicated and particle-surfactant complexes are filtered out before conductivity is measured. (b) Conductivity difference between the pre-particle samples and the particle-filtered samples from part a is converted to absorbed mass of surfactant. Horizontal axis is the initial concentration of the filtered samples in pph..... 149

Figure 7.6: Conductivity measurements to determine conductivity increments due to particle charging. (a) The open squares are conductivity measurements of carbon black and OLOA 11000 suspensions at a given initial surfactant concentration. The black triangles are conductivity measurements of the same samples with the particle-surfactant complexes filtered out. (b) Difference in conductivity between the filtered and unfiltered samples as a function of the initial surfactant concentration in pph..... 150

Figure 8.1: Schematic diagram of millifluidic SANSDrop device. Two to three dispersed phase pumps are automatically controlled by preprogrammed commands. A silicone oil continuous phase meets the mixed dispersed phase at the droplet production sites and droplets are produced

via a co-flow mechanism. Droplets flow through an in-line neutron beam source followed by a UV-Vis spectrophotometer and scattering and absorbance are continuously measured. 165

Figure 8.2: (a-c) Programmed pump flow rates for three independently controlled syringe pumps corresponding to a (a) non-varying component, (b) varying component, (c) and solvent component. (d) Results of combined flow rate in Component A-Component B phase space. Blue lines correspond to a vertical gauntlet with fixed Component A concentration and gradients in Component B concentration. Red lines correspond to a horizontal gauntlet with fixed Component B concentration and gradients in Component A concentration..... 168

Figure 8.3: Neutron scattering results for 1.9 vol% Ludox HS-40 in pure D₂O droplets at a dispersed phase flow rate of 30 μ L/min and continuous silicone oil outer phase flow rate of 5 μ L/min. Black circles correspond to a bin size of 20 seconds, red squares a bin size of 5 seconds, and blue hexagons a bin size of 1 second. Flat plateaus denote droplets and sharp valleys denote spacers..... 171

Figure 8.4: Characteristic neutron scattering results from a gauntlet experiment binned into 5 second bins to determine droplet-spacer location. The black curve is binned neutron scattering results and the open blue circles denote separation points between droplets. The time between two points is used to distinguish individual droplet scattering curves. 172

Figure 8.5: UV-Vis absorbance measurements performed during a contrast match experiment. Black line denotes absorbance results at $\lambda = 525$ nm recorded every second. Long plateau sections denote droplets and higher plateau values denote spacers. Red circles correspond to average absorbance measurements of each droplet and blue diamonds correspond to average absorbance measurements of spacers. Sharp spikes in absorbance are measurements performed through a curved droplet-spacer interface. Inset displays identical results for 1 hr to demonstrate monodispersity of droplet production. 174

Figure 8.6: Macroscopic phase diagrams for Ludox systems used in millifluidic experiments. (a) Ludox TMA and C₄E₁, (b) Ludox TMA and NaCl, (c) Ludox TMA and 600 g/mol PEO..... 175

Figure 8.7: Neutron scattering and transmission results for an H₂O/D₂O contrast match experiment with 1.9 vol% Ludox HS-40 binned into 5 second bins. The black curve denotes binned neutron scattering data and red points denote average scattering for each droplet. For $t = 0-20$ min, pumps are programmed to produce steady state droplets at 15 vol% D₂O. For $t = 20-40$ min, a linear gradient from 15-77 vol% D₂O is introduced. For $t = 40-60$ min, droplets are produced at a constant 77 vol% D₂O. Dot-dashed red line denotes the predicted contrast match point based on the position of the gradient. Particle concentration remains constant throughout experiment..... 177

Figure 8.8: Comparison between macroscopic and millifluidic contrast match results. Black diamonds correspond to the raw scattering intensity of individual droplets from Figure 8.7. The

y-axis is the square root of the raw scattering intensity average. Open red circles correspond to reduced scattering results from macroscopic samples of identical particle concentration. The magnitude is shown on the right Y-axis as the square root of the reduced scattering intensity. The solid red line denotes a linear fit of macroscopic results to find point of minimum intensity.

..... 179

Figure 8.9: Neutron scattering profiles for individual droplets containing 1.9 vol% Ludox HS-40 at various H₂O/D₂O compositions from the contrast match experiment. The D₂O concentration of each droplet are 15.4, 46.1, 63.6, and 77 vol% D₂O described by circles, triangles, hexagons, and squares respectively. Droplet samples pass through the contrast match point for silica particles of 58 vol% D₂O. 180

Figure 8.10: Droplet quality results for droplets of a Ludox TMA, C₄E₁, and water system. Dotted black lines denote sections of constant non-varying component. Circles correspond to individual droplet varying component concentration and time. Circle size corresponds proportionally to droplet length. Example minimum, average, and maximum circle sizes are shown in the top right. Droplets within the minimum-maximum limit are blue and considered well produced. Droplets outside the limit are red and considered poorly produced. Droplet production follows direction of black arrows. (a) Denotes results for vertical gauntlet and (b) displays results for horizontal gauntlet. 184

Figure 8.11: Neutron scattering intensity results for individual droplets in Ludox TMA-C₄E₁ phase space. (a-b) Results from vertical gauntlet and (c-d) results from horizontal gauntlet. (a&c) Uphill sections of each gauntlet and (b&d) downhill sections of each gauntlet. Circles denote droplet composition with circle size corresponding to average scattering intensity. Closed circles denote droplets with lower scattering and open circles denote droplets with higher scattering. Solid blue and dotted red lines depict droplet quality results from Figure 8.10 with blue denoting regions of well-produced droplets and red denoting regions of poorly-produced droplets. 186

Figure 8.12: Neutron scattering profiles for individual droplets from the Ludox TMA and C₄E₁ gauntlet experiments. Insets show the measured region for each figure with the arrow depicting uphill or downhill direction. (a) Droplets along an uphill gradient in the vertical gauntlet (b) droplets along a downhill gradient in the vertical gauntlet (c) droplets along an uphill gradient in the horizontal gauntlet. Droplet concentrations are denoted in respective legends. 188

Figure 8.13: Droplet quality results for Ludox TMA, NaCl, and water system. Dotted black lines denote sections of constant non-varying component. Circles correspond to individual droplet varying component concentration and time. Circle size correspond proportionally to droplet length. Example minimum, average, and maximum circle sizes are shown in the top right. Droplets within the minimum-maximum limit are blue and considered well produced. Droplets outside the limit are red and considered poorly produced. Droplet production follows

direction of black arrows. (a) Denotes results for vertical gauntlet and (b) displays results for horizontal gauntlet. 191

Figure 8.14: Neutron scattering intensity results for individual droplets in Ludox TMA-NaCl phase space. (a-b) Results from vertical gauntlet and (c-d) results from horizontal gauntlet. (a&c) Uphill sections of each gauntlet and (b&d) downhill sections of each gauntlet. Circles denote droplet composition with circle size corresponding to average scattering intensity. Closed circles denote droplets with lower scattering and open circles denote droplets with higher scattering. Solid blue and dotted red lines depict droplet quality results from Figure 8.13 with blue denoting regions of well-produced droplets and red denoting regions of poorly-produced droplets..... 192

Figure 8.15: Neutron scattering profiles for individual droplets from the Ludox TMA and NaCl gauntlet experiments. Insets show probed gradient region for each figure with the arrow depicting uphill or downhill direction. (a) Droplets along an uphill gradient in the horizontal gauntlet (b) droplets along the first half of a downhill gradient in the horizontal gauntlet (c) droplets along the second half of a downhill gradient in the horizontal gauntlet. Droplet concentrations are denoted in respective legends. 194

Figure 8.16: Droplet quality results for Ludox TMA, 600 g/mol PEO, and water system. Dotted black lines denote regions of constant particle concentration. Circles correspond to individual droplet PEO concentration and time. Circle size correspond proportionally to droplet length. Example minimum, average, and maximum circle sizes are shown in the top right. Droplets within the minimum-maximum limit are blue and considered well produced. Droplets outside the limit are red and considered poorly produced. Droplet production follows direction of black arrows. Overall experiment is half the time of original gauntlet experiment. 195

Figure 8.17: Neutron scattering intensity results for individual droplets in Ludox TMA-PEO phase space. (a-b) Results from vertical gauntlet with (a) describing uphill sections the gauntlet and (b) describing downhill sections of the gauntlet. Circles denote droplet composition with circle size corresponding to average scattering intensity. Closed circles denote droplets with lower scattering and open circles denote droplets with higher scattering. Solid blue and dotted red lines depict droplet quality results from Figure 8.16 with blue denoting regions of well-produced droplets and red denoting regions of poorly-produced droplets. Dotted black line denotes a line of constant SLD equal to the SLD of silica. 196

Figure 8.18: Neutron scattering profiles for individual droplets from the Ludox TMA and 600 g/mol PEO gauntlet experiment. Insets show probed gradient region for each figure with the arrow depicting uphill or downhill direction. (a) Droplets along an uphill gradient and (b) droplets along the same downhill gradient in the vertical gauntlet. Droplet concentrations are denoted in respective legends. 197

Figure A. 1: Phase diagram of Ludox TMA particles and 7500 g/mol PEO mapped using microfluidic droplet drying. (a) The red circles denote initial droplet concentrations, open circles denote the final droplet concentration, and the single closed black circle denotes the only system that displays phase separation. The thin dotted black lines depict the composition paths of each experiment, the thick dotted black lines represent maximum concentration of particles and polymer, and the solid black line shows the system composition when no water remains in the droplet. The dotted red line denotes the saturation line (1.2 mg/m^2 , $\xi = 0.17$).² (b) Images of droplet behavior at the final stages of the drying experiment. First row of images is characteristic of droplets above the saturation limit and the second row is characteristic of droplets below the saturation limit..... 220

Figure A. 2: Phase behavior of concentrating Ludox TM-40 and 7500 g/mol PEO droplets. (a) Images of droplet dehydration in separate regimes. (b) Phase diagram of the dehydration results. Closed red circles denote initial droplet concentrations and closed blue and green points denote phase separation concentration. Open points denote final droplet concentrations with blue, green, and red corresponding to sections of phase separation, transition, and bridging flocculation respectively. 222

Figure A. 3: Images of dehydrating Ludox TMA and 7500 g/mol PEO droplets with different concentrations of added Na_2SO_4 224

Figure A. 4: Effect of Na_2SO_4 concentration on the phase separation concentration for Ludox TMA and 7500 g/mol PEO. Red circles denote initial concentrations, black circles denote phase separation concentration with Ludox TMA particles, black triangles denote phase separation concentration with Ludox TM-40 particles, and open circles denote final droplet concentration. 225

Chapter 1. Introduction

Colloidal suspensions are present in a number of industrial and biological products including coatings, lotions, personal care items, pharmaceuticals, and drug delivery applications among other products. Colloidal systems show rich phase behavior increasing in complexity with increasing number of components. Typical industrial products can have 20-30 individual components in a product, creating an enormous experimental parameter space. Classical experiments to probe this parameter space involve producing discrete macroscale samples varying in concentration and observing phase behavior either visually or with colloidal characterization techniques. This approach allows for broad coverage of large parameter space but the discrete nature can easily miss regions of phase behavior on a complex phase diagram. When designing products, it is important to be able to induce or avoid specific phases and not unintentionally produce them. In this work, we produce high composition resolution droplet-based techniques in conjunction with classical colloidal characterization methods to efficiently map large regions of phase space while maintaining high resolution in the composition variables.

A number of techniques have been developed and adapted to study colloidal suspensions and investigate their underlying dynamics. Typical measurement techniques of bulk suspension properties include light scattering (dynamic and static),^{1,2} turbidimetry,³ optical absorbance measurements,⁴ optical microscopy,⁵ and rheological measurements.⁶⁻⁸ Structural information can be gained from neutron scattering⁹ and X-ray scattering.¹⁰ Characterization of interfacial behavior in colloidal suspensions can be quantified with quartz crystal microbalance measurements (QCM),¹¹ ellipsometry,¹² interfacial tension measurements,¹³ atomic force microscopy (AFM),¹⁴ and neutron reflectometry.¹⁵ Compositional information can be inferred from Raman spectroscopy¹⁶ and Fourier transform infrared spectroscopy (FTIR).¹⁷

Clearly, there are numerous techniques developed to examine colloidal systems, yet each technique performed on the macroscale requires single sample measurements. This results in the same problem of discrete, and often low resolution compositional sampling when large parameter space must be characterized. In addition, samples typically require milliliters of material per data point. For systems where material is precious such as pharmaceutical products, synthesized chemicals, batch depended systems, and materials with expensive components, this will lead to even further reduction in composition resolution. An alternative approach to achieve high composition resolution while maintaining low cost is to employ droplet-based technologies for colloidal stability measurements.

Droplets provide a unique alternative due to their small volume sizes, uniformity, and precise laminar control. Droplet production and manipulation has been well studied and defined.¹⁸⁻²¹ Droplets range in size from femtoliters to microliters with characteristic length scales ranging from micrometers to millimeters and with production frequencies up to 1000 drops per second. Droplets can be controlled with electric fields,²²⁻²⁴ magnetic fields,²⁵ acoustics,²⁶ temperature,²⁷ and flow.²⁰ Droplets have been used to study chemical reactions initiated through mixing^{28,29} or exposure³⁰ as well as biological applications working with single cell experiments,³¹ biological assays,^{32,33} and protein network characterizations.³⁴ Droplets have been produced at dilute concentrations and dehydrated to investigate crystallization kinetics,³⁵⁻³⁹ phase separation,⁴⁰⁻⁴³ and particle synthesis.⁴⁴⁻⁴⁸ However, very few experiments have been performed merging droplet-based techniques with colloidal stability characterization and understanding. This provides a unique opportunity to draw from the vast library of knowledge of droplet production and composition control and apply it towards colloidal suspension stability to create colloidal benchtop analytical experiments in micro-sized droplet form.

In this thesis, two types of droplet-based techniques are developed and characterized to achieve high composition resolution for complex colloidal fluid applications. In Chapters 4-6, we utilize dehydrating microfluidic droplets to characterize phase space. Droplets are produced on-chip and retained in a hydrodynamic trap for continued observation and recording. In these experiments, time is the parameter that controls composition resolution. Frames are recorded often such that over 1000 frames (samples) are taken per experiment. Device feasibility and accuracy is determined in Chapter 4 by investigating the liquid-liquid phase separation of an organic-inorganic system and comparing with macroscopic phase behavior results. In Chapter 5, a non-phase separating particle-polymer system is investigated in the device. A broad range of particle-polymer mass ratios is examined to fully characterize phase space and aggregation mechanisms. In Chapter 6, a depletion induced phase separating particle-polymer system is studied on-chip. Systematic control of the phase separation process is performed by varying the interparticle potential through controlling particle size, polymer size, and polymer type. In these chapters, the microfluidic platform allows for very high composition resolution along dehydrating composition paths, producing orders of magnitude more composition points than current macroscopic test.

In Chapters 7-8, a millifluidic droplet device with droplet volumes on the order of microliters is used compared to the microfluidic device from Chapters 4-6 with volumes on the order of nanoliters. In these experiments, droplets are produced with a gradient of composition along a continuous droplet train, producing individual droplets with unique compositions. Gradient length and droplet size are the parameters that controls composition resolution in these experiments. With a longer gradient length or with smaller droplet sizes, the number of samples per gradient will increase. In Chapter 7, a sedimenting nanoparticle system is investigated with

this technique. A novel, millifluidic containment device is created to store droplets for extended periods (weeks to months) to observe and quantify sedimentation and classify stability. In Chapter 8, this technique is expanded to small angle neutron scattering (SANS). To our knowledge, we are the first to combine millifluidic droplets and SANS. Composition paths are preprogrammed and automated. Gradient capabilities are expanded with the addition of a third inlet stream, allowing for precise, complex composition control.

In this thesis, microfluidic and millifluidic devices are used to marry classical benchtop colloidal experiments with high composition resolution droplet-based experiments. Experimental design and feasibility is demonstrated with simple, model systems and expanded to more complex particulate colloidal fluids. Hundreds to thousands of sample points are collected per experiment to increase resolution in composition space and decrease necessary time and material to fully characterize system behavior. These results can be used as novel techniques to improve formulation characterization for a broad range of colloidal fluid systems.

References

- (1) Van Megen, W.; Pusey, P. N. Dynamic Light-Scattering Study of the Glass Transition in a Colloidal Suspension. *Phys. Rev. A* **1991**, *43* (10), 5429–5441.
- (2) Holthoff, H.; Egelhaaf, S. U.; Borkovec, M.; Schurtenberger, P.; Sticher, H. Coagulation Rate Measurements of Colloidal Particles by Simultaneous Static and Dynamic Light Scattering. *Langmuir* **1996**, *12* (23), 5541–5549.
- (3) Melik, D. H.; Fogler, H. S. Turbidimetric Determination of Particle Size Distributions of Colloidal Systems. *J. Colloid Interface Sci.* **1983**, *92* (1), 161–180.
- (4) Brause, R.; Möltgen, H.; Kleinermanns, K. Characterization of Laser-Ablated and Chemically Reduced Silver Colloids in Aqueous Solution by UV/VIS Spectroscopy and STM/SEM Microscopy. *Appl. Phys. B Lasers Opt.* **2002**, *75* (6–7), 711–716.
- (5) Crocker, J.; Grier, D. Methods of Digital Video Microscopy for Colloidal Studies. *J. Colloid Interface Sci.* **1996**, *179* (1), 298–310.
- (6) Boek, E. S.; Coveney, P. V.; Cross, H.; Road, M. Simulating the Rheology of Dense Colloidal Suspensions Using Dissipative Particle Dynamics. *Phys. Rev. E* **1997**, *55* (3), 3124–3133.
- (7) Bergenholtz, J.; Brady, J. F.; Vicic, M. The Non-Newtonian Rheology of Dilute Colloidal Suspensions. *J. Fluid Mech.* **2002**, *456*, 239–275.
- (8) Lee, Y. S.; Wagner, N. J. Dynamic Properties of Shear Thickening Colloidal Suspensions. *Rheol. Acta* **2003**, *42* (3), 199–208.
- (9) Pozzo, D. C.; Walker, L. M. Small-Angle Neutron Scattering of Silica Nanoparticles Templated in PEO-PPO-PEO Cubic Crystals. *Colloids Surfaces A Physicochem. Eng. Asp.* **2007**, *294* (1–3), 117–129.
- (10) Sirota, E. B.; Ou-Yang, H. D.; Sinha, S. K.; Chaikin, P. M.; Axe, J. D.; Fujii, Y. Complete Phase Diagram of a Charged Colloidal System: A Synchrotron X-Ray Scattering Study. *Phys. Rev. Lett.* **1989**, *62* (13), 1524–1527.
- (11) Fatisson, M.; Domingos, R. F.; Wilkinson, K. J.; Tufenkji, N. Deposition of TiO₂ Nanoparticles onto Silica Measured Using a Quartz Crystal Microbalance with Dissipation Monitoring. *Langmuir* **2009**, *25* (11), 6062–6069.
- (12) de Hoog, E. H. A.; Lekkerkerker, H. N. W.; Schulz, J.; Findenegg, G. H. Ellipsometric Study of the Liquid/Liquid Interface in a Phase-Separated Colloid–Polymer Suspension. *J. Phys. Chem. B* **1999**, *103* (48), 10657–10660.
- (13) Vignati, E.; Piazza, R.; Lockhart, T. P. Pickering Emulsions: Interfacial Tension, Colloidal Layer Morphology, and Trapped-Particle Motion. *Langmuir* **2003**, *19* (17), 6650–6656.
- (14) Drelich, J.; Long, J.; Xu, Z.; Masliyah, J.; Nalaskowski, J.; Beauchamp, R.; Liu, Y. AFM Colloidal Forces Measured between Microscopic Probes and Flat Substrates in Nanoparticle Suspensions. *J. Colloid Interface Sci.* **2006**, *301* (2), 511–522.

- (15) Jean, B.; Dubreuil, F.; Heux, L.; Cousin, F. Structural Details of Cellulose Nanocrystals/polyelectrolytes Multilayers Probed by Neutron Reflectivity and AFM. *Langmuir* **2008**, *24* (7), 3452–3458.
- (16) Hildebrandt, P.; Stockburger, M. Surface-Enhanced Resonance Raman Spectroscopy of Rhodamine 6G Adsorbed on Colloidal Silver. *J. Phys. Chem.* **1984**, *88* (24), 5935–5944.
- (17) Kung, K. H. S.; Hayes, K. F. Fourier Transform Infrared Spectroscopic Study of the Adsorption of Cetyltrimethylammonium Bromide and Cetylpyridinium Chloride on Silica. *Langmuir* **1993**, *9* (1), 263–267.
- (18) Christopher, G. F.; Anna, S. L. Microfluidic Methods for Generating Continuous Droplet Streams. *J. Phys. D. Appl. Phys.* **2007**, *40* (19), 319–336.
- (19) Teh, S.-Y.; Lin, R.; Hung, L.; Lee, A. P. Droplet Microfluidics. *Lab Chip* **2008**, *8*, 198–220.
- (20) Seemann, R.; Brinkmann, M.; Pfohl, T.; Herminghaus, S. Droplet Based Microfluidics. *Rep. Prog. Phys.* **2012**, *75*, 016601:1-41.
- (21) Anna, S. L. Droplets and Bubbles in Microfluidic Devices. *Annu. Rev. Fluid Mech.* **2016**, *48* (1), 285–309.
- (22) Ahn, K.; Kerbage, C.; Hunt, T. P.; Westervelt, R. M.; Link, D. R.; Weitz, D. A. Dielectrophoretic Manipulation of Drops for High-Speed Microfluidic Sorting Devices. *Appl. Phys. Lett.* **2006**, *88* (2), 1–3.
- (23) Fidalgo, L. M.; Whyte, G.; Bratton, D.; Kaminski, C. F.; Abell, C.; Huck, W. T. S. From Microdroplets to Microfluidics: Selective Emulsion Separation in Microfluidic Devices. *Angew. Chemie - Int. Ed.* **2008**, *47* (11), 2042–2045.
- (24) Guo, F.; Ji, X. H.; Liu, K.; He, R. X.; Zhao, L. B.; Guo, Z. X.; Liu, W.; Guo, S. S.; Zhao, X. Z. Droplet Electric Separator Microfluidic Device for Cell Sorting. *Appl. Phys. Lett.* **2010**, *96* (19).
- (25) Shikida, M.; Takayanagi, K.; Inouchi, K.; Honda, H.; Sato, K. Using Wettability and Interfacial Tension to Handle Droplets of Magnetic Beads in a Micro-Chemical-Analysis System. *Sensors Actuators, B Chem.* **2006**, *113* (1), 563–569.
- (26) Franke, T.; Abate, A. R.; Weitz, D. A.; Wixforth, A. Surface Acoustic Wave (SAW) Directed Droplet Flow in Microfluidics for PDMS Devices. *Lab Chip* **2009**, *9* (18), 2625.
- (27) Baroud, C. N.; Delville, J. P.; Gallaire, F.; Wunenburger, R. Thermocapillary Valve for Droplet Production and Sorting. *Phys. Rev. E - Stat. Nonlinear, Soft Matter Phys.* **2007**, *75* (4), 1–5.
- (28) Song, H.; Tice, J. D.; Ismagilov, R. F. A Microfluidic System for Controlling Reaction Networks in Time. *Angew. Chemie - Int. Ed.* **2003**, *42* (7), 768–772.
- (29) Shestopalov, I.; Tice, J. D.; Ismagilov, R. F. Multi-Step Synthesis of Nanoparticles Performed on Millisecond Time Scale in a Microfluidic Droplet-Based System. *Lab Chip* **2004**, *4* (4), 316.

- (30) Jeong, W. J.; Kim, J. Y.; Choo, J.; Lee, E. K.; Han, C. S.; Beebe, D. J.; Seong, G. H.; Lee, S. H. Continuous Fabrication of Biocatalyst Immobilized Microparticles Using Photopolymerization and Immiscible Liquids in Microfluidic Systems. *Langmuir* **2005**, *21* (9), 3738–3741.
- (31) He, M.; Edgar, J. S.; Jeffries, G. D. M.; Lorenz, R. M.; Shelby, J. P.; Chiu, D. T. Selective Encapsulation of Single Cells and Subcellular Organelles into Picoliter- and Femtoliter-Volume Droplets. *Anal. Chem.* **2005**, *77* (6), 1539–1544.
- (32) Theberge, A. B.; Courtois, F.; Schaerli, Y.; Fischlechner, M.; Abell, C.; Hollfelder, F.; Huck, W. T. S. Microdroplets in Microfluidics: An Evolving Platform for Discoveries in Chemistry and Biology. *Angew. Chemie - Int. Ed.* **2010**, *49* (34), 5846–5868.
- (33) Vyawahare, S.; Griffiths, A. D.; Merten, C. A. Miniaturization and Parallelization of Biological and Chemical Assays in Microfluidic Devices. *Chem. Biol.* **2010**, *17* (10), 1052–1065.
- (34) Evans, H. M.; Surenjav, E.; Priest, C.; Herminghaus, S.; Seemann, R.; Pfohl, T. In Situ Formation, Manipulation, and Imaging of Droplet-Encapsulated Fibrin Networks. *Lab Chip* **2009**, *9* (13), 1933.
- (35) Zheng, B.; Roach, L. S.; Ismagilov, R. F. Screening of Protein Crystallization Conditions on a Microfluidic Chip Using Nanoliter-Size Droplets. *J. Am. Chem. Soc.* **2003**, *125* (37), 11170–11171.
- (36) Shim, J.; Cristobal, G.; Link, D. R.; Thorsen, T.; Fraden, S. Using Microfluidics to Decouple Nucleation and Growth of Protein Crystals. *Cryst. Growth Des.* **2007**, *7* (11), 2192.
- (37) Shim, J.; Patil, S. N.; Hodgkinson, J. T.; Bowden, S. D.; Spring, D. R.; Welch, M.; Huck, W. T. S.; Hollfelder, F.; Abell, C. Controlling the Contents of Microdroplets by Exploiting the Permeability of PDMS. *Lab Chip* **2011**, *11*, 1132–1137.
- (38) Solvas, X. C.; Turek, V.; Prodromakis, T.; Ede, J. B. Microfluidic Evaporator for ON-Chip Sample Concentration. *Lab Chip* **2012**, *12*, 4049–4054.
- (39) Shirk, K.; Steiner, C.; Kim, J. W.; Marquez, M.; Martinez, C. J. Assembly of Colloidal Silica Crystals Inside Double Emulsion Drops. *Langmuir* **2013**, *29* (38), 11849–11857.
- (40) Shim, J. U.; Cristobal, G.; Link, D. R.; Thorsen, T.; Jia, Y. W.; Piattelli, K.; Fraden, S. Control and Measurement of the Phase Behavior of Aqueous Solutions Using Microfluidics. *J. Am. Chem. Soc.* **2007**, *129*, 8825–8835.
- (41) Ziane, N.; Guirardel, M.; Leng, J.; Salmon, J. Drying with No Concentration Gradient in Large Microfluidic Droplets. *Soft Matter* **2015**, *11*, 3637–3642.
- (42) Nandy, L.; Dutcher, C. S. Phase Behavior of Ammonium Sulfate with Organic Acid Solutions in Aqueous Aerosol Mimics Using Microfluidic Traps. *J. Phys. Chem. B* **2018**, *Accepted*.
- (43) Bleier, B. J.; Anna, S. L.; Walker, L. M. Microfluidic Droplet-Based Tool To Determine Phase Behavior of a Fluid System with High Composition Resolution. *J. Phys. Chem. B*

2018, acs.jpcc.8b01013.

- (44) Carroll, N. J.; Rathod, S. B.; Derbins, E.; Mendez, S.; Weitz, D. A.; Petsev, D. N. Droplet-Based Microfluidics for Emulsion and Solvent Evaporation Synthesis of Monodisperse Mesoporous Silica Microspheres. **2008**, No. 18, 658–661.
- (45) Dendukuri, D.; Doyle, P. S. The Synthesis and Assembly of Polymeric Microparticles Using Microfluidics. *Adv. Mater.* **2009**, *21* (41), 4071–4086.
- (46) Chen, C. H.; Shah, R. K.; Abate, A. R.; Weitz, D. A. Janus Particles Templated from Double Emulsion Droplets Generated Using Microfluidics. *Langmuir* **2009**, *25* (8), 4320–4323.
- (47) Hung, L.; Teh, S.; Lee, A. P. PLGA Micro/Nanosphere Synthesis by Droplet Microfluidic Solvent Evaporation and Extraction Approaches. *Lab Chip* **2010**, 1820–1825.
- (48) Shum, H. C.; Abate, A. R.; Lee, D.; Studart, A. R.; Wang, B.; Chen, C.-H.; Thiele, J.; Shah, R. K.; Krummel, A.; Weitz, D. A. Droplet Microfluidics for Fabrication of Non-Spherical Particles. *Macromol. Rapid Commun.* **2010**, *31*, 108–118.

Chapter 2. Background

2.1 Droplets

2.1.1 Droplet production

For a droplet to exist, it is required that a dispersed droplet phase (sample) is contained within and completely surrounded by a continuous outer phase fluid. The most common material for microfluidic devices is polydimethylsiloxane (PDMS) due to its low cost, elasticity, and permeability. PDMS is naturally hydrophobic, making droplet production of aqueous or polar droplets in a nonpolar continuous fluid simple.^{1,2} However, much progress has been made tuning the PDMS surface wetting conditions to flip the phases and create oil-in-water droplets³⁻⁵ and even droplets within droplets.⁶

To physically produce droplets, multiple methods have been developed and well characterized, each containing benefits and drawbacks for specific applications. T-junction droplet production is arguably one of the simplest droplet production techniques. This technique requires two fluid streams to meet at a “T” shaped intersection. The continuous phase fluid flows along the horizontal channel and the dispersed phase flows along the vertical channel. Droplet size, frequency, and pinching technique have been well studied and depend on magnitude of the flow rates, channel sizes, capillary number, and flow rate ratios between the continuous and dispersed phases.^{7,8}

Flow focusing is an alternative method to produce microfluidic droplets and is useful for very rapid droplet production (up to 1000 drops/s),² precise droplet control, and production of small droplets even by microfluidic standards via tip streaming (single micrometer sized droplets).⁹ Flow focusing functions by having a dispersed phase stream surrounded by a

continuous fluid stream on two sides and flowed through a small opening. As the fluid elements travel through the opening, droplets are forced to pinch off depending on the overall flow rates, flow rate ratios, interfacial tension, and opening size.¹

A third approach to droplet production, and used for the millifluidic work in this thesis, is co-flow droplet production. With co-flow, an inner capillary containing the dispersed phase fluid is threaded concentrically through a larger capillary containing the outer phase fluid. With appropriate wetting conditions, droplets of dispersed phase are created reproducibly with fine droplet size control.^{10,11} Droplet size is controlled by the channel dimensions, the capillary number, the flow rate ratio, and the cross-sectional area ratio.¹ Co-flow is an excellent choice for millifluidic droplet production due to the simplicity of device setup and the availability of commercial tubing for inner and outer capillary choice.

A final approach to droplet production, used for microfluidic work in this thesis, is to utilize hydrodynamic traps to produce and store droplets. This type of droplet production is useful for experiments where samples must be maintained and observed for extended periods of time without moving or coalescing. The technique was originally devised Boukellal *et al.* and Bithi and Vanapalli.¹²⁻¹⁴ With this method, long slugs of droplet phase fluid are flowed through a device and into a droplet trap. A continuous phase fluid slug is then injected behind the dispersed phase slug and used to pinch droplets off inside of the trap. The ability to pinch off droplets depends largely on the capillary number of the system. This is controlled by varying the flow rates (varies the velocity), the outer phase fluid (varies viscosity), or adding a surfactant to the outer phase (varies interfacial tension).

2.1.2 *Microfluidic versus millifluidic droplets*

As mentioned previously, microfluidic droplets have been utilized extensively since the inception of the microfluidic device for applications ranging from particle synthesis to biological assays.² The major advantages of microfluidic devices arise from scaling down and working in regimes unattainable on the macroscale. Droplets on the microfluidic length scale are typically on the order of tens to hundreds of micrometers with volumes in the high picoliter to low nanoliter range. At this small length scale, Reynolds numbers are low ($O\sim 0.1-1$) and systems are dominated by interfacial forces as opposed to inertial or viscous forces. Flow is slow, laminar, and reversible, leading to controlled, predictable streamlines.¹⁵ Peclet number is typically $O(1000)$ with convection dominating diffusion of material. Surface area-to-volume ratio is orders of magnitude larger than bulk phase samples, providing a mechanism for dehydration of material through immiscible fluids.^{16,17} In addition, device fabrication has been perfected since its inception and complex, multilayered networks are now simple to produce.

Performing experiments at microfluidic length scales has drawbacks compared to larger scale experiments under certain conditions. Due to the low Reynolds number and laminar flow, mixing at the micrometer length scale is challenging and specific techniques must be integrated to induce homogenous mixing.¹⁸ Because of dominating interfacial forces, wetting conditions can cause unfavorable interactions if not accounted for. The high surface area-to-volume ratio makes experiments of dilute surface active material problematic, as depletion of the material to the interface can induce changes in bulk concentration. Finally, spectroscopic measurements are difficult due to the small path length of material ($\sim 100 \mu\text{m}$) and relatively large path lengths of PDMS device material (mm).

Table 2.1: Characteristic dimensionless groups and droplet information for comparison between microfluidic and millifluidic droplets

	Flow Rate ($\mu\text{L}/\text{min}$)	Reynolds Number ($\rho u D/\mu$)	Peclet Number (uL/D)	Capillary Number ($u\mu/\gamma$)	Bond Number ($\Delta\rho g L^2/\gamma$)	Path Length (mm)	Droplet Volume (nL)	Droplet Surface Area (mm^2)	Surface Area:Volume Ratio ($1/\text{mm}$)
Microfluidic	1-10	0.1-1	100-1000	10^{-4} - 10^{-5}	10^{-3}	0.05-0.1	1-25	0.1-1	30-250
Millifluidic	10-100	01-1	10-100	10^{-5} - 10^{-6}	0.1	0.5-5	1000-25000	1-10	2-10

Droplets produced in millifluidic devices are orders of magnitude larger than those produced with microfluidic devices. Droplets have characteristic length scales O(mm) and volumes in the μL range. Table 2.1 shows the comparative differences of characteristic parameters between microfluidic and millifluidic experiments performed in this work. Most notably, the volume of millifluidic droplets is approximately 1000 times that of microfluidic systems with 1 to 2 orders of magnitude less surface area per volume. This results in an infeasible amount of time necessary for an aqueous droplet to dehydrate in an oil continuous phase, creating the potential for long term stability experiments. In addition, the path length of millifluidic devices is on the order of millimeters, providing ample material for inline measurements including optical absorbance, neutron scattering, X-ray scattering, light scattering, and Raman spectroscopy to be performed.

2.2 Colloidal Suspensions

2.2.1 Stability of particulate suspensions

Particle based colloidal suspensions consist of small sized (nanometer to micrometer) solid matter dispersed in a liquid solvent. A suspension is not the same as a solution, for a solution is comprised of one material dissolved in another down to the molecular level. Particles are known to exert strong attractive forces through van der Waals interactions, but only at close

distances. As particles diffuse through a liquid medium, random collisions will occur and particles can fall into a potential well and stick together if attractive forces are strong enough. When aggregates become large enough, gravity will dominate over diffusion and particles will sediment and induce phase separation of the material. A real world example of this phenomenon is old paint that separates into a top liquid layer and a bottom solid layer if left undisturbed for long enough.

In order to delay aggregation, stabilizing mechanisms have been developed to counteract attractive van der Waals forces. There are two stabilization mechanisms: steric stabilization and electrostatic stabilization. Steric stabilization involves adsorbing material on particle surfaces to act like a fine brush, resistant to bending. Electrostatic stabilization involves charging the particle surface with same-sign charge in order to repel two approaching particles. It is important to note that these stabilization mechanisms will never permanently stabilize the material, but only extend the time until aggregation occurs. Aggregation is a statistical phenomenon, and repulsion simply lowers the probability that two approaching particles will aggregate. The balance between attractive and repulsive interparticle interactions is discussed much more in depth in Chapter 6.

2.2.2 Phase changes

When colloidal systems become unstable, there are a few types of phase changes that can occur based on the components of the system and their relative concentrations. One of the most common phase changes for particulate systems is flocculation and sedimentation of large aggregate structures.^{19,20} This occurs when colloidal aggregates become large enough to be sedimented by gravitational forces. If aggregated particles form loose, flocculated networks instead of tight, aggregated structures, a colloidal gel can form.^{21,22} If the particles become so

highly concentrated that they create cages around one another and arrest diffusive motion of their nearest neighbors, a colloidal glass will form.²³ In addition, there are other attractive forces such as depletion interactions that can induce liquid-liquid phase separation or even solid-liquid-gas phase separation at appropriate concentrations and particle sizes.²⁴

In all of these phase separation mechanisms, there are two underlying parameters that determine the mechanism of phase behavior. The first controlling parameter is the interparticle potential. The relationship and magnitude of attractive and repulsive forces determine the type of phase change that can occur. The interparticle potential can be changed by varying the particle size, particle type, particle shape, temperature, pH, electrolyte concentration, addition of polymer, and addition of surfactant among other possibilities. The second important parameter is the concentration of the system. Stability is largely concentration dependent, since it is a statistical phenomenon, and higher concentration results in more particle collisions. In this work, both the interparticle potential and system concentration are independently controlled and varied via droplet-based experiments to investigate stability and phase behavior of multiple particulate colloidal suspensions.

2.3 References

- (1) Christopher, G. F.; Anna, S. L. Microfluidic Methods for Generating Continuous Droplet Streams. *J. Phys. D: Appl. Phys.* **2007**, *40* (19), 319–336.
- (2) Seemann, R.; Brinkmann, M.; Pfohl, T.; Herminghaus, S. Droplet Based Microfluidics. *Rep. Prog. Phys.* **2012**, *75*, 016601:1-41.
- (3) Okushima, S.; Nisisako, T.; Torii, T.; Higuchi, T. Controlled Production of Monodisperse Double Emulsions by Two-Step Droplet Breakup in Microfluidic Devices. *Langmuir* **2004**, *20* (23), 9905–9908.
- (4) Xu, J. H.; Li, S. W.; Tan, J.; Wang, Y. J.; Luo, G. S. Preparation of Highly Monodisperse Droplet in T-Junction Microfluidic Device. *AIChE J.* **2006**, *52* (9), 3005–3010.
- (5) Chae, S.-K.; Lee, C.-H.; Lee, S. H.; Kim, T.-S.; Kang, J. Y. Oil Droplet Generation in PDMS Microchannel Using an Amphiphilic Continuous Phase. *Lab Chip* **2009**, *9* (13), 1957.
- (6) Utada, A. S.; Chu, L. Y.; Fernandez-Nieves, A.; Link, D. R.; Holtze, C.; Weitz, D. A. Dripping, Jetting, Drops, and Wetting: The Magic of Microfluidics. *MRS Bull.* **2007**, *32* (9), 702–708.
- (7) Garstecki, P.; Fuerstman, M. J.; Stone, A.; Whitesides, G. M. Formation of Droplets and Bubbles in a Microfluidic T-Junction - Scaling and Mechanism of Break-Up. *Lab Chip* **2006**, *6*, 437–446.
- (8) De Menech, M.; Garstecki, P.; Jousse, F.; Stone, H. a. Transition from Squeezing to Dripping in a Microfluidic T-Shaped Junction. *J. Fluid Mech.* **2008**, *595*, 141–161.
- (9) Anna, S. L.; Mayer, H. C. Microscale Tipstreaming in a Microfluidic Flow Focusing Device. *Phys. Fluids* **2006**, *18* (12).
- (10) Lorber, N.; Pavageau, B.; Mignard, E.; Laboratoire, U. M. R.; Schweitzer, A. A. Droplet-Based Millifluidics as a New Miniaturized Tool to Investigate Polymerization Reactions. *Macromolecules* **2010**, *43*, 5524–5529.
- (11) Lorber, N.; Sarrazin, F.; Guillot, P.; Panizza, P.; Colin, A.; Pavageau, B.; Hany, C.; Maestro, P.; Marre, S.; Delclos, T.; Aymonier, C.; Subra, P.; Prat, L.; Mignard, E. Some Recent Advances in the Design and the Use of Miniaturized Droplet-Based Continuous Process : Applications in Chemistry and High-Pressure Microflows. *Lab Chip* **2011**, *11*, 779–787.
- (12) Boukellal, H.; Selimovic, S.; Jia, Y.; Cristobal, G.; Fraden, S. Simple, Robust Storage of Drops and Fluids in a Microfluidic Device. *Lab Chip* **2009**, *9*, 331–338.
- (13) Bithi, S. S.; Vanapalli, S. A. Behavior of a Train of Droplets in a Fluidic Network with Hydrodynamic Traps. *Biomicrofluidics* **2010**, *4* (4), 44110.
- (14) Sun, M.; Bithi, S. S.; Vanapalli, S. A. Microfluidic Static Droplet Arrays with Tuneable Gradients in Material Compositions. *Lab Chip* **2011**, *11*, 3949–3952.

- (15) Song, H.; Chen, D. L.; Ismagilov, R. F. Reactions in Droplets in Microfluidic Channels. *Angew. Chemie - Int. Ed.* **2006**, *45*, 7336–7356.
- (16) Watson, J. M.; Baron, M. G. The Behaviour of Water in Poly(dimethylsiloxane). *J. Memb. Sci.* **1996**, *110*, 47–57.
- (17) Eslami, F.; Elliott, J. A. W. Stability Analysis of Microdrops During Concentrating Processes. *J. Phys. Chem. B* **2014**, *118*, 3630–3641.
- (18) Teh, S.-Y.; Lin, R.; Hung, L.; Lee, A. P. Droplet Microfluidics. *Lab Chip* **2008**, *8*, 198–220.
- (19) Allain, C.; Cloitre, M.; Wafra, M. Aggregation and Sedimentation in Colloidal Suspensions. *Phys. Rev. Lett.* **1995**, *74* (8), 1478–1481.
- (20) Phenrat, T.; Saleh, N.; Sirk, K.; Tilton, R. D.; Lowry, G. V. Aggregation and Sedimentation of Aqueous Nanoscale Zerovalent Iron Dispersions. *Environ. Sci. Technol.* **2007**, *41* (1), 284–290.
- (21) Brinker, C. J.; Scherer, G. W. Sol → Gel → Glass: I. Gelation and Gel Structure. *J. Non. Cryst. Solids* **1985**, *70* (3), 301–322.
- (22) Lu, Y.; Yin, Y.; Mayers, B. T.; Xia, Y. Modifying the Surface Properties of Superparamagnetic Iron Oxide Nanoparticles through a Sol-Gel Approach. *Nano Lett.* **2002**, *2* (3), 183–186.
- (23) Hunter, G.; Weeks, E. The Physics of the Colloidal Glass Transition. *Rep. Prog. Phys.* **2012**, *75* (6), 66501.
- (24) Ilett, S. M.; Orrock, A.; Poon, W. C. K.; Pusey, P. N. Phase Behavior of a Model Colloid-Polymer Mixture. *Phys. Rev. E* **1995**, *51* (2), 1344–1352.

Chapter 3. Materials and Methods

3.1 Materials

Continuous phase oils used in this work are mineral oil, silicone oil, and fluorinated oil. Light mineral oil is purchased from Fisher Scientific (Hampton, NH), 50 cSt and 100 cSt silicone oils are purchased from Gelest Inc. (Morrisville, PA), and fluorinated FC-70 oil is purchased from Hampton Research (Aliso Viejo, CA). All Ludox silica particles are purchased from Sigma-Aldrich (St. Louis, MO). Materials used in specific experiments will be discussed further in their respective chapters.

3.2 Microfluidic Device Fabrication

3.2.1 Mold fabrication

Microfluidic photoresist molds are created using standard photolithography techniques.¹⁻⁴ Three inch silicon wafers (Cz, P/Boron, 1-10 ohm-cm, 15 ± 2 mm) are used as a substrate material to coat with photoresist. The wafers are cleaned with a cycle of acetone, IPA, and DI water and heated on a hotplate (PMC Dataplate 720 Series Digital Hot Plate) at 200 °C for 5 minutes to completely dehydrate the surface. A spincoater (Laurell Technologies 150 mm Spin Coater Model WS-650Mz-23NPP) is used to spincoat SU-8 3050 photoresist (purchased from Microchem Corp.) onto the substrate surface in a layer approximately 100 μm thick. A spread cycle of 50 RPM and ramp speed of 85 RPM/s is performed for 20 seconds followed by a spin cycle at 1500 RPM with a ramp speed of 340 RPM/s for 30 seconds to achieve a 100 μm thick coating. Once coated, the wafer is soft baked at 65 °C for 5 minutes followed by 95 °C for 15 minutes.

After the soft bake step, the wafer is exposed to UV light for 90 seconds while covered with a transparency mask containing the geometric device design. The transparency mask specifications are 8.5" x 11", 20,000 dpi, negative, emulsion down and printed by CAD/Art Services, Inc. (Bandon, OR). After exposure, the device is post baked at 65 °C for 1 minute followed by 95 °C for 5 minutes. Finally, the wafer is developed in SU-8 developer (Microchem Corp.) for approximately 20 minutes to remove any un-cross linked photoresist, leaving designed channel structure.

3.2.2 Device fabrication

Microfluidic PDMS devices are produced with Sylgard 184 PDMS elastomer (Dow Corning, Midland, MI) using standard techniques.¹⁻⁴ The PDMS pre-polymer is first mixed with curing agent in a 10:1 ratio by mass. The mixture is stirred and de-foamed using a centrifugal mixer (Thinky Mixer AR-100). After mixing, 15.0 g of the PDMS mixture is poured onto the photoresist structured silicon wafer substrate contained in a petri dish. In addition, 15.0 g of the PDMS mixture is poured into a blank petri dish to create an unstructured PDMS slab. The two samples are degassed under vacuum for approximately 15 minutes to remove bubbles from the pouring process and then heated at 60 °C for 2 hours to increase the cross-linking and solidification rate of the mixture.

Once cooled, the PDMS device and blank PDMS slab are cut and peeled from the molds and inlet and outlet holes are punched using a tissue punch (Harris 17 Uni-Core, Tip ID 1.0mm, OD 1.26mm). They are then plasma treated with a plasma cleaner (Harrick Plasma Cleaner PDC-32G) for 1 minute to clean and hydrophilize the PDMS surfaces. The structured PDMS device and blank PDMS slab are quickly bonded together after plasma treatment and baked at 180 °C for one hour. Once cooled, the devices are cleaned with scotch tape, cut into individual

devices, and soaked in an outer phase fluid (mineral oil or silicone oil) for at least 5 days before use in an experiment.

3.3 Millifluidic Device Fabrication

Millifluidic devices for Chapter 7 experiments are created out of three layers of clear Plexiglas each 1/16" thick. The center Plexiglas layer has a serpentine track pattern laser cut into the sheet to fit the 0.680 mm I.D. PTFE tubing. The two additional Plexiglas sheets sandwich the tubing and hold the device together without deforming the tubing and are held in place by 4 screws. The front Plexiglas sheet is slightly offset vertically to allow for a small section of tubing to leave the device for an inlet and outlet stream.

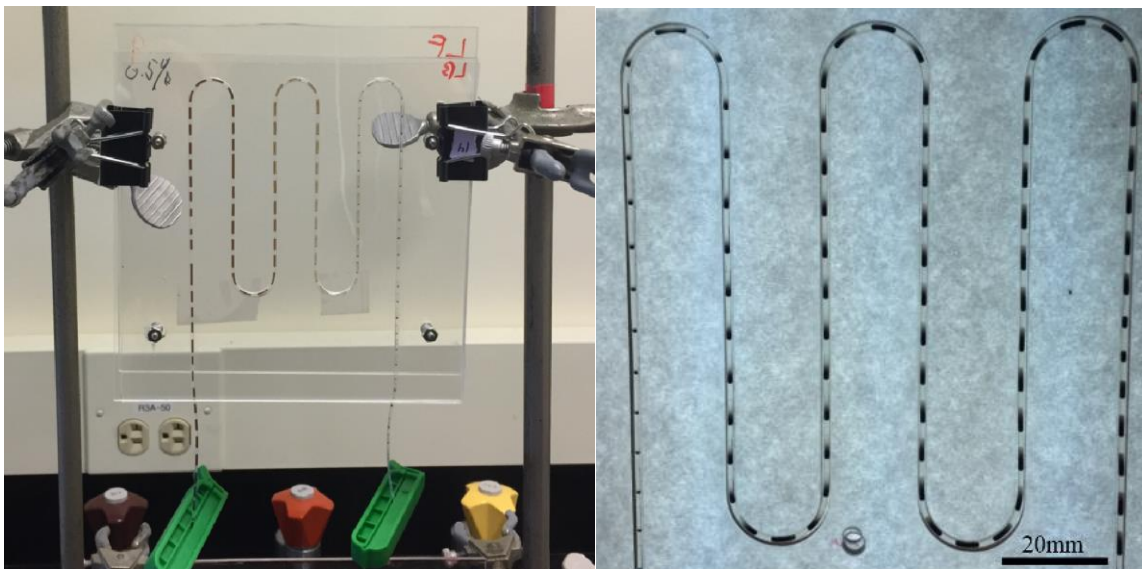


Figure 3.1: Images of millifluidic containment device containing Teflon tubing inside of a lasercut Plexiglas sheet. Droplets are contained in the device indefinitely with order 50-100 droplets per device. Devices are held vertically to detect phase separation in sedimenting droplets.

Images of the millifluidic device are shown in Figure 3.1. Once the droplets are loaded into the device, droplet flow is arrested and the inlet and outlet tubing sections are clamped with dialysis clips to seal the device and inhibit droplet motion. Once clamped, the device can be

moved to a new location and maintain droplet structure and order. Devices are held vertically to allow for detection of sedimentation along the length of a droplet.

3.4 Microfluidic Droplet Production

Microfluidic droplets are produced using hydrodynamic traps previously characterized and used in literature.⁵⁻⁸ Figure 3.2 shows the mechanism for droplet production. Initially the droplet trapped is filled with a continuous outer phase fluid, either mineral oil or 100 cSt silicone oil, to induce desirable wetting conditions. A long slug of the aqueous dispersed phase is then flowed into the trap which simultaneously fills the trap and the bypass channel. A secondary slug of continuous phase fluid is injected into the device behind the dispersed phase. When the end of the dispersed phase slug reaches the droplet trap, the viscous forces pinch off a droplet inside the trap while the remaining fluid goes around the bypass channel to fill the next droplet trap.

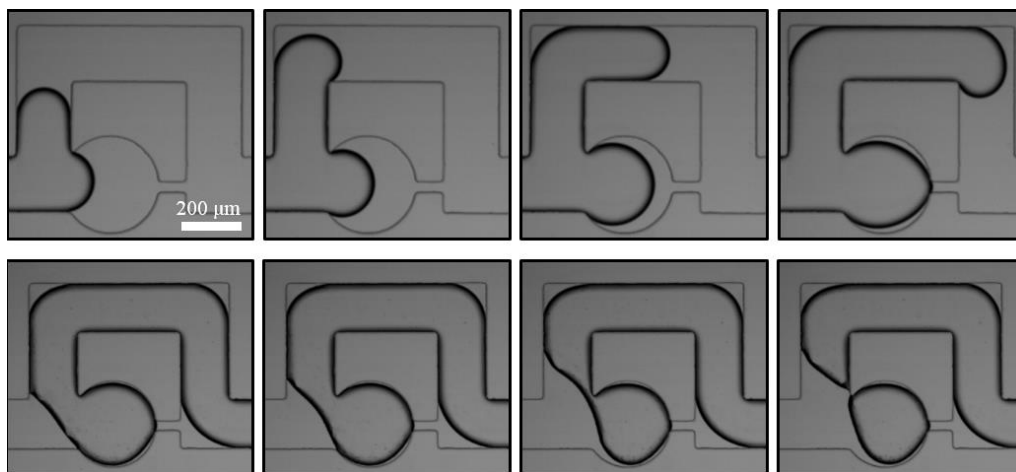


Figure 3.2: Time sequenced images of the droplet pinching mechanism for microfluidic droplet production in hydrodynamic traps. The continuous phase in mineral oil with 2 wt% Span-80 and the dispersed droplet phase is water. Scale bar in shown in top left image and corresponds to 200 μm . Images courtesy of Chris Nelson.

In order to achieve good droplet production, the capillary number should be kept approximately between $10^{-4} - 10^{-2}$.⁷ The capillary number is a balance between the viscous forces attempting to break up a droplet and the interfacial forces keeping the droplet from splitting. Neither force can be allowed to dominate too strongly. If the capillary number is too high, droplets will easily pinch off in the trap, but will also squeeze through the restriction channel and create a cascading effect where faulty upstream droplets disrupt downstream droplet production. If the capillary number is too low, droplets will not squeeze through the restriction channel, but will strongly oppose pinching and will be pulled from the trap before pinching occurs.

3.5 Millifluidic Droplet Production

3.5.1 UV-Vis experiments with 2 inlet syringe pumps

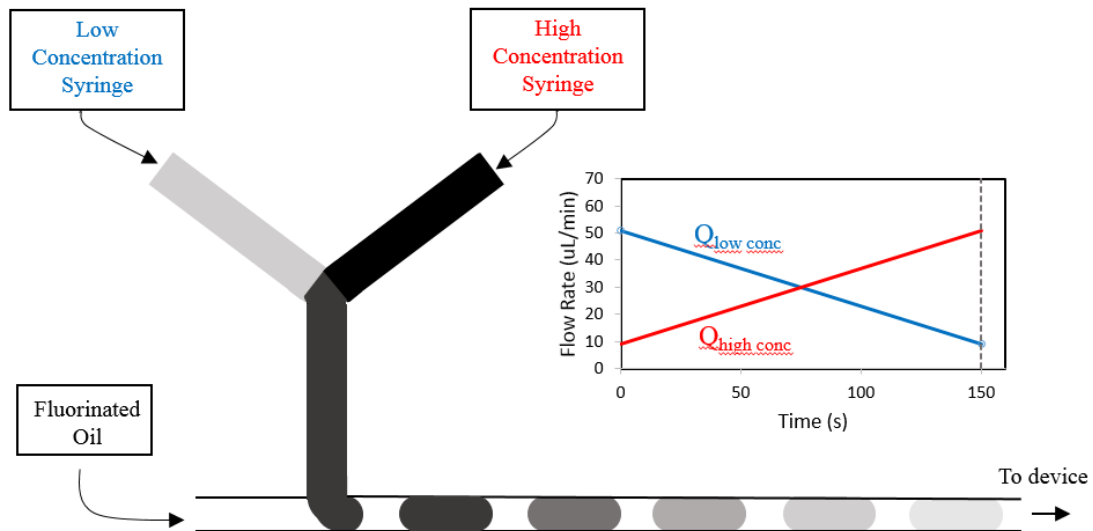


Figure 3.3: Schematic diagram and images of the experimental set up for production of droplets with a gradient in concentration. Two inlet suspensions are mixed (low and high concentrations) at an upstream Y-junction. Droplets of dispersed suspension are produced at the T-junction in a continuous phase of fluorinated oil. Quantitative values of flow rates during gradient production are shown in the inset.

Millifluidic droplets are produced using either a co-flow production method or a T-junction droplet production method. In both techniques, droplets are produced on the millimeter

length scale and are surrounded by a thin film of an immiscible continuous outer phase fluid on all sides. Outer phase fluids and tubing materials are selected to optimize wetting conditions and produce the most stable droplets. Fluorinated oils work best with any type of fluorinated tubing (PTFE or FEP), mineral oil works best with polyethylene (PE) tubing, and silicone oil works best with quartz capillaries.

In all millifluidic experiments, a gradient in droplet concentration is created along a droplet train of predetermined length. Droplets are produced, each with a unique composition to achieve high composition resolution along the gradient. Chapter 7 experiments use T-junction droplet production with a fluorinated oil (FC-70) outer phase fluid and PTFE tubing with an inner diameter of 0.680 mm. Chapter 8 experiments use a co-flow droplet generator with a 50 cSt silicone oil outer phase fluid and quartz tubing with an inner diameter of 2 mm. Preliminary experiments are performed in both systems to verify droplet concentration along the gradient.

Figure 3.3 demonstrates the gradient concept and outlines the T-junction droplet production technique used in Chapter 7 experiments. Two unique dispersed phase fluid streams are connected and merged with a Y-junction and flowed downstream to a T-junction. At the T-junction, the dispersed phase comes in contact with the continuous outer phase fluid of fluorinated FC-70 oil and droplets of the dispersed phase are produced similar to previous micro- and millifluidic studies.⁹⁻²³ In these experiments, pumps are programmed to have three separate sections. In the first section, droplets are produced at a constant composition to remove start up effects. After a set amount of time, the gradient is initiated and begins a linear decrease in the low concentration syringe and a linear increase of equal and opposite slope in the high concentration syringe shown in the inset of Figure 3.3. In the last section, droplets are produced at a constant composition corresponding to the final composition in the inset of Figure 3.3 to

allow for droplets to reach the detector. Small slugs of additional outer phase fluid are injected into the stream at the beginning and end of gradient production to mark the starting and ending point. The gradient time, total flow rates, and flow rate ratios all determine the number of droplets (and therefore composition resolution) of a given gradient.

Optical absorbance measurements are performed to determine the accuracy of the concentration of each droplet in a gradient and to determine the impact of flow rate ratio on accuracy of droplet concentrations in a gradient. Solutions of pure dodecane and 0.05 mg/mL Nile Red in dodecane are used as “low” and “high” concentration feeds that can be easily quantified in the resulting drops. These solutions are mixed with the same device set-up shown in Figure 3.3. Droplet concentration is calculated by measuring the absorbance through a droplet and converting using the Beer-Lambert relation show in Equation 3.1

$$A = \varepsilon CL , \tag{3.1}$$

where A is the absorbance measurement, ε is the extinction coefficient, C is the concentration of dye, and L is the path length of the material. The absorbance of the fluid is measured through the 0.680 mm PTFE tubing as a function of time using a Phototronics Series 400 Colorimetry Spectrophotometer. The absorbance is measured at a wavelength of 490 nm, the peak absorbance value for Nile Red. It is determined that a concentration of 0.05 mg/mL Nile Red falls within the linear regime of the Beer-Lambert relation. The extinction coefficient at this wavelength is determined through a series of calibration experiments to be $\varepsilon = 25400 \text{ M}^{-1}\cdot\text{cm}^{-1}$.

Droplets are produced at a constant combined dispersed flow rate of 36 $\mu\text{L}/\text{min}$ and a continuous phase flow rate of 15 $\mu\text{L}/\text{min}$ for 12 minutes to remove start up effects. During this time, the dispersed phase is mixed at a composition determined by the maximum flow rate ratio of

the dispersed phase components for the particular experiment. For example, if the maximum flow rate ratio is equal to 6, then the pure dodecane has a flow rate of 30.86 $\mu\text{L}/\text{min}$ and the Nile Red dodecane solution has a flow rate of 5.14 $\mu\text{L}/\text{min}$. After 12 minutes of constant flow rates, the gradient in the dispersed phase is initiated and varies such that the ratio of pure solution:Nile Red solution changes from $x:1$ to $1:x$ over 255 seconds, where x is the maximum flow rate ratio of the individual experiment. 255 seconds is the time required at the given flow rates for the fluid to fill all the tubing in the millifluidic device.

Figure 3.4 demonstrates the results for four separate maximum flow rate ratios, starting with a ratio of 4 and increasing up to an infinite ratio. The infinite flow rate ratio means the pure dodecane pump is set to the total dispersed phase flow rate (36 $\mu\text{L}/\text{min}$) and the Nile Red pump is set to a flow rate of zero for the first 12 minutes. The measured absorbance in each experiment is plotted as a solid black line and alternates between the droplets and the outer phase fluorinated oil (reference value) as the droplets are flowed continuously. Each plateau with a positive value is an absorbance measurement within a droplet and each plateau near a value of zero is a measurement of the fluorinated oil spacer between the droplets. The sharp jumps between plateaus are measurements taken through the curved endcap of a droplet, leading to additional scattering interpreted as absorbance. Measurements taken through the curved endcaps are ignored in further analysis. The position of the first droplet in the gradient is located by either an abnormally large plateau for a fluorinated oil spacer or an abnormally short plateau for a droplet near the 12 minute 20 second mark due to the extra injection of continuous phase fluid that marks the starting point of the gradient. Similarly, the final droplet is located using the same method near the 16 minute 35 second mark. All measurements within a single droplet plateau are averaged and the resulting value is displayed as a red circle. The green line shows the predicted absorbance based on the

position of the droplet in the gradient and the extinction coefficient of Nile Red. The important result to observe is the difference in each case between the predicted value (green line) and the measured droplet value (red points).

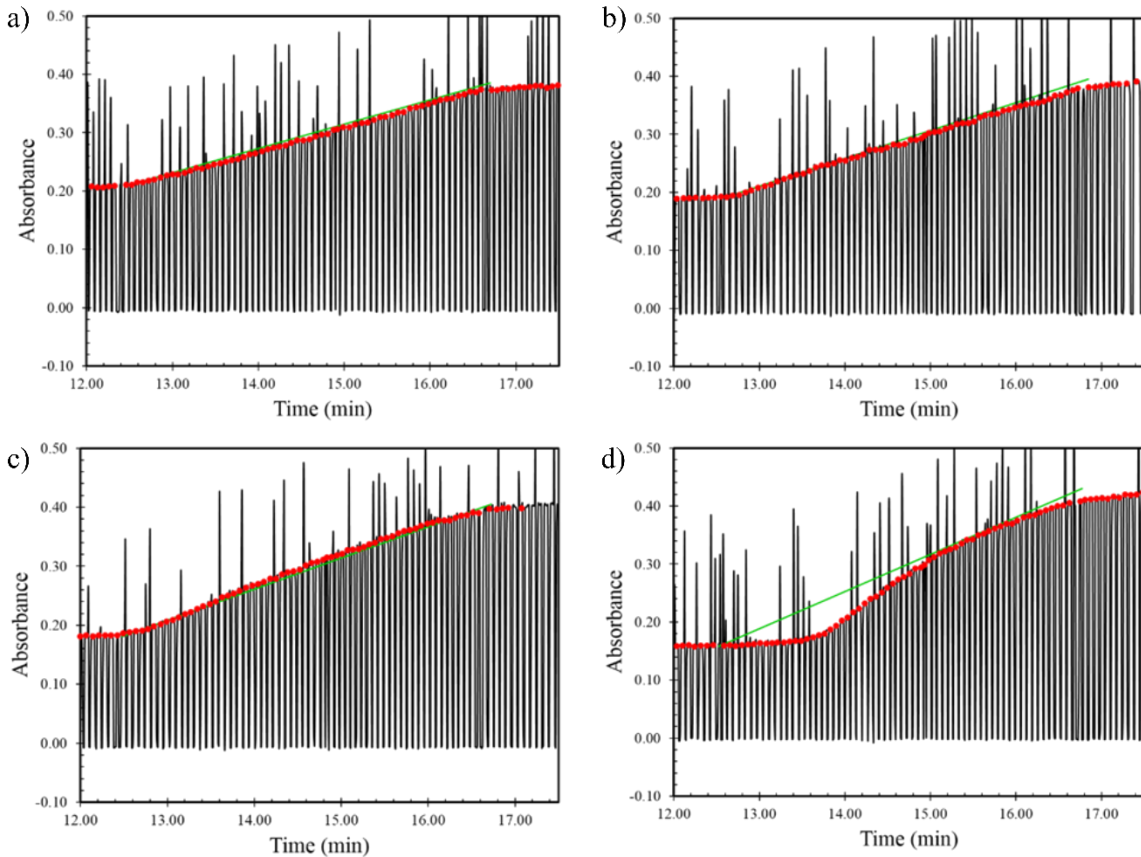


Figure 3.4: Absorbance measurements to determine the concentration accuracy of droplet production. In each graph, the solid black lines are the absorbance data as a function of time. The green line demonstrates the calculated expected absorbance of each droplet starting at the beginning of the droplet gradient. The red points plot the average absorbance of each measured droplet. The graphs have a maximum flow rate ratio of (a) 4, (b) 6, (c) 8, and (d) infinite.

From the results, it is clear that maximum flow rate ratios of 4, 6, and 8 have good agreement between the predicted and measured droplet concentrations. In each case, the green line tracks the red points well with the average difference between those values being less than 2 percent and a maximum difference between those values of approximately 4 percent. In the experiment with an infinite flow rate ratio, there is a large discrepancy between the predicted and

measured values with an average difference of 8 percent and a maximum difference of 21 percent. Figure 3.4d demonstrates a 14 drop lag between the first droplet in the gradient and the first droplet with an increase in absorbance. This is likely due to a pressure build-up at the Y-junction that needs to be overcome by the Nile Red solution once the pump is engaged

Additional droplet experiments are performed to determine the effect of overall flow rate and flow rate ratio between the dispersed and continuous phases on droplet size and reproducibility. 50 cSt silicone oil, 350 cSt silicone oil, and FC-70 fluorinated oil are used as different outer phase fluids. Pure DI water and water with 1 mM KMnO_4 are used as the two dispersed phase inlet streams discussed in Figure 3.3. Untreated 1 mm ID borosilicate capillaries are used as the outer capillary and 0.5 mm ID, 0.9 mm OD borosilicate capillaries are used as the inner capillary for co-flow droplet production. The objective of this preliminary work is to determine the flow rates at which droplet production is consistent and reproducible along the gradient, but provides enough droplet residence time in-beam to collect measurable scattering curves (1-2 minutes per droplet).

Figure 3.5 shows the residence time of individual droplets in the UV-Vis detector as a function of continuous and dispersed phase flow rates. Each point corresponds to a single droplet for a given set of conditions shown in the legend as a gradient in droplet composition is introduced. Figure 3.5a shows the absorbance of each droplet as a function of experiment time where time zero is the initiation of the gradient. Dispersed phase flow rate is defined by shape and continuous phase flow rate is defined by color as shown in the legend in Figure 3.5. Optical absorbance measurements are collected and analyzed using the same method as Figure 3.4 to determine individual droplet absorbance. 10 minute gradients and 20 minute gradients are tested over various flow rate conditions. The black lines in Figure 3.5a display the predicted absorbance for a 10

minute and 20 minute gradient based on the position of the droplet in the gradient and the absorbance value calculated using Beer-Lambert's law for a given droplet concentration with an extinction coefficient $\epsilon = 2450 \text{ M}^{-1}\cdot\text{cm}^{-1}$ at $\lambda = 525 \text{ nm}$ for KMnO_4 determined through calibration experiments.

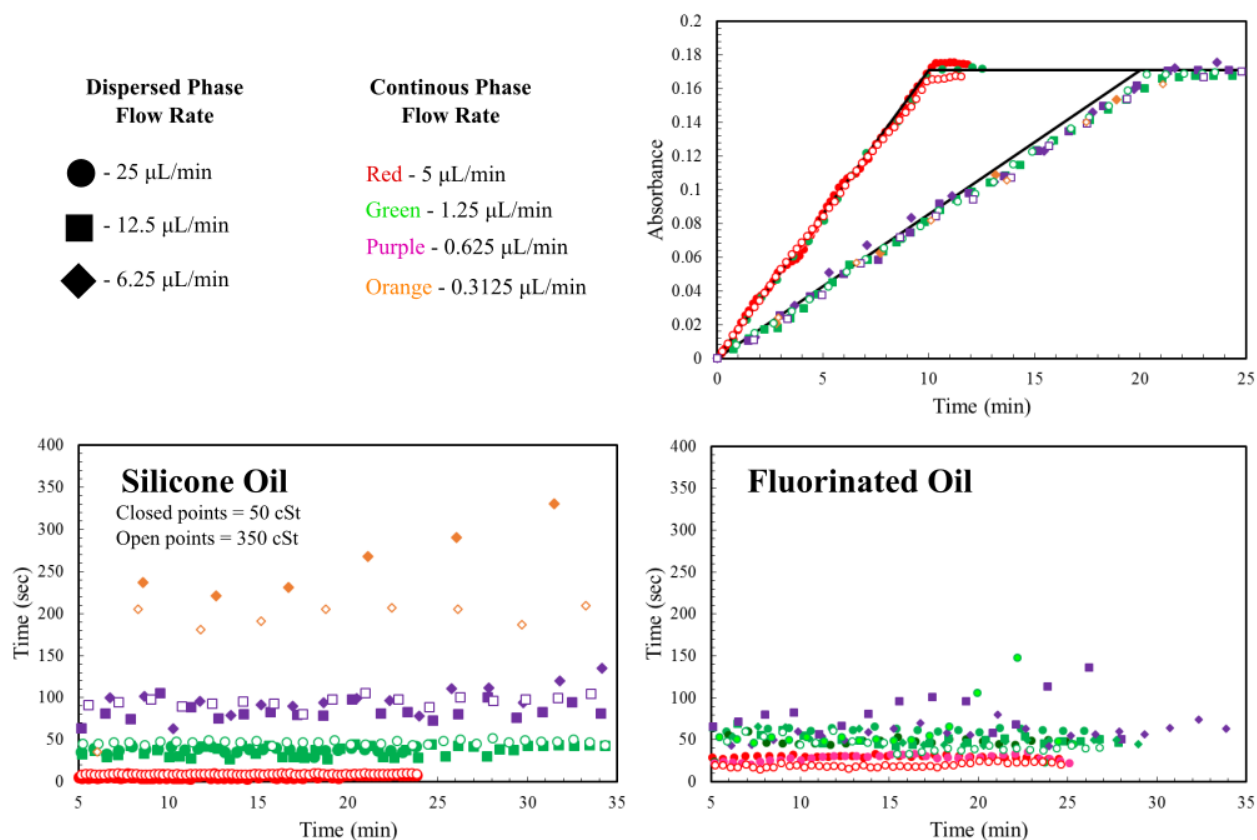


Figure 3.5: Droplet absorbance and size measurements of aqueous droplets produced in a continuous outer phase oil (silicone oil or fluorinated oil) using co-flow droplet production. Gradients are formed by combining pure H_2O and 1 mM KMnO_4 . The legend containing dispersed and continuous phase flow conditions is shown in the top left. (a) Droplet absorbance as a function of time for 10 and 20 minute gradients. Black lines show predicted absorbance values and data points show measured values with the shape and color depicting flow conditions. (b-c) Droplet time spend in-beam (droplet size) for gradient experiments with a silicone oil and fluorinated oil continuous phase respectively.

Droplets along the 10 minute gradient track the predicted absorbance values well and have an average error between predicted and measured of 2%. Droplets along the 20 minute gradient track the prediction well for the first half of the gradient, but lag slightly behind on the second half with an average droplet concentration error of 4%.

With various combinations of continuous and dispersed phase flow rate, droplets are produced at different sizes and flow at different velocities. This leads to different droplet residence times in-beam for each set of conditions. Figure 3.5b shows the residence time of all droplets from Figure 3.5a where the continuous phase is silicone oil with the same shape and color coded characterization. For monodisperse droplet production, every droplet in the droplet train would have the same droplet residence time and the data set would appear as a flat horizontal line in Figure 3.5b. Large differences in droplet size begin when the continuous phase flow rate is lowered to 0.3125 $\mu\text{L}/\text{min}$.

Figure 3.5c shows the results from identical experiments performed with an FC-70 fluorinated oil continuous outer phase fluid. Droplet production with fluorinated oil was not as consistent as the silicone oil experiments, and large variations in droplet length begin at continuous phase flow rates of 0.625 and 1.25 $\mu\text{L}/\text{min}$.

3.5.2 UV-Vis experiments with 3 inlet syringe pumps

Figure 3.5 demonstrates the precise composition control available with the co-flow millifluidic droplet setup along a single linear gradient. Yet, more intricate compositional control is desired to more efficiently probe phase space and cross phase boundaries lines at different concentrations during one experiment. In addition, pumps can be programmed to perform long, complex automated procedures to minimize the need for user interaction. With the addition of a third dispersed phase inlet stream, 3 inlet pumps can be simultaneously controlled to probe nearly all of a 3-component phase diagram.

Figure 3.6a demonstrates the concept of controlling flow rate ratios to cover large composition space with a spiral pattern. Components A, B, and C can be thought of as pure components each with a unique syringe and inlet stream. Total dispersed phase flow rate is kept

constant at 20 $\mu\text{L}/\text{min}$ through the experiment. To vary composition, one of the three syringes is held constant while the other two undertake a linear gradient identical to those in Figure 3.5. For example, from node 1 to 2, the gradient varies from A:B:C flow rate ratios of 8:1:1 to 1:8:1. Syringes A and B invert their flow rates linearly over 7 minutes while syringe C remains constant. Once node 2 is reached, syringe A remains constant and syringes B and C linearly invert their flowrates to go from flow rate ratios of 1:8:1 to 1:1:8 over 7 minutes to node 3. To complete a cycle, syringes A and C invert flow rates towards node 4 while B remains constant to vary flow rate ratios from 1:1:8 to 7:1:2. The remainder of the flow rate conditions are shown in Table 3.1.

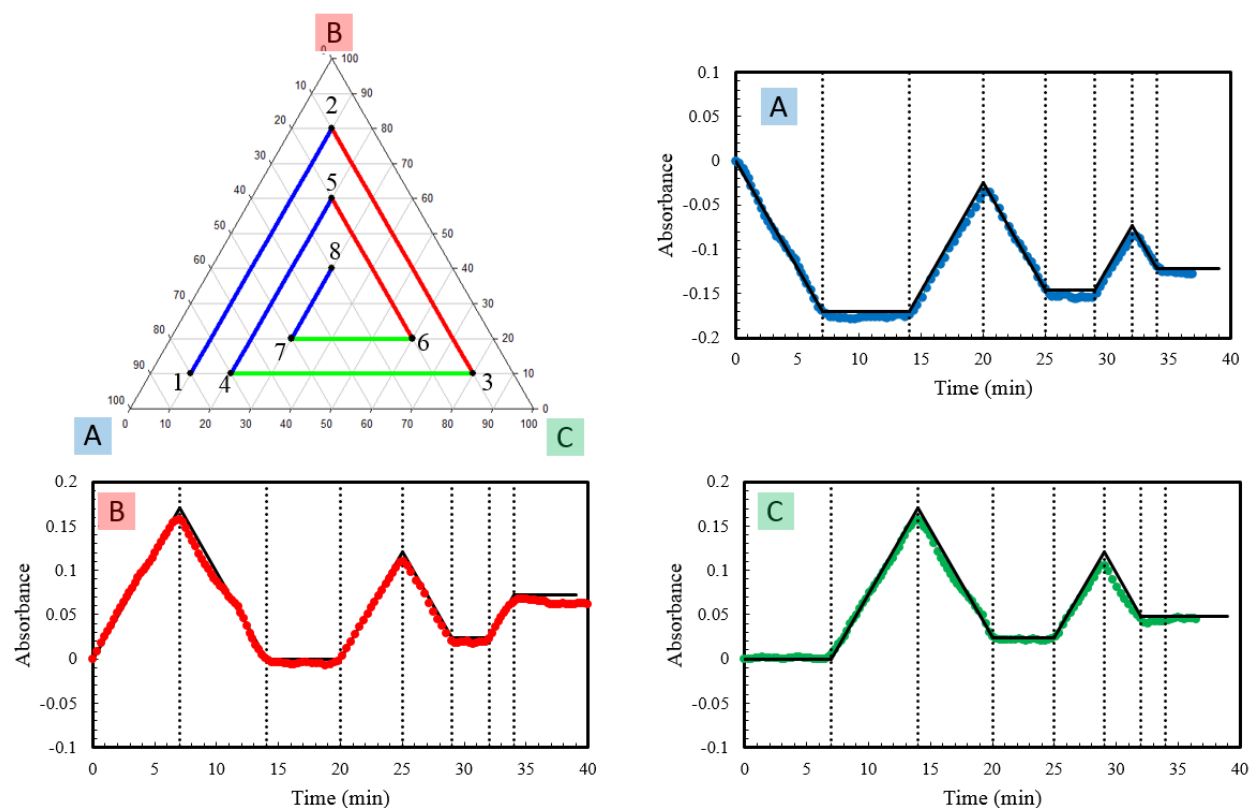


Figure 3.6: Absorbance measurements of droplets during a ternary millifluidic experiment. (a) Schematic of the flow rate composition paths starting and node 1 and progressing sequentially to node 8. (b-d) Absorbance measurements of individual droplets containing mixtures of pure water and 1 mM KMnO_4 . Data points correspond to droplet measurements, solid black lines correspond to predicted absorbance values, and dotted black lines correspond to locations where a node is reached and a new gradient begins.

Three optical absorbance droplet experiments are performed to verify droplet composition for spiral experiments by changing the syringe which contains KMnO_4 solution. KMnO_4 (1 mM) is introduced into one syringe per experiment while the other two syringes contain DI water. The predicted absorbance over the experiment is calculated using the Beer-Lambert's equation similar to results from Figure 3.5. Droplets are continuously produced along the entire spiral program and absorbance is measured every second. The combined dispersed phase flow rate is 20 $\mu\text{L}/\text{min}$ and the continuous fluorinated oil (FC-70) outer phase flow rate is 5 $\mu\text{L}/\text{min}$.

Figure 3.6b shows the absorbance results when syringe A contains the 1 mM KMnO_4 solution and syringes B and C contain water. The solid black line is the predicted absorbance and the data points are the absorbance measurements of individual droplets as a function of time. The dotted black lines show the time position when each node in Figure 3.6a is reached. Figure 3.6c shows results when syringe B contains the 1 mM KMnO_4 solution and Figure 3.6d shows results for when syringe C contains the 1 mM KMnO_4 solution. All results show good agreement between the predicted absorbance and the measured droplet absorbance with an average error of 3%, indicating a high level of compositional control using the millifluidic droplet based setup.

Table 3.1: Dispersed phase flow rate conditions for all 3 inlet syringe pumps during spiral gradient experiment. Flow rates vary linearly along each line.

	A ($\mu\text{L}/\text{min}$)	B ($\mu\text{L}/\text{min}$)	C ($\mu\text{L}/\text{min}$)	Time (min)	Total Time (min)
Line 1 Beginning	16	2	2	0	0
Line 1 End	2	16	2	7	7
Line 2 End	2	2	16	7	14
Line 3 End	14	2	4	6	20
Line 4 End	4	12	4	5	25
Line 5 End	4	4	12	4	29
Line 6 End	10	4	6	3	32
Line 7 End	6	8	6	2	34

3.6 References

- (1) Duffy, D. C.; McDonald, J. C.; Schueller, O. J. A.; Whitesides, G. M. Rapid Prototyping of Microfluidic Systems in Poly(dimethylsiloxane). *Anal. Chem.* **1998**, *70* (23), 4974–4984.
- (2) Xia, Y.; Whitesides, G. M. Soft Lithography. *Angew. Chem. Int. Ed.* **1998**, *37*, 550–575.
- (3) McDonald, J. C.; Duffy, D. C.; Anderson, J. R.; Chiu, D. T.; Wu, H.; Schueller, O. J. A.; Whitesides, G. M. Fabrication of Microfluidic Systems in Poly(dimethylsiloxane). *Electrophoresis* **2000**, *21*, 27–40.
- (4) Seemann, R.; Brinkmann, M.; Pfohl, T.; Herminghaus, S. Droplet Based Microfluidics. *Rep. Prog. Phys.* **2012**, *75*, 016601:1-41.
- (5) Boukellal, H.; Selimovic, S.; Jia, Y.; Cristobal, G.; Fraden, S. Simple, Robust Storage of Drops and Fluids in a Microfluidic Device. *Lab Chip* **2009**, *9*, 331–338.
- (6) Cohen, D. E.; Schneider, T.; Wang, M.; Chiu, D. T. Self-Digitization of Sample Volumes. *Anal. Chem.* **2010**, *82*, 5707–5717.
- (7) Bithi, S. S.; Vanapalli, S. A. Behavior of a Train of Droplets in a Fluidic Network with Hydrodynamic Traps. *Biomicrofluidics* **2010**, *4* (4), 44110.
- (8) Sun, M.; Bithi, S. S.; Vanapalli, S. A. Microfluidic Static Droplet Arrays with Tuneable Gradients in Material Compositions. *Lab Chip* **2011**, *11*, 3949–3952.
- (9) Nisisako, T.; Torii, T.; Higuchi, T. Droplet Formation in a Microchannel Network. *Lab Chip* **2002**, *2*, 24–26.
- (10) van der Graaf, S.; Nisisako, T.; Schroe, C. G. P. H.; van der Sman, R. G. M.; Boom, R. M. Lattice Boltzmann Simulations of Droplet Formation in a T-Shaped Microchannel. *Langmuir* **2006**, *22* (15), 4144–4152.
- (11) Christopher, G. F.; Anna, S. L. Microfluidic Methods for Generating Continuous Droplet Streams. *J. Phys. D. Appl. Phys.* **2007**, *40* (19), 319–336.
- (12) Garstecki, P.; Fuerstman, M. J.; Stone, A.; Whitesides, G. M. Formation of Droplets and Bubbles in a Microfluidic T-Junction - Scaling and Mechanism of Break-Up. *Lab Chip* **2006**, *6*, 437–446.
- (13) Christopher, G. F.; Noharuddin, N. N.; Taylor, J. A.; Anna, S. L. Experimental Observations of the Squeezing-to-Dripping Transition in T-Shaped Microfluidic Junctions. *Phys. Rev. E* **2008**, *78*, 1–12.
- (14) Nelson, C. W. Probing the Phase Behavior of Complex Fluids Using Microliter Droplet Reactors, 2016.
- (15) Engl, W.; Backov, R.; Panizza, P. Controlled Production of Emulsions and Particles by Milli- and Microfluidic Techniques. *Curr. Opin. Colloid Interface Sci.* **2008**, *13*, 206–216.
- (16) Trivedi, V.; Doshi, A.; Kurup, G. K.; Ereifej, E.; Vandevord, P. J.; Basu, A. S. A Modular

- Approach for the Generation , Storage , Mixing , and Detection of Droplet Libraries for High Throughput Screening. *Lab Chip* **2010**, *10* (18), 2433–2442.
- (17) Lorber, N.; Pavageau, B.; Mignard, E.; Laboratoire, U. M. R.; Schweitzer, A. A. Droplet-Based Millifluidics as a New Miniaturized Tool to Investigate Polymerization Reactions. *Macromolecules* **2010**, *43*, 5524–5529.
- (18) Lorber, N.; Sarrazin, F.; Guillot, P.; Panizza, P.; Colin, A.; Pavageau, B.; Hany, C.; Maestro, P.; Marre, S.; Delclos, T.; Aymonier, C.; Subra, P.; Prat, L.; Mignard, E. Some Recent Advances in the Design and the Use of Miniaturized Droplet-Based Continuous Process : Applications in Chemistry and High-Pressure Microflows. *Lab Chip* **2011**, *11*, 779–787.
- (19) Baraban, L.; Bertholle, F.; Salverda, M. L. M.; Bremond, N.; Panizza, P.; Baudry, J.; Arjan, J.; Visser, G. M. De. Millifluidic Droplet Analyser for Microbiology. *Lab Chip* **2011**, *11*, 4057–4062.
- (20) Wang, W. S.; Vanapalli, S. A. Millifluidics as a Simple Tool to Optimize Droplet Networks : Case Study on Drop Traffic in a Bifurcated Loop. *Biomicrofluidics* **2014**, *8* (64111), 1–23.
- (21) Lourdes, M.; Baños, M. De; Carrier, O.; Bouriat, P.; Broseta, D. Droplet-Based Millifluidics as a New Tool to Investigate Hydrate Crystallization : Insights into the Memory Effect. *Chem. Eng. Sci.* **2015**, *123*, 564–572.
- (22) Boitard, L.; Cottinet, D.; Bremond, N.; Baudry, J.; Bibette, J. Growing Microbes in Millifluidic Droplets. *Eng. Life Sci.* **2015**, *15*, 318–326.
- (23) Feuerborn, A.; Prastowo, A.; Cook, P. R.; Walsh, E. Merging Drops in a Teflon Tube, and Transferring Fluid between Them, Illustrated by Protein Crystallization and Drug Screening. *Lab Chip* **2015**, *15*, 3766–3775.

Chapter 4. Microfluidic Droplet-Based Tool to Determine Phase Behavior of a Fluid System with High Composition Resolution

4.1 Introduction

Systems containing mixtures of particles, polymers, surfactants, salts, or other additives demonstrate complex phase separation at high solute concentrations.¹⁻⁴ The ability to control and map the phase behavior of colloidal systems is needed in many types of fluid formulations, including coating, pharmaceutical, and food products. Aqueous two-phase systems (ATPS) are used extensively in bioseparation processes,⁵⁻⁸ nanomaterials separations,⁹⁻¹¹ and other synthetic processes.¹² Within ATPS, organic-inorganic systems such as polymer-salt systems have been shown to phase separate into an organic-rich phase and an organic-poor phase at high concentrations.¹³⁻¹⁷ This is likely to occur in situations in which concentrated salt solutions contain organics such as oil recovery,¹⁸⁻²⁰ oil spill cleanup,^{21,22} and even water droplets in the atmosphere.²³⁻²⁵ These systems exhibit liquid-liquid phase separation, the composition of which is dependent on a number of system parameters including the chemical composition of the organic and inorganic,^{13,16,26} the molecular weight of the organic molecule,^{2,13} and the temperature of the system.^{2,13,15} Mapping out the phase behavior in three component systems (solvent, organic and salt) is complicated by this large parameter space, both experimentally and theoretically. In addition, prediction of the thermodynamics of ionic species and larger molecular weight organics is complex and rarely at a level capable of predicting liquid-liquid extraction behavior. Finally, for some expensive or toxic materials, there is a pragmatic need to limit the amount of material required in characterization.

The typical approach to characterizing the phase behavior of an unknown system is to systematically prepare macroscopic samples that provide a discrete sampling of the phase space.⁴ While effective, this approach requires a large number of samples, material, and time to fully characterize the phase space; a problem that grows exponentially as the number of components increases. An alternative approach is to produce nanoliter sized droplets containing dilute mixtures and then slowly concentrate the droplets until phase separation is observed. In these experiments, significantly less sample is required per experiment and each experiment returns a point on the phase boundary with high compositional resolution, increasing the efficiency and simplicity of the technique.

Within the field of microfluidics, numerous methods have been devised to produce and control droplets on the micrometer scale. A few influential review papers detail the broad capabilities offered by the use of different microfluidic droplet techniques.²⁷⁻³⁰ In many cases, it is necessary not only to produce droplets, but to capture them to characterize their behavior over long timescales. To accomplish this, many studies produce droplets upstream and capture them downstream through various geometrical droplet traps.³¹⁻³⁷ An alternative approach is to initially fill droplet traps with the dispersed phase solution and then utilize the traps to hydrodynamically produce droplets.³⁸⁻⁴⁰ This is the approach taken in the present work. Once droplets are produced, we take advantage of the slight solubility of water in the continuous phase oil and diffusion of water through PDMS to slowly increase the concentration in the droplet.⁴¹⁻⁴³ The ability to dehydrate droplets in microfluidic devices has been used in previous studies to investigate crystallization kinetics,⁴⁴⁻⁴⁷ phase separation,⁴⁸⁻⁵¹ and particle synthesis.⁵²⁻⁵⁶ In addition, ATPS have been widely studied in microfluidic devices both in droplets⁵⁷⁻⁶⁴ and in channels.⁶⁵⁻⁷¹

The goal of this work is to develop a simple approach to characterizing liquid-liquid phase behavior in complex aqueous mixtures of organic molecules and salts. The method developed is inexpensive, robust and uses small amounts (milliliters or less) of sample. A well-studied system consisting of an organic, poly(ethylene oxide) (PEO), and a salt, ammonium sulfate, is chosen as a test case and the accuracy of the method demonstrated.^{2,23–26,72,73} Aqueous droplets of the PEO-ammonium sulfate system are loaded at dilute concentrations and allowed to dehydrate as the aqueous solvent partitions through the device. The projected image of the droplet is recorded through the phase separation process and the volume quantified to calculate the composition at which phase separation occurs. This approach allows for rapid characterization of a three component phase diagram with high compositional accuracy.

4.2 Materials and Methods

Ammonium sulfate salt ((NH₄)₂SO₄) is purchased from Sigma-Aldrich (St. Louis, MO). Two different molecular weight poly(ethylene oxide), PEO, polymers are used in this work: 600 g/mol purchased from Sigma-Aldrich and 7500 g/mol purchased from Polysciences Inc. (Warminster, PA). The 600 g/mol PEO is sold as a viscous fluid while the 7500 g/mol PEO is sold as a powder. Both are expected to be polydisperse in molecular weight.

Light mineral oil is obtained from Fisher Scientific (Hampton, NH) and 100 cSt silicone oil is obtained from Gelest Inc. (Morrisville, PA). Span-80 is purchased from Sigma-Aldrich and added to the mineral oil for the droplet production process. PDMS is purchased from Dow Corning (Midland, MI) and used to produce the microfluidic devices. It comes as a two-part elastomer kit (Sylgard 184) containing both the pre-polymer and curing agent.

Deionized water (18.2 MΩ-cm) is used for all solutions. Ammonium sulfate salt is dried under vacuum at 60°C for 4 hours and used immediately to produce salt solutions at appropriate

concentrations and allowed to dissolve overnight. The 600 g/mol PEO is dried under vacuum at 40°C for 4 hours to dry and melt any small crystallites which have been observed after extended storage. The 7500 g/mol PEO is supplied as a powder and used as received. All solutions are prepared by weight.

For microfluidic experiments, bulk samples of 10 wt% PEO and 2.5 wt% ammonium sulfate are produced and allowed to dissolve overnight. Once dissolved, these solutions are combined in different ratios by mass to provide various polymer/salt compositions. Once prepared, the stock solutions are sonicated for 15 minutes and allowed to rest overnight to ensure homogenous mixing. We define ξ as the mass ratio of polymer to salt, and stock solutions of $\xi = 36, 9.3, 4, 1.7,$ and 0.4 are prepared. We define θ as the total solute mass per volume in the system. Initial solutions of $\theta = 0.094, 0.079, 0.063, 0.048,$ and 0.033 g/mL are prepared for the five different mass ratios. A density relationship of $\rho = 1.018 - 3 \cdot 10^{-4}(\xi)$ g/mL is determined by measuring the density of 5 solutions and fitting a line through the results. At any point in the experiment, a concentration is defined using the two solute concentrations or by the (ξ, θ) pair. During an evaporation experiment, ξ is constant and θ changes with time.

For macroscopic experiments, salt solutions are prepared at significantly higher concentrations. Salt solutions are added directly to pure 600 g/mol PEO to achieve the appropriate target concentrations. Samples are shaken vigorously on a Fisherbrand Vortex Genie 2 and sonicated before observations are made.

4.2.1 *Device fabrication*

Microfluidic devices are generated using standard photolithography techniques.^{74,75} SU-8 3050 (Microchem Corp., Westborough, MA) is used to produce a mold of the droplet traps 100

μm thick on top of a 3" silicon wafer. Sylgard 184 PDMS pre-polymer (Dow Corning, Midland, MI) is mixed with the curing agent, poured over the mold, and allowed to cure for 2 hours in a 60 °C oven. Once cured, the PDMS device is peeled off the mold, bonded to a flat PDMS slab via plasma treatment, and heated in an oven at 180 °C oven for 1 hour. After cooling, the devices are soaked in the outer phase fluid (mineral oil or silicone oil) for at least 5 days before being used in an experiment.

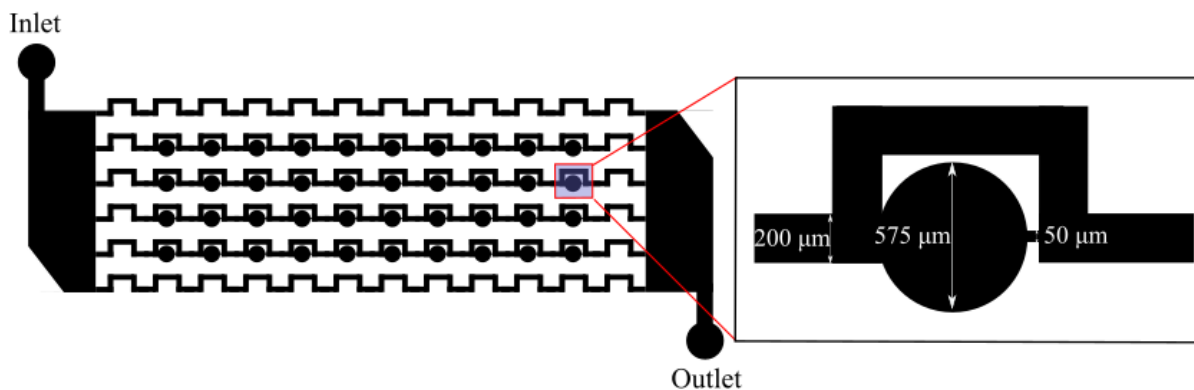


Figure 4.1: Schematic diagram of full microfluidic droplet device and a single droplet trap. Droplets are produced and stored in the 575 μm circular droplet trap. All channels are approximately 100 μm in height, the exact value is determined for each device after an experiment. The schematic depicts the microfluidic device when no droplets are present.

Droplets are produced via the method described previously.^{38–40} A schematic of a droplet trap is shown in Figure 4.1 which consists of a 575 μm diameter trap, a 200 μm wide bypass channel, a 50 μm wide restriction channel, and is 100 μm in depth across the entire microfluidic network. Each device contains four rows of ten droplets producing forty droplets in total. For the work presented here, only one droplet is imaged during the experiment to maximize resolution, but the final droplet shapes are compared across the entire device.

Two different continuous phase fluids were used in the work. For experiments performed with mineral oil, soaked devices are flushed with a 2wt% Span-80 solution in mineral oil. At least 5 minutes are allowed for the surfactant to adsorb to the walls of the channels to provide

appropriate wetting conditions for droplet formation. An approximately 1.5 μL slug of dispersed phase fluid is then pushed through the channels followed by another slug of continuous mineral oil fluid with 2wt% Span-80. After the droplets are produced and the channels are cleared of excess dispersed phase fluid, clean mineral oil is flowed through the channels for 20 minutes in attempt to remove any remaining Span-80. Experiments with a silicone oil outer phase do not use surfactant in the initial steps and therefore this step is not required for these experiments.

After 20 minutes, the droplets are imaged at 4X magnification with a pixel resolution of 2.9 $\mu\text{m}/\text{pixel}$ to determine a starting droplet size and then placed on a microscope for continuous observation. Drops of continuous phase fluid are placed over the inlet and outlet to prevent air from entering the system during the dehydration process. The devices are open to lab conditions (typically 22°C and 35% RH) without additional environment control. Typical droplet dehydration times are on the order of 24-36 hours.

4.2.2 Analysis of droplet concentration

Experiments are performed for the case that the droplets are confined in the traps, adopting a pancake shape with a circular projected area. Imaged drops are analyzed using ImageJ to fit a circle to the droplet perimeter and extract a diameter. The height of the channel is measured *post mortem* by slicing the devices into small slivers and imaging channel depth on a microscope. The height is measured by microscopy on devices cut apart after use and is $95 \pm 5 \mu\text{m}$ across several devices. The height is measured accurately for each device after use. The droplet diameter is initially the size of the trap, or 575 μm , and experiments are designed such that phase separation occurs at a droplet diameter close to 200 μm (at least twice the height). Equation 4.1 is used to calculate the volume of the pancake-shaped droplet,⁷⁶

$$V^* = \frac{V_{pancake}}{\left(\frac{4}{3}\pi\left(\frac{h}{2}\right)^3\right)} = 1 + \frac{3}{2h^2} \left((D-h) \left(D - \frac{1}{2}(2-\pi)h \right) \right), \quad (4.1)$$

where $V_{pancake}$ is the droplet volume, D is the diameter of the circular projection when viewed from the top of the pancake, and h is the channel height. Images are captured every 2 minutes resulting in up to 1000 images, or data points, per experiment. Equation 4.1 is normalized by the volume of a spherical drop that has a diameter equivalent to the channel height. Initial droplets are based on the trap size and V^* is on the order of 50. Experiments are designed so droplet diameter remains greater than 200 μm at the phase separation point, corresponding to $V^* > 4-5$ and a pancake droplet shape.

4.2.3 Microscopy

Images are recorded on an inverted Nikon Ti-U microscope and an inverted Nikon TE2000-U microscope. Initial droplet sizes are imaged using an inverted Nikon Ti-U microscope at 4X magnification and a Vision Research Phantom v9.1 camera with a resolution of 2.9 $\mu\text{m}/\text{pixel}$. Dehydrating droplets are imaged on an inverted Nikon TE2000-U microscope at 15X magnification with a Diagnostic Instruments Inc. SPOT-RT camera with a resolution of 0.49 $\mu\text{m}/\text{pixel}$. All images are recorded at the middle plane of each droplet.

4.3 Results

Figure 4.2 shows an example of the dehydration sequence. Images of single droplets are captured every two minutes for the duration of the experiment. The entire dehydration process requires approximately 24 hours. Images in the figure are at different time intervals to demonstrate the visual observations during a typical dehydration process. The aqueous droplet in image (*i*) has a concentration of 7 wt% 600 g/mol PEO, 0.75 wt% salt and 92.25 wt% water (polymer/salt mass ratio $\xi = 9.3$, total solute mass concentration $\theta_0 = 0.079$ g/mL) and the continuous phase is mineral

oil. The droplet decreases in size as the solvent, water, diffuses out of the drop, into the continuous phase and then through the PDMS.

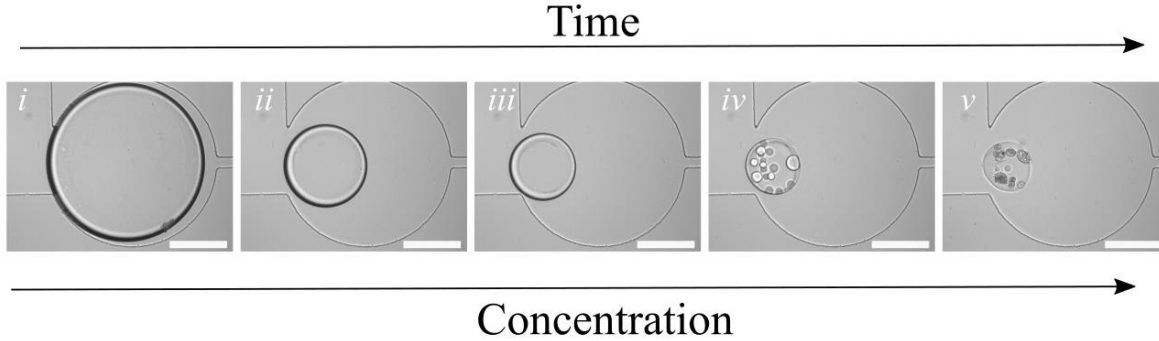


Figure 4.2: Images of a single droplet containing ammonium sulfate and 600 g/mol PEO during dehydration ($\xi = 9.3$, $\theta_o = 0.079$ g/mL). The droplet is a single-phase fluid in images (i-iii), two liquid phases in (iv) and two phases with solid crystals in (v). Scale bar is 200 μm .

In Figure 4.2, images (i-iii) show single phase solutions while images (iv-v) demonstrate phase separated solutions. The onset of phase separation is detected within 1 frame (or +/- 2 minutes) providing high compositional resolution for the phase separation event. The diameter of single phase droplets is measured and the volume of the drop calculated using Equation 4.1. For this example, the droplet diameter is initially $D_o = 550$ μm , corresponding to $V_o^* = 42.1$ and $\theta_o = 0.079$ g/mL. After some period of time, two liquid phases are observed at a droplet diameter of $D = (233 \pm 1)$ μm , corresponding to a volume of $V_{pancake} = 3.56$ nL ($V^* = 6.8$). Since the concentration and volume are known accurately at the start of the experiment, the concentration at phase separation is calculated as $\theta = 0.49$ g/mL assuming that none of the solute leaves the droplet. After phase separation or at points when the droplet no longer has a circular projection, the pancake shape is lost and volume cannot be calculated accurately. The final image in this figure shows the final state of a droplet; the darker regions are assumed to be salt crystals (refractive index of $n = 1.52$) while the matrix of the droplet is assumed to be a PEO melt (refractive index of $n = 1.45$).

Each device has 40 wells, the final state is characterized in all 40 samples, while the evolution of phase separation is captured on just one droplet to maximize optical resolution and minimize uncertainty in volume. Multiple droplet traps are used per device to ensure production of at least one suitable droplet, specifically when silicone oil is used as the outer phase fluid. In addition, future work intends to create preprogrammed automatic camera movements between droplets to record phase separation across the entire device with high image resolution. This will expand our view for stochastic processes and allow for statistical characterization of a phenomena. Figure 4.3 shows the phase diagram of ammonium sulfate salt and two different molecular weights of PEO measured with this microfluidic droplet technique. The squares correspond to a 600 g/mol PEO polymer and the circles correspond to a 7500 g/mol PEO polymer. The solid black lines are phase boundaries drawn to guide the eye between the one phase region in the bottom left and the two phase region at the top right. The dashed bold line defines the infeasible region set by the density of pure PEO and the solubility of salt. We do not expect to be able to access this region. Dashed lines on the figure denote lines of constant ξ . In Figure 4.3a, the units are displayed on a per volume basis. Droplet diameter is accurately measured and used to calculate droplet volume, resulting in the data points shown in Figure 4.3a. Since the mass concentration of the initial droplet is known and neither solute is soluble in mineral oil, the concentration at any point in the experiment is calculated in mass per unit volume, or molar units in the case of salt. During dehydration, the composition moves along a line of constant ξ as θ increases, so the phase separation is defined by the pair (ξ, θ) . In Figure 4.3a, five experiments were performed for each different molecular weight of PEO. Initial dilute samples are loaded into the device and the phase separation determined for each device resulting in the phase boundary shown. By loading dilute

solutions, there is no concern about heterogeneity between different drops on a single device or concentration gradients within a droplet.

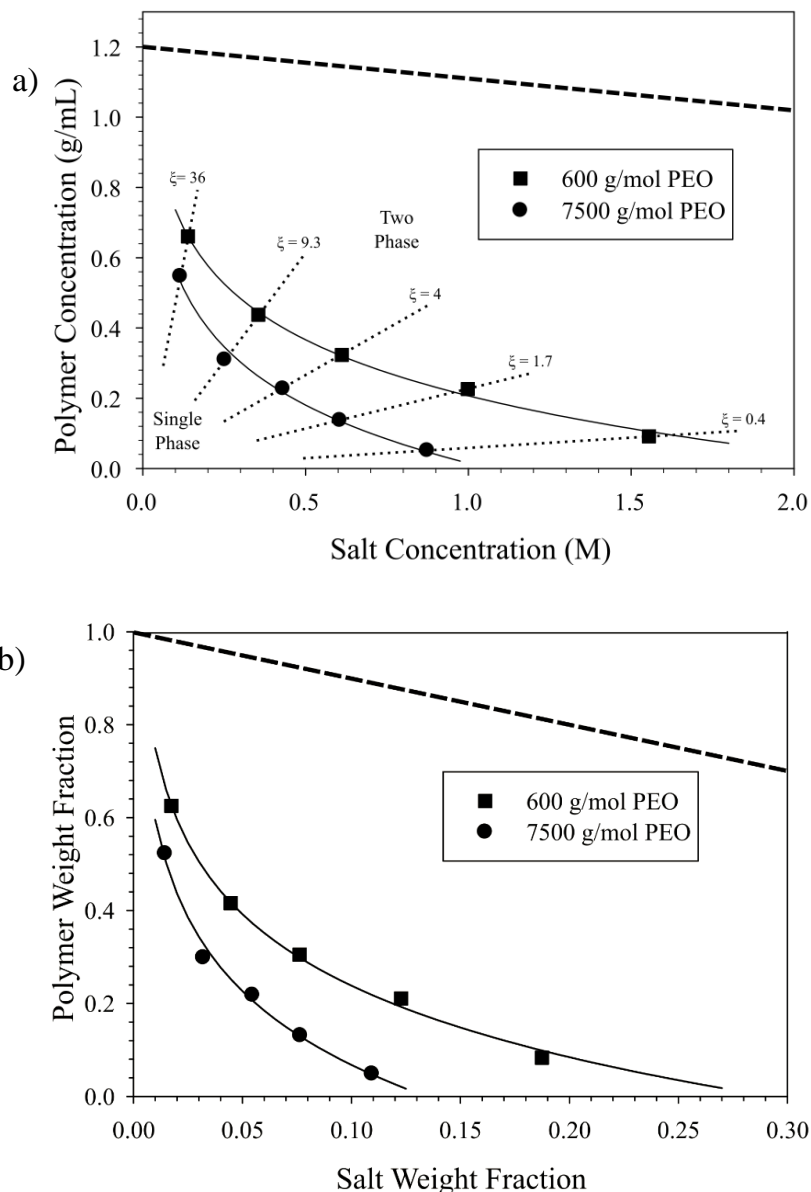


Figure 4.3: The phase diagram for ammonium sulfate and PEO of two different molecular weights developed through the microfluidic experiments provided on (a) a volume basis and (b) a weight basis. The points correspond to the phase boundary for 600 g/mol PEO (■) and 7500 g/mol PEO (●). Solid lines denote the phase boundary and are drawn to guide the eye. Dotted lines are lines of constant mass ratio of the two solutes. The dashed line is the upper limit that can be reached in the experiment.

For comparison to literature, it is convenient to report phase diagrams as mass fractions. This is done in Figure 4.3b. The same data is shown and the limits adjusted for the composition units. Since the densities of different three-component compositions are not known, to convert to a mass basis, assumptions must be made about the density of the solution at each concentration. A density of each sample is estimated as a linear relationship between the known densities of the individual solutions, based on mass fraction.

Using densities of 1.12 g/mL for pure PEO and 1.77 g/mL for pure ammonium sulfate, the volume based concentrations are converted to the mass based concentrations in Figure 4.3b. The impact of this assumption will vary with the system and depends on the volume change on mixing of different components. However, no assumptions about solution density are required for the mass per volume concentration units shown in Figure 4.3a.

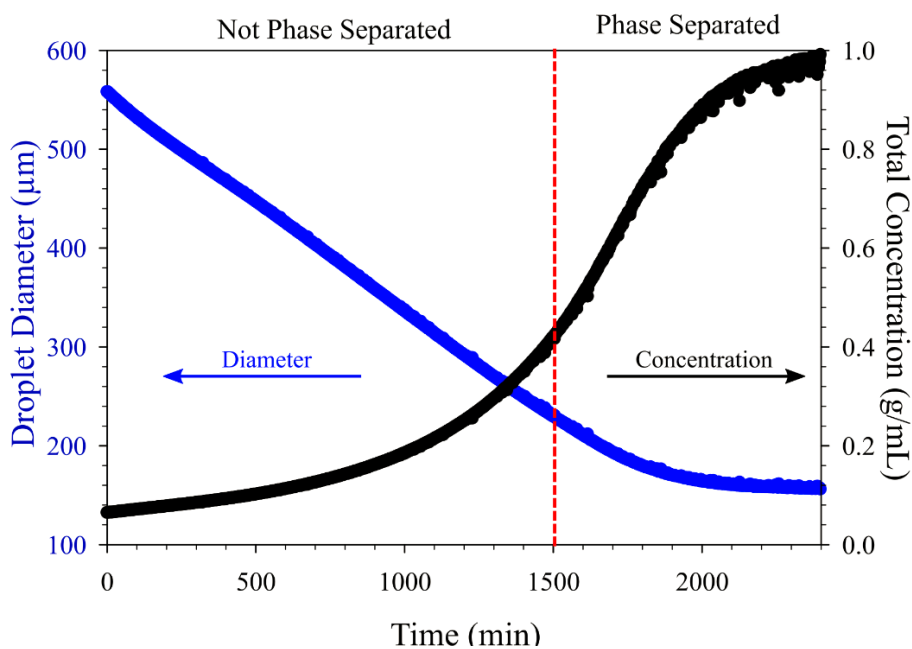


Figure 4.4: Temporal progression of experiment and measured parameters. The blue points are the measured diameter for a single droplet as a function of time. The black points are the combined salt/polymer concentration in the droplet. The dotted red line indicates the first frame where phase separation is observed. Note that the phase separation is not detectable in the volume change of the droplet.

Figure 4.4 shows the progression of the experiment. Droplets are initially produced at dilute concentrations where the system is a single phase. The droplets are then allowed to concentrate while being imaged and the diameter is measured. The blue points in Figure 4.4 correspond to the measured droplet diameter as a function of time for a single droplet of the PEO-ammonium sulfate system ($\theta_o = 0.063$ g/mL, $\xi = 4$) in a mineral oil outer (continuous) phase. The initial mass of solute in the droplet is determined from the initial diameter and initial concentration; in this case $D_o = 558$ μm and $\theta_o = 0.063$ g/mL providing an accurate measure of 1.41 μg for this example. The measured diameter is used to calculate the droplet volume using Equation 4.1, which is then converted to θ , or the total PEO-ammonium sulfate mass as shown by the black points in Figure 4.4. Droplets are observed until a concentration at which phase separation occurs, denoted by the dotted red line in Figure 4.4. The dotted red line demonstrates the break between concentrations that are single-phase or two-phase. While it is not possible to identify the phase separation by following the diameter alone, the visual observation is clear (see Figure 4.2). Images are captured every 2 minutes which results in over 1000 frames per experiment and phase separation can be detected within 1 frame. The compositional resolution obtained with this technique will depend on the rate of change of the diameter, $D(t)$, the initial size of the drop, D_o , and the time step between images Δt . For example, for many of the experiments presented here, the diameter decreases linearly with time over most of the experiment at a rate of $D(t) = D_o - \alpha t$, where α is a constant determining the rate of change of droplet diameter and images are taken every $\Delta t = 2$ min. This functional form for the rate of decrease of the diameter results in a change of the volume of the pancake given by

$$\frac{d}{dt} \left[\frac{V_{\text{pancake}}}{\left(\frac{4}{3}\pi\left(\frac{h}{2}\right)^3\right)} \right] = \frac{3}{2h^2} (-2\alpha D_o + 2\alpha^2 t) + \frac{3}{2h^2} \left(1 + \frac{1}{2}(2 - \pi)\right) h\alpha \quad , \quad (4.2)$$

which assumes that the height of the pancake does not change with time. This is reasonable as the experiments are designed to maintain the pancake geometry ($D > 2h$). For this example and typical of experiments reported here, $\alpha = 0.2 \mu\text{m}/\text{min}$, so the rate of change of volume at the point of phase separation ($t = 1506 \text{ min}$) is approximately $\Delta V/\Delta t \sim 10 \text{ pL}/\text{min}$. For a time step of $\Delta t = 2 \text{ min}$, the difference in volume between one image and the next is 20 pL. To determine the compositional resolution of our technique, we compare this to the volume of the drop at this point in the analysis (typically on the order of 4 nL) and it is straightforward to show that the error in determining concentration given a discretization of the phenomenon into images is $C^*\Delta V/V$ where C is droplet concentration, ΔV is droplet volume change between frames, and V is current droplet volume. This value during phase separation is $\sim 2\text{-}3 \text{ mg}/\text{mL}$. At this point, the concentration in the drop is $\theta = 415 \pm 2 \text{ mg}/\text{mL}$, or 0.5%. This is the resolution of the composition due to the analytical technique. This is lower than the reproducibility error from both droplet to droplet error (observed to be 3%) and device to device error (observed to be 3%).

Rates of solvent removal are slow. The entire process is typically 24-36 hours. If we define a 1-D flux of solvent out of the top of the drop, typical rates are $0.03 \text{ g H}_2\text{O}/(\text{m}^2\text{min})$. This provides an estimate of the velocity of the solvent, $v \sim 3 \text{ nm}/\text{sec}$, which is used to construct a Peclet number, $Pe = Lv/D$, using a characteristic dimension for the drop of $100 \mu\text{m}$, we find that this process is in a very low Pe regime $Pe \sim O(10^{-4})$, so compositions inside the drop will be uniform until viscosities reach several orders of magnitude greater than that of the solvent.

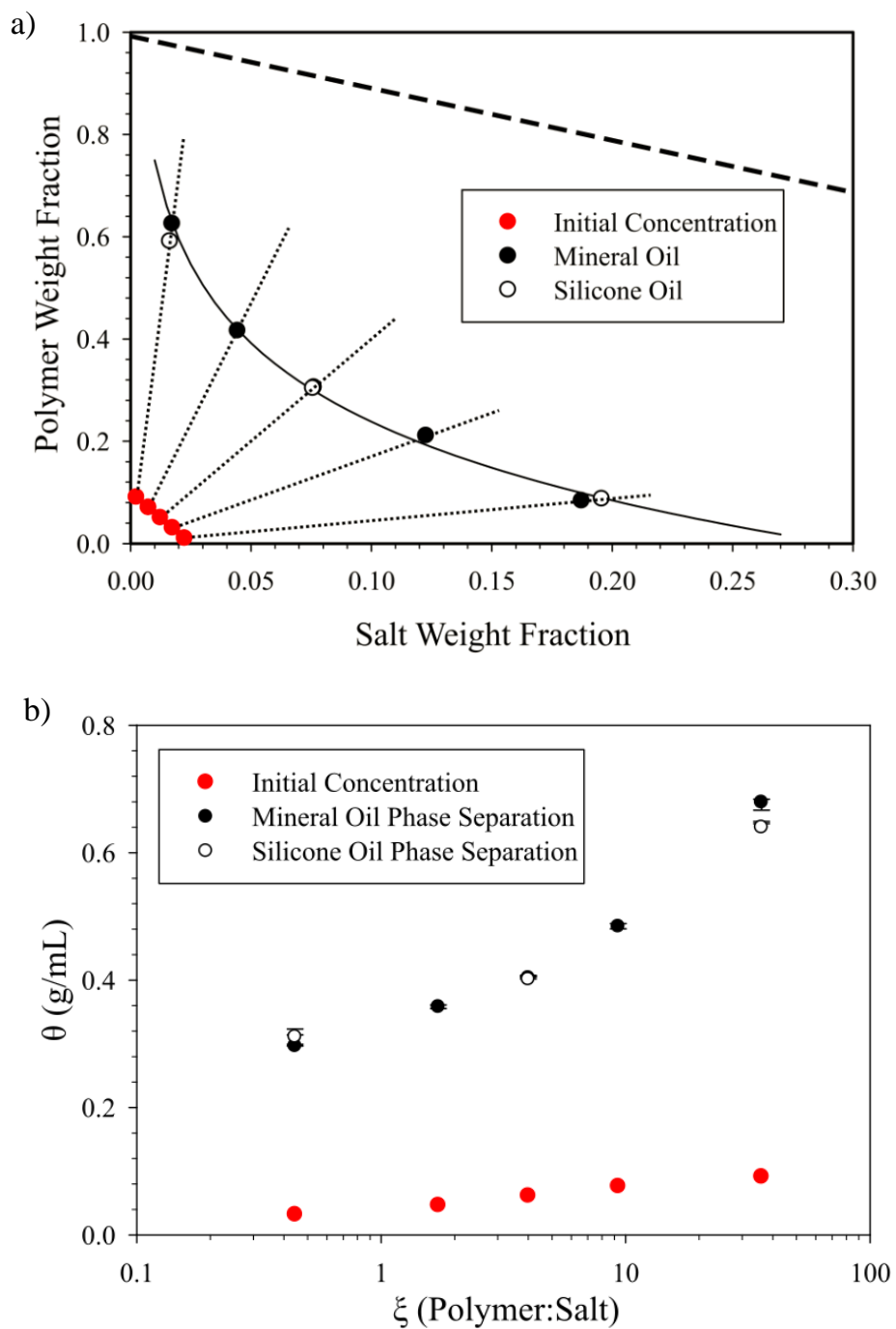


Figure 4.5: Phase diagram for two different continuous phase oils. (a) Phase separation points for (\circ) 100cSt silicone oil with no surfactant and (\bullet) mineral oil with 2% Span-80. (b) Data replotted in θ - ξ space. Error bars correspond to volume calculations from images taken one frame before and after phase separation.

Figure 4.5a shows that the continuous phase oil and added surfactant do not influence the conditions at which phase separation occurs. Each red point corresponds to the initial concentration of a different microfluidic device. As the droplets concentrate via dehydration, both the salt and the polymer will increase in concentration. The dotted black lines demonstrate the compositional path of each respective droplet as it concentrates, the slope of which is determined by the mass ratio of polymer to salt. The droplets continue to dehydrate until phase separation is observed, as in Figure 4.2.

Most experiments were conducted with a mineral oil outer phase initially containing 2wt% Span-80 and later flushed with clean mineral oil as described in the experimental section. The results from these experiments are plotted as the filled black points. A subset of experiments was conducted with a 100 cSt silicone oil outer phase with no added surfactant, plotted as the open circle points. This is expected to change the rate of concentration due to the difference in water partitioning in the two oils, but it is not expected to change the phase diagram.

Figure 4.5b plots the same results in θ - ξ space with ξ as the x-axis and θ as the y-axis. This allows for error bars to be plotted in θ coordinates for each experiment. Error bars are derived by calculating the droplet concentration 1 frame before and after phase separation, demonstrating the high compositional resolution of the technique.

Overall, the differences observed are within the error in composition except for the highest ratio of polymer to salt, where the difference is slightly larger. The timescales of the experiments are different (silicone oil experiments dehydrate two to three times as quickly), but not enough to change the compositional resolution analysis. The change in the interface between the two oil-water systems is a potential cause of the difference. Polymer could be depleted to the oil-water

interface and that would differ by oil type. To estimate the amount depleted, using the experiment with the least amount of polymer ($\xi=0.44$) as an example, initial polymer loading is approximately $0.25 \mu\text{g}$ and the surface area of the pancake is 0.65 mm^2 . Assuming a surface concentration of 1 mg/m^2 , approximately 0.3% of the free polymer would be adsorbed on the droplet interface. This is not a significant amount and we do not expect this to impact the results, or be the cause of the difference between the two oils. In the case of the mineral oil, an oil-soluble surfactant, Span-80, is used in the droplet production stage of the process, but is rinsed out of the system, so we do not expect it to impact the results.

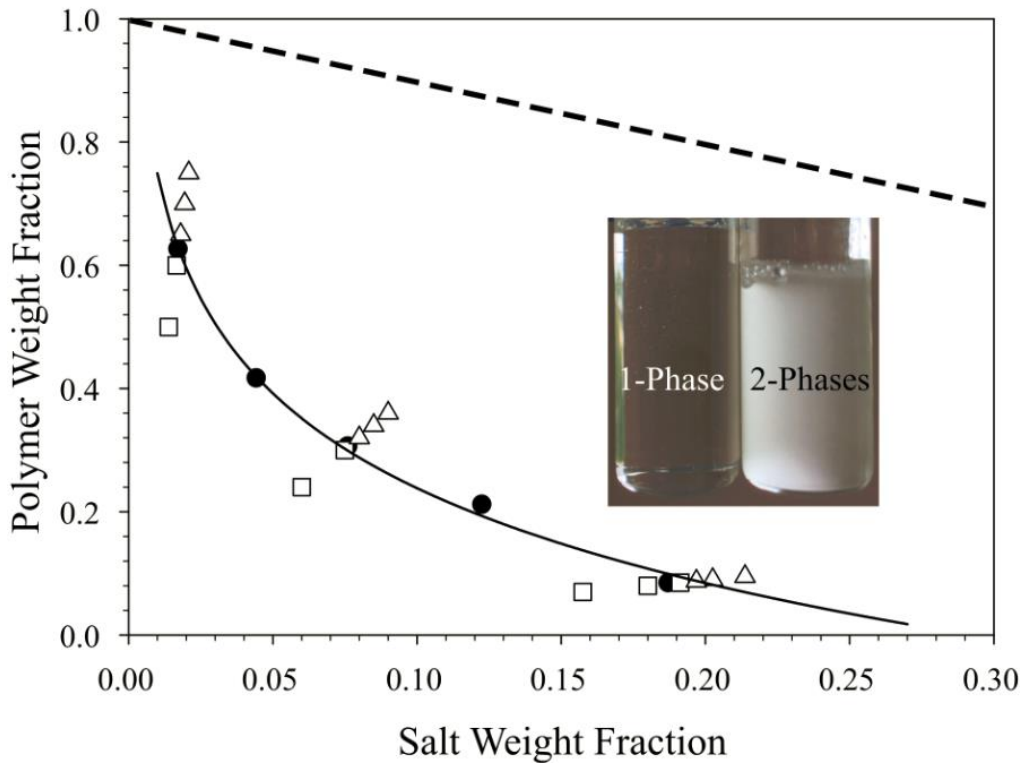


Figure 4.6: Comparison between microfluidic and macroscopic phase separation experiments for an ammonium sulfate and 600 g/mol PEO system. The closed points are the microfluidic phase boundary points from Figure 4.3a. The open points are results from macroscopic experiments for (square) one phase and (triangle) two phase solutions. The inset shows the clear visual difference between a macroscopic 1-phase and 2-phase system.

Figure 4.6 compares phase separation results between microfluidic and macroscopic samples for ammonium sulfate salt and 600 g/mol PEO. The filled black points show the phase boundary determined in the microfluidic device from Figure 4.3a. The open square symbols show the compositions of macroscopic samples that are single phase while the open triangle symbols denote compositions of macroscopic samples that exhibit two distinct phases. Macroscopic samples (6 mL) stabilize after mixing for 24 hours and then the phase behavior is observed. Phase separation in the macroscopic samples is apparent by turbidity of the system as small droplets of one fluid phase form in the second fluid phase. The minor phase coalesces and after about an hour, the system fully phase separates into two distinct regions separated by a smooth liquid-liquid interface. The image in Figure 4.6 shows images of macroscopic samples taken minutes after the samples are produced. The sample on the left is in the single-phase region of the boundary line and the sample on the right is in the two-phase region of the phase diagram. The two-phase sample is opaque or turbid in the phase separated region demonstrating a clear macroscopic differentiation between one phase and two-phase systems, allowing for visual characterization. The results show agreement between the locations of the microfluidic boundary line and the macroscopic experiments even though the macroscopic samples provide only a discrete sampling of composition space.

These results are consistent with literature results for this salt and PEO combination in aqueous solution.² In this work, two different molecular weights of PEO (1000 & 2000 g/mol) were tested with ammonium sulfate salt. The results show a phase boundary shift to lower concentrations of polymer and salt with an increase in molecular weight of the organic, PEO. This is consistent with our results shown in Figure 4.3b.

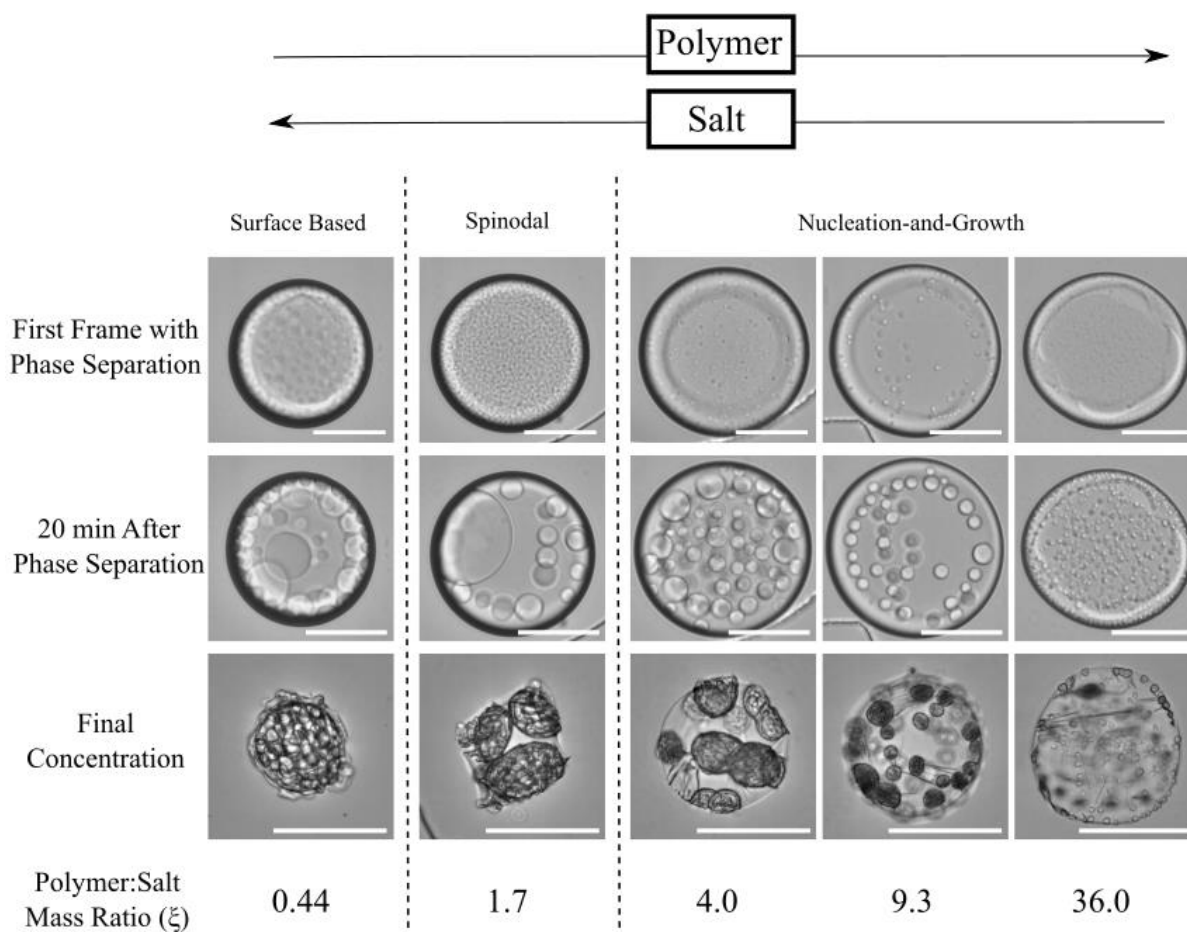


Figure 4.7: Images of phase separating droplets at various polymer:salt mass ratios and at 3 different time points. The first row of images shows representative droplets 1 frame after noticeable phase separation, the second row shows droplets 20 minutes after phase separation, and the third row of shows droplets 5 days after droplet production. Scale bars are equivalent to 100 μm .

Figure 4.7 shows representative images of droplets of different polymer/salt ratios immediately after phase separation, 20 minutes after phase separation, and at their final dehydrated composition. The first row of images is the first frame for each droplet where phase separation is observed (frames are recorded every 2 minutes). The second row of images is of droplets at exactly 20 minutes after phase separation is observed in each experiment. At the typical rates of dehydration, these will be at concentrations of approximately $\Delta\theta = 20 \text{ mg/mL}$ beyond the phase separation point. The third row of images is taken at least 5 days after the droplets are produced and assumed to be completely dehydrated. The concentrations should be near the upper limit

(dashed line) on Figure 4.2. The dehydration process generally takes on the order of 24 hours with minimal to no change observed in droplets after one day. Initial samples are produced by combining an ammonium sulfate solution and a 600 g/mol PEO solution at various mass ratios indicated by ξ below each image in Figure 4.7. As the images go from left to right, the relative concentration of salt decreases while the relative concentration of polymer increases.

Images in the first row can be used to differentiate between the mechanisms of phase separation for each composition. As shown previously, systems containing ammonium sulfate and PEO can phase separate via spinodal decomposition, a nucleation-and-growth mechanism, or growth of a second phase at the interface depending upon the organic-to-inorganic mass ratio.²³ High polymer/low salt systems lead to a nucleation-and-growth mechanism while low polymer/high salt systems lead to a spinodal or surface based mechanism. A mass ratio of $\xi = 0.4$ is on the boundary between spinodal and surface based described by Ciobanu et al.²³ Visually, the separation of two phases appears differently than all other experiments, potentially a surface based separation. A mass ratio of $\xi = 1.7$ is on the boundary between spinodal and nucleation-and-growth and visually appears to be spinodal decomposition during the onset of phase separation, as shown in Figure 4.7. Mass ratios of $\xi = 4.0, 9.3$ and 36 are all within the nucleation-and-growth regime and appear to form small nucleated sites that expand and coalesce as the droplets continue to dehydrate.

The inner phase of the droplet is the salt-rich liquid phase that eventually crystallizes and the outer phase of the droplet is the polymer-rich phase. It is important to note that in this case “inner” and “outer” phase corresponds to the two liquid phases within the droplet, not the inner aqueous solution and outer mineral oil solution. As the droplets continue to concentrate, the inner phase coalesces to a certain degree before crystallization is observed. A video of this can be

viewed in the supplemental material. As the salt:polymer ratio decreases, the inner phase coalesces to a lesser degree before efflorescence occurs. This is more apparent when looking at the images in their final state. The bottom row of images shows the various droplet concentrations when they are fully dehydrated. The dark crystalline structures are the salt-rich inner phase after crystallization and the clear fluid between them is the polymer-rich outer phase. The first droplet in the second row appears to have coalesced into one large salt-rich phase before crystallization. As the images go from left to right, the crystalline-like structures become smaller in size but greater in quantity. In the case of the right-most image, minimal coalescence is observed before the inner phases crystallize. The remaining PEO is close to the refractive index of the oil and PDMS, so appears as transparent although a film remains and the PEO is low enough in molecular weight so that it does not crystallize.

Figure 4.8 exhibits the ability for a dehydrated droplet to be fully rehydrated and then dehydrated a second time while maintaining the original drop in a fixed trap. The experimental process is shown in schematic form in Figure 4.8a. The droplets are produced using the same method as in previous experiments and allowed to fully dehydrate. After 5 days, the entire device is then submerged in a water bath and recorded on a microscope. The droplet begins to swell within hours and continues to increase in size for 2 days. The first row of images in Figure 4.8b shows the dehydration of the ammonium salt and 600 g/mol PEO system. The second row of images shows the rehydration process. As the droplet begins to swell, the inner salt-rich phase moves to the outside of the droplet and almost completely de-wets from the polymer-rich phase. Eventually the salt-rich phase begins to melt and slowly becomes liquid like again. The salt-rich phase then becomes engulfed by the polymer-rich phase once again until the two phases finally remerge and become a single fluid phase.

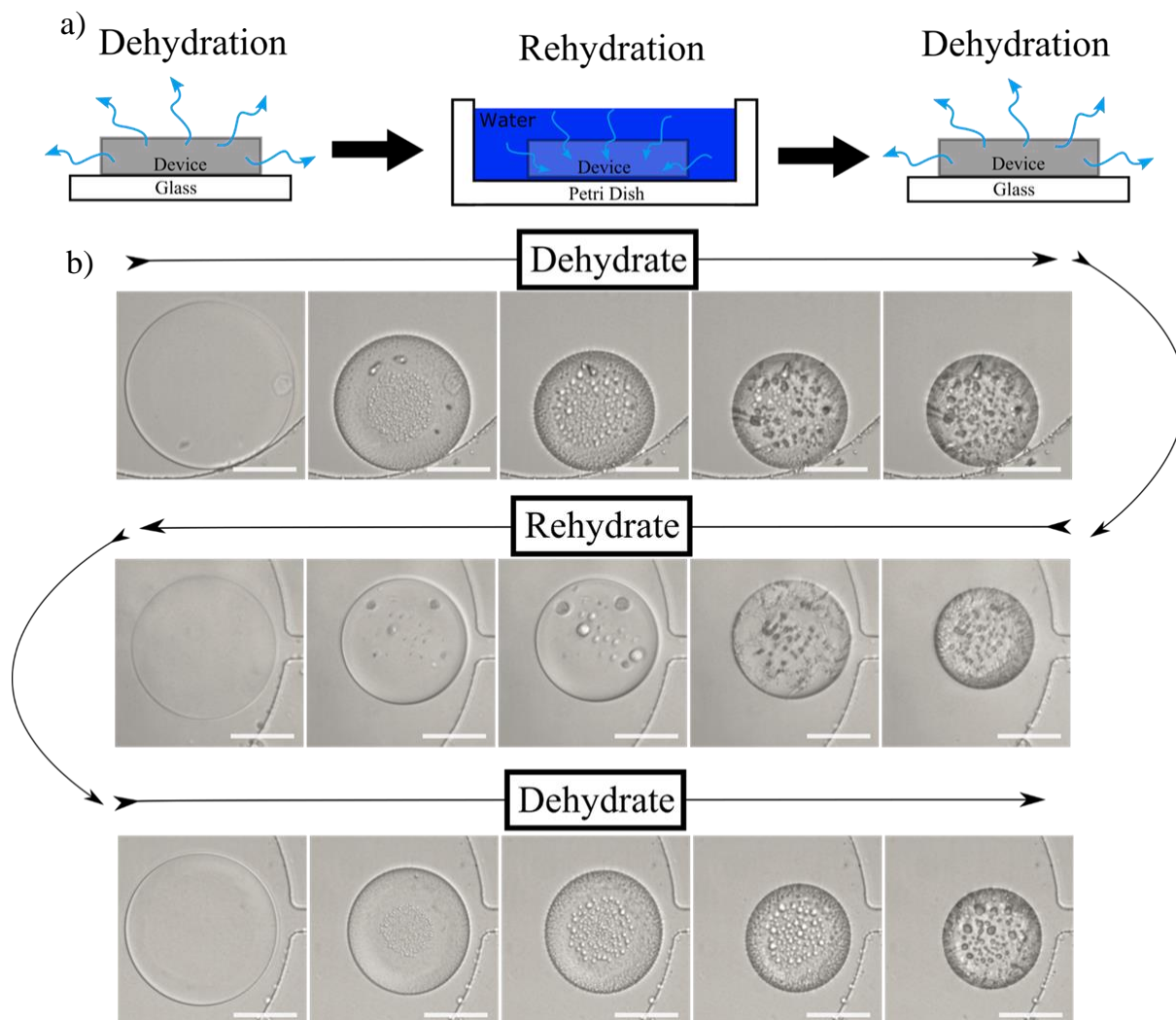


Figure 4.8: (a) Schematic of the dehydrating and rehydrating cycle performed in experiments. ($\xi = 36$) (b) Images of droplets at different time points during the rehydration cycle and the second dehydration cycle. Images in the top row progress in time from left to right as the droplet dehydrates. Images in the second row progress in time from right to left as the droplet rehydrates. Images in the third row progress left to right as the droplet dehydrates a second time. Scale bar is equivalent to $100 \mu\text{m}$.

The bottom row of images in Figure 4.8b shows the same droplet dehydrating a second time. After being rehydrated, the device is removed from the water bath and placed in ambient conditions, allowing for dehydration of the system. From left to right in the images in the bottom row, the droplet is becoming more concentrated with time. A similar phase separation process is observed compared with the first dehydration cycle. The composition values at the phase separation point of the dehydration-rehydration-dehydration cycle for $\xi = 36$ are $\theta = 0.64, 0.71$,

and 0.72 g/mL respectively. A similar experiment at $\xi = 9.3$ returned dehydration-rehydration-dehydration phase separation values of $\theta = 0.49, 0.61, \text{ and } 0.60$ g/mL. This suggests that there is a measurable hysteresis in the rehydration-dehydration cycle. It is most likely that this is due to limited dimensional stability of the device with large changes in environment. The devices are pre-swollen with oil, but the initial step in the process just described is a long dehydration (over days) which may result in a change in the channel height. This height is expected to remain changed through the re-hydration and second dehydration. Devices with better dimensional stability should be designed for these types of studies, but the potential is interesting so we demonstrate it here.

4.4 Discussion

The microfluidic device has proven to be a valuable instrument to map the phase behavior of an unknown system with a minimal number of experiments. Figure 4.5 demonstrates the reproducibility of the technique and the ability to use multiple outer phase fluids depending on the compatibility of the sample. Figure 4.6 shows excellent agreement between microfluidic and macroscopic results, validating the application of the approach to real-world bulk systems. The high compositional resolution compared to macroscopic experiments is the major advantage of the device and will depend on the evaporation rate, optics, and frequency of recorded images. Figure 4.4 demonstrates a nearly constant decrease in droplet diameter as a function of time with a slope equal to $\alpha = 0.3 \mu\text{m}/\text{min}$ for most of the experiment. The volume depends nonlinearly on the diameter as shown in Equation 4.1. This results in a slower change in concentration at the beginning of the experiment and a faster change in concentration towards the end of the experiment. Typical concentration resolution between two images in these experiments is 0.1-0.2 mg/mL at the beginning of the experiment, 3-4 mg/mL at the phase separation point, and 10-15 mg/mL at the end of the experiment.

There are numerous advantages to performing phase mapping experiments on the microscale compared to the macroscopic scale. The first arises from the concentrating nature of the experiment. If a droplet is produced in a 1-phase stable region and is allowed to completely dehydrate, it is guaranteed that the system will concentrate up to the phase boundary line if one exists. Therefore, each experiment will return a point on the phase boundary line, significantly decreasing the number of experiments required to characterize the phase space. Another major advantage of the device, similar to all microfluidic experiments, is the low sample volume required to run each experiment. If a phase diagram is required for a system with precious materials or materials that are difficult to synthesize, microfluidics provides a low risk, low cost method to map the phase behavior of that system. Each experiment requires only about 200-300 μL of sample volume and will return a phase boundary point. By contrast, each macroscopic experiment can require milliliters of sample and probes discrete points on the phase diagram leading to significantly more experiments and sample volume to map the phase space. In addition, the device has the capability to controllably rehydrate the sample and observe potential hysteresis in the phase behavior, as shown in Figure 4.8.

Important design constraints should be observed to maximize the effectiveness of the technique. Droplets need to be produced in a dilute, 1-phase region to ensure phase separation at a later point in the experiment. However, the initial concentration of surface active components cannot be too dilute due to the high surface area to volume ratio. If a surface active component is initially too dilute, then a significant amount of depletion to the interface can occur before the droplet begins concentrating, leading to an incorrectly assumed initial concentration in the droplet. Additionally, if a component is too surface active, it can lead to issues in the droplet production process. If a system becomes too viscous, it's possible that the transport of water from the center

of the droplet to the droplet interface can become slower than the transport of water from the droplet interface to the outer phase oil, leading to potential internal concentration gradients. Basic calculations conclude a viscosity of approximately 1000 cP is required before internal gradients form. Lastly, it is recommended to maintain a pancake-shaped droplet throughout the experiment. This requires the droplet diameter to always remain larger than the height of the channels. In cases where the droplet diameter becomes smaller than the channel height, the droplets do not always assume a spherical shape but instead wet the top and/or bottom of the channels and form hemispheres or hourglass shaped droplets. This can be avoided by producing droplets with larger initial diameters, but constant channel heights.

4.5 Conclusions

This work offers a simple method to map the phase behavior of an unknown system using small amounts of sample but with high compositional resolution. Nanoliter-size droplets of a PEO-ammonium sulfate model system are produced on-chip at dilute compositions and concentrated. With this common organic-inorganic system, phase separation is observed in droplet form at high concentrations, yielding a phase diagram with high compositional resolution. With only five experiments, the full phase behavior is characterized. The microfluidic phase diagram agrees well with macroscopic results.

This technique requires significantly fewer experiments and sample volume to characterize the behavior of a new system. In addition, the phase separation can be observed *in situ* leading to valuable information about the phase separation process for atmospheric or formulations interests. The resulting dried system can be observed across the entire device for long term statistics, removed off chip for further analysis, or even rehydrated.

4.6 References

- (1) Pusey, P. N.; van Megen, W.; Megen, W. van. Phase Behavior of Concentrated Suspensions of Nearly Hard Colloidal Spheres. *Nature* **1986**, *320* (6060), 340–342.
- (2) Voros, N.; Proust, P.; Fredenslund, A. Liquid-Liquid Phase Equilibria of Aqueous Two-Phase Systems Containing Salts and Polyethylene Glycol. *Fluid Phase Equilib.* **1993**, *90*, 333–353.
- (3) Kline, S. R.; Kaler, E. W. Colloidal Interactions in Water/2-Butoxyethanol Solvents. *Langmuir* **1994**, *12*, 412–417.
- (4) Ilett, S. M.; Orrock, A.; Poon, W. C. K.; Pusey, P. N. Phase Behavior of a Model Colloid-Polymer Mixture. *Phys. Rev. E* **1995**, *51* (2), 1344–1352.
- (5) Diamond, A. D.; Hsu, J. T. Fundamental Studies of Biomolecule Partitioning in Aqueous Two-Phase Systems. *Biotechnol. Bioeng.* **1989**, *34*, 1000–1014.
- (6) Diamond, A. D.; Hsu, J. T. Aqueous Two-Phase Systems for Biomolecule Separation. *Adv. Biochem. Eng.* **1992**, *47*, 90–131.
- (7) Hachem, F.; Andrews, B. A.; Asenjo, J. A. Hydrophobic Partitioning of Proteins in Aqueous Two-Phase Systems. *Enzyme Microb. Technol.* **1996**, *19*, 507–517.
- (8) Dallora, N. L. P.; Klemz, J. G. D.; Filho, P. de A. P. Partitioning of Model Proteins in Aqueous Two-Phase Systems Containing Polyethylene Glycol and Ammonium Carbamate. *Biochem. Eng. J.* **2007**, *34*, 92–97.
- (9) Zhang, M.; Khripin, C. Y.; Faga, J. A.; Mcphie, P.; Ito, Y.; Zheng, M. Single-Step Total Fractionation of Single-Wall Carbon Nanotubes by Countercurrent Chromatography. *Anal. Chem.* **2014**, *86*.
- (10) Subbaiyan, N. K.; Cambre, S.; Parra-Vasquez, N. G.; Haroz, E. H.; Doorn, S. K.; Duque, J. G. Role of Surfactants and Salt in Aqueous Two-Phase Separation of Carbon Nanotubes toward Simple Chirality Isolation. *ACS Nano* **2014**, *8* (2), 1619–1628.
- (11) Fagan, J. A.; Khripin, C. Y.; Batista, C. A. S.; Simpson, J. R.; Hároz, E. H.; Walker, A. R. H.; Zheng, M. Isolation of Specific Small-Diameter Single-Wall Carbon Nanotube Species via Aqueous Two-Phase Extraction. *Adv. Mater.* **2014**, 2800–2804.
- (12) Iqbal, M.; Tao, Y.; Xie, S.; Zhu, Y.; Chen, D.; Wang, X.; Huang, L.; Peng, D.; Sattar, A.; Abu Bakr Shabbir, M.; Hussain, H. I.; Ahmed, S.; Yuan, Z. Aqueous Two-Phase System (ATPS): An Overview and Advances in Its Applications. *Biol. Proced. Online* **2016**, *18* (18), 1–18.
- (13) Ananthapadmanabhan, K. P.; Goddard, E. D. Aqueous Biphasic Formation in Polyethylene Oxide-Inorganic Salt Systems. *Langmuir* **1987**, *3*, 25–31.
- (14) Zafarani-Moattar, M. T.; Sadeghi, R. Liquid-Liquid Equilibria of Aqueous Two-Phase Systems Containing Polyethylene Glycol and Sodium Dihydrogen Phosphate or Disodium Hydrogen Phosphate Experiment and Correlation. *Fluid Phase Equilib.* **2001**, *181*, 95–112.

- (15) Zafarani-moattar, M. T.; Sadeghi, R.; Hamidi, A. A. Liquid-Liquid Equilibria of an Aqueous Two-Phase System Containing Polyethylene Glycol and Sodium Citrate: Experiment and Correlation. *Fluid Phase Equilib.* **2004**, *219*, 149–155.
- (16) Martins, J. P.; Carvalho, C. D. P.; da Silva, L. H. M.; Sélia dos Reis Coimbra, J.; da Silva, M. do C. H.; Rodrigues, G. D.; Minim, L. A. Liquid–Liquid Equilibria of an Aqueous Two-Phase System Containing Poly(ethylene) Glycol 1500 and Sulfate Salts at Different Temperatures. *J. Chem. Eng. Data* **2008**, *53*, 238–241.
- (17) Roosta, A.; Jafari, F.; Javanmardi, J. Liquid–Liquid Equilibrium in an Aqueous Two-Phase System of Polyethylene Glycol 6000, Sodium Sulfate, Water, Glucose, and Penicillin-G Experimental and Thermodynamic Modeling. *J. Chem. Eng. Data* **2016**, *61*, 565–570.
- (18) Taylor, K. C.; Nasr-el-din, H. A. Water-Soluble Hydrophobically Associating Polymers for Improved Oil Recovery: A Literature Review. *J. Pet. Sci. Eng.* **1998**, *19*, 265–280.
- (19) Wever, D. A. Z.; Picchioni, F.; Broekhuis, A. A. Polymers for Enhanced Oil Recovery : A Paradigm for Structure-Property Relationship in Aqueous Solution. *Prog. Polym. Sci.* **2011**, *36*, 1558–1628.
- (20) Abidin, A. Z.; Puspasari, T.; Nugroho, W. A. Polymers for Enhanced Oil Recovery Technology. *Procedia Chem.* **2012**, *4*, 11–16.
- (21) Pelletier, E.; Siron, R. Silicone-Based Polymers as Oil Spill Treatment Agents. *Environ. Toxicol. Chem.* **1999**, *18* (5), 813–818.
- (22) Banat, I. M.; Makkar, R. S.; Cameotra, S. S. Potential Commercial Applications of Microbial Surfactants. *Appl Microbiol Biotechnol* **2000**, *53*, 495–508.
- (23) Ciobanu, V. G.; Marcolli, C.; Krieger, U. K.; Weers, U.; Peter, T. Liquid-Liquid Phase Separation in Mixed Organic/Inorganic Aerosol Particles. *J. Phys. Chem. A* **2009**, *113*, 10966–10978.
- (24) Brien, R. E. O.; Wang, B.; Kelly, S. T.; Lundt, N.; You, Y.; Bertram, A. K.; Leone, S. R.; Laskin, A.; Gilles, M. K. Liquid–Liquid Phase Separation in Aerosol Particles: Imaging at the Nanometer Scale. *Environ. Sci. Technol.* **2015**, *49*, 4995–5002.
- (25) Stewart, D. J.; Cai, C.; Nayler, J.; Preston, T. C.; Reid, J. P.; Krieger, U. K.; Marcolli, C.; Zhang, Y. H. Liquid–Liquid Phase Separation in Mixed Organic/Inorganic Single Aqueous Aerosol Droplets. *J. Phys. Chem. A* **2015**, *119*, 4177–4190.
- (26) Hey, M. J.; Jackson, D. P.; Yan, H. The Salting-Out Effect and Phase Separation in Aqueous Solutions of Electrolytes and Poly(Ethylene Glycol). *Polymer (Guildf)*. **2005**, *46*, 2567–2572.
- (27) Song, H.; Chen, D. L.; Ismagilov, R. F. Reactions in Droplets in Microfluidic Channels. *Angew. Chemie - Int. Ed.* **2006**, *45*, 7336–7356.
- (28) Christopher, G. F.; Anna, S. L. Microfluidic Methods for Generating Continuous Droplet Streams. *J. Phys. D. Appl. Phys.* **2007**, *40* (19), 319–336.

- (29) Pompano, R. R.; Liu, W.; Du, W.; Ismagilov, R. F. Microfluidics Using Spatially Defined Arrays of Droplets in One, Two, and Three Dimensions. *Annu. Rev. Anal. Chem.* **2011**, *4*, 59–81.
- (30) Seemann, R.; Brinkmann, M.; Pfohl, T.; Herminghaus, S. Droplet Based Microfluidics. *Rep. Prog. Phys.* **2012**, *75*, 016601:1-41.
- (31) Shi, W.; Qin, J.; Ye, N.; Lin, B. Droplet-Based Microfluidic System for Individual *Caenorhabditis Elegans* Assay. *Lab Chip* **2008**, *8*, 1432–1435.
- (32) Schmitz, C. H. J.; Rowat, A. C.; Koster, S.; Weitz, D. A. Dropspots: A Picoliter Array in a Microfluidic Device. *Lab Chip* **2009**, *9*, 44–49.
- (33) Wang, W.; Yang, C.; Li, C. M. On-Demand Microfluidic Droplet Trapping and Fusion for On-Chip Static Droplet Assays. *Lab Chip* **2009**, 1504–1506.
- (34) Huebner, A.; Bratton, D.; Whyte, G.; Yang, M.; DeMello, A. J.; Abell, C.; Hollfelder, F. Static Microdroplet Arrays : A Microfluidic Device for Droplet Trapping , Incubation and Release for Enzymatic and Cell-Based Assays. *Lab Chip* **2009**, *9*, 692–698.
- (35) Bithi, S. S.; Vanapalli, S. A. Behavior of a Train of Droplets in a Fluidic Network with Hydrodynamic Traps. *Biomicrofluidics* **2010**, *4* (4), 44110.
- (36) Fradet, E.; McDougall, C.; Abbyad, P.; Dangla, R.; MccGloin, D.; Baroud, C. N. Combining Rails and Anchors with Laser Forcing for Selective Manipulation within 2D Droplet Arrays. *Lab Chip* **2011**, *11*, 4228–4234.
- (37) Simon, M. G.; Lin, R.; Fisher, J. S.; Lee, A. P. A Laplace Pressure Based Microfluidic Trap for Passive Droplet Trapping and Controlled Release. *Biomicrofluidics* **2012**, *6*, 014110:1-13.
- (38) Boukellal, H.; Selimovic, S.; Jia, Y.; Cristobal, G.; Fraden, S. Simple, Robust Storage of Drops and Fluids in a Microfluidic Device. *Lab Chip* **2009**, *9*, 331–338.
- (39) Cohen, D. E.; Schneider, T.; Wang, M.; Chiu, D. T. Self-Digitization of Sample Volumes. *Anal. Chem.* **2010**, *82*, 5707–5717.
- (40) Sun, M.; Bithi, S. S.; Vanapalli, S. A. Microfluidic Static Droplet Arrays with Tuneable Gradients in Material Compositions. *Lab Chip* **2011**, *11*, 3949–3952.
- (41) Watson, J. M.; Baron, M. G. The Behaviour of Water in Poly(dimethylsiloxane). *J. Memb. Sci.* **1996**, *110*, 47–57.
- (42) Eslami, F.; Elliott, J. A. W. Design of Microdrop Concentrating Processes. *J. Phys. Chem. B* **2013**, *117*, 2205–2214.
- (43) Eslami, F.; Elliott, J. A. W. Stability Analysis of Microdrops During Concentrating Processes. *J. Phys. Chem. B* **2014**, *118*, 3630–3641.
- (44) Talreja, S.; Kim, D. Y.; Mirarefi, A. Y.; Zukoski, C. F.; Kenis, P. J. A. Screening and Optimization of Protein Crystallization Conditions through Gradual Evaporation Using a Novel Crystallization Platform. *J. Appl. Crystallogr.* **2005**, *38*, 988–995.

- (45) Shim, J.; Patil, S. N.; Hodgkinson, J. T.; Bowden, S. D.; Spring, D. R.; Welch, M.; Huck, W. T. S.; Hollfelder, F.; Abell, C. Controlling the Contents of Microdroplets by Exploiting the Permeability of PDMS. *Lab Chip* **2011**, *11*, 1132–1137.
- (46) Goh, L.; Chen, K.; Bhamidi, V.; He, G.; Kee, N. C. S.; Kenis, P. J. A.; Zukoski, C. F.; Braatz, R. D. A Stochastic Model for Nucleation Kinetics Determination in Droplet-Based Microfluidic Systems. *Cryst. Growth Des.* **2010**, 2515–2521.
- (47) Solvas, X. C.; Turek, V.; Prodromakis, T.; Ede, J. B. Microfluidic Evaporator for ON-Chip Sample Concentration. *Lab Chip* **2012**, *12*, 4049–4054.
- (48) Shim, J. U.; Cristobal, G.; Link, D. R.; Thorsen, T.; Jia, Y. W.; Piattelli, K.; Fraden, S. Control and Measurement of the Phase Behavior of Aqueous Solutions Using Microfluidics. *J. Am. Chem. Soc.* **2007**, *129*, 8825–8835.
- (49) Chen, H.; Fang, Q.; Yin, X.; Fang, Z. Microfluidic Chip-Based Liquid – Liquid Extraction and Preconcentration Using a Subnanoliter-Droplet Trapping Technique. *Lab Chip* **2005**, *5*, 719–725.
- (50) Ziane, N.; Guirardel, M.; Leng, J.; Salmon, J. Drying with No Concentration Gradient in Large Microfluidic Droplets. *Soft Matter* **2015**, *11*, 3637–3642.
- (51) Nandy, L.; Dutcher, C. S. Phase Behavior of Ammonium Sulfate with Organic Acid Solutions in Aqueous Aerosol Mimics Using Microfluidic Traps. *J. Phys. Chem. B* **2018**, *Accepted*.
- (52) Carroll, N. J.; Rathod, S. B.; Derbins, E.; Mendez, S.; Weitz, D. A.; Petsev, D. N. Droplet-Based Microfluidics for Emulsion and Solvent Evaporation Synthesis of Monodisperse Mesoporous Silica Microspheres. **2008**, No. 18, 658–661.
- (53) Hung, L.-H.; Teh, S.-Y.; Jester, J.; Lee, A. P. PLGA Micro/nanosphere Synthesis by Droplet Microfluidic Solvent Evaporation and Extraction Approaches. *Lab Chip* **2010**, *10* (14), 1820.
- (54) Shum, H. C.; Abate, A. R.; Lee, D.; Studart, A. R.; Wang, B.; Chen, C.-H.; Thiele, J.; Shah, R. K.; Krummel, A.; Weitz, D. A. Droplet Microfluidics for Fabrication of Non-Spherical Particles. *Macromol. Rapid Commun.* **2010**, *31*, 108–118.
- (55) Kuehne, A. J. C.; Weitz, D. A. Highly Monodisperse Conjugated Polymer Particles Synthesized with Drop-Based Microfluidics. *Chem. Commun.* **2011**, 12379–12381.
- (56) Kim, J. H.; Jeon, T. Y.; Choi, T. M.; Shim, T. S.; Kim, S.; Yang, S. Droplet Microfluidics for Producing Functional Microparticles. *Langmuir* **2014**, *30*, 1473–1488.
- (57) Wijethunga, P. A. L.; Moon, H. On-Chip Aqueous Two-Phase System (ATPS) Formation, Consequential Self-Mixing, and Their Influence on Drop-to-Drop Aqueous Two-Phase Extraction Kinetics. *J. Micromechanics Microengineering* **2005**, *25*, 094002:1-11.
- (58) Ziemecka, I.; van Steijn, V.; Koper, G. J. M.; Kreutzer, M. T.; van Esch, J. H. All-Aqueous Core-Shell Droplets Produced in a Microfluidic Device. *Soft Matter* **2011**, *7*, 9878–9880.

- (59) Ziemecka, I.; van Steijn, V.; Koper, G. J. M.; Rosso, M.; Brizard, A. M.; van Esch, J. H.; Kreutzer, M. T. Monodisperse Hydrogel Microspheres by Forced Droplet Formation in Aqueous Two-Phase Systems. *Lab Chip* **2011**, *11*, 620–624.
- (60) Lai, D.; Frampton, J. P.; Sriram, H.; Takayama, S. Rounded Multi-Level Microchannels with Orifices Made in One Exposure Enable Aqueous Two-Phase System Droplet Microfluidics. *Lab Chip* **2011**, *11*, 3551–3554.
- (61) Song, Y.; Shum, H. C. Monodisperse W/w/w Double Emulsion Induced by Phase Separation. *Langmuir* **2012**, *28*, 12054–12059.
- (62) Kojima, T.; Takayama, S. Microscale Determination of Aqueous Two Phase System Binodals by Droplet Dehydration in Oil. *Anal. Chem.* **2013**, *85*, 5213–5218.
- (63) Boreyko, J. B.; Mruetusatorn, P.; Retterer, S. T.; Collier, P. Aqueous Two-Phase Microdroplets with Reversible Phase Transitions. *Lab Chip* **2013**, *13*, 1295–1301.
- (64) Moon, B.; Jones, S. G.; Hwang, D. K.; Tsai, S. S. H. Microfluidic Generation of Aqueous Two-Phase System (ATPS) Droplets by Controlled Pulsating Inlet Pressures. *Lab Chip* **2015**, *15*, 2437–2444.
- (65) Yamada, M.; Kasim, V.; Nakashima, M.; Edahiro, J.; Seki, M. Continuous Cell Partitioning Using an Aqueous Two-Phase Flow System in Microfluidic Devices. *Biotechnol. Bioeng.* **2004**, *88* (4), 489–494.
- (66) Nam, K.; Chang, W.; Hong, H.; Lim, S.-M.; Kim, D.-I.; Koo, Y.-M. Continuous-Flow Fractionation of Animal Cells in Microfluidic Device Using Aqueous Two-Phase Extraction. *Biomed. Microdevices* **2005**, 189–195.
- (67) Meagher, R. J.; Light, Y. K.; Singh, A. K. Rapid, Continuous Purification of Proteins in a Microfluidic Device Using Genetically-Engineered Partition Tags. *Lab Chip* **2008**, *8*, 527–532.
- (68) Soohoo, J. R.; Walker, G. M. Microfluidic Aqueous Two Phase System for Leukocyte Concentration from Whole Blood. *Biomed Microdevices* **2009**, 323–329.
- (69) Frampton, J. P.; Lai, D.; Sriram, H.; Takayama, S. Precisely Targeted Delivery of Cells and Biomolecules Within Microchannels Using Aqueous Two-Phase Systems. *Biomed Microdevices* **2011**, *13*, 1043–1051.
- (70) Hu, R.; Feng, X.; Chen, P.; Fu, M.; Chen, H.; Guo, L.; Liu, B. Rapid , Highly Efficient Extraction and Purification of Membrane Proteins Using a Microfluidic Continuous-Flow Based Aqueous Two-Phase System. *J. Chromatogr. A* **2011**, *1218*, 171–177.
- (71) Silva, D. F. C.; Azevedo, A. M.; Fernandes, P.; Chu, V.; Conde, J. P.; Aires-Barros, M. R. Determination of Aqueous Two Phase System Binodal Curves Using a Microfluidic Device. *J. Chromatogr. A* **2014**, *1370*, 115–120.
- (72) Goa, Y.-L.; Peng, Q.-H.; Li, Z.-C.; Li, Y.-G. Thermodynamics of Ammonium Sulfate-Polyethylene Glycol Aqueous Two-Phase Systems. Part 1. Experiment and Correlation Using Extended Uniquac Equation. *Fluid Phase Equilib.* **1991**, *63*, 157–171.

- (73) Zafarani-moattar, M. T.; Hamzehzadeh, S. Liquid–Liquid Equilibria of Aqueous Two-Phase Systems Containing Polyethylene Glycol and Sodium Succinate or Sodium Formate. *Comput. Coupling Phase Diagrams Thermochem.* **2005**, *29*, 1–6.
- (74) Xia, Y.; Whitesides, G. M. Soft Lithography. *Angew. Chem. Int. Ed.* **1998**, *37*, 550–575.
- (75) McDonald, J. C.; Duffy, D. C.; Anderson, J. R.; Chiu, D. T.; Wu, H.; Schueller, O. J. A.; Whitesides, G. M. Fabrication of Microfluidic Systems in Poly(dimethylsiloxane). *Electrophoresis* **2000**, *21*, 27–40.
- (76) Vuong, S. M. A Microfluidic Platform for the Control and Analysis of Phase Transitions in Concentrating Droplets. *PhD Thesis, Carnegie Mellon* **2014**.

Chapter 5. Dehydrating Particle-Polymer Droplets to Investigate Jamming at High Particle Concentrations

5.1 Introduction

Concentrating nanoparticle based colloidal systems is a common practice in many industrial processes including paints, coatings, and inks. The microstructure, stability, and resilience of the final material are important characteristics of the coating. The understanding and control of these parameters is valuable for industrial applications. Typical procedures involve spraying or coating a material with a colloidal suspension and allowing the volatile solvent to evaporate. When the coating achieves high particle concentrations, systems will transition from a viscous fluid-like material to an elastic solid-like material.¹⁻³ When the system completely dries, the final particle concentration and structure will depend on the dehydration rate,¹ particle shape,⁴⁻⁶ polydispersity,^{7,8} and interparticle interactions.^{9,10}

A common simplification to study concentrated particulate systems is to assume hard sphere particles. For theoretical “hard spheres”, particles have zero attractive or repulsive forces and the potential is approximated as an infinite repulsion on contact. The particles effectively bounce off each other². Hard sphere systems are conducive to theoretical modelling and this model system has been characterized thoroughly in terms of phase behavior^{11,12}, kinetics¹³⁻¹⁵, and evolution^{16,17} of the behavior of these systems in different concentration regimes.

The different phases of highly concentrated hard sphere colloidal systems have been investigated and observed to depend strongly on particle volume fraction^{1,2,18}. The effect of volume fraction on phase behavior was first systematically analyzed by Poon et al.². Samples of various particle concentrations were produced and allowed to reach equilibrium. The resulting

samples were then binned into four distinct groupings based on phase properties – fluid, fluid-crystal, crystal, and glass. Below a freezing volume fraction cutoff, the system remains as a homogenous fluid and shows no signs of phase separation. Once the phase boundary is reached, crystals form and increase in relative volume until the entire sample is crystallized. Different crystal shapes were observed until a secondary boundary at which the particles became trapped in a metastable non-equilibrium “glassy” state.

The freezing volume fraction is determined to be $\phi = 0.494$ which is consistent with computer simulations¹⁹ and the melting volume fraction is determined to be $\phi = 0.545$, where the entire system becomes fully crystalline.¹ These three phases are considered the thermodynamic equilibrium states for a given colloidal volume fraction. However if the concentration is increased too rapidly, the system may remain supercooled or jam into a glass. This metastable state can persist for extended periods (years) due to the effective “cages” particles create around one another, with each particle thought to be confined by its nearest neighbors and unable to rearrange into a crystalline structure. The transition from a supercooled fluid to a glass occurs when the viscosity of the system reaches about 10^{13} poise²⁰ and occurs at a volume fraction of approximately $\phi = 0.58$. Simulations have been conducted to examine the glass transition^{3,7,13}. However, there is still significant controversy regarding the exact nature and microscopic structure of the glass transition.

Removing the hard sphere assumption and adding repulsive and attractive forces complicates both the equilibrium and metastable behavior.²¹ Attractive forces such as bridging flocculation, depletion flocculation, and van der Waals attractive forces can cause aggregation of particulate systems leading to loose, flocced particle networks as opposed to tight, compact, glassed structures.^{22–25} Repulsive forces such as steric or electrostatic repulsion will counter

balance the attractive forces and prevent aggregation if strong enough.²⁶ Therefore, a firm understanding of the effect of interparticle attractive and repulsive forces on concentrated particle behavior and structure is necessary to predict behavior of industrial coatings and materials.

Traditional macroscopic drying experiments often lead to cracking and fracturing of drying systems,^{27–31} as well as requiring large quantities of material. Dehydrating sessile droplets use much less material, but both the drop generation and drying process are difficult to control. A sessile droplet containing nanoparticle material is subject to the “coffee ring effect”,³² resulting in contact line pinning and heterogeneities in the sample.^{33–35} Microfluidic droplets provide a unique, well controlled dehydration technique with a non-pinned liquid-liquid interface to produce and concentrate nanoparticle systems on-chip. Previous dehydrating microfluidic droplet experiments have been performed investigating crystallization kinetics,^{36–40} phase separation,^{41–44} and particle synthesis.^{45–49}

The goal of this work is to characterize the design limitations of a droplet-based microfluidic device and dehydrate droplets containing electrostatically stabilized silica nanoparticles with PEO polymer. Droplet concentration accuracy is demonstrated with refractive index matching experiments containing aqueous sucrose droplets and a mineral oil outer phase. Dehydrating silica nanoparticle droplets are characterized and the final particle volume fraction is investigated with varying interparticle potential. Interparticle potential is tuned via interactions with the PEO polymer source. Final particle volume fraction is strongly dependent on polymer concentration, specifically at low polymer concentration, and a particle bridging to jamming aggregation mechanism is proposed as a function of polymer to particle mass ratio.

5.2 Materials and Methods

Ludox TM-40 and Ludox TMA silica particles are purchased from Sigma-Aldrich (St. Louis, MO). Two different molecular weight poly(ethylene oxide), PEO, polymers are used in this work: 7500 g/mol and 100k g/mol both purchased from Polysciences Inc. (Warminster, PA) and expected to be polydisperse in molecular weight. Light mineral oil (40 cP) is obtained from Fisher Scientific (Hampton, NH) and Span-80 is purchased from Sigma-Aldrich and added to the mineral oil for the droplet production process. PDMS is purchased from Dow Corning (Midland, MI) and used to produce the microfluidic devices. It comes as a two-part elastomer kit (Sylgard 184) containing both the pre-polymer and curing agent. Deionized water (18.2 M Ω -cm) is used to dilute the particle suspensions and create the polymer solutions.

For microfluidic experiments, stock solutions of 4 wt% PEO polymer and 4 wt% silica particles are produced and allowed to sit overnight. These solutions are then combined in different ratios by mass to provide various polymer/particle compositions. Once mixed, the samples are sonicated for 15 minutes before being injected into a device to produce microfluidic droplets.

As in Chapter 4, the mass ratio of polymer to particles is defined as ξ and the mass per volume in the system is defined as θ . At any point in the experiment, a concentration is defined using the two solute concentrations or by the (ξ, θ) pair. Initial droplet concentration is determined in a mass/volume ratio by measuring the density of the initial solution and converting to wt/volume of polymer and volume/volume of particles. Solution density is measured by weighing the mass of known volumes of solution 5 times and averaging the results.

Microfluidic devices are fabricated using the method previously described in Chapter 3 and are made of PDMS elastomer. Devices are soaked for a minimum of 5 days in light mineral

oil to allow for complete absorption and saturation of mineral oil in the device. A 2 wt% Span-80 mineral oil solution is used to lower interfacial tension and create favorable wetting conditions during droplet production and then flushed from the device with clean mineral oil for 20 minutes after droplet production. Droplet analysis is performed using the method described in Chapter 4.

5.3 Results

5.3.1 Verification of volume measurement

Microfluidic droplets provide a unique, controlled dehydration process to probe colloidal phenomena with high composition resolution. The capabilities of the device strongly depend on accurate concentration measurements during dehydration. To determine measurement accuracy, a system with known concentration is used as a standard and compared with measured droplet concentration. This demonstrates feasibility of the technique and provides error values on measured concentrations.

Droplets containing various initial concentrations of sucrose are produced in a microfluidic device to verify measured and predicted system concentrations using the known value at which the sucrose solution refractive index matches the oil and the drop disappears. Sucrose dissolved in water changes the refractive index of the aqueous solution linearly depending on the sucrose concentration described in Equation 5.1^{50,51}

$$n_{solution} = (0.048 \frac{1}{M}) C_{sucrose} + n_{solvent} \cdot \quad (5.1)$$

where $n_{solution}$ is the refractive index of the mixture, $C_{sucrose}$ is the concentration of sucrose in mol/L, and $n_{solvent}$ is the refractive index of the solvent (1.33 for water at 25 °C). The refractive index of mineral oil used as the continuous outer phase fluid is $n = 1.46$ and remains constant

throughout the experiment. As an aqueous sucrose droplet dehydrates, the refractive index of the droplet increases linearly from 1.33 for pure water through the value of 1.46 at a sucrose concentration of 2.7 M and to higher concentrations. At a concentration of 2.7 M, the refractive index of the droplet matches that of the oil and the droplet will become optically invisible. The droplet volume at this concentration will depend on the initial concentration and initial size of the droplet. This allows the refractive index match point to be used to compare the calculated concentration from Equation 4.1 in Chapter 4 with the known concentration from Equation 5.1 for droplets of various sizes.

For comparison, it is convenient to rearrange Equation 5.1. Combining Equation 5.1 with conservation of mass and equating $n_{solution}$ with the refractive index value of the solvent n_{oil} ($n = 1.46$) results in Equation 5.3

$$\frac{V_{match}}{V_{initial}} = \frac{(0.048 \text{ 1/M})C_{sucrose}}{n_{oil} - n_{water}}. \quad (5.2)$$

This allows for a direct comparison between the actual volume of a refractive index matched sucrose droplet and the measured volume of droplet.

Figure 5.1a shows images of a sucrose droplet in a microfluidic device as it concentrates through a refractive index match point. Droplets are initially 575 μm in diameter with a volume of approximately 23 nL. Figure 5.1a shows images of the droplet as time progresses and the droplet dehydrates. Figure 5.1a-iv shows the droplet as its refractive index matches, resulting in what appears to be an empty droplet trap. Images are recorded every two minutes for approximately 24 hours. Droplets remain refractive index matched for 10-15 minutes with a volume change of 3-4%. Droplet concentration is measured and calculated for the last image

before droplets disappear and the first image after droplets reappear. The average concentration between these two values is considered the refractive index match concentration. Six experiments are performed at different initial sucrose concentrations and the refractive index matching results are shown in Figure 5.1b.

a)

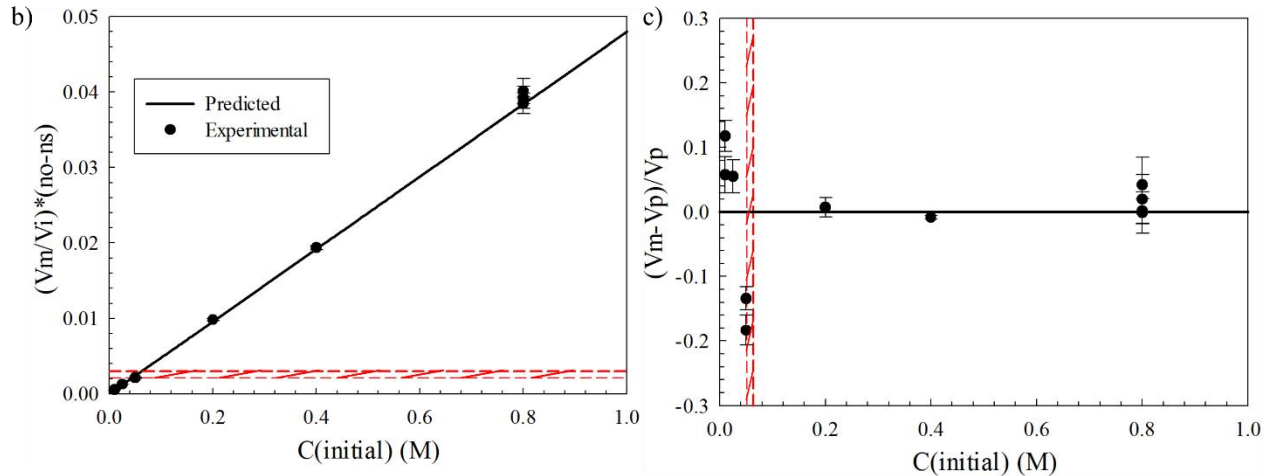
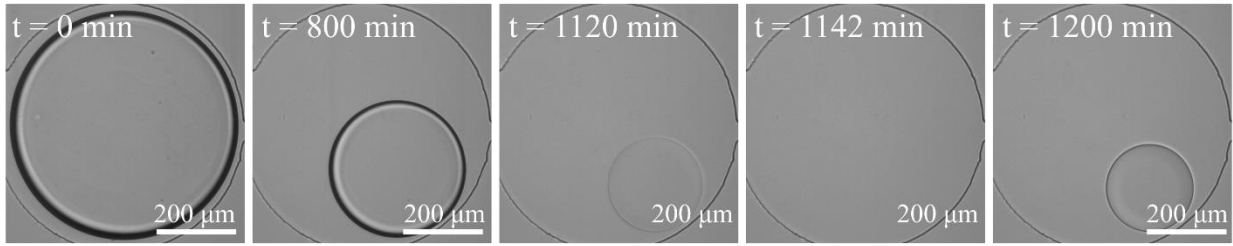


Figure 5.1: (a) Images of a sucrose droplet drying refractive index match experiment. Time goes from left to right along images with a refractive index match between the droplet and the oil at $t = 1142$ min. (b) Scaled volume refractive index verification of sucrose droplets in mineral oil as a function of initial droplet concentration. Solid black line is the predicted value and closed circles are experiment results. The hashed red line depicts the pancake to sphere transition at $95 \pm 5 \mu\text{m}$. (c) Scaled volume measurements replotted as an error percentage. Partial results courtesy of Deyu Yang.

Figure 5.1b plots $(V_{\text{match}}/V_{\text{initial}})/(n_{\text{oil}} - n_{\text{water}})$ as a function of initial sucrose concentration in mol/L. The solid black line is the predicted volume of the refractive index matched droplet based on the initial sucrose concentration from Equation 5.2. The black points are the measured volumes from the image analysis technique described in Chapter 4. The hashed red box indicates the transition where droplets change shape from a pancake to a sphere as the droplet diameter

becomes smaller than the height of the channel ($95 \pm 5 \mu\text{m}$). A similar analysis has been performed⁵² and shows comparable behavior. There is good agreement between the measured versus predicted volumes at which the droplet matches the refractive index of the oil for all initial concentrations, suggesting that the droplet based technique accurately measures droplet concentration across all droplet sizes. However, slight differences in volume at small droplet sizes can lead to large errors in calculation that can be masked by plotting results in this method. A direct comparison between the measured volume and predicted volume is necessary to accurately evaluate the technique.

Figure 5.1c plots the percentage difference between the measured volume and predicted volume at the refractive index match point defined by $(V_{measured} - V_{predicted})/V_{predicted}$ as a function of initial sucrose concentration in mol/L. The solid black line highlights a difference of zero percent, where deviations from this line indicate error in droplet concentration calculation. The hashed red box indicates the position where droplets of initial diameter $d = 575 \mu\text{m}$ change from pancake shapes to spheres, with pancake shaped droplets to the right of the box and spherical droplets to the left. The solid black points show the results from Figure 5.1b replotted in $(V_{measured} - V_{predicted})/V_{predicted}$ units. There is great agreement between the measured and predicted droplet volumes for droplets that retain a pancake shape as the refractive index point is reached with a difference of approximately $\pm 2\%$. It is important to note that although the difference is within 2%, droplets are refractive index matched and invisible for 3-4 vol%, resulting in an error of 3-4%. This can be reduced by imaging at more frequent intervals or using phase contrast microscopy to more finely detect differences between the droplet and oil. Droplets that transition to a spherical shape have poorer agreement between measured and predicted volumes with errors from 5-20%. This suggests that droplets above the pancake-to-

sphere transition return accurate concentration measurements, but droplets below the transition return inaccurate measurements. The relationship between droplet shape and concentration accuracy is further investigated with droplets containing Ludox TM-40 silica particles.

5.3.2 *Valid range of technique*

Microfluidic droplets containing Ludox® TM-40 are produced in a continuous mineral oil outer phase and concentrated on-chip to analyze the shape behavior and concentration range of the drying process. When droplets are initially produced at dilute particle concentrations, they are optically clear and fluid like. As the droplets concentrate, they decrease in size as the aqueous solvent partitions through the oil/device and out into the atmosphere. When the final particle volume fraction in the droplet is reached, a ring begins to form at the edge of the droplet and moves concentrically towards the center of the droplet. Once the ring reaches the middle of the droplet, the droplet returns to optical clarity and remains the same size and concentration indefinitely. This concentration is the final particle volume fraction found using the image analysis method described in Chapter 4. Note that bulk dispersions of electrostatically stabilized Ludox TM-40 dry to opaque, glassy films.

Figure 5.2a shows the typical drying process of a Ludox TM-40 aqueous droplet as a series of images. Images of the same droplet at various time points are shown to demonstrate the observed ring effect that occurs at high particle concentrations. The ring effect only occurs at the last stages of dehydration and lasts for approximately 1 hr. Figure 5.2b shows the diameter of a droplet as a function of time for a typical dehydration experiment. The droplet is initially 543 μm in diameter and dehydrates to a final droplet diameter of 156 μm . The ring formation begins at 1336 minutes and ends at 1400 minutes. The droplet diameter decreases linearly through the dehydration process until ring formation begins, after which droplet diameter remains flat at a

final fixed value as shown in Figure 5.2b. The inset shows a magnified view of droplet diameter at the end of the dehydration process.

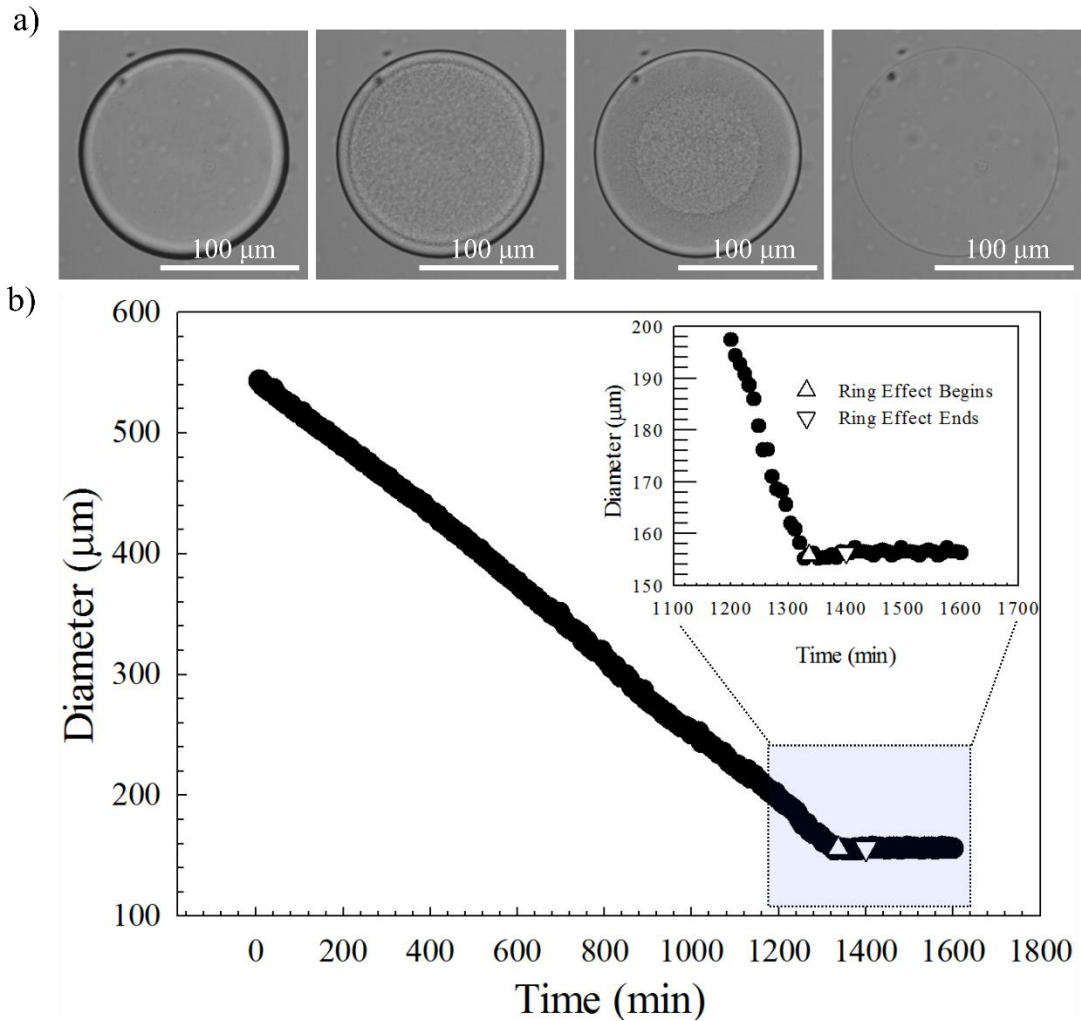


Figure 5.2: Analysis of characteristic ring formation during final stages of droplet drying. (a) Images of observable ring as a function of time. Images times with respect to ring formation correspond to 0 min, 18 min, 40 min, and 64 min. (b) Droplet diameter as a function of time during the dehydration process.

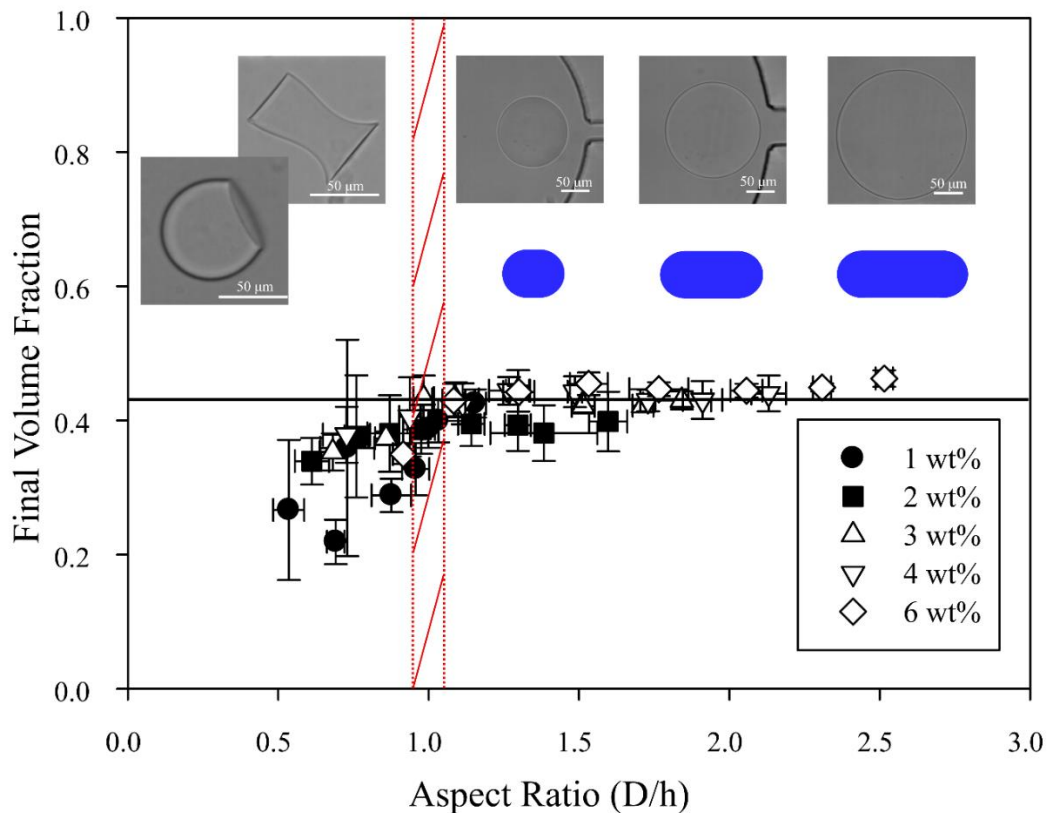


Figure 5.3: Final particle volume fraction of Ludox TM-40 silica nanoparticles as a function of final aspect ratio for 5 initial concentrations. Each data point is the average of 8 droplets with error bars displaying the standard deviation. Corresponding initial droplet concentrations are shown in the legend. The hashed red line is the pancake to sphere transition at $95 \pm 5 \mu\text{m}$. Images show characteristic droplet shapes based on aspect ratio.

Figure 5.3 shows the effect of droplet aspect ratio on the final calculated volume fraction for aqueous droplets containing a range of initial concentrations of Ludox TM-40 silica particles. The x-axis is defined as the aspect ratio (D/h) of the droplet at its final dried state where D is the measured diameter of the droplet and h is the height of the channel. The y-axis is the particle volume fraction of the system when the droplets no longer concentrate. Droplets of Ludox-TM40 suspensions are produced over a range of initial droplet sizes and particle concentrations. A modified version of the microfluidic device design from Chapter 4 is used for these

experiments. Instead of having 40 droplets in device all produced at the same initial droplet size, 4 rows of 8 droplets are produced where each column has a different droplet trap diameter. The trap sizes increase sequentially from 300-1000 μm in diameter by increments of 100 μm . This results in each droplet trap size having 4 traps (or droplets) per device. Systematic droplet drying experiments are performed at various initial particle loadings from 1 wt% to 6 wt%. Two experiments are performed for each initial concentration to produce 8 droplets per trap size for a given initial concentration and to increase the statistical resolution on final droplet size.

Aspect ratio is determined by dividing the measured final droplet diameter from image analysis by the height of the channels (taken to be $95 \mu\text{m} \pm 5 \mu\text{m}$). The hashed red box represents the aspect ratio at the pancake-sphere transition. Final volume fraction is calculated through the volume equation from Vuong *et al.*,⁵³ previously described in Chapter 4. Each point on the plot is an average of 8 droplets for a given trap size and initial concentration. Error bars in final volume fractions are the standard deviation between the 8 droplets. Droplets for a given trap size are not produced at exactly the same size, so there is also some variation in the initial aspect ratio and therefore final aspect ratio. This variation is shown by the error bars in the x-axis direction, calculated as the standard deviation difference between the final aspect ratios for a set of initial conditions.

The results show a final measured volume fraction of approximately $\phi = 0.43 \pm 0.03$ for aspect ratio ≥ 1 , shown by the solid black line in Figure 5.3. For aspect ratio ≤ 1 , there is a significant deviation in final measured volume fraction with an increase in variation in final concentration as seen by the standard deviation. Above an aspect ratio of 1, the droplet diameters are larger than the height of the droplets, resulting in a pancake shaped droplet. The droplets will retain this shape as long as droplet diameter is larger than channel height and can be

used to accurately calculate the final particle volume fraction. Issues arise when attempting to calculate the concentration of droplets with an aspect ratio ≤ 1 . Droplet diameters are measured by imaging from the viewpoint of the top of a droplet. This provides no information on the three dimensional shape and will only return the point of largest width. To calculate a volume from one projection of the droplet shape, droplets at these conditions are assumed to be spherical as this is the minimal energy configuration. However, wetting on either the top or bottom channels can lead to abnormal droplet shapes including partially spherical or hourglass shaped droplets. Images of these droplet shapes are shown to the left of the dotted line in Figure 5.3b in comparison with droplets above an aspect ratio of 1 to the right. If droplets below an aspect ratio of 1 are erroneously considered to remain pancake-shaped, final volume fraction will be further under predicted.

These results suggest that an inaccurate concentration calculation will occur when droplet diameters result in an aspect ratio less than 1. Therefore in all future experiments, initial concentrations are chosen to ensure droplets remain above an aspect ratio of 1 for the duration of an experiment. In addition, the results provide a reliable and consistent measure of a final particle volume fraction of $\phi = 0.43$ for Ludox TM-40 in water dispersions.

5.3.3 Particle-polymer mixtures

Polymer is introduced to the particle filled dehydrating droplets to investigate the phase behavior and particle interactions of a concentrated complex system. 7500 g/mol PEO is added as the polymer source and droplets containing particle-polymer mixtures are produced on-chip and dehydrated. Ludox TMA ($d = 22$ nm, $\zeta = -25$ mV)⁵⁴ is used as the particle source for these experiments. Ludox TMA has the same particle diameter as Ludox TM-40, but is reported to have less residual salt in the stock solution (0.1 wt% Na₂SO₄ for TM-40 compared with salt free

for TMA). The mass ratio of polymer/particle (ξ) is varied across droplet drying experiments to examine a large region of compositional space. Droplets are produced in the same microfluidic droplet trap from Chapter 4 with 40 droplets per device and a droplet trap size of 575 μm . One droplet is recorded per experiment with high optical resolution to observe phase separation and behavior. All 40 droplets are used to calculate an average final particle volume fraction.

Figure 5.4 shows the results of the Ludox TMA and 7500 g/mol PEO system as a phase diagram. The x-axis is Ludox TMA concentration in particle volume fraction and the y-axis is polymer concentration in g/mL. Each thin dotted black line represents the compositional path of a tested droplet for a given polymer/particle mass ratio ξ . The closed red circles denote droplet samples at their initial dilute concentration. The single closed black circle represents the only concentration at which phase separation is observed. The open circles correspond to the final concentration of droplets once dehydration has stopped. The thick dotted black lines show the maximum possible concentration of polymer (1.13 g/mL)⁵⁶ and particles (random close packed limit, $\phi = 0.63$). The dotted red line displays the saturation concentration of PEO on silica particles (1.2 mg/m², $\xi = 0.17$) for highly concentrated systems.⁵⁵ The solid black line denotes the concentration of the fully dehydrated system with only particles and polymer remaining. Error bars would be in the diagonal direction along the composition paths and are instead shown later in Figure 5.5.

Several behaviors are observed as droplets approach final concentrations shown as a series of images in Figure 5.4b. For all samples above the saturation limit, droplets start and remain optically clear through the entire process until dehydration is arrested. For the samples below the saturation limit, a ring forms at the edge of the droplet and moves radially towards the center of the droplet, similar to the polymer free case. There is one sample (indicated by the

filled symbol) where phase separation is briefly observed. This is likely salt-polymer phase separation from the minute amounts of salt introduced from particle stock and is discussed much more in depth in Appendix A.

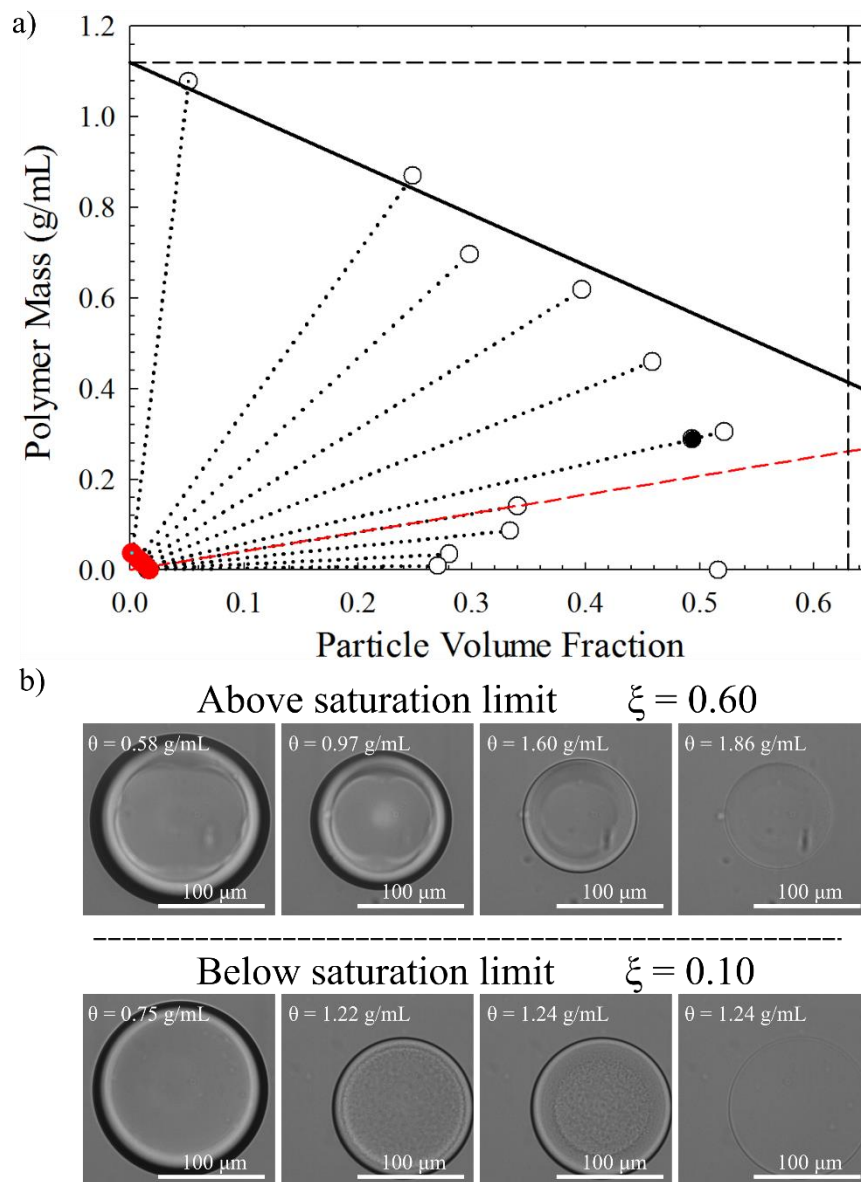


Figure 5.4: Phase diagram of Ludox TMA particles and 7500 g/mol PEO mapped using microfluidic droplet drying. (a) The red circles denote initial droplet concentrations, open circles denote the final droplet concentration, and the single closed black circle denotes the only system that displays phase separation. The thin dotted black lines depict the composition paths of each experiment, the thick dotted black lines represent maximum concentration of particles and polymer, and the solid black line shows the system composition when no water remains in the droplet. The dotted red line denotes the saturation line (1.2 mg/m^2 , $\xi = 0.17$).⁵⁵ (b) Images of droplet behavior at the final stages of the drying experiment. First

row of images is characteristic of droplets above the saturation limit and the second row is characteristic of droplets below the saturation limit.

An intriguing and unexpected result is observed for droplet drying of systems with mass ratios below the saturation limit. A final particle volume fraction of $\phi = 0.52$ is observed for droplets only containing Ludox TMA particles. However, with the addition of even a small amount of polymer to the system ($\xi = 0.013$), the final particle volume fraction decreases to approximately $\phi = 0.27$.

Figure 5.5a shows the final particle volume fraction from Figure 5.4a replotted as a function of the polymer/particle mass ratio, ξ . The dotted black line depicts the concentration at which droplets with no added polymer (Ludox TMA only) reach their final particle volume fraction ($\phi = 0.52$). The dotted red line denotes the mass ratio at which the particle surface becomes saturated with polymer. The solid black line shows the final particle volume fraction if fully dehydrated and only particles and polymer remain. Error bars correspond to the standard deviation of final particle volume fraction for 40 droplets in a device. Most error bars are of similar size to the data points.

At the lowest polymer/particle mass ratio of $\xi = 0.013$, the final particle volume fraction of $\phi = 0.27$ is far below the particle only final volume fraction of $\phi = 0.52$. Using a BET surface area measurement of $140 \text{ m}^2/\text{g}$ Ludox TMA,⁵⁷ the polymer/particle number ratio at this concentration is equivalent to 14 polymer molecules/particle. A mass ratio of $\xi = 0.0009$ is required to achieve a polymer/particle number ratio of 1 chain/particle. As more polymer is introduced into the system (increase in ξ), the final particle volume fraction is observed to increase to a maximum at $\xi = 0.23$, which has a number ratio of 250 chains/particle. The maximum particle volume fraction at this mass ratio is approximately equivalent to that of the

particle only case. As polymer/particle mass ratio increases beyond this value, the final particle volume fraction decreases monotonically and matches well with the predicted line for a completely dehydrated droplet (no retained water).

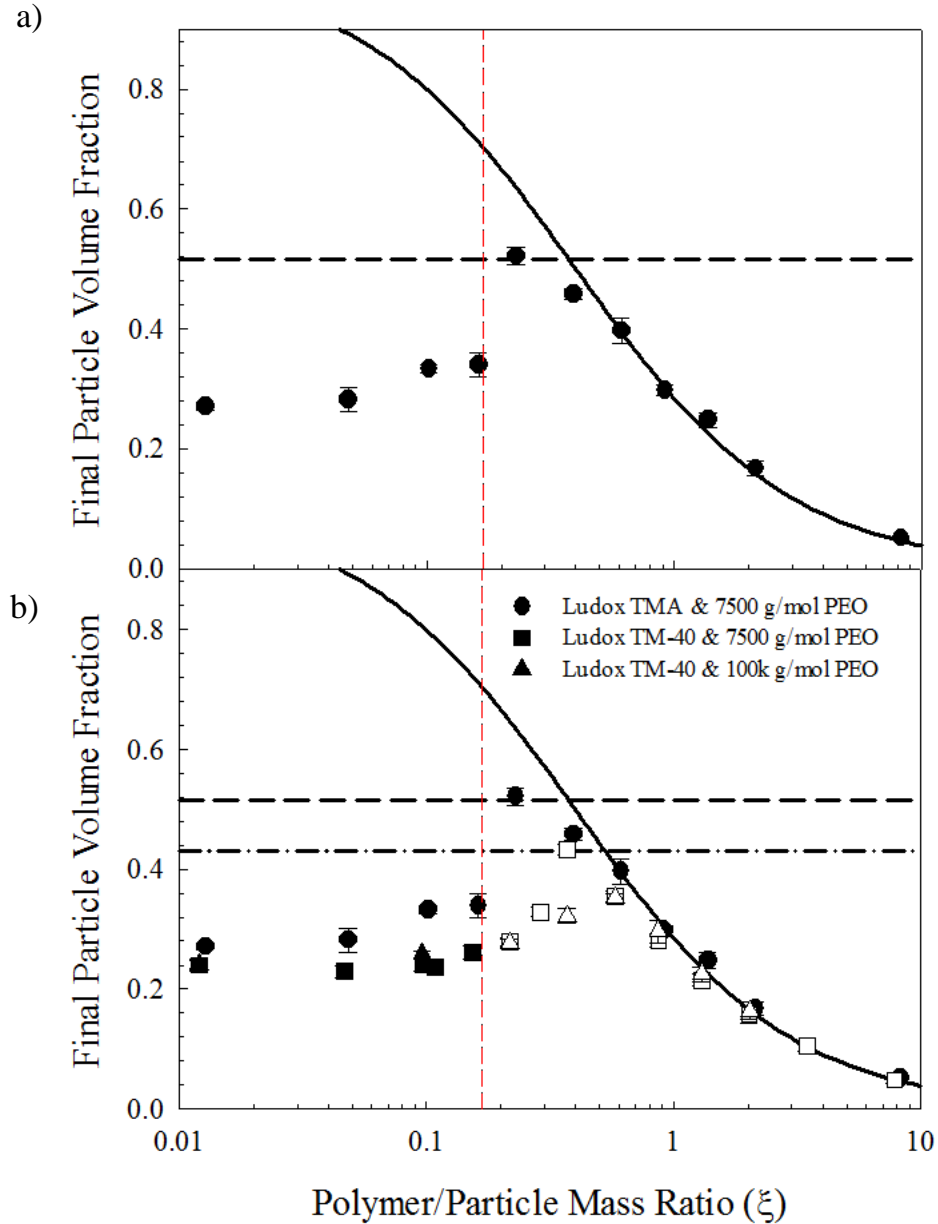


Figure 5.5: Final droplet particle concentration as a function of polymer-particle mass ratio. (a) Solid black circles show final concentrations for the Ludox TMA and 7500 g/mol PEO system. Dotted black line demonstrates final particle concentration with no polymer. Solid black line shows the particle volume fraction at which no water remains in the system (only particles and polymer). (b) Similar results with two additional tested systems, labeled in the legend. The dashed black line demonstrates the final particle volume fraction for Ludox TMA particles and the dot-dash black line for Ludox TM-40 particles.

Figure 5.5b shows final particle volume fraction as a function of polymer-particle mass ratio for the Ludox TMA and 7500 g/mol PEO system along with similar results for Ludox TM-40 with 7500 or 100k g/mol PEO. The dotted black line in Figure 5.5b shows the final particle concentration for Ludox TMA and the dot-dash black line shows the final particle concentration for Ludox TM-40. The circles correspond to the Ludox TMA & 7500 g/mol PEO system, the squares correspond to the Ludox TM-40 and 7500 g/mol PEO system, and the triangles correspond to the Ludox TM-40 and 100k g/mol PEO system. In all cases, closed points denote concentrations where no phase separation is observed during the dehydration process and the open points denote concentrations where phase separation occurs. Phase separation in these systems is likely organic-inorganic (salt-polymer) phase separation from Chapter 4 at dilute salt concentrations and is discussed further in Appendix A.

All three systems follow a similar trend in final particle volume fraction as a function of polymer/particle mass ratio (ξ). At low ξ , the final concentration is far below the particle only case and increases to a maximum value as ξ increases. Beyond the maximum, the final particle volume fraction decreases similarly between all systems. It is interesting to point out that when phase separation occurs in the Ludox TM-40 case, there is very minimal effect on the final particle volume fraction compared to that of the Ludox TMA case where no phase separation occurs.

The location and value of the maximum volume fraction is different for each system. For Ludox TMA, the maximum is at the highest volume fraction ($\phi = 0.52 \pm 0.02$) and the lowest mass ratio of $\xi = 0.23$. Ludox TM-40 with 7500 g/mol PEO has a maximum at $\xi = 0.37$ with a final volume fraction approximately equivalent to the particle only system ($\phi = 0.43 \pm 0.02$).

Ludox TM-40 with 100k g/mol PEO has a maximum at $\xi = 0.58$ with a final particle value below that of the particle only system.

5.4 Discussion

Figure 5.4 and Figure 5.5 demonstrate an interesting observation at low polymer/particle mass ratio. At these mass ratios, the final particle volume fraction is significantly lower than that of the particle only case. This means that with the addition of a small amount of polymer, a drying particulate system reaches a stable, solid-like configuration at significantly more dilute concentrations than a polymer free case ($\phi = 0.27$ compared with $\phi = 0.52$). As more polymer is introduced into the system, the final particle volume fraction increases towards the polymer free case. A potential mechanism for this observed phenomena is bridging flocculation due to polymer-particle interactions.

Bridging flocculation occurs when particle surfaces are only partially covered by an adsorbing polymer. If a single polymer chain can contact and adsorb to two separate particles, it can cause them to aggregate and form open, flocced networks. Adsorption of PEO on silica surfaces has been studied extensively^{55,58-61} and found to display polymer bridging characteristics.⁶²⁻⁶⁴ Zaman studied the rheological effects of adding 7500 g/mol PEO to 600 nm in diameter silica particles⁶⁴ and found that at low polymer concentrations (<1 mg PEO/g silica), the viscosity of the system increased from 0.2 to 0.5 Pa·s compared to the viscosity of high polymer or no polymer systems, argued to be due to bridging flocculation.

Interparticle spacing and polymer chain length are necessary to determine the feasibility of a bridging flocculation mechanism. It has been shown that bridging flocculation will only occur if the end to end length of a polymer chain is on the order of the interparticle spacing.⁶⁵ If

an adsorbed polymer chain cannot reach a second particle, then it cannot induce aggregation.

The average center-to-center interparticle spacing is estimated by $D \approx (8a/\phi)^{1/3}$, resulting in $D = 30\text{-}40$ nm for $2a = 22$ nm particles at $\phi = 0.23$.

For PEO in water, the mean end-to-end polymer distance is approximated by⁶⁵ $L \approx (6)^{1/2} \cdot R_g$ where L is the end-to-end length and R_g is the radius of gyration of the polymer chain (3.6 nm for 7500 g/mol PEO)⁶⁴. This results in a mean end-to-end polymer distance of approximately 9 nm for 7500 g/mol PEO and 32 nm for 100k g/mol PEO assuming a square root dependence of radius of gyration on polymer molecular weight. The contour length of a fully stretched 7500 g/mol PEO molecule, for comparison, is much larger at approximately 56 nm assuming 170 repeat units each equivalent to 0.33 nm in length. This comparison demonstrates that the mean end-to-end distance of a polymer chain (O(10 nm)) is comparable to the surface-to-surface interparticle spacing (O(10-20 nm)) and is plausible as an aggregation mechanism.

Figure 5.6 demonstrates the concepts detailed in this description. At low polymer/particle mass ratios, there are far more open adsorption sites than polymer chains. This leads to only partial coverage of particle surfaces. As the systems become highly concentrated ($\phi \approx 0.25$), polymer bridging can occur which causes particle aggregation and flocculation. Ludox has a large Hamaker constant ($A = 0.83 \cdot 10^{-20}$ J)⁶⁶ causing particles to be stuck in a deep potential well and unlikely to separate once brought together. This can lead to the formation of a loose, flocculated particle network connected by bridged polymer chains as shown in Figure 5.6. Once the structure becomes elastic and solid-like, it can resist further compression and remain as a stable concentrated droplet. The droplet size will be significantly larger than a more concentrated, close packed system.

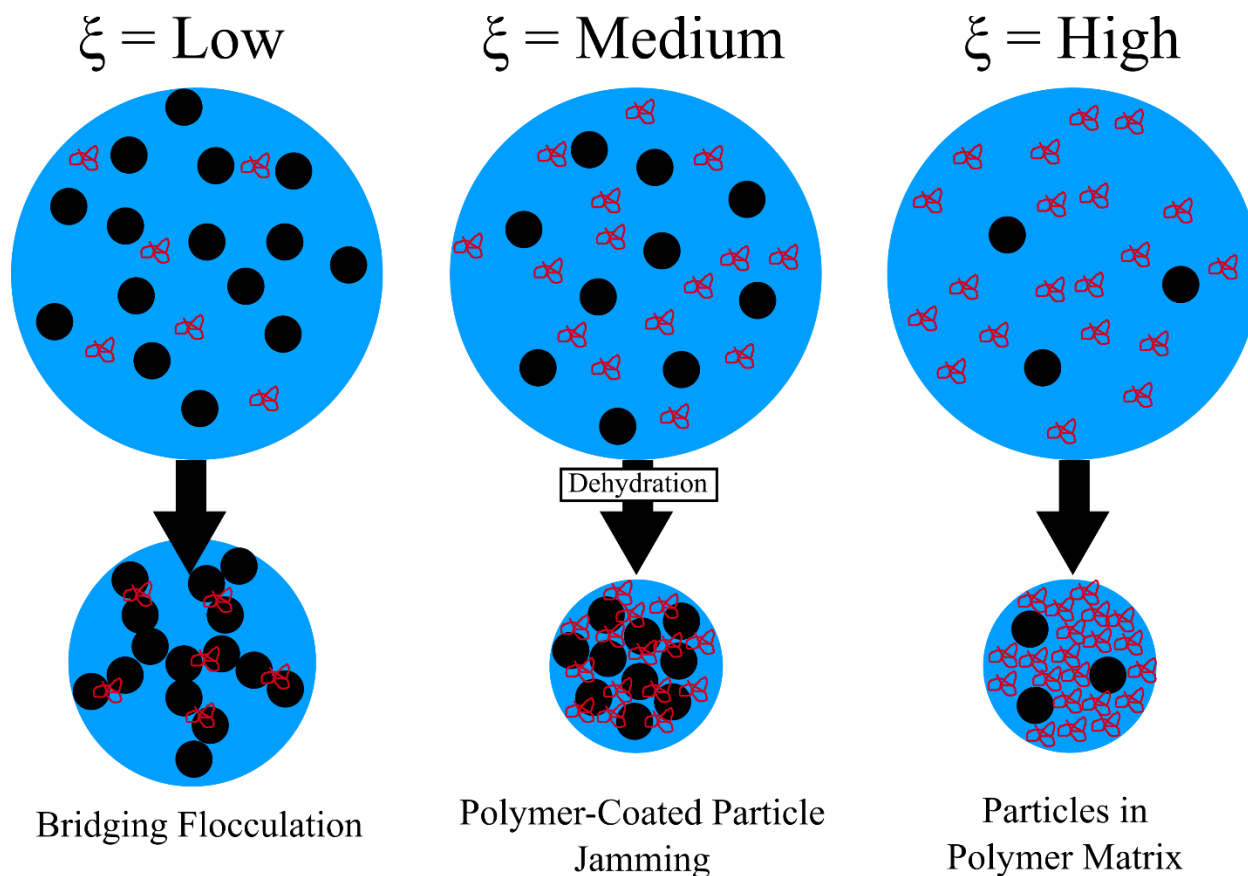


Figure 5.6: Cartoon describing the proposed system behavior at different polymer-particle mass ratios. Large droplets in the first row are representative droplets at dilute concentrations and the small droplets in the second row are of the same droplets after dehydration. Proposed mechanism is shown below each droplet. Note the increase in size of the dehydrated bridging flocculation droplet with respect to the higher mass ratio mechanisms.

Once enough polymer is added to fully coat the particles, the particles will behave as a sterically stabilized particulate system. Bridging flocculation will not play a role, and classical glassing/jamming behavior will be recovered, as shown in Figure 5.6. The final concentration of a system right at the saturation limit should be approximately the same as a system with no polymer. This is consistent with the results from Figure 5.5a. As ξ is increased from 0.013 to 0.23, final particle volume fraction increases from $\phi = 0.27$ to the particle only equivalent of $\phi = 0.52$, suggesting a decrease in the effect from polymer induced bridging flocculation.

At high polymer/particle mass ratios, there is far more free polymer than particles. The particles initially become fully saturated with polymer chains, but are more dilute in concentration than the mid-range mass ratio. When enough water leaves the droplet, the water/polymer mixture becomes a more viscous, polymeric matrix and the particles become trapped, leading to a decrease in final particle volume fraction. For a mass ratio $\xi = 8.3$, the interparticle spacing equals 28.5 nm at the final particle volume fraction, significantly larger than the 9 nm end-to-end polymer distance. In addition, for all high mass ratios experiments, the final particle volume fractions are consistent with systems where all water has left the droplet.

In the limit of significantly low polymer concentration (<1 chain/particle, $\xi < 0.001$), there will not be enough bridging flocculation to cause the formation of a flocculated network. Therefore, as polymer concentration heads towards zero, the final particle volume fraction is expected to also recover to the particle only value. Polymer concentrations this low were not tested in this work.

In Figure 5.5b, the three systems all follow the same overall trend, but reach a maximum final volume fraction at different mass ratios. For a given mass ratio, if the particles are able to remain separated at a larger distance, the polymer will have a more difficult time bridging two particles together and the droplet will be able to dehydrate to a larger degree. Therefore, if bridging flocculation is assumed to be the aggregation mechanism at low ξ , then having a maximum at a lower mass ratio is consistent with a smaller bridging aggregation force while having a maximum at a higher mass ratio is consistent with a larger bridging aggregation force.

Ludox TM-40 and Ludox TMA are 22 nm in diameter silica particles. Ludox TM-40 stock suspension is a 40 wt% suspension with 0.1 wt% (7mM) Na_2SO_4 with pH = 8.7 while Ludox TMA stock suspension is a 34 wt% suspension that is reportedly salt free with pH = 6.1.

The higher salt concentration in Ludox TM-40 will screen the particle charge more than the Ludox TMA system and cause the particles to move to closer interparticle distances due to a lower repulsive electrostatic interaction. With smaller interparticle distances, bridging aggregation will have larger effect. Therefore with the same 7500 g/mol PEO polymer source, it is expected that Ludox TM-40 will flocculate due to bridging interaction at a lower concentration than Ludox TMA, suggesting that the Ludox TMA system will reach a point where bridging flocculation no longer plays a role (maximum final volume fraction) at a lower polymer/particle mass ratio, consistent with results seen in Figure 5.5b.

A similar argument can be used to explain the difference between the 7500 g/mol PEO and the 100k g/mol PEO Ludox TM-40 systems. The difference between these two systems comes from the polymer source as opposed to the particle source. 100k g/mol PEO will have nearly identical particle-polymer adsorption interactions as the 7500 g/mol polymer, but can extend much farther into the solvent due to the greater than 10 fold increase in molecular weight. This increase in molecular weight translates into a greater reach for a single polymer chain to bridge two particles simultaneously, resulting in a maximum particle volume fraction at higher polymer/particle mass ratio as seen in Figure 5.5b.

Figure 5.7 shows the results from Figure 5.5b rescaled to demonstrate the regions discussed in Figure 5.6. The y-axis is the final particle volume fraction scaled by the final particle volume fraction of the polymer free case (particles only), an independent measurement. For the Ludox TM-40 and 100k g/mol PEO, the final volume fraction is normalized by the maximum final volume fraction for that system ($\phi = 0.35$). The x-axis is the polymer/particle mass ratio shifted by a value of the ξ_{\max} value for a particular system minus the ξ_{\max} of the Ludox TMA and 7500 g/mol system. This shifts the data to the left or right such that the maximum ξ of

each system is at ξ_{\max} of the Ludox TMA system. The shift to the left for each system corresponds to $\xi = 0$ for Ludox TMA and 7500 g/mol PEO, $\xi = 0.15$ for Ludox TM-40 and 7500 g/mol PEO, and $\xi = 0.35$ for Ludox TM-40 and 100k g/mol PEO.

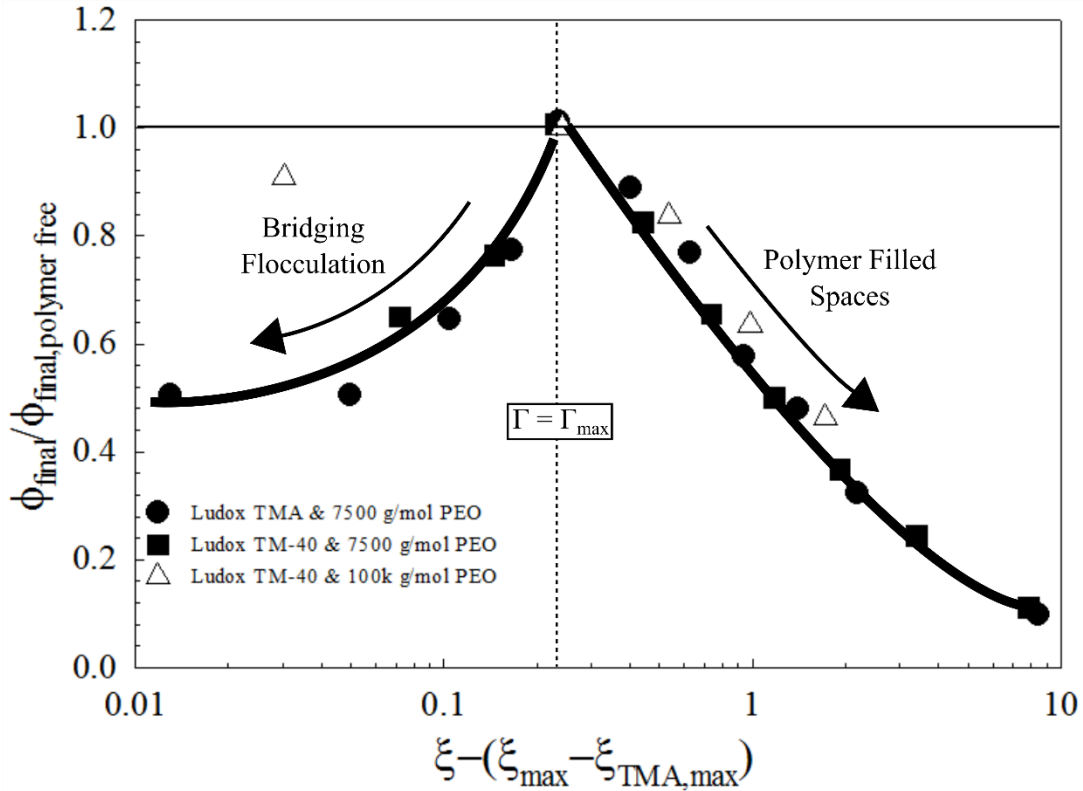


Figure 5.7: Results from droplet dehydration experiments rescaled to overlay. Final volume fraction for 7500 g/mol PEO systems is normalized by final volume fraction of the polymer free case. Final volume fraction of Ludox TM-40 and 100k g/mol PEO is normalized maximum volume fraction of that system. Mass ratio is shifted in the horizontal direction by the difference between the maximum mass ratio and the maximum mass ratio of the Ludox TMA and 7500 g/mol PEO system. To the left of the dotted line is the bridging flocculation regime and to the right is the polymer filled spaces regime. System components are described in the legend.

With this scaling, the three plots collapse where the peak occurs at ξ equivalent to where $\Gamma = \Gamma_{\max}$ and the maximum volume fraction is equivalent to the polymer free final volume fraction. For ξ values to the left of the peak, bridging flocculation is the dominant aggregation mechanism and increases in strength as ξ decreases. For ξ values to the right of the peak, there is significantly more polymer than particles in the system, leading to particles suspended in a

polymer-rich matrix. The data point in the bridging regime for Ludox TM-40 and 100k g/mol PEO does not collapse on the same trend as the other systems. This is because the final particle volume fraction was scaled with the maximum final particle volume fraction of that polymer-particle system as opposed to the particle only case. The addition of 100k g/mol PEO to the silica particles lowered the maximum packing, likely because of bridging interactions at larger interparticle distances due to increased polymer chain length.

To determine the mechanism behind final particle volume fraction, a discussion of the potential mechanical reasons is necessary. Particulate colloidal systems are known to obtain a compressive yield stress at high particle concentrations. The viscosity of a particulate system increases exponentially at a maximum packing concentration⁶⁷ as does the compressive yield stress.⁶⁸ The droplet itself will have a Laplace pressure difference between the inside and outside of the droplet due to the interfacial tension between fluid phases, described by Equation 5.3

$$\Delta P = \gamma \left(\frac{1}{R_1} + \frac{1}{R_2} \right), \quad (5.3)$$

where ΔP is the pressure drop across the droplet, γ is the interfacial tension, and R_1 and R_2 are the radii of curvature of a droplet. We hypothesize that the point at which a droplet stops concentrating is where there is a force balance between the Laplace pressure of the droplet balances with the compressive yield stress of the particle suspension. When the microstructure obtains enough solidity to withstand the Laplace pressure and not buckle, then a droplet can retain its shape and arrest its dehydration. If an additive such as a polymer changes the compressive yield stress functionality, then it would change where the droplet stops dehydrating.

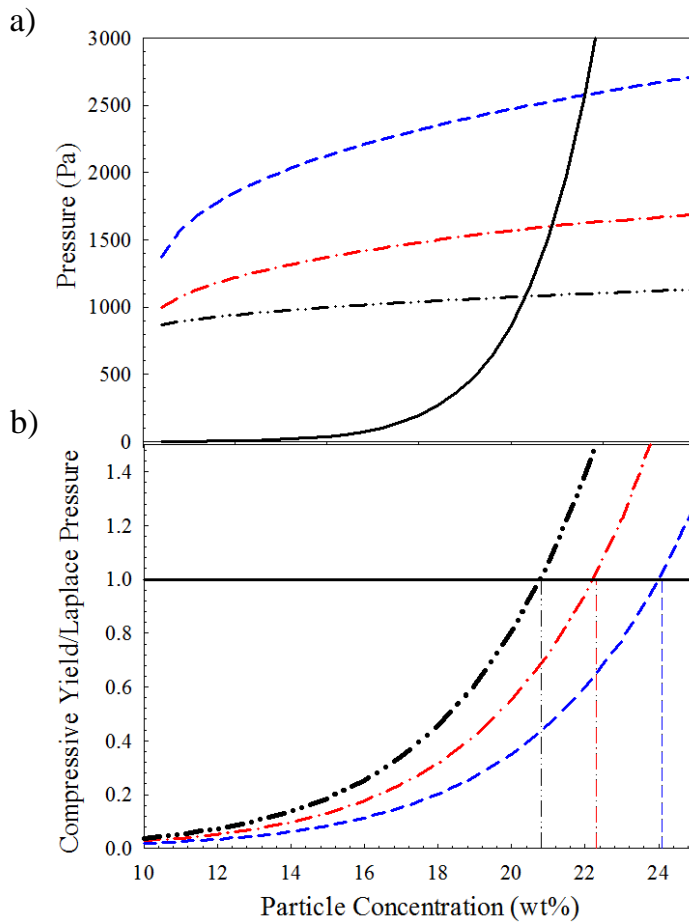


Figure 5.8: Predicted calculations of Laplace pressure and compressive yield stress based on initial droplet concentration. (a) The solid black line shows the compressive yield stress of a zirconia oxide particulate system as concentration increases.⁶⁸ The dotted lines denote Laplace pressure of droplets initially 575 μm in diameter and 100 μm in height with initial concentrations of 0.05 wt%, 0.5 wt%, and 5 wt% denoted as the dashed blue, dot-dash red, and dot-dot-dash black lines respectively. (b) Compressive yield stress normalized by the Laplace pressure for each initial concentration as a function of particle concentration. The thin dotted lines display the particle concentrations at which the stresses are equal.

A simple way to test this hypothesis is to create droplets with the same suspended material, but at different sizes which will obtain different Laplace pressures at the same concentration. The method to create these droplets is to produce droplets in device at the same initial droplet size, but different initial concentrations. Droplets that begin dilute will need to concentrate significantly before compressive yield stress increases. Conversely, droplets that start concentrated will only need to slightly dehydrate before compressive yield stress increases.

Therefore the dilute droplet will be small (large Laplace pressure) when compressive yield stress increases while the concentrated droplet will be large (small Laplace pressure) when the compressive yield stress increases.

Figure 5.8a shows a comparison between the Laplace pressure of a droplet for a given set of conditions compared with the compressive yield stress of a zirconia oxide system.⁶⁸ The three dotted lines correspond to the Laplace pressure of a droplet as a function of particle concentration for a given initial droplet concentration. The blue dashed line corresponds to an initial concentration of 0.05 wt%, the red dot-dash line corresponds to an initial concentration of 0.5 wt% and the black dot-dot-dash line corresponds to an initial concentration of 5wt%. Droplets are assumed to have an initial diameter of 575 μm and a height of 100 μm , identical to previous experiments. The solid black line plots the compressive yield stress of zirconia oxide from Miller *et al.*⁶⁸

Figure 5.8b shows the ratio of compressive yield stress to Laplace pressure as a function of particle concentration for the three initial concentration conditions. When the forces balance ($P_y/L_p = 1$), the droplet will stop concentrating. The concentration at which the droplet will stop dehydrating is different based on the initial droplet concentration and can be used as a way to verify this theory. However, practical issues make it a challenge to perform these experiments with our current technique. Figure 5.3 demonstrates that aspect ratios below one cause incorrect calculation of particle concentration. A system loaded at 0.05 wt% in a 575 μm diameter droplet is expected to reach $P_y/L_p = 1$ at a spherical droplet diameter of 45 nm with an aspect ratio of 0.47, well below the aspect ratio cutoff of one. Droplets produced at high initial concentrations will remain pancakes through the experiment, however, they obtain a relatively flat Laplace pressure as a function of particle concentration due to the channel height ($h = 95 \mu\text{m}$) being the

dominant principal radii of curvature as seen in Figure 5.8a. This makes it difficult to create separation in particle concentration where $P_y/L_p = 1$ for different systems, unless they adopt a spherical droplet shape.

An alternative method is to find a colloidal system with a less exponential increase in compressive yield stress with particle volume fraction. Because the yield stress of zirconia oxide increases so rapidly, small errors in droplet size measurements lead to large errors in compressive yield stress. If the yield stress of a particulate system increases more gradually, differences in compressive yield stress may be possible while maintaining droplet aspect ratios larger than 1. Therefore, in order to accurately run these experiments, wetting conditions must be improved to create reliable concentration measurements below an aspect ratio of one, or a particulate system with a more gradual compressive yield stress dependence must be used.

5.5 Conclusions

In this work, colloid-polymer suspensions containing silica particles and PEO polymer are characterized via a microfluidic droplet-based technique. Nanoliter sized sucrose droplets and Ludox TM-40 droplets are used to determine that droplets must retain a diameter/height aspect ratio greater than 1 to return accurately measured droplet concentrations. Samples containing combinations of two different Ludox silica particles and two different molecular weight PEO chains are dried on-chip to observe final particle volume fraction. It is found that final particle volume fraction drastically decreases at dilute polymer concentrations (low polymer/particle mass ratios).

A colloidal bridging flocculation theory is proposed to explain the variation in final particle volume fraction as a function of polymer/particle mass ratio (ξ). The data suggests that

at low polymer/particle mass ratios, the system undergoes bridging flocculation caused by the polymer-particle interactions. At the particle saturation concentration, bridging flocculation has no effect and polymer-free final particle volume fractions are recovered. At higher polymer concentrations, particles become trapped in a polymer-rich matrix, leading to a decreasing trend in final particle volume fraction. It is hypothesized that a force balance between Laplace pressure and compressive yield stress is responsible for the final composition of a droplet. Separate experiments to verify this claim are proposed.

5.6 References

- (1) Hunter, G.; Weeks, E. The Physics of the Colloidal Glass Transition. *Rep. Prog. Phys.* **2012**, *75* (6), 66501.
- (2) Pusey, P. N.; van Megen, W.; Megen, W. van. Phase Behavior of Concentrated Suspensions of Nearly Hard Colloidal Spheres. *Nature* **1986**, *320* (6060), 340–342.
- (3) Pusey, P. N.; Zaccarelli, E.; Valeriani, C.; Sanz, E.; Poon, W. C. K.; Cates, M. E. Hard Spheres: Crystallization and Glass Formation. *Philos. Trans. A. Math. Phys. Eng. Sci.* **2009**, *367* (1909), 4993–5011.
- (4) Mourchid, A.; Delville, A.; Lambard, J.; Lécolier, E.; Levitz, P. Phase Diagram of Colloidal Dispersions of Anisotropic Charged Particles: Equilibrium Properties, Structure, and Rheology of Laponite Suspensions. *Langmuir* **1995**, *11* (6), 1942–1950.
- (5) Dijkstra, M.; Hansen, J. P.; Madden, P. A. Statistical Model for the Structure and Gelation of Smectite Clay Suspensions. *Phys. Rev. E - Stat. Physics, Plasmas, Fluids, Relat. Interdiscip. Top.* **1997**, *55* (3), 3044–3053.
- (6) Levitz, P.; Lecolier, E.; Mourchid, A.; Delville, A.; Lyonnard, S. Liquid-Solid Transition of Laponite Suspensions at Very Low Ionic Strength: Long-Range Electrostatic Stabilisation of Anisotropic Colloids. *Europhys. Lett.* **2000**, *49* (5), 672–677.
- (7) McRae, R.; Haymet, A. D. J. Freezing of Polydisperse Hard Spheres. *J. Chem. Phys.* **1988**, *88* (2), 1114.
- (8) Auer, S.; Frenkel, D. Suppression of Crystal Nucleation in Polydisperse Colloids due to Increase of the Surface Free Energy. *Nature* **2001**, *413* (6857), 711–713.
- (9) Grant, M. C.; Russel, W. B. Volume-Fraction Dependence of Elastic-Moduli and Transition-Temperatures for Colloidal Silica-Gels. *Phys. Rev. E* **1993**, *47* (4), 2606–2614.
- (10) Trappe, V.; Prasad, V.; Cipelletti, L.; Segre, P. N.; Weitz, D. a. Jamming Phase Diagram for Attractive Particles. *Nature* **2001**, *411* (6839), 772–775.
- (11) Lekkerkerker, H. N. W.; Poon, W. C.-K.; Pusey, P. N.; Stroobants, A.; Warren, P. B. Phase Behaviour of Colloid + Polymer Mixtures. *Europhys. Lett.* **1992**, *20* (6), 559–564.
- (12) Dijkstra, M.; Brader, J. M.; Evans, R. Phase Behaviour and Structure of Model Colloid-Polymer Mixtures Phase Behaviour and Structure of Model Colloid – Polymer Mixtures. *J.Phys.:Condens.Matter* **1999**, *11*, 10079–10106.
- (13) Zaccarelli, E.; Valeriani, C.; Sanz, E.; Poon, W. C. K.; Cates, M. E.; Pusey, P. N. Crystallization of Hard-Sphere Glasses. *Phys. Rev. Lett.* **2009**, *103* (13), 1–4.
- (14) Nešić, S.; Vodnik, J. Kinetics of Droplet Evaporation. *Chem. Eng. Sci.* **1991**, *46* (2), 527–537.
- (15) Weeks, E. R.; Weitz, D. a. Properties of Cage Rearrangements Observed near the Colloidal Glass Transition. *Phys. Rev. Lett.* **2002**, *89* (9), 95704.

- (16) Kadja, M.; Bergeles, G. Modelling of Slurry Droplet Drying: Erratum. *Appl. Therm. Eng.* **2003**, *23* (7), 829–844.
- (17) Cheong, H. W.; Jeffreys, G. V.; Mumford, C. J. A Receding Interface Model for the Drying of Slurry Droplets. *AIChE J.* **1986**, *32* (8), 1334–1346.
- (18) Cheng, Z.; Russel, W. B.; Chaikin, P. M. Controlled Growth of Hard-Sphere Colloidal Crystals. *Nature* **1999**, *401*, 893–895.
- (19) Hoover, W. G. Melting Transition and Communal Entropy for Hard Spheres. *J. Chem. Phys.* **1968**, *49* (8), 3609.
- (20) Angell, C. A. Formation of Glasses from Liquids and Biopolymers. *Science* **1995**, *267* (5206), 1924–1935.
- (21) Dawson, K. The Glass Paradigm for Colloidal Glasses, Gels, and Other Arrested States Driven by Attractive Interactions. *Curr. Opin. Colloid Interface Sci.* **2002**, *7* (3–4), 218.
- (22) Weitz, D. A.; Oliveria, M. Fractal Structures Formed by Kinetic Aggregation of Aqueous Gold Colloids. *Phys. Rev. Lett.* **1984**, *52* (16), 1433–1436.
- (23) Lin, M. Y.; Lindsay, H. M.; Weitz, D. A.; Klein, R.; Ball, R. C.; Meakin, P. Universal Diffusion-Limited Colloid Aggregation. *J. Phys. Chem. B* **1990**, *2*, 3093–3113.
- (24) Carpineti, M.; Giglio, M. Spinodal-Type Dynamics in Fractal Aggregation of Colloidal Clusters. *Phys. Rev. Lett.* **1992**, *68* (22), 3327–3330.
- (25) Poling-Skutvik, R.; Lee, J.; Narayanan, S.; Krishnamoorti, R.; Conrad, J. C. Tunable Assembly of Gold Nanorods in Polymer Solutions to Generate Controlled Nanostructured Materials. *ACS Appl. Nano Mater.* **2018**, acsanm.7b00277.
- (26) Shaw, D. J. *Colloid & Surface Chemistry*; 1992.
- (27) Routh, A. F.; Russel, W. B. Horizontal Drying Fronts during Solvent Evaporation from Latex Films. *AIChE J.* **1998**, *44* (9), 2088–2098.
- (28) Persello, J.; Boisvert, J.; Guyard, A.; Cabane, B. Structure of Nanometric Silica Clusters in Polymeric Composite Materials. *J. Phys. Chem. B* **2004**, *108* (10), 9678–9684.
- (29) Tirumkudulu, M. S.; Russel, W. B. Cracking in Drying Latex Films. *Langmuir* **2005**, *21* (4), 4938–4948.
- (30) Singh, K. B.; Tirumkudulu, M. S. Cracking in Drying Colloidal Films. *Phys. Rev. Lett.* **2007**, *98* (21), 218302.
- (31) Routh, A. F. Drying of Thin Colloidal Films. *Reports Prog. Phys.* **2013**, *76* (4), 46603.
- (32) Deegan, R. D.; Bakajin, O.; Dupont, T. F.; Huber, G.; Nagel, S. R.; Witten, T. a. Capillary Flow as the Cause of Ring Stains from Dried Liquid Drops. *Lett. to Nat.* **1997**, *389*, 827–829.
- (33) Parisse, F.; Allain, C. Drying of Colloidal Suspension Droplets: Experimental Study and Profile Renormalization. *Langmuir* **1997**, *13* (9), 3598–3602.

- (34) Bodiguel, H.; Leng, J. Imaging the Drying of a Colloidal Suspension: Velocity Field. *Soft Matter* **2010**, *6*, 5451–5460.
- (35) Kim, J. Y.; Cho, K.; Ryu, S.; Kim, S. Y.; Weon, B. M. Crack Formation and Prevention in Colloidal Drops. *Sci. Rep.* **2015**, *5*, 13166.
- (36) Zheng, B.; Roach, L. S.; Ismagilov, R. F. Screening of Protein Crystallization Conditions on a Microfluidic Chip Using Nanoliter-Size Droplets. *J. Am. Chem. Soc.* **2003**, *125* (37), 11170–11171.
- (37) Shim, J.; Cristobal, G.; Link, D. R.; Thorsen, T.; Fraden, S. Using Microfluidics to Decouple Nucleation and Growth of Protein Crystals. *Cryst. Growth Des.* **2007**, *7* (11), 2192.
- (38) Shim, J.; Patil, S. N.; Hodgkinson, J. T.; Bowden, S. D.; Spring, D. R.; Welch, M.; Huck, W. T. S.; Hollfelder, F.; Abell, C. Controlling the Contents of Microdroplets by Exploiting the Permeability of PDMS. *Lab Chip* **2011**, *11*, 1132–1137.
- (39) Solvas, X. C.; Turek, V.; Prodromakis, T.; Ede, J. B. Microfluidic Evaporator for ON-Chip Sample Concentration. *Lab Chip* **2012**, *12*, 4049–4054.
- (40) Shirk, K.; Steiner, C.; Kim, J. W.; Marquez, M.; Martinez, C. J. Assembly of Colloidal Silica Crystals Inside Double Emulsion Drops. *Langmuir* **2013**, *29* (38), 11849–11857.
- (41) Shim, J. U.; Cristobal, G.; Link, D. R.; Thorsen, T.; Jia, Y. W.; Piattelli, K.; Fraden, S. Control and Measurement of the Phase Behavior of Aqueous Solutions Using Microfluidics. *J. Am. Chem. Soc.* **2007**, *129*, 8825–8835.
- (42) Ziane, N.; Guirardel, M.; Leng, J.; Salmon, J. Drying with No Concentration Gradient in Large Microfluidic Droplets. *Soft Matter* **2015**, *11*, 3637–3642.
- (43) Nandy, L.; Dutcher, C. S. Phase Behavior of Ammonium Sulfate with Organic Acid Solutions in Aqueous Aerosol Mimics Using Microfluidic Traps. *J. Phys. Chem. B* **2018**, *Accepted*.
- (44) Bleier, B. J.; Anna, S. L.; Walker, L. M. Microfluidic Droplet-Based Tool To Determine Phase Behavior of a Fluid System with High Composition Resolution. *J. Phys. Chem. B* **2018**, *acs.jpcc.8b01013*.
- (45) Carroll, N. J.; Rathod, S. B.; Derbins, E.; Mendez, S.; Weitz, D. A.; Petsev, D. N. Droplet-Based Microfluidics for Emulsion and Solvent Evaporation Synthesis of Monodisperse Mesoporous Silica Microspheres. **2008**, No. 18, 658–661.
- (46) Dendukuri, D.; Doyle, P. S. The Synthesis and Assembly of Polymeric Microparticles Using Microfluidics. *Adv. Mater.* **2009**, *21* (41), 4071–4086.
- (47) Chen, C. H.; Shah, R. K.; Abate, A. R.; Weitz, D. A. Janus Particles Templated from Double Emulsion Droplets Generated Using Microfluidics. *Langmuir* **2009**, *25* (8), 4320–4323.
- (48) Hung, L.; Teh, S.; Lee, A. P. PLGA Micro/Nanosphere Synthesis by Droplet Microfluidic Solvent Evaporation and Extraction Approaches. *Lab Chip* **2010**, 1820–1825.

- (49) Shum, H. C.; Abate, A. R.; Lee, D.; Studart, A. R.; Wang, B.; Chen, C.-H.; Thiele, J.; Shah, R. K.; Krummel, A.; Weitz, D. A. Droplet Microfluidics for Fabrication of Non-Spherical Particles. *Macromol. Rapid Commun.* **2010**, *31*, 108–118.
- (50) Sucrose Conversion Table - Technical Inspection Procedures. *United States Dep. Agric.* **1981**.
- (51) Vuong, S. A Microfluidic Platform for the Control and Analysis of Phase Transitions in Concentrating Droplets. *PhD Thesis, Carnegie Mellon* **2014**.
- (52) Vuong, S. M. A Microfluidic Platform for the Control and Analysis of Phase Transitions in Concentrating Droplets. *PhD Thesis, Carnegie Mellon* **2014**.
- (53) Vuong, S. M.; Anna, S. L. Tuning Bubbly Structures in Microchannels. *Biomicrofluidics* **2012**, *6* (2).
- (54) Kirby, S. M.; Anna, S.; Walker, L. Effect of Surfactant Tail Length and Ionic Strength on the Interfacial Properties of Nanoparticle-Surfactant Complexes. *Soft Matter* **2017**, *14*, 112–123.
- (55) Bjelopavlicl, M.; Zaman, A. A.; Moudgi, B. M. Adsorption of Poly (Ethylene Oxide) Onto Silica at Different Solids Loadings. *KONA Powder Part. J.* **2000**, *18* (18), 60–65.
- (56) *Polyethylene Oxide Product Specification Document*; St. Louis, MO.
- (57) *Ludox Technical Information Document*; Columbia, MD, 2008.
- (58) Trens, P.; Denoyel, R. Conformation of Poly(ethylene Glycol) Polymers at the Silica/Water Interface: A Microcalorimetric Study. *Langmuir* **1993**, *9* (2), 519–522.
- (59) Mathur, S.; Moudgil, B. M. Adsorption Mechanism(s) of Poly (Ethylene Oxide) on Oxide Surfaces. *J. Colloid Interface Sci.* **1997**, *98* (196), 92–98.
- (60) Esumi, K.; Iitaka, M.; Koide, Y. Simultaneous Adsorption of Poly (Ethylene Oxide) and Cationic Surfactant at the Silica/Water Interface. *J. Colloid Interface Sci.* **1998**, *182*, 178–182.
- (61) Voronin, E. F.; Gun'ko, V. M.; Guzenko, N. V.; Pakhlov, E. M.; Nosach, L. V.; Leboda, R.; Skubiszewska-Zięba, J.; Malysheva, M. L.; Borysenko, M. V.; Chuiko, A. A. Interaction of Poly(ethylene Oxide) with Fumed Silica. *J. Colloid Interface Sci.* **2004**, *279* (2), 326–340.
- (62) Rubio, J.; Kitchener, J. A. The Mechanism of Adsorption of Poly(Ethylene Oxide) Flocculant on Silica. *J. Colloid Interface Sci.* **1976**, *57* (1).
- (63) Killmann, E.; Wild, T.; Gutling, N.; Maier, H. Flocculation of Pyrogenic and Precipitated Silica by Polyethylene Oxides. *Colloids and Surfaces* **1986**, *18*, 241–259.
- (64) Zaman, A. A. Effects of Polymer Bridging and Electrostatics on the Rheological Behavior of Aqueous Colloidal Dispersions. *Part. Part. Syst. Charact.* **2003**, *20*, 342–350.
- (65) Swenson, J.; Smalley, M. V.; Hatharasinghe, H. L. M. Mechanism and Strength of Polymer Bridging Flocculation. *Phys. Rev. Lett.* **1998**, *81* (26), 5840–5843.

- (66) Israelachvili, J. *Intermolecular & Surface Forces*, 2nd ed.; Academic Press: London, 1991.
- (67) Pal, R. Viscosity Models for Concentrated Suspensions of Solid Core-Porous Shell Particles. *Can. J. Chem. Eng.* **2015**, *93* (3), 590–598.
- (68) Miller, K. T.; Melant, R. M.; Zukoski, C. F. Comparison of the Compressive Yield Response of Aggregated Suspensions: Pressure Filtration, Centrifugation, and Osmotic Consolidation. *J. Am. Ceram. Soc.* **1996**, *79* (10), 2545–2556.

Chapter 6. Controlling Colloid-Polymer Phase Separation in

Dehydrating Microfluidic Droplets

6.1 Introduction

Suspensions containing colloidal particles and free nonadsorbing polymer are used in a number of industrial products including coatings and paints, cosmetics, adhesives, and medical devices. The phase behavior and kinetics of high volume fraction suspensions are important in establishing design criteria for these consumer products. In many of these applications, suspensions approach high particle volume fraction due to evaporation or process design, which can result in intended or unintended phase transitions¹⁻⁴. Therefore it is important for developers to understand and fine tune formulations to utilize the specific properties of the suspensions. To do so, it is necessary to first understand the fundamentals of stability and phase behavior in polymer-particle systems.

Colloidal particles are attracted to each other due to van der Waals attractive forces and will fall into a deep potential well if the particle surfaces are left bare⁵. To counter attractive forces, repulsive forces can be generated in a colloidal system in the form of steric⁵⁻⁷ or electrostatic^{5,8} stabilizing forces. If the repulsive forces are large enough, repulsion will dominate and the system will be stabilized against aggregation for extended periods.

When a non-adsorbing polymer is added to a particle system, the phase behavior becomes increasingly more complex. This arises from an additional attractive force, or “depletion attraction”, first proposed by Asakura and Oosawa^{9,10} and further advanced by Vrij¹¹. An unbalanced osmotic pressure due to the exclusion of polymer chains near two close colloidal particles leads to an effective flocculation at specific polymer and particle concentrations. The

onset of depletion flocculation occurs when the polymer radius of gyration (R_g) is larger than the interparticle distance of two neighboring particles. This phenomena has been observed in non-aqueous systems containing poly(methyl methacrylate) (PMMA) particles with polystyrene (PS) polymer in cis-decalin,^{2,12} silica particles and PS polymer in toluene¹³, silica particles with poly(isoprene) in cyclohexane¹⁴, and silica particles with PS in decalin,¹⁵ as well as aqueous systems containing PMMA particles and PEO polymer,^{16,17} PS particles and poly(acrylic acid) (PAA) polymer,¹⁸ PS particles and dextran¹⁹, and PS particles and hydroxyl(ethyl cellulose).²⁰⁻³²

Different approaches have been taken to model the polymer-particle interactions including statistical mechanics,³ thermodynamic perturbation theory,^{22,33} and Monte Carlo Simulations³⁴. The statistical mechanical approach of Lekkerkerker *et al.*³ has provided a theoretical foundation and has been experimentally tested and verified as a reasonable approximation for phase behavior of these systems.^{2,12,35,36}

However, many assumptions must be made to simplify the polymer-particle interactions in order to approximate phase behavior. Particles are assumed to be hard spheres with no attractive or repulsive interactions. Polymer chains are assumed to not adsorb to particle surfaces and to not interact with one another. Charge in the system is assumed to be negligible. In order to account for these assumptions, the experimental system of Ilett *et al.*² required a refractive index matched particle and solvent system to reduce the Hamaker constant and remove attractive forces, sterically stabilizing the particles with preadsorbed poly-12-hydroxystearic acid to prevent aggregation and avoid adsorption of PS chains, and cis-decalin as an organic solvent to remove charge effects. This system provided a comparable experimental study and helped solidify the underlying aggregation mechanism, but is restricted and not characteristic of the typical industrial formulation.

Most industrial products are mixtures of many components (up to 20-30) with limited control on interparticle behavior. Parameter space is large and further investigation is needed to obtain a complete theoretical and experimental understanding of these systems. Macroscopic bulk phase separation tests have been the general experimental practice thus far,² but they can be time consuming and cumbersome to accurately produce samples, especially if the phase behavior is not known *a priori*.

In this work, we utilize a novel droplet based experimental technique developed in Chapter 4 that allows for continuous observation and quantitative analysis of colloidal structure as the system concentrates. We use the device to map the phase diagram of a specific polymer-particle-solvent system consisting of electrostatically stabilized polystyrene particles with free hydroxyethyl cellulose (HEC) polymer. Interparticle potential is controlled through particle size, polymer molecular weight, and polymer type to investigate respective effects on phase behavior. Optical darkening (interpreted as phase separation) is clearly observed on the microscale and characterized based on the polymer-particle mass ratio.

6.2 Background

Interparticle pair potential is described best with Derjaguin-Landau-Verwey-Overbeek (DLVO) theory. With DLVO, the individual attractive and repulsive potentials add together to create a complete pair potential description. Common attractive forces include van der Waals forces and polymer-induced depletion attraction while the two main repulsive forces are steric stabilization and electrostatic repulsion. Each mechanism has been characterized and described by an analytical solution depending on the system conditions. A common expression used for steric stabilization is shown in Equation 6.1^{7,37}

$$V_s = \frac{4\pi akT}{v_1} (\phi_2^a) \left(\frac{1}{2} - \chi \right) \left(\delta - \frac{h}{2} \right)^2, \quad (6.1)$$

where a is the particle radius, k is the Boltzmann constant, T is temperature, v_1 is the molar volume of the solvent, ϕ_2^a is the average volume fraction of surfactant in the adsorbed layer, χ is the Flory-Huggins parameter, δ is the adsorbed layer thickness, and h is the particle surface separation distance. Electrostatic repulsion occurs when particles obtain surface charge groups that repel other particles with charge of the same sign. Electrostatic stabilization is described by Equation 6.2³⁸

$$V_e = 2\pi\epsilon_0\epsilon_r\Psi_0^2 \ln \left[1 + \exp(-\tau(S-2)) \right], \quad (6.2)$$

where ϵ_0 is the permittivity of free space and ϵ_r is the permittivity of the medium, Ψ_0 is the surface potential, τ is the ratio of the particle radius to the double-layer thickness (l/κ), and S is the ratio of the separation between the centers of two particles (R) to the particle radius (a). Van der Waals attractive forces between colloidal particles occur due to the attractive forces between polar molecules and induced dipoles in nonpolar molecules. The van der Waals forces exerted on two approaching colloidal particles is described in Equation 6.3³⁸

$$V_a = -\frac{A_{121}}{6} \left[\frac{2}{S^2-4} + \frac{2}{S} + \ln \frac{S^2-4}{S^2} \right], \quad (6.3)$$

where A is the composite Hamaker constant. Another attractive pair potential mechanism is polymer-induced depletion attraction, where a coiled polymer chain unable to fit between two neighboring particles induces an osmotic force between particles resulting in aggregation. This occurs when the polymer radius of gyration (R_g) is larger than the interparticle distance and is described by Equation 6.4³⁹

$$V_{dep} = -\frac{2}{3} \pi n_2 kT \left(R_g - \frac{S_0}{2} \right)^2 \left(3a + 2R_g + \frac{S_0}{2} \right), \quad (6.4)$$

where R_g is the radius of gyration of the polymer and S_0 is the distance of closet approach of the bare particle surfaces.

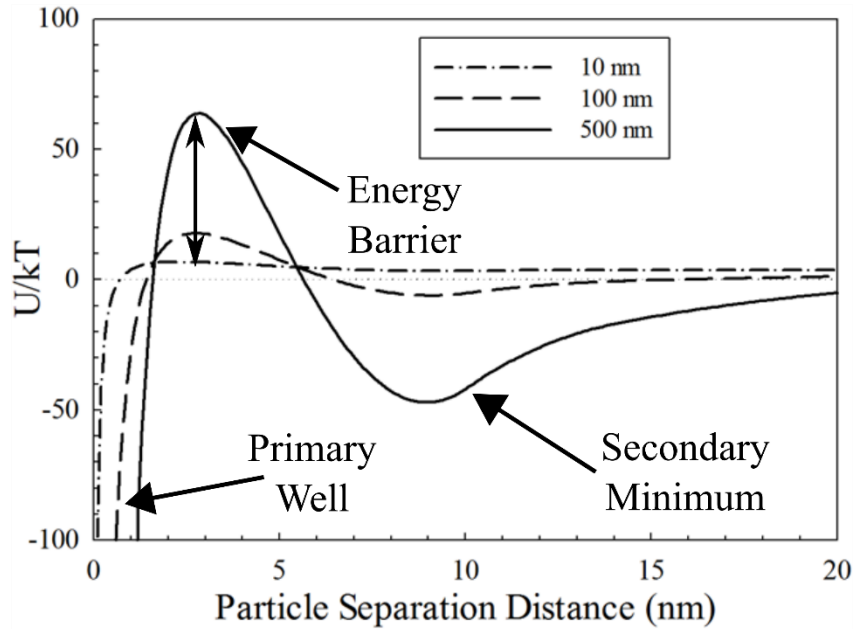


Figure 6.1: Combined van der Waals, steric, electrostatic, and depletion pair potential forces with varying particle size for illustrative purposes. Chosen parameters are $\Psi_0 = -10$ mV, $\epsilon_r = 80$, $R_g = 10$ nm, $\kappa^{-1} = 50$ nm, $A_{121} = 3 \times 10^{-20}$ J, $T = 298$ K, and $\chi = 0.35$, and $\Phi_2^a = 0.1$. Particle size is denoted in the legend.

Figure 6.1 shows the combined pair potential of all four contributing mechanisms as a function of particle separation distance for three unique particle sizes. The following parameters are chosen for demonstration: $\Psi_0 = -10$ mV, $\epsilon_r = 80$, $R_g = 10$ nm, $\kappa^{-1} = 50$ nm, $A_{121} = 3 \times 10^{-20}$ J, $T = 298$ K, and $\chi = 0.35$, and $\Phi_2^a = 0.1$ with particle size denoted in the legend with the dash-dot line corresponding to a particle radius $a = 10$ nm, the dashed line corresponding to a particle radius $a = 100$ nm, and the solid line corresponding to a particle radius $a = 500$ nm.. At large particle distances, the interparticle potential trends towards a value of zero. As the particles begin to approach, the combination of attraction and repulsion determines the interparticle

behavior. Under certain conditions, a secondary potential minimum can form, as shown in Figure 6.1. A potential well of a few kT in depth is strong enough to induce attraction between particles, but the aggregation is typically reversible. As the particles continue to move closer together (smaller particle separation distance), a strong energy barrier is present due to a combination of steric and electrostatic stabilization. However, if enough energy is supplied to the system, the energy barrier can be overcome and the particle system will fall into a deep primary well. Once particles become aggregated and stuck in the primary well, they are unlikely to redisperse without added energy such as agitation or sonication.

The magnitude of the secondary minimum, energy barrier, and primary potential well can be altered by varying system parameters including particle size, polymer size, concentration, temperature, pH, electrolyte concentration, solvent choice, particle material, and polymer molecular weight among other factors.³⁹ The interparticle potential can be adjusted to create or avoid a secondary minimum. This is accomplished through fine-tuning the attractive and repulsive potentials and shifting the peak above or below a potential value of 0 kT .

6.3 Materials and Methods

Polystyrene particles are purchased from Invitrogen (Carlsbad, CA) as 4 wt/vol% suspensions and are reportedly surfactant free. Hydroxy(ethyl cellulose) polymer, HEC, is purchased from Sigma-Aldrich (St. Louis, MO) at 4 different molecular weights: 90k g/mol, 260k g/mol, 380k g/mol, and 720k g/mol. An additional 90k g/mol HEC is purchased from the Aldrich Chemical Company (Milwaukee, WI). 100k g/mol poly(ethylene oxide), PEO, is purchased from Polysciences Inc. (Warminster, PA). All polymer sources are used as received.

Particles are sonicated for 20 minutes in a sonication bath, diluted, and filtered with a 200 nm polyethersulfone filter from VWR International (Radnor, PA). Filtered particle suspensions are sonicated for 15 minutes before each additional use. Mixtures are produced by combining a 2 wt/vol% particle suspension and a 2 wt/wt% polymer solution by volume. The density of the polymer solution ($\rho = 1.003$ g/mL for 2 wt% 90k g/mol HEC) is used to convert to a mass/volume polymer concentration. Volume change of mixing for dilute solutions is assumed to be negligible. Polymer/particle mass ratios of $\xi = 0.05, 0.11, 0.17, 0.25, 0.43, 0.54, 0.67, 1.00, 1.50, 2.34, 4.01,$ and 9.03 with initial concentrations ranging from $\theta = 0.019$ - 0.020 g/mL for 20 nm PS and 90k g/mol HEC are created and used in microfluidic studies. Deionized water (18.2 M Ω -cm) is used for all solutions.

Triton X-405 is purchased from Sigma-Aldrich and used as received. Triton X-405 solutions are premixed with 20nm PS particle suspensions and left to sit overnight to allow for adsorption of surfactant to particle surfaces. 90k g/mol HEC solutions are then added to the particle-triton complexes and sonicated for 20 minutes before use.

Gel permeation chromatography (GPC) experiments are performed with a Malvern Viscotek GPCmax instrument on all HEC samples to determine average molecular weight and polydispersity. Measurements are performed on 1 wt% samples in a 0.05 M Na₂SO₄ solution with 100 μ L injections. Molecular weight distributions are shown in Figure 6.2 with the reported molecular weights from the manufacturers shown in the legend. Molecular distributions are observed to increase monotonically as the reported molecular weight increases. The two 90k g/mol samples have similar distributions at low molecular weight, but deviate at higher molecular weight with 90k-B containing a higher concentration of higher molecular weight

molecules than the 90k-A sample. Pertinent parameters from the GPC measurements are shown in Table 6.1.

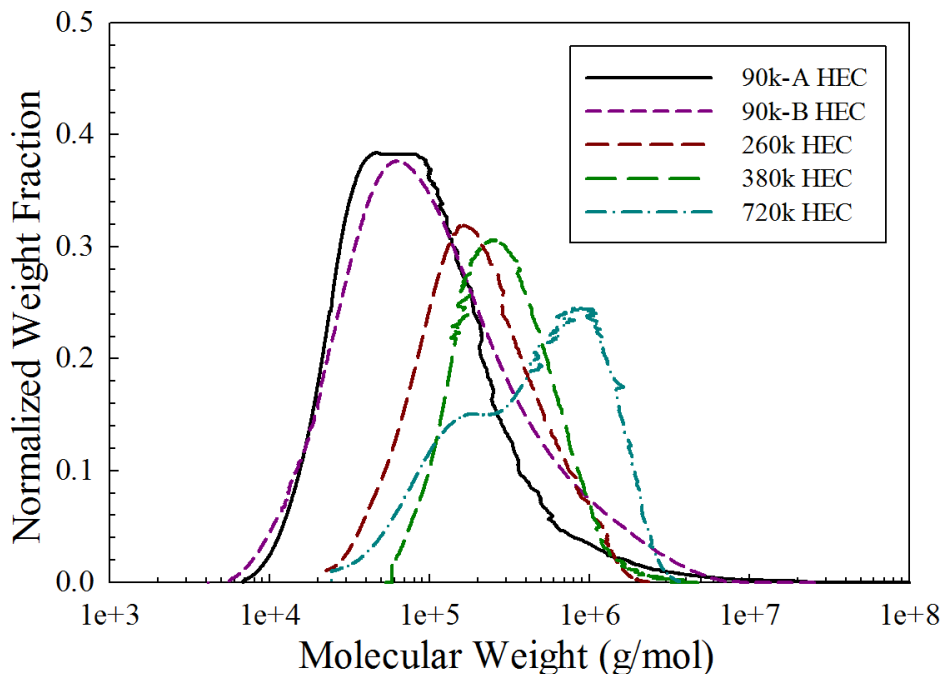


Figure 6.2: Molecular weight distributions of all HEC material measured with GPC. 100 μ L samples of 1 wt% polymer solution in 0.05 M Na_2SO_4 are injected into the GPC instrument. Manufacturer reported molecular weights are shown in the legend in the top right.

Table 6.1: Molecular weight results from GPC measurements performed on all HEC samples

Reported MW	90k-A	90k-B	260k	380k	720k
M_w (g/mol)	149000	214000	261000	316000	727000
PDI	3.22	4.30	2.08	1.62	2.77
R_g (nm)	13.5	15.3	22.0	26.9	41.6

6.4 Results

6.4.1 Observation of phase separation

Droplets containing 20 nm carboxylated PS particles and 90k g/mol HEC are produced on-chip and concentrated using the microfluidic device from Chapter 4 to investigate the phase behavior of the colloid-polymer system. Droplets are produced at approximately 575 μm in diameter and 100 μm in height. 100 cSt silicone oil is used as a continuous outer phase fluid with no added surfactant during droplet production. Mineral oil with Span-80 is not used with this system due to an interaction between the Span-80 and particles. Single droplets for each mass ratio are observed and recorded every two minutes for the duration of an experiment (typically 6-8 hrs).

Figure 6.3a shows representative images of dehydrating droplets for various polymer/particle mass ratios. Top to bottom represents an increase in mass ratio and left to right represents time for each experiment as dehydration occurs. Images of circular droplets have mass/volume values (θ) of the combined particle and polymer mass in the top left corner of each image. Scale bars are all 100 μm . Polymer/particle mass ratio $\xi = 0.11$ is shown in the first row of images. These images show a representative case where droplets remain optically clear through the experiment. For mass ratio $\xi = 1.00$, which has equal mass of particle to polymer, the droplet is initially clear and remains clear for dilute system concentrations. When higher concentrations are reached, the droplet becomes optically dark over a small concentration range in a consistent and reproducible manner. The first few images where the droplet begins to appear grey is at $\theta = 0.08$ g/mL and progresses until the droplet appears optically black at concentration of $\theta = 0.24$ g/mL. At the end of the dehydration process, the droplet becomes slightly lighter and non-circular. This optical darkening is suggestive of a colloidal aggregation

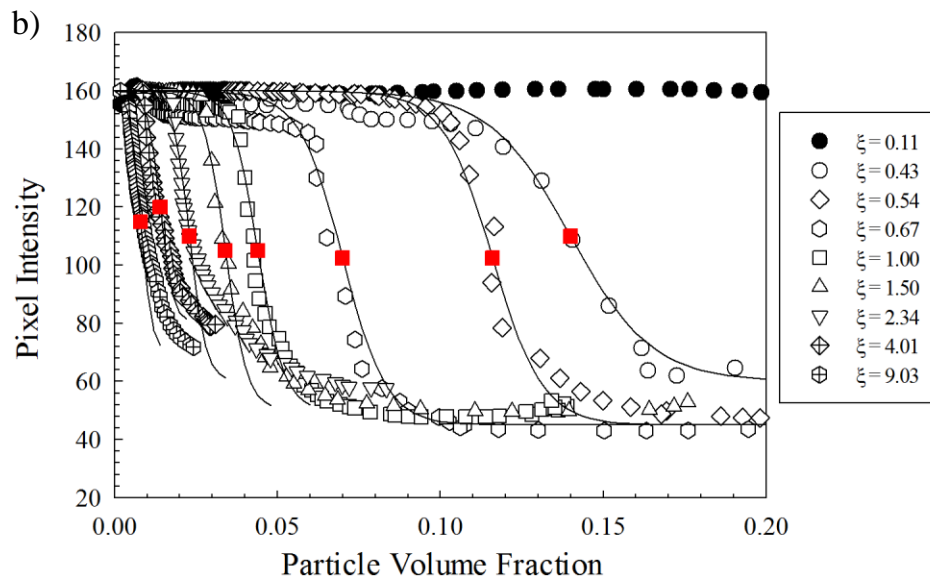
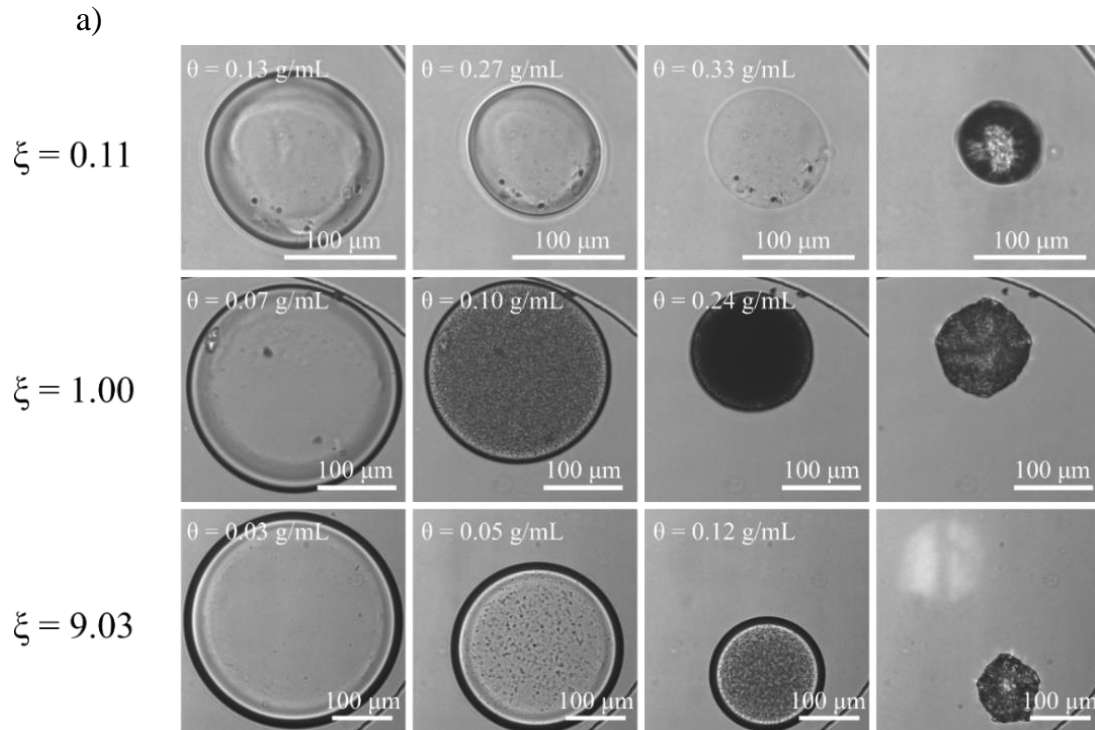


Figure 6.3: (a) Images of droplets containing 20 nm PS particles and 90k g/mol HEC at different polymer-particle mass ratios (ξ) as droplet dehydration and phase separation occurs. Time progresses from left to right along images. Total solute mass is shown in the upper left corner of each image in which droplet size could be accurately measured. $\xi = 0.11$ shows no phase separation while $\xi = 1.00$ and 9.03 display optical darkening. (b) Average droplet intensity as a function of particle volume fraction for several mass ratios. Black curves are exponential decay fits to droplet intensity with time and the red squares denote the midpoints, taken to be a characteristic time of the phenomenon. Mass ratio of each droplet is displayed in the legend.

and phase separation mechanism between the particles, induced by polymer interactions. For the remainder of this chapter, this phenomenon will be referred to as phase separation, but it is important to note that all that is observed is a dense, reproducible optical darkening. Mass ratio $\xi = 9.03$ has almost ten times more polymer than particle. The onset of optical darkening is slower than the $\xi = 1.00$ system, but phase separation is still observed.

Figure 6.3b demonstrates the image analysis method used to determine a characteristic time scale for the observed darkness of a droplet. For each experiment, droplet diameters and average intensities are measured for every other image (every 4 minutes) and plotted as a function of particle concentration. The closed points denote a droplet of mass ratio $\xi = 0.11$ where phase separation is not observed. The open points each represent a unique mass ratio where phase separation is observed with the specific mass ratios described in the legend. Each intensity measurement is normalized such that the first image in an experiment has an average pixel intensity value of 160. This allows for a simple comparison between experiments with different background intensities.

Sample $\xi = 0.11$ is unique compared to all other tested mass ratios in that the average pixel intensity stays relatively constant through the full experiment. There is a slight dip in the intensity at a particle concentration of $\phi = 0.4$, although this is not thought to be caused by phase separation. All other experiments show trends of a rapid decrease in pixel intensity at a particular particle volume fraction. This quick drop is consistent with the droplet darkening as shown in Figure 6.3a. Each curve is fit with a logistic function defined by Equation 6.5

$$f(x) = \frac{L}{1 + e^{-k(x-x_0)}}, \quad (6.5)$$

where L is the maximum value of the function, k is the steepness of the curve, and x_o is the x value of the midpoint of the sigmoid. The midpoint of the exponential fit is used as the characteristic time or volume fraction for the phenomenon to create a criteria for phase separation. These points are highlighted as the red squares in Figure 6.3b and used to quantify phase separation concentrations in Figure 6.4.

Figure 6.4a shows the phase separation results from microfluidic dehydrating drop experiments as a function of the polymer-particle mass ratio and is compared with macroscopic phase separation results. The dotted black lines denote the composition paths of the ξ mass ratios tested. Droplet concentrations are initially at the beginning of the dotted lines and concentrate through the phase separation region. The solid black points show the phase separation point of each experiment determined with the technique from Figure 6.3. The open squares correspond to macroscopic composition points where no phase separation is observed and the open triangles correspond to macroscopic points where there is phase separation. Macroscopic experiments are performed at the same polymer/particle mass ratios (ξ), but only at single composition points as opposed to concentrating systems. The dotted red line denotes the mass ratio at which there is complete adsorption of polymer on the particle surface ($\Gamma = 1$ mg/m²).^{40,41} Five repeat experiments are performed for a single mass ratio of $\xi = 1.00$ to demonstrate the device to device reproducibility error.

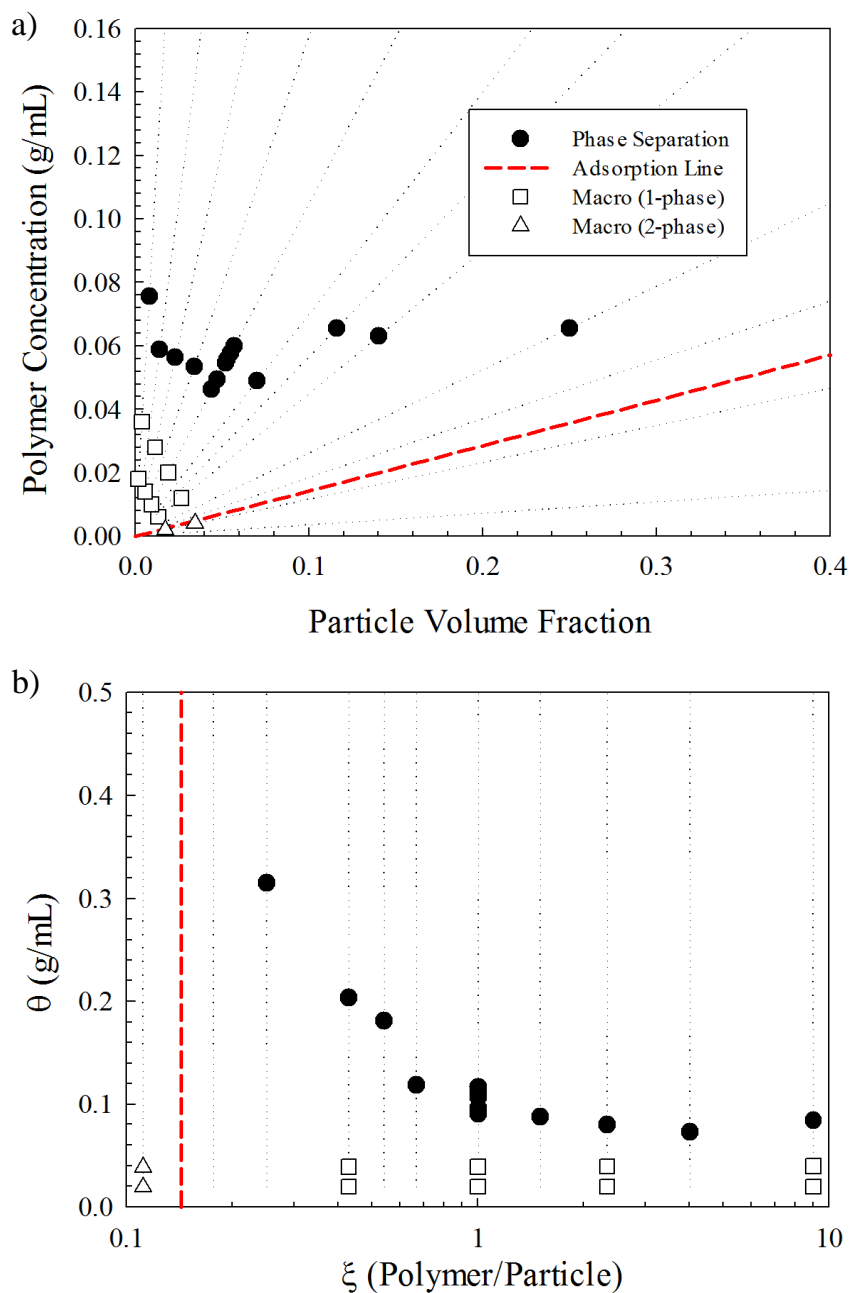


Figure 6.4: Phase behavior results for 20 nm PS and 90k g/mol HEC system. (a) Macroscopic and microfluidic results in polymer-particle phase space. Closed circles denote measured microfluidic phase separation points determined from Figure 6.3. Open points denote tested macroscopic concentrations with squares denoting no observed phase separation and triangles denoting phase separation. Dotted black lines depict the composition paths for each droplet-based experiment. Dashed red line shows the adsorption limit of HEC on PS (1 mg/m^2).^{40,41} (b) Data replotted in θ - ξ coordinates.

Figure 6.4b shows the same phase separation results replotted in solute mass θ (g/mL) as a function of polymer/particle mass ratio (ξ). In these coordinates, a droplet drying experiment

occurs at a single ξ value and increases in θ as the droplet dehydrates. The dotted black lines denote the concentration path for each droplet drying experiment. The solid black points correspond to the phase separation points from Figure 6.3b. The open squares correspond to macroscopic tests where no phase separation is observed and the open triangles correspond to macroscopic tests where there is phase separation. The dotted red line denotes the mass ratio $\xi = 0.14$ where particles are completely coated in polymer chains. There should be free non-adsorbed polymer at mass ratios to the right of the red dotted line, but there should be no free polymer to the left of the line.

Samples with the three lowest mass ratios ($\xi = 0.05, 0.11, \text{ and } 0.17$) show no phase separation during the dehydration process. Droplets look similar to those in the first row of images in Figure 6.3a and therefore have no phase separation points in Figure 6.4. Above $\xi = 0.25$, all compositions show phase separation characteristics. In Figure 6.4b, a trend is observed in the phase separation concentrations. At high ξ values, the required mass (θ) to observe phase separation is relatively constant at a value of $\theta = 0.075 \text{ g/mL}$. As the mass ratio (ξ) decreases towards the adsorption line, the required mass in the system to observe phase separation increases until mass ratios that show no phase separation are reached ($\xi \leq 0.17$).

6.4.2 Controlling phase behavior by controlling interparticle interactions

Phase behavior can be induced at more dilute or concentrated compositions by manipulating system parameters. Polymer material and size has been shown to affect phase boundary location.²⁰ In addition, polymer adsorption strongly influences the behavior, so competitive adsorption with the surface should shift the transition. Competitive adsorption between HEC and a pre-adsorbed surface active species has been shown for polystyrene particles with PEO-PPO-PEO triblock copolymers²⁷ and Triton X-405 surfactant.^{20,26}

Figure 6.5 shows phase separation results comparing HEC polymers sources of the same reported molecular weight of 90k g/mol. HEC is highly polydisperse with differing degrees of substitution based on the supplier. Figure 6.5a shows phase separation results in units of particle volume fraction and polymer mass/volume. The solid red circles denote initial concentrations of each mass ratio. The dotted black lines show the compositional paths for each of those experiments. The closed black circles denote phase separation points determined from the method in Figure 6.3 and repeated from Figure 6.4a, with the polymer source labeled as 90k-A. The closed black squares denote phase separation points for similar mass ratios but with the second 90k g/mol HEC sample labeled as 90k-B. The dotted red line shows the mass ratio at which there is saturation coverage of the polymer on the particle surfaces. The solid black line and dotted black line are drawn to guide the eye and demonstrate differences between polymer sources. The inset of Figure 6.5a shows the effect of adding pre-adsorbed Triton X-405 on the phase separation concentration. All experiments in the Triton work are performed at the highlighted mass ratio of $\xi = 1.00$. The closed black point in the inset corresponds to the phase separation concentration with no added Triton X-405, the open circle corresponds to 0.04 mg Triton/m², the open triangle denotes 0.22 mg Triton/m², and the open diamond denotes 1.53 mg Triton/m².

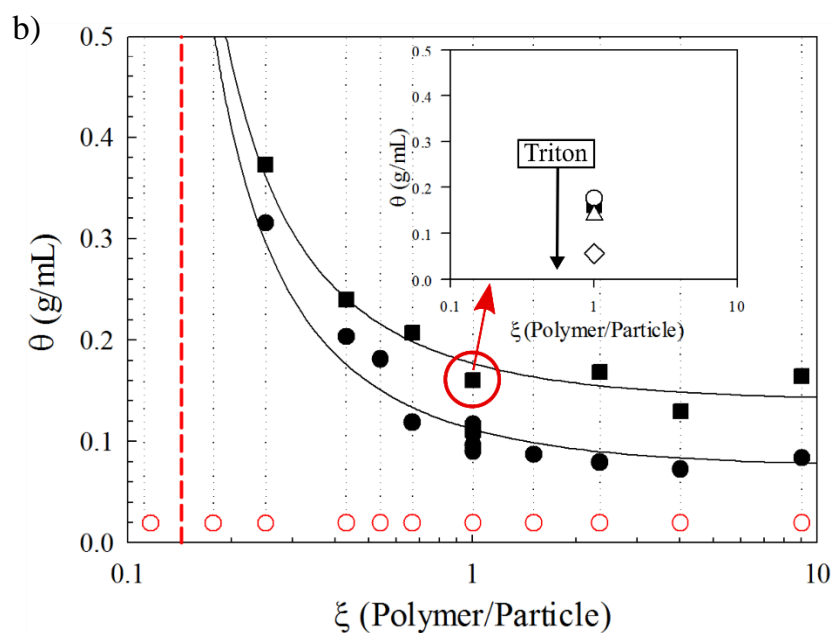
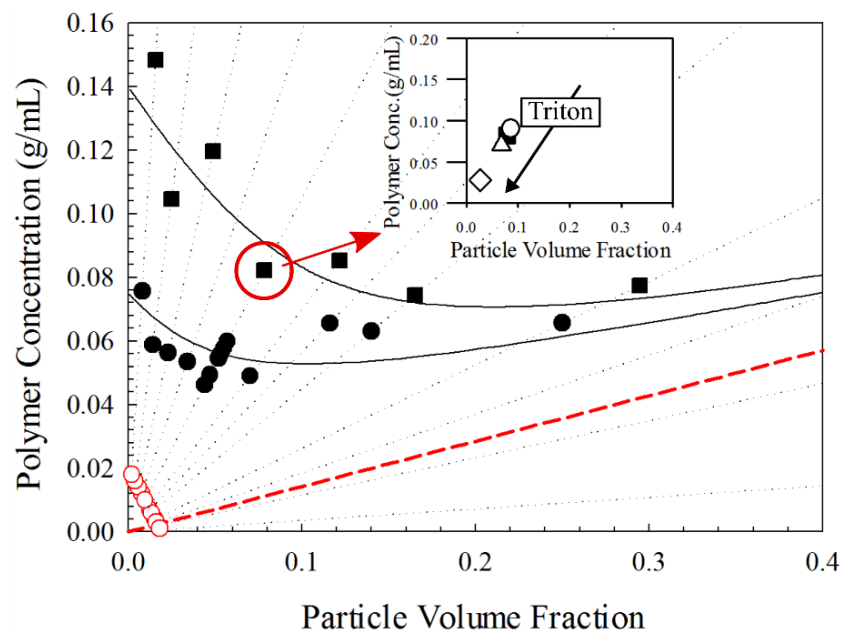


Figure 6.5: Phase behavior results for 20 nm PS particles and 2 different HEC polymer sources. (a) Microfluidic results in polymer-particle phase space. The closed points show measured microfluidic phase separation points for both 90k g/mol HEC samples with the open circles corresponding to 90k-A and the closed squares corresponding to 90k-B. Dotted black lines depict composition paths for each droplet-based experiment. Dashed red line shows the adsorption limit of HEC on PS (1 mg/m^2). Inset shows experiments with 90k-B HEC at $\xi = 1.00$ with preadsorbed Triton X-405 with concentrations of circle = $0.04 \text{ mg Triton/m}^2$, triangle = $0.22 \text{ mg Triton/m}^2$, and diamond = $1.53 \text{ mg Triton/m}^2$. (b) Data replotted in θ - ξ coordinates.

Figure 6.5b shows the same phase separation results as Figure 6.5a replotted in units of solute mass/volume (θ) as a function of polymer/particle mass ratio (ξ). Similarly, the red points denote initial concentrations, the black circles denote phase separation in the 90k-A HEC system, the black squares denote phase separation in the 90k-B HEC system, the dotted black lines demonstrate compositional paths of each experiment, and the dotted red lines shows the mass ratio of complete coverage. The solid black lines show fit lines with an inverse function. Solute concentration (θ) approaches $\theta = 0.075$ g/mL for 90k-A HEC and $\theta = 0.14$ g/mL for 90k-B HEC as mass ratio heads towards infinity. The fit lines are converted into particle and polymer concentration and plotted on Figure 6.5a.

Both plots in Figure 6.5 show a shift in the phase separation boundary line between the two polymer sources. The 90k-B HEC polymer source requires higher particle-polymer concentrations to achieve phase separation than the 90k-A HEC system. This may be caused by a difference in the degree of substitution or the polydispersity of the polymer chains. The degree of substitution of the polymer samples is not measured in this work, but GPC measurements from Figure 6.2 show $MW = 149$ k g/mol for the 90k-A HEC polymer and $MW = 214$ k g/mol for the 90k-B HEC polymer.

The insets of both plots in Figure 6.5 show the strong dependence of phase separation on Triton X-405 concentration. The inset of Figure 6.5b shows a clear decrease in phase separation concentration as a function of pre-adsorbed Triton X-405 concentration. Triton X-405 will adsorb to a saturated concentration of approximately 2 mg Triton/m² for 20 nm PS particles for bulk concentrations above 1.5 mM.^{42,43} When polymer is later introduced into the system, pre-adsorbed Triton prevents the polymer from coating the surface leaving more free polymer in the bulk than the Triton free system. This additional free polymer can induce depletion aggregation

and lead to phase separation at lower particle concentrations as suggested by the data in Figure 6.5.

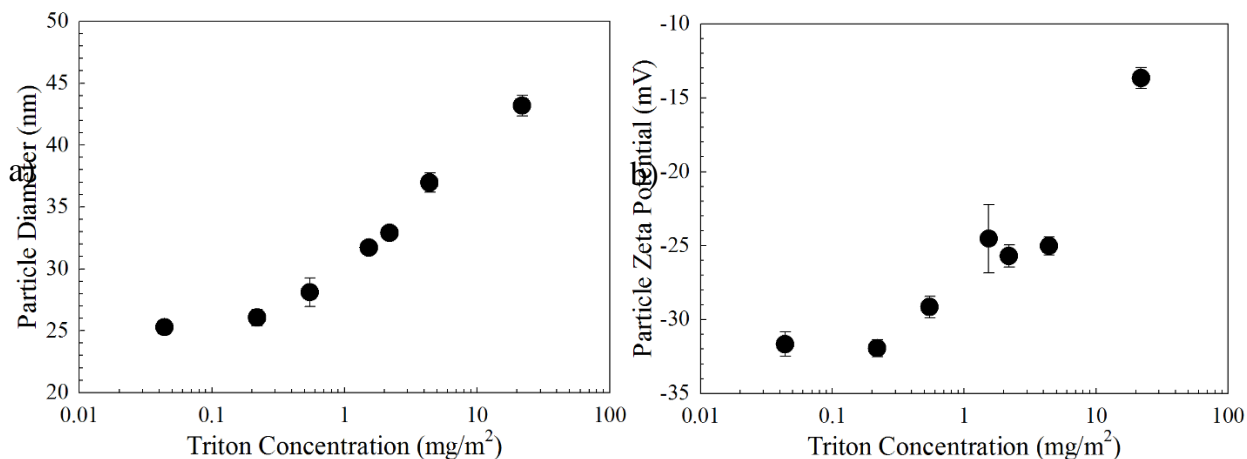


Figure 6.6: (a) Intensity average size and (b) zeta potential measurements of 20 nm PS particles as a function of preadsorbed Triton X-405 concentration. Error bars are standard deviation of triplicate runs.

Figure 6.6 shows the size and mobility measurements for PS particles coated with different concentrations of Triton X-405 measured with a Malvern Zetasizer Nano ZSP (Malvern, Worcestershire, UK). Zeta potential is calculated from electrophoretic mobility using the Smoluchowski approximation. Various concentrations of Triton X-405 are pre-mixed with particles at a constant particle concentration of 0.5 wt/vol% ($\phi = 0.0048$). The density of PS ($\rho = 1.05 \text{ g/mL}$)⁴⁴ is used to convert particle mass to particle volume. A particle diameter of $d = 25 \text{ nm}$ is used to convert volume of particles to particle surface area (m^2) assuming monodisperse, spherical PS particles, resulting in an estimate of $229 \text{ m}^2/\text{g}$ specific surface area. Figure 6.6a shows the average particle size in nm as a function of the Triton concentration in mg/m^2 . An increase in surfactant concentration causes an increase in measured particle size starting at approximately $0.5 \text{ mg}/\text{m}^2$ and increasing linearly on a semilog plot. Similarly, particle zeta potential increases as Triton X-405 concentration increases starting at approximately $0.5 \text{ mg}/\text{m}^2$

as shown in Figure 6.6b. In both figures, the error bars are reported as the standard deviation from triplicate measurements of each surfactant concentration.

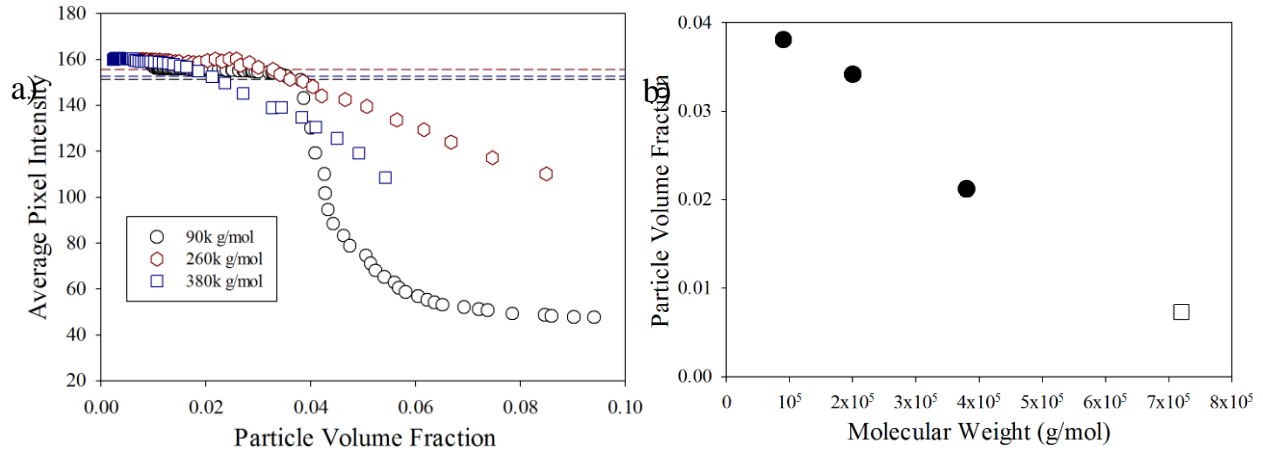


Figure 6.7: (a) Droplet intensity measurements as a function of particle volume fraction with a mass ratio $\xi = 1.00$ for 20 nm PS particles and 3 different molecular weight HEC polymers. Open circles correspond to 90k g/mol HEC, open hexagons to 260k g/mol HEC, and open squares to 380k g/mol HEC. Phase separation is determined by a cut-off boundary value of 10 times the standard deviation of the flat average pixel intensity regions for each experiment. Cut-off values for each experiment is shown by the dotted lines corresponding to the color of the data set. (b) Phase separation particle concentration as a function of molecular weight. The closed circles denote droplets where concentration is measured and the open square denotes a droplet where concentration is inferred from a dehydration calibration.

Colloid-polymer samples are produced at a mass ratio $\xi = 1.00$ and initial concentration $\theta = 0.02$ g/mL for four HEC polymer samples of different molecular weight purchased from the same supplier. The molecular weights are 90k, 260k, 380k, and 720k g/mol. Droplets are produced at an initial size of approximately 575 μm , dehydrated, and recorded through the phase separation process.

In all four experiments, optical darkening is observed during the dehydration process, suggesting similar phase behavior. The 720k g/mol HEC and PS droplet wets the PDMS channels and becomes non-spherical early in the dehydration process, resulting in a loss of measureable concentration. The other three molecular weight samples dehydrate with a consistent pancake shape allowing for further analysis.

Figure 6.7a shows the average pixel intensity of a droplet as a function of particle volume fraction for three different molecular weight HEC samples described by the legend. The 90k g/mol sample is reproduced from Figure 6.3b for a mass ratio $\xi = 1.00$ and displays a rapid exponential decrease in average pixel intensity. The 260k g/mol and 380k g/mol HEC systems show similar darkening behavior compared with the 90k g/mol sample, but over a much longer timescale. Therefore, the exponential fitting technique developed in Figure 6.3 is not applicable in this situation. Instead, the standard deviation of the flat portion for each data set is calculated and reported to be 0.8, 0.4, and 0.7 pixels for 90k, 260k, and 380k g/mol HEC respectively. The average pixel intensity of each image is subtracted by the average pixel intensity of the first image to determine a change in pixel intensity. The first image where this change in pixel intensity is greater than 10 times the standard deviation is considered the phase separation point. This is chosen as a cutoff value to characterize a phase separation point far outside measurement noise. The results of this analysis are shown in Figure 6.7b.

Figure 6.7b displays the phase separation particle volume fraction as a function of polymer molecular weight. The closed circles correspond to droplets that remained circular during the dehydration process and retained accurate concentration measurements. The open square corresponds to the 720k g/mol HEC droplet which loses shape early in the dehydration process. In order to estimate the phase separation concentration for the 720 g/mol HEC droplet, a droplet containing 90k g/mol HEC with identical initial size in the same position in the microfluidic device is used as a dehydration calibration. The time at which the 720k g/mol droplet phase separates is estimated by the observation of the onset of optical darkening. The rate of dehydration of the 90k g/mol droplet is used to predict the concentration at the time of

phase separation. The error on this value will be large, but provides a relative concentration for comparison.

The results show a steady decrease in phase separation concentration with an increase in polymer molecular weight. This is consistent with the expected effect of polymer molecular weight on depletion induced phase separation. A larger polymer molecular weight achieves phase separation at more dilute particle concentrations.²⁰

To examine the potentially stochastic nature of this process, an experiment is performed using all 40 droplets in a microfluidic device. Droplets containing 20nm PS particles and 90k g/mol HEC polymer at a mass ratio $\xi = 1.00$ and initial mass concentration $\theta = 0.02$ g/mL are produced with a 100 cSt continuous silicone oil outer phase. Initial droplet sizes are measured at high image resolution before the dehydration process begins. Dehydration is recorded with all 40 droplets in view.

At sufficiently high concentration, droplets undergo optical darkening similar to the second row of images in Figure 6.3a. The time at which an individual droplet becomes dark is considered a phase separation point. The concentration of the droplet at this point is not calculated due to the poor image resolution when zoomed out to this magnification, demonstrating the tradeoff between image resolution and statistical information. However, if the phase separation process is not a stochastic process, then the phase separation time should be a function of initial droplet volume (measured as droplet size).

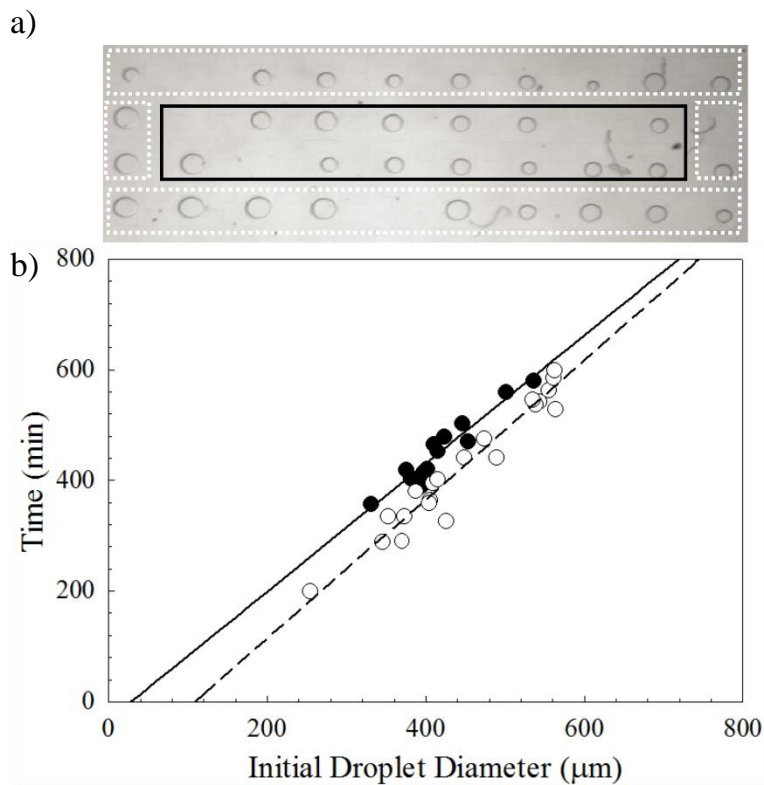


Figure 6.8: (a) Initial image of all droplets in device demonstrating initial sizes and number density (34 traps out of 40 traps filled). Black rectangle denotes inner droplets and white dotted rectangles denote outer, edge droplets. (b) Droplet dehydration time until phase separation is observed as a function of initial droplet size. Solid black circles correspond to inner droplets and open circles denote outer droplets. Solid line and dotted line are least squared linear fits through inner and outer droplet results respectively.

Figure 6.8 shows the results from the full device droplet drying stochastic experiment.

Figure 6.8a displays an image of the initial droplets and Figure 6.8b shows the observed phase separation trend versus time until phase is observed in minutes. The closed points correspond to results from droplets within the black rectangle in Figure 6.8a and the open points correspond to results from droplets within the white dotted rectangles. The solid black line is the least squares linear fit of the closed points and the dotted black line is the linear fit of the open points. This distinction is necessary because it has been observed that droplets near the edge dehydrate faster than droplets in the center of the device. The higher flux of solvent out of the drops will influence this figure.

A linear trend in phase separation time as a function of initial droplet size is observed. The droplets in the center of the device require more time than the droplets on the exterior of the device. However, both regions show a similar effect that the larger the initial droplet, the longer it takes to observe phase separation (or reach the critical concentration). If the phase separation was a stochastic process and droplets could supersaturate, one might expect a much weaker correlation between initial droplet size and phase separation time.

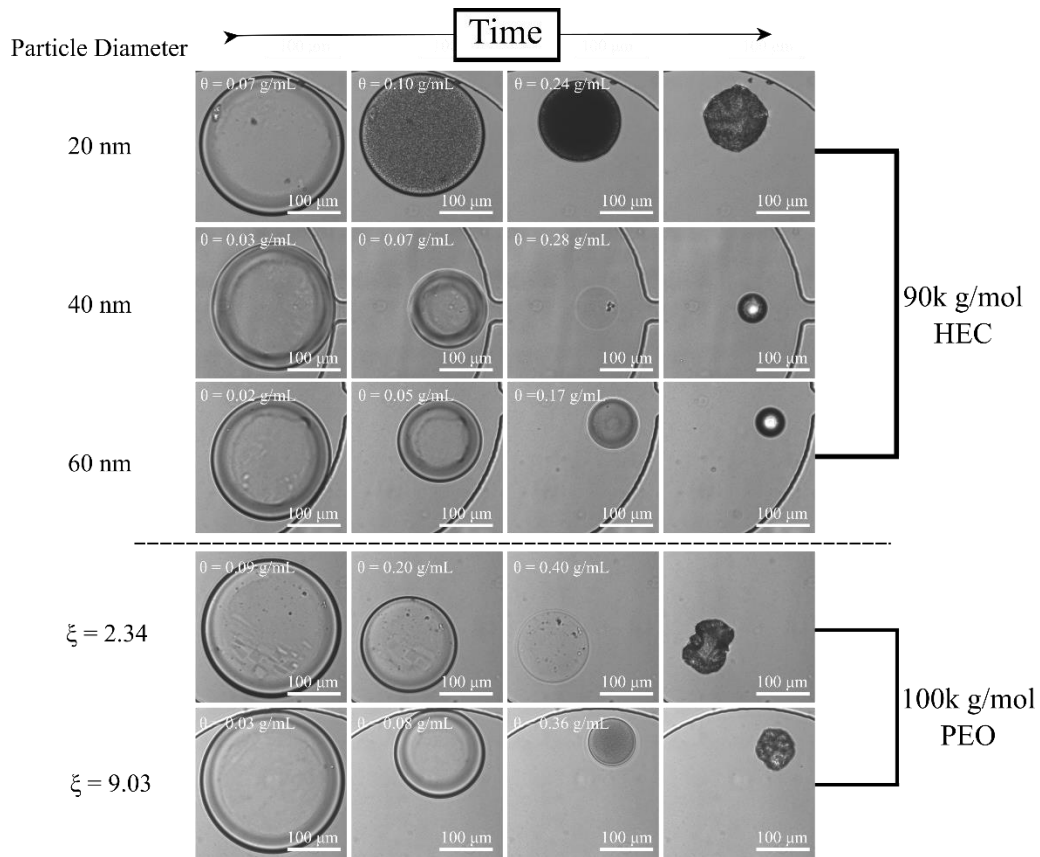


Figure 6.9: Images of various polystyrene particles and polymer combinations during the dehydration process. Time progresses from left to right along images. First three rows show systems of PS particles increasing in particle size with 90k g/mol HEC polymer source. Last two rows show images for 20 nm PS particles and 100k g/mol PEO at different polymer-particle mass ratios.

Instead of systematically shifting the phase separation as shown in Figure 6.5, the optical detection of phase separation (and potentially the phase separation itself) can be suppressed by varying the interparticle potentials. Figure 6.9 demonstrates two system parameters that can be

changed to suppress the phase separation optical changes under certain conditions. The first parameter is the size of the PS nanoparticles and the second is the polymer source, which is changed from HEC to poly(ethylene oxide) or PEO. All particle sources are electrostatically stabilized with carboxyl groups and purchased from the same vendor. 100k g/mol PEO molecular weight is chosen to be similar to 90k g/mol HEC and minimize the effects of varying molecular weight.

The first three rows of images in Figure 6.9 demonstrate the differences in the dehydration process caused by particle size while at the same mass ratio of $\xi = 1.00$ with the same 90k g/mol HEC polymer source. The first row of images are identical to images from Figure 6.3 for $\xi = 1.00$ to demonstrate the clear optical effects that occur with the 20 nm system. The second row of images show an identical experiment performed with 40 nm PS instead of 20 nm PS. There is no darkening of the droplet during the dehydration process and the droplet goes through a refractive index match point between $\theta = 0.24$ - 0.33 g/mL similar to sucrose experiments from Chapter 5. 60 nm PS does appear slightly dark at high concentrations, but shows a steady, slow decrease in pixel intensity as the droplet concentrates compared with a sharp drop-off in pixel intensity for the 20 nm system shown in Figure 6.3b.

The bottom two rows of images show representative experiments for different mass ratios of a 20 nm PS and 100k g/mol PEO system. The first of those rows shows the dehydration process for a mass ratio of $\xi = 2.34$, typical of most experiments performed with this system. Droplets dehydrate without darkening and reach a refractive index match point at a concentration of $\theta = 0.41$ g/mL. Other mass ratios where this same observation is observed is at $\xi = 1.00$ and pure polymer. The last row of images shows the dehydration process for a PS-PEO system with a polymer/particle mass ratio of $\xi = 9.03$. At this particular mass ratio, phase separation is

observed for this system, but appears less dark due to the high ξ mass ratio (low particle concentration, high polymer concentration). This observation is also seen at a mass ratio of $\xi = 19.1$. This optical phase separation only occurs in the PS-PEO system at concentrations where there is significantly more polymer than particles ($\xi \geq 9.03$).

6.5 Discussion

6.5.1 Demonstration of depletion induced aggregation

Interparticle potential plays a large role in determining phase behavior for many complex colloidal systems. Parameters including particle size, polymer size, and adsorption behavior are varied in this work to tune and control phase separation. Figure 6.3 shows images of observed phase separation for a 20 nm PS and 90k g/mol HEC system while Figure 6.4 shows the resulting phase behavior of the system. The saturation limit for the PS-HEC system corresponds to a polymer/particle mass ratio of $\xi = 0.14$.^{40,41} Below the saturation limit, much if not all of the polymer will be depleted from the bulk and onto the particle surface. This leaves minimal polymer to induce depletion interactions and flocculate the system. Without free polymer to induce depletion interactions, the system remains as one phase through the complete dehydration process. Once adsorption is reached and there are free polymer chains in the bulk ($\xi > 0.14$), phase separation can occur. However, because most of the polymer is still on the particle surface, high particle concentrations (small interparticle distances) are necessary to achieve phase separation and may be why these systems phase separate at high θ values. As free polymer chains become more abundant, less total mass in the system is required to achieve phase separation and the θ values decrease as polymer/particle mass ratio increases. This suggests that polymer induced depletion attraction is causing the optical darkening phase separation behavior observed in Figure 6.3.

Triton X-405 experiments are used to verify this hypothesis that phase separation is caused by depletion attraction by pre-adsorbing Triton X-405 before the addition of HEC polymer to the system. Triton X-405 adsorbs strongly to PS particles and has been shown to keep HEC off PS particle surfaces if pre-adsorbed.²⁰ When Triton X-405 is initially added to the particles, the surfactant will adsorb to the particle surface, occupying potential adsorption sites. When HEC polymer is added sequentially, any remaining open adsorption sites will be filled with polymer chains. This effectively increases the bulk HEC concentration for a given polymer-particle initial concentration. With an increase in bulk polymer concentration, depletion attraction should occur at a more dilute particle concentration. The insets in Figure 6.5 show phase separation results for pre-adsorbed Triton X-405 experiments for 3 different surfactant concentrations all performed at a mass ratio $\xi = 1.00$. As mentioned previously, Triton X-405 has an adsorption saturation at approximately 2 mg/m^2 at a bulk concentration of 1.5 mM .⁴² At low Triton concentration ($0.04 \text{ mg Triton/m}^2$, 0.05 mM Triton), very few of the adsorption sites are filled with surfactant. When polymer is then added to the PS-Triton complexes, there is little difference in the number of adsorbed polymer chains compared to the Triton free system. This small difference in bulk polymer concentration leads to minimal variation in the polymer-particle phase separation concentration. When an intermediate concentration of Triton X-405 is added to the particles ($0.22 \text{ mg Triton/m}^2$, 0.25 mM Triton), a maximum of 10% of the adsorption sites are filled with surfactant, leading to a small increase in the initial bulk concentration of HEC, as fewer polymer chains will be able to adsorb to the particle surfaces. This induces phase separation at a more dilute particle concentration as shown in Figure 6.5. When a high concentration of Triton X-405 is added to the particle surfaces ($1.53 \text{ mg Triton/m}^2$, 0.64 mM Triton), a significant portion of the adsorption sites are filled with surfactant (up to 75%).

Therefore, much added polymer remains in the bulk, causing phase separation at a more dilute concentration than the surfactant free case. These results verify the hypothesis that free polymer chains in the PS-HEC system induce depletion attraction and are the mechanism for phase separation.

For additional verification, effects of molecular weight on phase separation are investigated with the results are shown in Figure 6.7. An increase in molecular weight is expected to decrease the particle concentration at which phase separation occurs.²⁰ The results in Figure 6.7b follow this trend, demonstrating that an increase in polymer molecular weight leads to a decrease in particle concentration at the phase separation point.

6.5.2 Varying interparticle potential

As mentioned previously, varying the interparticle potential can change phase separation behavior based on the position and depth of the primary and secondary potential wells. There are two modes of aggregation limits: diffusion-limited colloidal aggregation (DLCA) and reaction-limited colloidal aggregation (RLCA). The likelihood of a system to be classified under one of these characterizations depends on the kinetics of aggregation and diffusion timescales. There is an energy barrier of aggregation described by the interparticle potential that must be overcome for two particles to aggregate. If the energy barrier is low and particle diffusion is slow, then nearly any particle collision will result in particle aggregation, but collisions occur infrequently due to slow particle diffusion. This is described as DLCA and leads to loose, flocculated, fractal-like aggregated structures.⁴⁵⁻⁴⁸ Conversely, if the energy barrier is high and diffusion is quick, then many interparticle collisions will occur, but there is a low probability of the particles sticking together. This is described by RLCA and leads to large, tight, aggregated particle clusters.⁴⁹⁻⁵²

A crossover from one aggregation limit to the other is possible through variation in the kinetics, described by the interparticle potential. The overall interparticle potential will depend on the attractive forces including Van der Waals forces, depletion attraction, and/or bridging flocculation and the repulsive forces including electrostatic and steric repulsion. The magnitude of these forces depend on the size of the particles and polymers, the Hamaker constant, electrolyte concentration, pH, temperature, and concentration.³⁹

Particle size has a direct effect on the van der Waals forces, depletion attraction, steric repulsion, and electrostatic repulsion. Figure 6.1 shows the theoretical pair potential calculations for sterically and electrostatically stabilized particles undergoing depletion attraction at various particle sizes. The net variation in pair potential with an increase in particle size is a deepening of the secondary potential well, or a decrease in the aggregation energy barrier. This results in a higher probability of two approaching particles to aggregate as the particles become larger. There is also a large increase in the energy barrier to the primary potential well.

Figure 6.9 demonstrates that phase separation can be suppressed in the PS-HEC system with an increase in particle size. Significant optical darkening is clearly observed in the 20nm system, but not in the 40 nm or 60 nm system. As shown in Figure 6.1, an increase in the particle size will increase the depth of the secondary minimum well, lowering the energy barrier of aggregation. With a lower energy barrier, two colliding particles have a higher probability to aggregate and stick together. This translates to a potential classification shift away from RLCA towards DLCA, producing looser, flocculated networks as opposed to large, aggregated clusters. The 20 nm, smaller PS particles may be experiencing more kinetic limited aggregation, resulting in aggregated clusters, while the larger 40 nm and 60 nm PS particles may be experiencing more diffusion limited aggregation resulting in flocculated networks. Colloidal particles scatter light

with a sixth power dependence on particle size for Rayleigh scattering.³⁹ Therefore, large aggregated particle structures will scatter significantly more light than smaller, loose, flocculated networks. This may explain why the 20 nm PS and 90k g/mol HEC system displays obvious optical darkening and particle aggregation while the 40 nm and 60 nm particle systems at the same concentrations show minimal optical darkening, shown in Figure 6.9.

Varying the polymer source will change the adsorption kinetics, saturation concentration, depletion attraction, and steric repulsion of a polymer-particle system. The two bottom rows of images in Figure 6.9 show the effect of changing from 90k g/mol HEC polymer to 100k g/mol PEO while maintaining 20 nm PS particles. In this system, optical darkening behavior is only observed at high mass ratios ($\xi \geq 9.03$) where there is significantly more polymer than particle. At lower mass ratios ($\xi < 9.03$), droplets remain clear through the dehydration process. It is unclear whether the system is changing from RLCA to DLCA as the mass ratio is increased or if depletion attraction forces are too weak until high mass ratios.

6.6 Conclusions

In this work, interparticle potential of colloid-polymer systems is systematically controlled to determine the effects on phase behavior in concentrating nanoliter sized microfluidic droplets. A system containing 20 nm PS particles and 90k g/mol HEC polymer is found to display significant and reproducible optical darkening (phase separation) as droplets dehydrate. Phase separation is only observed at polymer concentrations above the adsorption line, suggesting a polymer-induced depletion flocculation aggregation mechanism. Interparticle potential is varied by changing polymer molecular weight, particle size, and polymer type. Increasing polymer molecular weight resulted in a more dilute phase separation point. Increasing particle size suppressed optical darkening for an identical particle-polymer system,

suggesting a transition from reaction-limited (RLCA) to diffusion-limited (DLCA) aggregation with an increase in particle size. Changing the polymer source from HEC to PEO suppressed phase separation at all concentrations except large polymer/particle mass ratios ($\xi \geq 9.03$).

6.7 References

- (1) Pusey, P. N.; van Megen, W.; Megen, W. van. Phase Behavior of Concentrated Suspensions of Nearly Hard Colloidal Spheres. *Nature* **1986**, *320* (6060), 340–342.
- (2) Ilett, S. M.; Orrock, A.; Poon, W. C. K.; Pusey, P. N. Phase Behavior of a Model Colloid-Polymer Mixture. *Phys. Rev. E* **1995**, *51* (2), 1344–1352.
- (3) Lekkerkerker, H. N. W.; Poon, W. C.-K.; Pusey, P. N.; Stroobants, A.; Warren, P. B. Phase Behaviour of Colloid + Polymer Mixtures. *Europhys. Lett.* **1992**, *20* (6), 559–564.
- (4) Hunter, G.; Weeks, E. The Physics of the Colloidal Glass Transition. *Rep. Prog. Phys.* **2012**, *75* (6), 66501.
- (5) Shaw, D. J. *Colloid & Surface Chemistry*; 1992.
- (6) Ma, C. The Effect of Triton X-100 on the Stability of Polystyrene Latices. *Colloids and Surfaces* **1987**, *28*, 1–7.
- (7) Vincent, B.; Edwards, J.; Emmett, S.; Jones, A. Depletion Flocculation in Dispersions of Sterically-Stabilised Particles (“soft Spheres”). *Colloids and Surfaces* **1986**, *18*, 261–281.
- (8) Kepler, G. M.; Fraden, S. Attractive Potential between Confined Colloids at Low Ionic-Strength. *Phys. Rev. Lett.* **1994**, *73* (2), 356–359.
- (9) Oosawa, F.; Asakura, S. Surface Tension of High-Polymer Solutions. *J. Chem. Phys.* **1954**, *22* (7), 1255.
- (10) Asakura, S.; Oosawa, F. Interaction between Particles Suspended in Solutions of Macromolecules. *Journal of Polymer Science*. 1958, pp 183–192.
- (11) Vrij, a. Polymers at Interfaces and the Interactions in Colloidal Dispersions. *Pure Appl. Chem.* **1976**, *48* (4), 471–483.
- (12) Poon, W. C. K.; Selfe, J. S.; Robertson, M. B.; Ilett, S. M.; Pirie, A. D.; Pusey, P. N. An Experimental Study of a Model Colloid-Polymer Mixture. *J. Phys. II* **1993**, *3*, 1075.
- (13) Ramakrishnan, S.; Fuchs, M.; Schweizer, K. S.; Zukoski, C. F. Entropy Driven Phase Transitions in Colloid–polymer Suspensions: Tests of Depletion Theories. *J. Chem. Phys.* **2002**, *116* (5), 2201.
- (14) Zhang, Z. X.; van Duijneveldt, J. S. Experimental Phase Diagram of a Model Colloid-Polymer Mixture in the Protein Limit. *Langmuir* **2006**, *22* (1), 63–66.
- (15) Shah, S. A.; Chen, Y. L.; Schweizer, K. S.; Zukoski, C. F. Phase Behavior and Concentration Fluctuations in Suspensions of Hard Spheres and Nearly Ideal Polymers. *J. Chem. Phys.* **2003**, *118* (7), 3350–3361.
- (16) Santore, M. M.; Russel, W. B.; Prud’homme, R. K. Experimental and Theoretical Study of Phase Transitions Induced in Colloidal Dispersions by Associative Polymers. *Faraday Discuss.* **1991**, *90* (Colloidal Dispersion), 323–333,365.
- (17) Liu, J.; Men, Y. Phase Behavior of Charge Stabilized Colloid Dispersion with Added

- Water Soluble Polymers. *Chinese J. Polym. Sci.* **2013**, *31* (9), 1218–1224.
- (18) Liang, W.; Tadros, T. F.; Luckham, P. F. Flocculation of Sterically Stabilized Polystyrene Latex Particles by Adsorbing and Nonadsorbing Poly(acrylic Acid). *Langmuir* **1994**, *10* (2), 441–446.
 - (19) Patel, P. D.; Russel, W. B. An Experimental Study of Aqueous Suspensions Containing Dissolved Polymer: A. Phase Separation. *J. Colloid Interface Sci.* **1989**, *131* (1), 192–200.
 - (20) Sperry, P. R.; Hopfenberg, H. B.; Thomas, N. L. Flocculation of Latex by Water-Soluble Polymers: Experimental Confirmation of a Nonbridging, Nonadsorptive, Volume-Restriction Mechanism. *J. Colloid Interface Sci.* **1981**, *82* (1), 62–76.
 - (21) Sperry, P. R. Morphology and Mechanism in Latex Flocculated by Volume Restriction. *J. Colloid Interface Sci.* **1983**, *99* (1), 97–108.
 - (22) Gast, A. .; Russel, W. .; Hall, C. . An Experimental and Theoretical Study of Phase Transitions in the Polystyrene Latex and Hydroxyethylcellulose System. *J. Colloid Interface Sci.* **1986**, *109* (1), 161–171.
 - (23) Liang, W.; Tadros, T. F.; Luckham, P. F. Rheological Properties of Concentrated Sterically Stabilized Latex Dispersions in the Presence of Hydroxyethyl Cellulose. *Journal of Colloid and Interface Science.* 1993, pp 183–189.
 - (24) Biais, F. L. C.; J.Bibette; J. Experimental Phase Diagrams of Polymer and Colloid Mixtures. *EPL (Europhysics Lett.)* **1993**, *23* (9), 653.
 - (25) Smith, N. J.; Williams, P. A. Depletion Flocculation of Polystyrene Latices by Water-Soluble Polymers. *J. Chem. Soc., Faraday Trans.* **1995**, *91* (10), 1483–1489.
 - (26) Horner, K. D.; Topper, M.; Ballauff, M. Assessment of the Depletion Forces in Mixtures of a Polystyrene Latex and Hydroxyethyl Cellulose by Turbidimetry. *Langmuir* **1997**, *13* (25), 551–558.
 - (27) Faers, M. A.; Luckham, P. F. Effect of the Steric Stabilizing Layer on the Phase Behavior and Rheology of Small Polystyrene Latex Dispersions Induced by Changes to the Concentration of Nonadsorbing Hydroxyethylcellulose. *Langmuir* **1997**, *13* (11), 2922–2931.
 - (28) Kjoniksen, A. L.; Joabsson, F.; Thuresson, K.; Nystrom, B. Salt-Induced Aggregation of Polystyrene Latex Particles in Aqueous Solutions of a Hydrophobically Modified Nonionic Cellulose Derivative and Its Unmodified Analogue. *J. Phys. Chem. B* **1999**, *103* (45), 9818–9825.
 - (29) Kiratzis, N.; Faers, M.; Luckham, P. F. Depletion Flocculation of Particulate Systems Induced by Hydroxyethylcellulose. *Colloids Surfaces A Physicochem. Eng. Asp.* **1999**, *151* (3), 461–471.
 - (30) Lauten, R. A.; Kjoniksen, A.; Nystrom, B. Colloid Polymer Interactions and Aggregation in Aqueous Mixtures of Polystyrene Latex , Sodium Dodecyl Sulfate , and a Hydrophobically Modified Polymer : A Dynamic Light Scattering Study. *Langmuir* **2001**, No. 17, 924–930.

- (31) Olsson, M.; Linse, P.; Piculell, L. Influence of Added Particles on the Phase Behavior of Polymer Solutions. Analysis by Mean-Field Lattice Theory. *Langmuir* **2005**, *21* (23), 10862–10870.
- (32) Bayliss, K.; van Duijneveldt, J. S.; Faers, M. A.; Vermeer, A. W. P. Comparing Colloidal Phase Separation Induced by Linear Polymer and by Microgel Particles. *Soft Matter* **2011**, *7* (21), 10345–10352.
- (33) Vincent, B.; Edwards, J.; Emmett, S.; Croot, R. Phase Separation in Dispersions of Weakly-Interacting Particles in Solutions of Non-Adsorbing Polymer. *Colloids and Surfaces* **1988**, *31*, 267–298.
- (34) Bolhuis, P. G.; Louis, A. A.; Hansen, J.-P. Influence of Polymer-Excluded Volume on the Phase-Behavior of Colloid-Polymer Mixtures. *Phys. Rev. Lett.* **2002**, *89* (12), 128302.
- (35) Gast, A. P.; Hall, C. K.; Russel, W. B. Phase Separations Induced in Aqueous Colloidal Suspensions by Dissolved Polymer. *Faraday Discuss. Chem. Soc.* **1983**, *76*, 189–201.
- (36) Poon, W. C. K.; Pirie, A. D.; Pusey, P. N. Gelation in Colloid-Polymer Mixtures. *Faraday Discuss.* **1995**, No. 1, 65–76.
- (37) Snowden, M. J.; Clegg, S. M.; Williams, P. A.; Robb, I. D. Flocculation of Silica Particles by Adsorbing and Non-Adsorbing Polymers. *J. Chem. Soc., Faraday Trans.* **1991**, *87* (14), 2201–2207.
- (38) Verwey, E. J. W.; Overbeek, J. T. G. *Theory of the Stability of Lyophobic Colloids*; Elsevier: Amsterdam, 1948.
- (39) Berg, J. C. *An Introduction to Interfaces & Colloids*; World Scientific Publishing Co.: Singapore, 2010.
- (40) Tanaka, R.; Williams, P.; Meadows, J.; Phillips, G. The Adsorption of Hydroxyethyl Cellulose and Hydrophobically Modified Hydroxyethyl Cellulose onto Polystyrene Latex. *Colloids and surfaces* **1992**, *66*, 63–71.
- (41) Malmsten, M.; Tiberg, F. Adsorption of Ethyl(hydroxyethyl) Cellulose at Polystyrene. *Langmuir* **1993**, *9* (4), 1098–1103.
- (42) Colombie, D.; Landfester, K.; Sudol, E. D.; El-Aasser, M. S. Determination of the Adsorption Isotherm of the Nonionic Surfactant Triton X-405 on Polystyrene Latex Particles Using H NMR. *J. Colloid Interface Sci.* **1998**, *202*, 554–557.
- (43) Bolze, J.; Hörner, K. D.; Ballauff, M. Adsorption of the Nonionic Surfactant Triton X-405 on Polystyrene Latex Particles As Monitored by Small-Angle X-Ray Scattering. *Langmuir* **1996**, *12* (12), 2906–2912.
- (44) Sharp, D. G.; Beard, J. W. Size and Density of Polystyrene Particles Measured by Ultracentrifugation. *J. Biol. Chem.* **1950**, *185*, 247–253.
- (45) Weitz, D. A.; Oliveria, M. Fractal Structures Formed by Kinetic Aggregation of Aqueous Gold Colloids. *Phys. Rev. Lett.* **1984**, *52* (16), 1433–1436.
- (46) Lin, M. Y.; Lindsay, H. M.; Weitz, D. A.; Klein, R.; Ball, R. C.; Meakin, P. Universal

- Diffusion-Limited Colloid Aggregation. *J. Phys. Chem. B* **1990**, *2*, 3093–3113.
- (47) Carpineti, M.; Giglio, M. Spinodal-Type Dynamics in Fractal Aggregation of Colloidal Clusters. *Phys. Rev. Lett.* **1992**, *68* (22), 3327–3330.
- (48) Poling-Skutvik, R.; Lee, J.; Narayanan, S.; Krishnamoorti, R.; Conrad, J. C. Tunable Assembly of Gold Nanorods in Polymer Solutions to Generate Controlled Nanostructured Materials. *ACS Appl. Nano Mater.* **2018**, acsanm.7b00277.
- (49) Weitz, D. A.; Huang, J. S.; Lin, M. Y.; Sung, J. Limits of the Fractal Dimension for Irreversible Kinetic Aggregation of Gold Colloids. *Physical Rev. Lett.* **1985**, *54* (13), 1416–1419.
- (50) Lin, M. Y.; Lindsay, H. M.; Weitz, D. A.; Ball, R. C.; Klein, R.; Meakin, P. Universal Reaction-Limited Colloid Aggregation. *Phys. Rev. A* **1990**, *41* (4), 2005–2020.
- (51) Meakin, P.; Jullien, R. The Effects of Restructuring on the Geometry of Clusters Formed by Diffusion-Limited, Ballistic, and Reaction-Limited Cluster-Cluster Aggregation. *J. Chem. Phys.* **1988**, *89* (1), 246–250.
- (52) Lattuada, M.; Sandkühler, P.; Wu, H.; Sefcik, J.; Morbidelli, M. Aggregation Kinetics of Polymer Colloids in Reaction Limited Regime: Experiments and Simulations. *Adv. Colloid Interface Sci.* **2003**, *103* (1), 33–56.

Chapter 7: Droplet-Based Characterization of Surfactant Efficacy in Colloidal Stabilization of Carbon Black in Nonpolar Solvents

7.1 Introduction

The ability to predict and characterize the stability of colloidal particles in a solvent is one of the fundamental needs of colloidal science and is relevant to a wide range of industrial applications.^{1,2} The stability of aqueous colloidal suspensions has been extensively studied and mechanisms for charge stabilization and steric stabilization, or electrosterics, have been elucidated.^{3–11} However, less focus has been placed on understanding the mechanisms behind stabilization of systems in nonpolar media. The low dielectric constant ($\epsilon \approx 2$) of nonpolar systems leads to high energy barriers of charge separation and as a result, electrostatics are thought to be an unlikely mechanism for stability in nonpolar media. However, with the addition of surfactant or ‘dopant’, charging and electrostatic stabilization have been observed in nonpolar solvents.^{1,2,12–16} These systems are used extensively in industrial applications, but a fundamental understanding of the stabilization mechanism is still missing, partly due to a lack of detailed characterization.

It has been shown that the introduction of inverse micelles in nonpolar fluids leads to a measurable conductivity increase that is proportional to the inverse micelle concentration.^{1,17–21} The mechanism of the charge production has not yet been elucidated, but it is generally thought that charged species are stabilized within the inverse micelle core and that the inverse micelles behave as charge carriers.^{22–26} When particles are added to the system, some of the charge is imparted to the particle surface leading to electrostatic stabilization.^{2,14–16} Particle charging has been observed in nonpolar fluids with PMMA^{12,14,27}, PS^{14,28}, carbon black^{29–31}, silica^{23,32–34}, and alumina³⁴ particles using various surfactants or dopants. Systematic studies are underway to

understand the effects of each component and determine the underlying mechanism of particle charging.^{23,34} Smith and Eastoe provide a detailed introduction into the three proposed mechanisms for charge transfer and particle charging in nonpolar fluids.² The acid-base mechanism originally proposed by Pugh *et al.* is a likely candidate to describe particle charging, especially for nonionic surfactants.²⁹ The suggested idea is that initially uncharged micelles (or single surfactant molecules) adsorb to the particle surface. Charge is then imparted into the micelle or surfactant molecule via an acid-base reaction with the sign of the particle being determined by the acidity and basicity of the particle and surfactant. Finally the charged micelle or surfactant desorbs from the surface leaving behind a charged particle surface. The degree by which the particles are stabilized has been investigated by various theoretical methods including a direct extension of DLVO theory³⁵ as well as a sum of Hamaker and Coulomb forces (ignoring the electrical double layer effects)^{36,37} while some argue that at high concentrations the repulsive forces are not strong enough to stabilize the system.^{38,39} An in depth comparison of electrostatic contributions is available in a review article.¹

One of the first reports that identified particle charging and electrostatic stabilization in nonpolar solvents used a system of carbon black particles dispersed in dodecane with the surfactant OLOA 1200.^{29,30} Carbon black is a powder of primary particles composed of graphene layers and is produced through the incomplete combustion of heavy petroleum.⁴⁰ The surfactant, OLOA 1200, is a nonionic commercial product with a structure described as a polyisobutylene tail with a succinimide linker to an amine head group dispersed in a cosolvent.⁴¹

A simple method to characterize suspension stability is to place the formulated suspension in a vial and visually observe sedimentation in the sample with time.^{29,42} While simple, this approach is complicated in opaque suspensions or strong optical absorbers like carbon black. Pugh

et al. uses this methodology to characterize the stability of carbon black mixed with OLOA 1200 by visualizing samples with a fixed carbon black concentration and varying amounts of surfactant.²⁹ A gradual increase in suspension stability with increasing surfactant concentration is observed until a critical surfactant concentration is reached. Beyond this critical value, the suspensions are observed to be indefinitely stable. A shift in mechanism from steric stabilization at low OLOA 1200 concentration (weakly stable) to electrostatic stabilization above the critical OLOA 1200 concentration (highly stable) is proposed. The proposed stabilization mechanism is consistent with viscosity and conductivity measurements.²⁹

In this work, we demonstrate the potential to provide more detailed characterization of the stability of a colloidal system using droplet-based microfluidics. This approach offers the advantages of smaller sample volumes, a higher resolution in composition space, a shorter optical path length, and it removes issues associated with particle adsorption to solid walls of sample jars. A test case of carbon black and OLOA 11000 in dodecane is used, similar to that studied by Pugh *et al.*²⁹ The goal of this work is to probe the transition regime from steric to electrosteric stabilization with greater compositional resolution than previous studies. With this alternative measurement technique, it is possible to use sedimentation experiments to expand the understanding of the underlying stabilization mechanisms. A compact device is designed that allows for production and storage of droplets containing nonpolar colloidal suspensions. Each droplet in the device contains a different suspension composition which leads to significant increases in resolution and efficiency of the process. The droplets are observed for time periods up to many months and the sedimentation levels of suspension within the droplets are characterized as a function of time. The level of sedimentation provides insight into the degree of stabilization and information about the stabilization mechanism when paired with conductivity measurements.

7.2 Experimental

7.2.1 Materials

The carbon black used in these experiments is Monarch[®] 280 powdered carbon black donated by Cabot Corporation (Boston, MA, USA). The carbon black is reported to have a primary particle diameter of 30 nm and a BET adsorption surface area of 42 m²/g.⁴³ Light scattering using a Zetasizer Nano ZS90 is performed on dilute samples of the carbon black and determined a primary particle aggregate diameter of 200 nm. The dodecane is purchased from Fisher Scientific (Pittsburgh, PA, USA) and is used as supplied.

The OLOA 11000 is reported to have a molecular weight of 950 g/mol and is donated by Chevron Oronite (San Ramon, CA, USA). The structure is reported to be a polyisobutylene chain with a succinimide linker to a triamine head group and is diluted in mineral oil.⁴¹ The product is used as received. The fluorinated FC-70 oil is purchased from Hampton Research (Aliso Viejo, CA, USA) and is used as supplied.

7.2.2 Sample Preparation

Samples of Monarch 280 Carbon Black and OLOA 11000 suspended in dodecane are produced in 50mL vials at various concentrations of OLOA 11000. The OLOA 11000 is assumed to contain 75wt% active surfactant and 25wt% mineral oil.⁴⁴ Only the mass of the active surfactant is considered while producing suspensions and the amount of mineral oil is considered to have negligible impact on the particle stability and conductivity.

Dodecane and appropriate concentrations of OLOA 11000 are mixed and allowed to sit overnight before introducing carbon black to the system. Carbon black is heated in a vacuum oven at 200°C for 4 hours and then allowed to cool under vacuum to room temperature over 3

hours to remove any absorbed water. Once dry, the carbon black powder is immediately introduced into the OLOA 11000 and dodecane solvent mixture at a fixed concentration of 3.33 g/L. Water content in the dodecane and the OLOA 11000 is not controlled. The water content in dodecane before addition of OLOA 11000 was measured by Karl-Fischer titration and determined to typically fall between 15-20 ppm. The 50mL samples are sonicated for 20 minutes at 20% intensity using a 750W Cole-Parmer Ultrasonic Processor and allowed to sit overnight. The suspensions are sonicated in an ice bath to prevent overheating. All samples are stored in a desiccator after production. Before each use, bulk samples are sonicated again for 30 minutes at 35% intensity and used immediately. Identical sample preparation was used for macroscopic and millifluidic experiments.

7.2.3 Droplet production

Droplets of fixed carbon black concentration and varying amounts of OLOA 11000 suspended in dodecane are produced according to the schematic diagram in Figure 7.1a. Surfactant concentration is reported in units of active parts OLOA 11000 to 100 parts carbon black (pph) to be consistent with previous studies.²⁹ Two 50 mL bulk suspensions of 4 pph and 10 pph are used as the inlet streams to produce a gradient of surfactant concentration across a set of droplets. Both samples are injected using Harvard Apparatus PHD2000 infusion pumps containing 3mL syringes. The 4 pph sample is considered the low OLOA 11000 concentration sample and the 10 pph sample is considered the high OLOA 11000 concentration sample. Both suspensions have a constant concentration of carbon black of 3.33 g/L. Quantitative flow rates of the dispersed phase inlets are shown in the inset of Figure 7.1a.

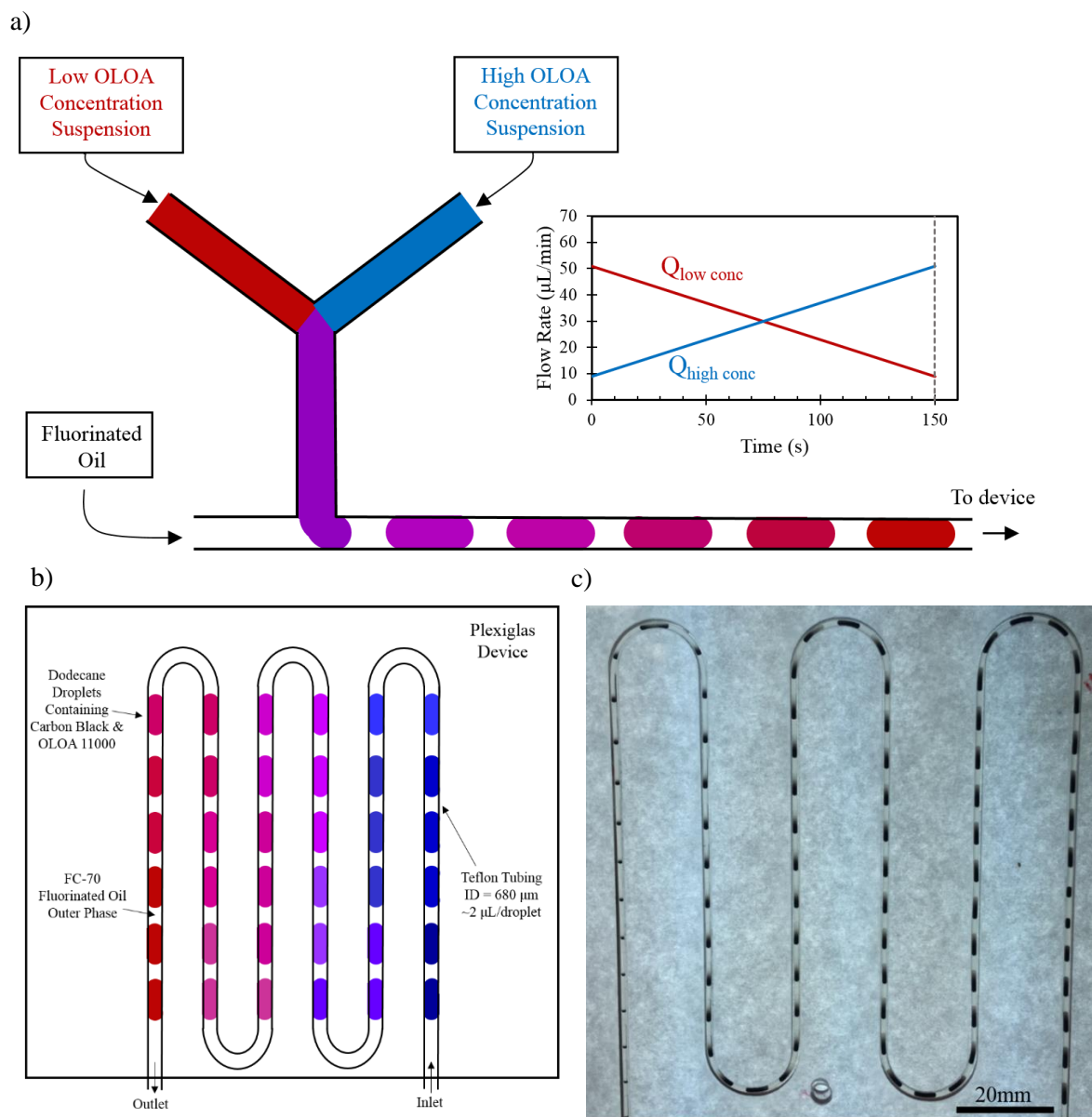


Figure 7.1: Schematic diagram and images of the experimental set up for production of droplets with a gradient in surfactant concentration. (a) Two bulk suspensions are mixed (low and high surfactant concentrations) at a starting volumetric ratio of 6:1. Droplets of dispersed suspension are produced at the T-junction in a continuous phase of fluorinated oil. Quantitative values of flow rates are shown in the inset. (b) Schematic diagram of the OLOA 11000 concentration gradient in droplets in device, colors to clarify the formation of a concentration gradient. (c) Image of device taken seven months after droplet production.

The flow rates begin in a volumetric ratio of 6:1 low OLOA 11000 concentration to high OLOA 11000 concentration samples with a constant combined flow rate of 60 $\mu\text{L}/\text{min}$. If this ratio becomes too large (>10) then pressure buildup decreases the accuracy of the droplet

concentrations. The two carbon black dispersed phases are combined using a Y-junction and flow downstream to a T-junction as seen in Figure 7.1a. At the T-junction, the dispersed phase comes in contact with the continuous outer phase fluid of fluorinated FC-70 oil and droplets of the dispersed phase are produced similar to previous micro- and millifluidic studies.⁴⁵⁻⁵⁹ The fluorinated oil is pumped into the device at a constant flow rate of 25 $\mu\text{L}/\text{min}$.

To produce accurate droplet concentrations and avoid startup effects, the droplet breakup is allowed to reach steady state by flowing at a steady continuous phase flow rate for 6 minutes. The dispersed phase flow rate during this time remains constant at a 6:1 ratio of low to high concentration feed suspensions with a combined dispersed phase flow rate of 60 $\mu\text{L}/\text{min}$ and a continuous phase flow rate of 25 $\mu\text{L}/\text{min}$. All droplets produced during this time are disregarded. After 6 minutes, the pumps are programmed to begin a linear decrease in the low concentration flow rate and a linear increase in the high concentration flow rate as shown in the graph in the inset of Figure 7.1a. Flow rates are designed such that the low concentration to high concentration flow rate ratio changes from 6:1 to 1:6 over 150 seconds, similar to previous microfluidic droplet gradient experiments.⁶⁰ Several techniques were used to verify the gradient in concentration and absolute values of concentration; these are described and details provided in Supplemental Information.

The time required for the merged dispersed phase fluid to move from the Y-junction to the T-junction is calculated at which point a small slug of additional outer phase fluid is injected to briefly disrupt droplet production and mark the first droplet in the gradient. Once the program is complete and the remaining fluid moves from the Y-junction to the T-junction, a second continuous phase slug is injected to mark the last droplet. The flow is arrested once all droplets within the gradient are moved into the viewing area of the millifluidic device, and the tubing is

clamped to prevent droplet motion. No change in droplet size is observed for months. Given the low solubility of alkanes in fluorinated oils, we do not expect drops to change size. For more details on droplet production, see the supplementary section.

7.2.4 Millifluidic droplet array

A schematic illustration of the millifluidic droplet array is shown in Figure 7.1b along with an image of the actual device in Figure 7.1c. The schematic diagram demonstrates a gradient in droplet color from red to blue depicting a change in the surfactant concentration. It is important to note that the carbon black concentration remains fixed at 3.33 g/L for all droplets in the device. For the 6:1 ratio and the number of drops in the device (~80), the difference in concentration from one drop to the next is approximately 0.1 pph.

The device is a sandwich of three layers of clear Plexiglas each 1/16” thick. The center Plexiglas layer has a serpentine track pattern laser cut into the sheet to fit the 0.680 mm I.D. PTFE tubing. The two additional Plexiglas sheets sandwich the tubing and hold the device together without deforming the tubing. Once droplets are loaded, devices are stored and imaged vertically.

7.2.5 Conductivity measurements

Conductivity of the carbon black and OLOA suspensions is measured using electrochemical impedance spectroscopy (EIS) in a 125 micron polarization cell previously used to measure the conductivity of Janus particles dispersed in dodecane.⁶¹ The cell consists of two glass slides coated with indium tin oxide ITO (Sigma-Aldrich) separated by a 125 micron polycarbonate gasket and attached to an external circuit with conductive epoxy (Allied Electronics) and attached to a VersaStat 3 (Princeton Applied Research) potentiostat with a low current interface. The same suspension preparation procedure used to make the macroscopic stability samples is used to prepare the samples for conductivity measurements. The fluid sample

is injected into the gasket between slides. The impedance is measured with a frequency response analyzer at a frequency range of 100 kHz to 10 MHz. The impedance spectra is fit to a simple circuit used previously to calculate the electrical conductivity from the fluid resistance.^{21,61,62} The electrical conductivity is measured for samples consisting of only OLOA 11000 in dodecane as well as with carbon black suspended in solutions of OLOA 11000 and dodecane at the same concentrations used in stability studies. Additionally, the carbon black particles are filtered out of solution with an anopore alumina matrix syringe filter with a pore size 0.02 μm (Whatman Anotop) and the conductivity of the remaining solution is measured.

7.2.6 Image analysis

Image analysis is used to quantitatively compare data sets. As the carbon black within a droplet aggregates and sediments, the sediment height and therefore the fraction of the droplet that appears black decreases. The normalized sediment area of each droplet is calculated to determine the relative degree of sedimentation. An example for a single droplet is shown in the top portion of Figure 7.2a. To determine the fraction of the droplet that contains carbon black, the normalized sediment area is calculated. Each image is converted to black and white using a threshold pixel intensity value of 50 (0 to 255 scale). The choice of a threshold pixel intensity value of 50 is an arbitrary choice, although numerous values between 20 and 70 are tested with 50 proving to be the optimal value. In most droplets, a diffuse sediment is observed varying from pure black sediment to clear dodecane. The chosen threshold value will define which portion of the gradient is defined as “sediment” and which portion is not. The same overall trends are observed regardless of threshold value, but the definition of the sediment height will depend on the chosen value. Since the goal is comparison across a series of droplets (surfactant concentration), an arbitrary choice of threshold does not impact the results. Once the threshold value is chosen, the analysis removes any

clear or gray portions lighter than the defined threshold value for each droplet and the resulting black sediment area is normalized by the initial size of the droplet as described by Equation 7.1,

$$A_i^* = \frac{A_i(t)}{A_{i,0}}, \quad (7.1)$$

where A_i^* is the normalized area of droplet i containing carbon black, A_i is the area of droplet i at time t containing carbon black, and $A_{i,0}$ is the initial area of droplet i , expressed as number of pixels of intensity below the threshold value. This definition returns a value between 0 and 1 for each droplet but values as high as 1.11 are obtained due to the pixel error from image-to-image reproducibility. There are approximately 300 to 400 pixels in each analyzed droplet. The image size was chosen to optimize the number of droplets per image and efficiency of the analysis. Imaging of individual drops would increase resolution but slow the analysis process significantly.

7.3 Results

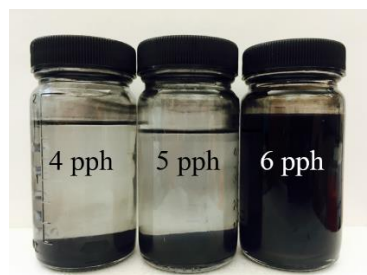
Initial stability characterization is performed by preparing 50 mL vials of carbon black suspended in dodecane at varying concentrations of the surfactant OLOA 11000. Samples at a fixed concentration of carbon black of 3.33 g/L (corresponding to a volume fraction of $\phi = 0.0019$ assuming a bulk density for carbon black of $\rho = 1.8 \text{ g/mL}^{29}$) are prepared, sonicated, and transferred to 7 mL glass vials.

Table 7.1 shows typical values of the observed sedimentation times of carbon black suspended in dodecane for different levels of added surfactant in macroscopic samples. The sedimentation time is defined as the time required for a clear supernatant layer of at least 1 mm to appear at the top of the sample in a glass vial with a 1.5 cm diameter. For surfactant concentrations below 3 parts OLOA 11000 per hundred parts carbon black (pph), the carbon black is not stabilized

and settles rapidly to form a clear solvent layer within minutes. In the 4-5 pph range, the sedimentation time is observed to increase with increasing surfactant concentration, but a clear solvent layer still forms within 1 day. At higher concentrations of surfactant, levels of 6 pph and above, the sample still appears fully dispersed after months. These results are qualitatively consistent with the observations of Pugh *et al.*^{29,30} Quantitative differences in the critical concentration for stability are likely due to differences in both the type of carbon black, the surfactant, and the co-solvent. The carbon black used by Pugh *et al.* has a lower surface area (25 m²/g compared to 42 m²/g)^{29,43} which would require less surfactant to achieve the same particle surface coverage. The detailed structural differences between OLOA 1200 and OLOA 11000 are not available, but the reported molecular weights are 1200 and 950 g/mol, respectively.⁴¹

Table 7.1: Sedimentation times of macroscopic 7mL carbon black and OLOA 11000 suspensions as a function of surfactant concentration in pph. Example images of 4 pph, 5 pph, and 6 pph samples taken after 9 months are shown on the right.

Concentration (pph)	Sedimentation Time
1	45 min
2	45 min
3	1 hr
4	3 hrs
5	24 hrs
6	>1 year
10	>1 year



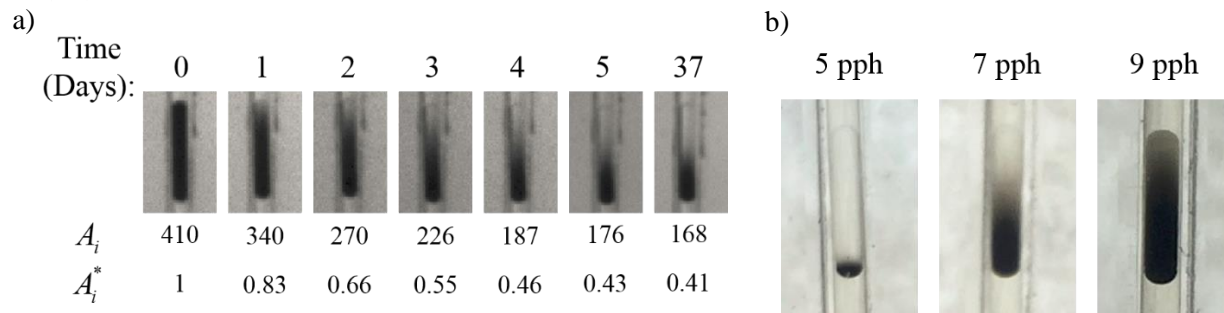


Figure 7.2: (a) Images of a single carbon black droplet (6.4pph OLOA 11000) at various time points (days) up to 37 days after initial droplet production with the sediment area (A_i) in pixels and normalized droplet area (A_i^*) displayed beneath. (b) Images of droplets at 3 different surfactant concentrations taken 7 months after droplet production.

Droplets of carbon black dispersed in dodecane with varying concentrations of OLOA 11000 in each drop are produced in the device in a continuous phase of fluorinated oil. Figure 7.2 shows the effects of both time and concentration on the visual appearance of individual droplets. Figure 7.2a shows a gradual decrease in the sediment height over the course of multiple days for a single droplet. The last two images are taken at 5 days and then at 37 days to indicate the long time behavior. As time progresses from left to right, the carbon black is observed to sediment to the bottom of the droplet, leaving a clear dodecane layer in the upper portion of the droplet. Note that the overall size of the droplet remains constant with respect to time, and a distinct interface between the solvent (dodecane) and the continuous phase fluid (fluorinated oil) is observed throughout the experiments. After about 5 days, it is observed that all droplets reach a final sediment height that remains constant with time. Lower surfactant concentrations reach a final sediment height earlier than 5 days. Figure 7.2b shows example images of droplets at concentrations of 5 pph, 7 pph, and 9 pph taken after several months to demonstrate the effects of surfactant concentration on final sediment height. These images show that the droplet containing the lowest surfactant concentration appears entirely sedimented after 7 months, the droplet containing an intermediate surfactant concentration has a clear supernatant layer but has not

sedimented into a compact layer, and the droplet containing the highest surfactant concentration obtains a slightly gray cap but otherwise appears to be fully dispersed. This demonstrates suspension behavior ranging from fully sedimented to fully dispersed after 7 months.

To quantify the effect of both concentration and time on suspension stability, each droplet within a device is imaged at multiple time points and the normalized sediment area is calculated from Equation 1. Final sediment heights ranging from 0.10 to 1, expressed in normalized area, are obtained as a function of the initial surfactant concentration and time.

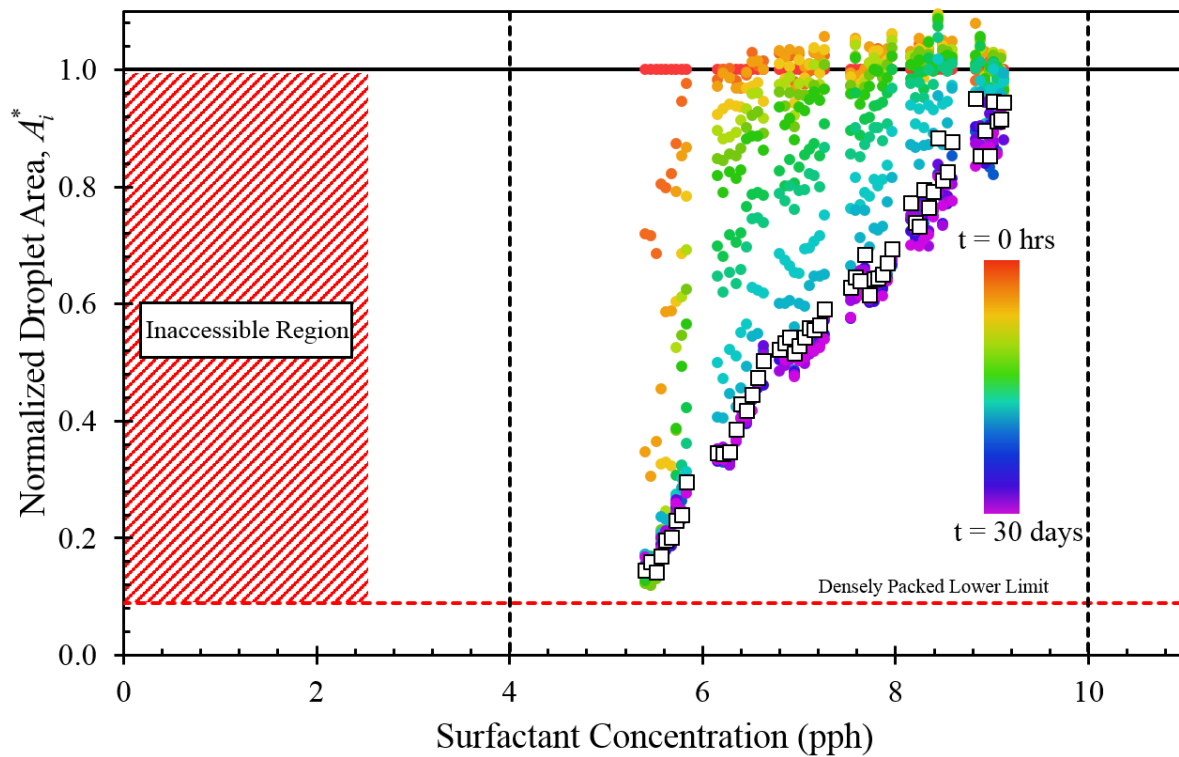


Figure 7.3: Evolution of suspension stability as a function of time and surfactant concentration. Normalized area is plotted as a function of surfactant concentration. Each color represents a different time after droplet generation up to 30 days. The open square points depict the sediment heights at 5 days which is observed to be the steady state value. The horizontal dashed red line is the densely packed lower limit that corresponds to the normalized area for a fully sedimented carbon black pellet at the bottom of a droplet. The vertical dashed black lines show the two bulk inlet sample concentrations. The inaccessible region marked at the left corresponds to sample concentrations too unstable to produce homogeneous droplets. The color scale is not linear.

Figure 7.3 shows the normalized area of the carbon black sediment as a function of surfactant concentration for a fixed carbon black concentration of 3.33 g/L. Each symbol in Figure 7.3 represents a single droplet at an instant in time. Immediately after the droplets are generated, the entire droplet is uniformly black and the normalized area has a value of 1. With time, sedimentation toward the bottom of the droplet is observed, decreasing the area that appears black. An example of this process is shown in Figure 7.2a. Images of the entire droplet array are taken at different points in time and converted to normalized area as a function of surfactant concentration. Each color indicates a different point in time up to 30 days after droplet generation. The colored bar is not to scale and is simply designed to demonstrate the order in which the time points occur. The open square points represent observations taken after 5 days of settling time. This data set is highlighted because no further change is observed after this time in any of the droplets. The vertical dashed black lines at 4 pph and 10 pph indicate the concentrations of the two bulk samples used to produce surfactant concentration gradients in the droplets. The dashed horizontal red line indicates the calculated lower limit of the normalized area assuming that the carbon black has fully sedimented to a solid packed layer. The total amount of carbon black in a typical 2 μL droplet is 6.6×10^{-6} g with a solid volume of 0.06 μL (assuming a density of $\rho = 0.110$ g/mL), corresponding to 9% of the projected droplet area assuming spherical end caps. The density value used is that of loosely flocculated powdered carbon black rather than a dense carbon black pellet and is estimated by weighing 30 mL of the powdered Monarch 280 carbon black used in these experiments. The hashed inaccessible region on the left portion of the figure indicates bulk concentrations that are so unstable that carbon black sediments during device filling, generating droplets with inhomogeneous compositions. The gaps in the data sets result from the droplets in the curved portions of the device that are not imaged or analyzed.

At a given surfactant concentration, the normalized area consistently decreases with time until a steady state value is reached. Droplets at the lowest surfactant concentrations sediment completely within hours. After five days, all droplets reach a time-independent normalized area. At each surfactant concentration, the normalized area decreases monotonically with time toward the steady state value.

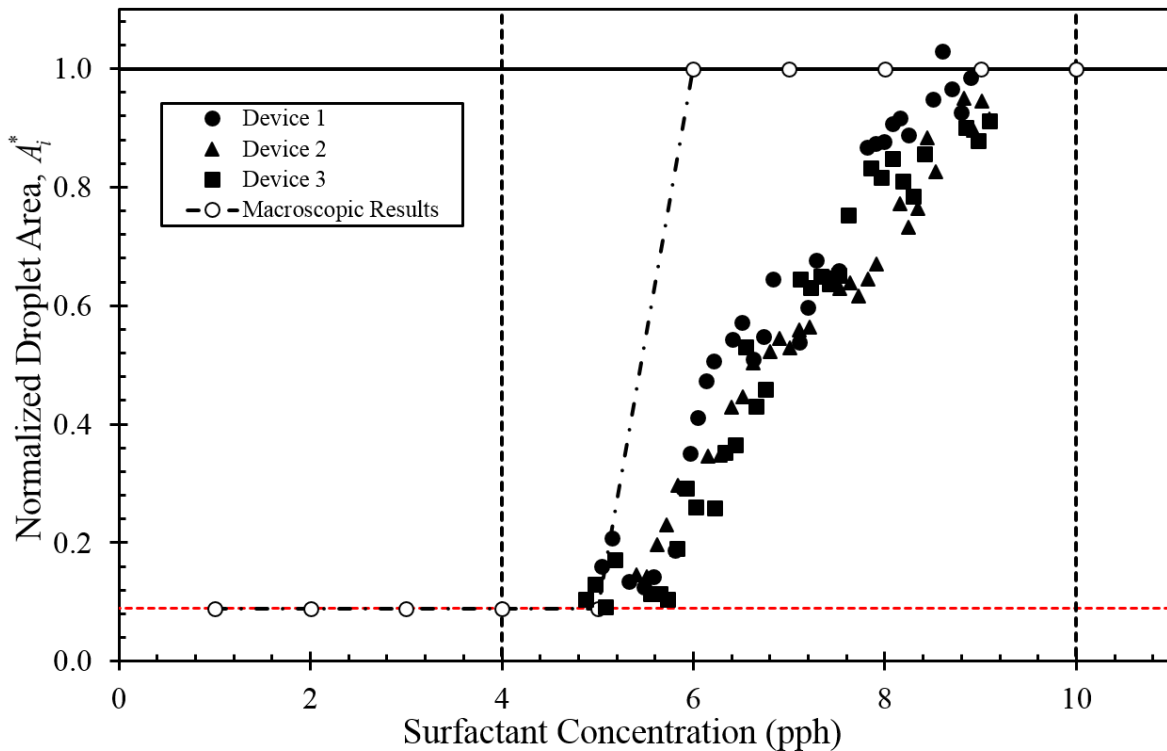


Figure 7.4: Comparison of macroscopic and millifluidic sedimentation results. Normalized droplet area is plotted versus surfactant concentration in pph. The filled symbols (circle, triangle, and square) correspond to three separate devices imaged 5 days after droplets were produced. The open points correspond to macroscopic long term results (months). The dashed horizontal red line corresponds to the densely packed lower limit and the vertical dashed black lines correspond to the bulk sample inlet concentrations.

Figure 7.4 shows the steady state, normalized sediment area as a function of surfactant concentration. Three data sets from three different devices are shown as closed symbols to demonstrate the reproducibility of the approach. The open circles represent the macroscopic

sedimentation results for comparison. For macroscopic results, fully sedimented samples are considered equivalent to the densely packed lower limit and samples showing no signs of sedimentation are considered to have a normalized droplet area of unity. The sediment height of fully sedimented macroscopic samples decreased slightly as surfactant concentration increased consistent with the previous work of Pugh *et al.*³⁰ In all millifluidic experiments, a gradual increase in normalized droplet area is observed with increasing concentration of added surfactant.

The droplets allow for a *more precise* measurement of the sedimentation process due to the small optical path lengths of the droplets ($\approx 0.5\text{mm}$), which is relevant for highly optically absorbing materials like carbon black. Measurements in droplets also have the advantage of a fluid-fluid interface rather than a solid glass wall. This avoids the issue of carbon black particles adhering to the glass walls and influencing measurement of sediment height. In droplets, carbon black dispersions with surfactant concentration from 5 pph to 6 pph are observed to be fully sedimented with a clear supernatant within five days. The surfactant is not effective in providing dispersion stability over this concentration range. At surfactant concentrations near 6 pph, the final sediment height is observed to increase with surfactant concentration. For surfactant concentrations greater than 9 pph, the dispersions appear to be stable at all times, suggesting effective long term stabilization. The results show a smooth onset of long term stability as the surfactant concentration increases from 5 pph to 9 pph, suggesting a regime that is “weakly” stable with sediment heights larger than a compact sediment. Differences between the macroscopic and millifluidic results are discussed in greater depth in the next section.

Conductivity is used to quantify the amount of OLOA 11000 adsorbed on the surface of the carbon black particles. Figure 7.5a shows measured conductivity values of OLOA 11000 in dodecane as a function of surfactant concentration; EIS is used to measure conductivity in these

low dielectric constant systems. The open triangles show conductivity of OLOA 11000 and dodecane and the closed triangles show conductivity of the same solutions after adding 3.33 g/L of carbon black added and then removing the particles with a 20 nm filter. For the filtered samples, the OLOA 11000 concentration on the horizontal axis is the mass concentration of OLOA 11000 in the original sample. At least 24 hours are allowed after sonication for the surfactant to adsorb to the particle surfaces before being filtered. The conductivity of the filtered samples is significantly lower than the conductivity before particles are added indicating the loss of surfactant to the particles. Conductivity of the filtered samples at low surfactant concentration cannot be detected within error of the instrumentation. The conductivity begins to increase above the instrument noise for samples just below 0.02wt% OLOA 11000 (added to a 3.33 g/L CB dispersion) and is observed to increase at higher surfactant concentrations. These results are used to estimate the relative amount of surfactant adsorbed to the particle surface for a given initial surfactant concentration based on depletion of surfactant from the bulk. Measured conductivity arises from the formation of inverse micelle charge carriers,²²⁻²⁶ consistent with the measured critical micelle concentration (CMC) of OLOA 11000 in dodecane of ≈ 0.005 wt%.¹⁷ Above the CMC the conductivity of OLOA 11000 in dodecane increases linearly with concentration.^{18,21} Assuming that any surfactant adsorbed to the particles will be filtered with the particles, the conductivity of the supernatant provides a measure of the concentration of nonadsorbed OLOA 11000. The conductivity difference between the particle free system and the filtered system allows for calculation of the adsorbed surfactant concentration.

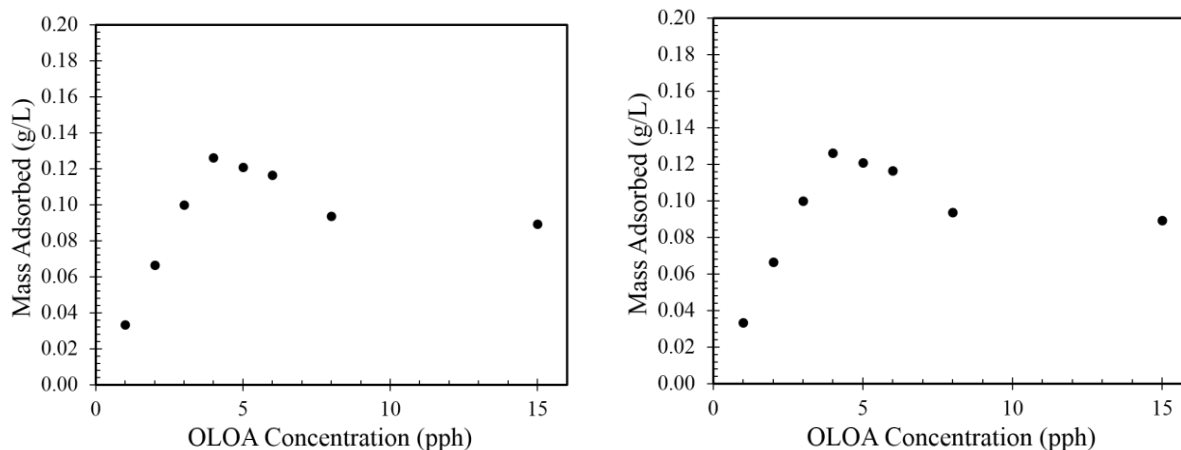


Figure 7.5: Conductivity experiments to determine OLOA 11000 adsorption onto carbon black particles. (a) Horizontal axis is the initial concentration of OLOA 11000 in wt% and the vertical axis is the conductivity of the suspension measured using EIS. The particle free samples (open points) contain dodecane and OLOA 11000 before carbon black is added to the solution. The filtered samples (closed points) contain the same amount of OLOA 11000 initially and 3.33 g/L carbon black. These samples are sonicated and particle-surfactant complexes are filtered out before conductivity is measured. (b) Conductivity difference between the pre-particle samples and the particle-filtered samples from part a is converted to adsorbed mass of surfactant. Horizontal axis is the initial concentration of the filtered samples in pph.

Figure 7.5b shows the estimated mass of OLOA 11000 adsorbed to 3.33 g/L of CB as a function of the initial OLOA 11000 concentration given in units of pph. The results indicate that OLOA 11000 does adsorb to the carbon black as expected. The adsorbed amount reaches a maximum at approximately 4pph and decreases slightly as surfactant concentration increases. The decrease at high concentrations may be a complication in the measurement of conductivity or in separating out the very stable carbon black particles which could impart additional conductivity to the suspension. For most of the relevant range, the adsorbed amount corresponds to a surface coverage of approximately 0.9 mg/m² or 1.7 nm²/molecule assuming a surface area of 42 m²/g for the carbon black. This value is close to what has been previously determined to be the surface coverage maximum.³⁰ The fact that OLOA 11000 adsorbs to carbon black suggests that it will provide steric stabilization even at low surfactant loadings. However, as argued by Pugh *et al.*, steric stabilization is not enough to provide long term stability.²⁹

Further analysis of the conductivity of the carbon black particles in suspension provides some indication of the colloidal stabilization mechanism. Figure 7.6a plots the measured conductivity of carbon black and OLOA 11000 suspensions as a function of the initial surfactant concentration. The closed triangle symbols are the conductivity values for filtered carbon black and OLOA 11000 suspensions as shown in Figure 7.5a. The open square symbols are conductivity measurements of the same samples prior to filtering the particle-surfactant complexes; note that all samples contain the same initial loading of carbon black. In this case, conductivity can arise from both the OLOA 11000 and the OLOA 11000-coated carbon black particles.

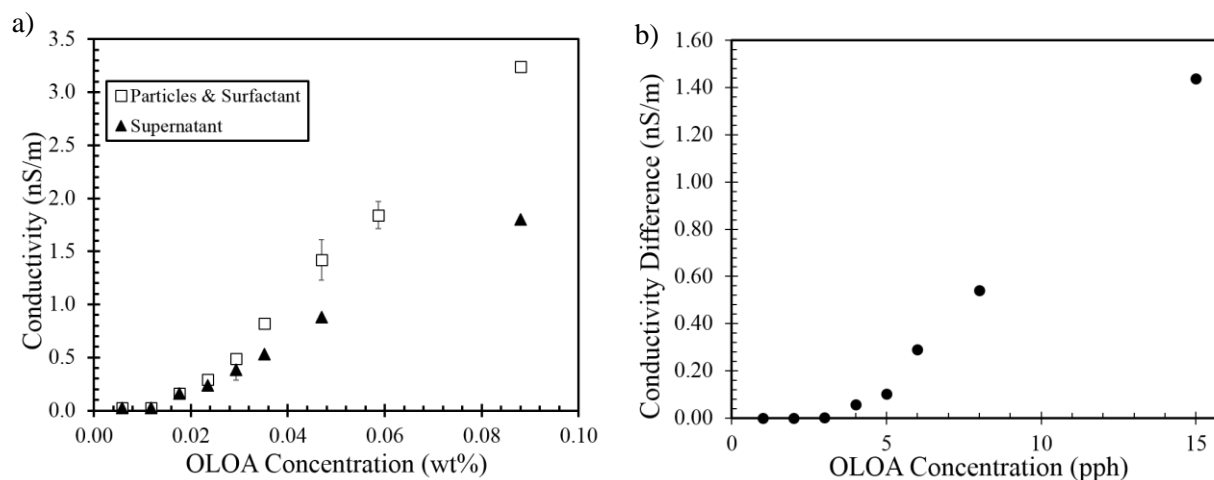


Figure 7.6: Conductivity measurements to determine conductivity increments due to particle charging. (a) The open squares are conductivity measurements of carbon black and OLOA 11000 suspensions at a given initial surfactant concentration. The black triangles are conductivity measurements of the same samples with the particle-surfactant complexes filtered out. (b) Difference in conductivity between the filtered and unfiltered samples as a function of the initial surfactant concentration in pph.

For both sample types, the conductivity of the lowest surfactant concentrations cannot be detected within error of the instrumentation. The conductivity becomes measurable at a value close to 0.02 wt% and continues to increase with increasing surfactant concentration. The conductivity of the unfiltered samples increases with surfactant concentration at a similar rate to the filtered samples until an initial surfactant concentration close to 0.03 wt%. Beyond this value,

the conductivity of the unfiltered samples increases faster than the filtered samples. The difference in measured conductivity values between the unfiltered and filtered samples is denoted by K_p . Values of K_p are displayed as a function of the OLOA 11000 surfactant concentration in pph in Figure 7.6b. Figure 7.6b shows that K_p is negligible below 4 pph, and becomes significant near a surfactant concentration of 5 to 6 pph. The conductivity difference continues to increase approximately linearly with a slope of 0.13 (nS/m)/pph as the surfactant concentration increases. For surfactant concentrations below 4 pph, the conductivity of the suspension arises from the formation of inverse micelle charge carriers. As the concentration increases, a significant contribution may arise from the OLOA 11000-coated carbon black particles themselves, which are likely acting as charged particles. This effect increases as surfactant concentration increases while the total amount of carbon black remains fixed.

7.4 Discussion

The macroscopic results from Table 7.1 show increasing sedimentation times for sample concentrations ranging from 1 to 5 pph. In millifluidic devices, samples ranging from 1 to 3 pph cannot be used to generate homogenous droplets due to rapid particle aggregation, and 4 pph is the lowest surfactant concentration that is stable on the timescale of filling the device. These results imply that when the surfactant concentration is too low, the suspension is highly unstable, but as the surfactant concentration increases the system becomes weakly stabilized. The results in Figure 7.5b demonstrate that almost all of the free OLOA 11000 adsorbs to the particle surfaces until an OLOA 11000 concentration of 4pph is reached (0.033 g/L is equivalent to 1pph). Beyond this concentration, the adsorbed mass levels off and may decrease slightly with increasing OLOA 11000 concentration. This suggests that the particle surfaces become saturated with OLOA 11000 at a concentration near 4pph and the remaining surfactant is dispersed in the bulk. Revisiting Table

7.1, the sedimentation times are observed to increase for concentrations from 1 to 4 pph while Figure 7.5b suggests nearly all of the available surfactant is adsorbing to the particle surface. This implies that the adsorbed surfactant molecules are providing some steric stability to the particles leading to increased sedimentation times, but the steric stabilization is insufficient to induce long term stabilization. Pugh *et al.* supported this claim by estimating the maximum carbon black particle size that could be sterically stabilized by the OLOA 11000.²⁹ Using a Hamaker constant for carbon black of 2.8×10^{-13} erg and an OLOA 1200 film thickness of 5nm, the largest stabilized particle radius is predicted to be 70 nm. Since the OLOA 11000 used here likely has a lower film thickness (lower molecular weight), we would predict an even smaller value for the largest particle size that can be stabilized.

Table 7.1 shows that OLOA 11000 concentrations of 6 pph and above are not observed to sediment macroscopically within the timescales considered to date. Figure 7.4 compares the macroscopic and millifluidic sedimentation observations and demonstrates the differences between experiments for concentrations of 6 pph to 9 pph. Within this range, the macroscopic samples show no sign of sedimentation, but the millifluidic droplets exhibit a measureable degree of sedimentation and an increase in sediment height with increasing surfactant concentration. Preliminary light scattering measurements are conducted to determine the effects of surfactant concentration and time on the particle size distribution of macroscopic samples. Average aggregate size in the surfactant concentration range of 6 pph to 10 pph varies between 100 nm and 400 nm with larger particles sizes at generally lower surfactant concentration indicating aggregation and sedimentation. However, these results did not show a systematic trend and a more in depth light scattering analysis is required. In addition, the size distributions on the macroscopic scale may not relate directly to the size distributions in the droplets due to significantly shorter distance for the

aggregates to sediment. This reinforces the idea of using the millifluidic technique to as a way to efficiently probe the underlying effects of an additive and determine a region of interest for further in depth studies.

The differences between the macroscopic and millifluidic results are likely due to a combination of path length differences and the fluid-fluid interface in the millifluidic device, indicating a significant advantage for the millifluidic approach. Sedimentation is still occurring macroscopically, but the centimeter length-scale vials are large enough that low concentrations of highly light absorbing carbon black are too turbid to see through, while the 700 μm tubing is thin enough to allow light to pass and enable sedimentation to be detected. We would expect a similar advantage for a highly scattering material like TiO_2 . In addition, adsorption of carbon black particles and aggregates at the glass-fluid interface of the jars hinders quantification of sedimentation. The detailed information gained from the millifluidic experiments suggests a much smoother onset of stabilization relative to the macroscopic tests which implies a smooth transition from steric to electrostatic stabilization compared to the previously observed sharp transition.

Figure 7.6 shows the conductivity results for OLOA 11000 suspensions containing carbon black and suspensions with carbon black removed by filtration. For the filtered samples, the only component contributing to the conductivity is the formation of inverse micelle charge carriers.²²⁻
²⁶ The exact critical micelle concentration (CMC) of inverse micelles of OLOA 11000 is not known due to the low concentration at which the micelles form, but it has been previously reported to be near 0.005 wt%.¹⁷ The unfiltered samples should have the same quantity of inverse micelles in the bulk, but contain additional surfactant-particle complexes. For concentrations from 1 to 4 pph, where it has been argued that almost all of the available surfactant is adsorbing to the particle surface, there is no difference in conductivity between the two data sets within experimental error.

At a starting concentration of 5pph, beyond the particle surface saturation concentration, K_p attains a small but measurable value. At 6pph, K_p becomes larger and continues to increase as surfactant concentration increases. The only difference between the filtered and unfiltered samples is the presence of the surfactant-particle complexes. This implies that the additional charge in the unfiltered samples is due to the complexes, suggesting that the particles have attained charge at moderate surfactant concentrations. If this is the case, then as more surfactant is added above 6pph, the particle surface charge density will increase causing an increase in the measured conductivity. This provides a mechanism for the increase in K_p with increase in OLOA 11000 concentration similar to the observed increase of the conductivity increment in dielectric spectroscopy of charged particle suspensions.⁶³ We have attempted to use this conductivity difference to infer a zeta potential on the carbon black particles. However, this calculation for the conductivity increment of concentrated dispersions is not trivial due to the polarization of the electrostatic double layer around the particles. A cell model describes the frequency-dependent conductivity of concentrated dispersions of spherical colloidal particles and can be used to solve for the zeta potential of the system from the conductivity data.⁶⁴ However, for our polydisperse system with some aggregation and poorly characterized, likely heterogeneous, surface chemistry and finite particle size, we were unable to extract unambiguous or reliable estimates of zeta potential. While carbon black particles are known to form percolating conductive networks, it is not believed to be the case in this system due to the increase of particle stability with surfactant concentration, providing unfavorable conditions for percolation.⁶⁵

The results from Figure 7.6 imply that electrostatic stabilization is not significant below 4 pph and begins to have a significant effect at concentrations of 6 pph and above. A surfactant concentration of 6 pph is the lowest concentration at which macroscopic sedimentation is not

observed and is the lowest concentration at which the millifluidic sediment height is observed to increase. These observations taken together suggest that for concentrations below 4 pph, the system obtains increasing but weak steric stabilization that reaches a maximum at 4 pph. At concentrations of 5 pph and above, the system increases in electrostatic stability, and 6 pph is the first concentration exhibiting a strong enough electrostatic effect to obtain long term macroscopic stability. The millifluidic experiments show that the sediment height, and therefore electrostatic stability, increases gradually from 6 to 9 pph, in contrast to the sudden change in macroscopic samples between 5 and 6 pph. The steric to electrostatic transition is consistent with the hypothesis proposed by Fowkes, however the onset of electrostatic stabilization appears to be more gradual relative to the previously observed sharp on-off effect.²⁹

7.5 Conclusions

We have developed a novel millifluidic sedimentation droplet-based device to revisit stability of particles in nonpolar solvents. The results obtained with the millifluidic device demonstrate a much broader transition region from steric to electrostatic stabilization of carbon black particles with OLOA 11000 in dodecane than was previously observed.^{29,30} The benefits of the millifluidic approach arise from the significantly smaller path lengths and fluid-fluid interfaces between the droplet phase and the continuous fluid. This combination allows for sedimentation detection previously unavailable on the macroscopic scale. The sedimentation results are paired with conductivity measurements to help develop a full understanding of the transition from steric to electrostatic stabilization as a function of surfactant concentration. Depletion studies are used to determine the concentration range in which steric stabilization contributes to particle stability based on the adsorbed surfactant concentrations. Additional conductivity measurements are used to determine the concentration range in which the particles become charged and electrostatic

effects begin to play a role in stability. Particle charging in nonpolar solvents has been observed in a number of particle-solvent systems.^{12,14,23,27-34} This work provides affirmation of the assumed steric to electrostatic transition and further insight into the slow degree by which the transition occurs, suggesting that electrostatic interactions in the system arise gradually as opposed to an “on-off” effect. Further experiments are being conducted to determine the effects of temperature, particle concentration, mixed surfactant, and water on the stability of the carbon black system.

7.6 References

1. Morrison ID. Electrical charges in nonaqueous media. *Colloids Surfaces A Physicochem Eng Asp.* 1993;71(1):1-37.
2. Smith GN, Eastoe J. Controlling colloid charge in nonpolar liquids with surfactants. *Phys Chem Chem Phys.* 2013;15:424-439.
3. Russel WB, Saville DA, Schowalter WR. *Colloidal Dispersions.* 1st ed. Cambridge: Cambridge University Press; 1989.
4. Yu W, Xie H. A review on nanofluids : preparation, stability mechanisms, and applications. *J Nanomater.* 2012;2012:1-17.
5. Jiang L, Gao L, Sun J. Production of aqueous colloidal dispersions of carbon nanotubes. *J Colloid Interface Sci.* 2003;260:89-94.
6. Grasso D, Subramaniam K, Butkus M, Strevett K, Bergendahl J. A review of non-DLVO interactions in environmental colloidal systems. *Views Environ Sci Bio/Technology.* 2002;1:17-38.
7. Kashyap S, Mishra S, Behera SK. Aqueous colloidal stability of graphene oxide and chemically converted graphene. *J Nanoparticles.* 2014;2014:1-6.
8. Greenwood R. Review of the measurement of zeta potentials in concentrated aqueous suspensions using electroacoustics. *Adv Colloid Interface Sci.* 2003;106(3):55-81.
9. Fazio S, Guzm J, Colomer MT, Salomoni A, Moreno R. Colloidal stability of nanosized titania aqueous suspensions. *J Eur Ceram Soc.* 2008;28:2171-2176.
10. Araki J, Wada M, Kuga S. Steric stabilization of a cellulose microcrystal suspension by poly (ethylene glycol) grafting. *Langmuir.* 2001;(17):21-27.
11. Zhulina EB, Borisov O V, Priamitsyn VA. Theory of steric stabilization of colloid dispersions by grafted polymers. *J Colloid Interface Sci.* 1990;137(2):495-511.
12. Hsu MF, Dufresne ER, Weitz DA. Charge stabilization in nonpolar solvents. *Langmuir.* 2005;21(11):4881-4887.
13. Briscoe WH, Horn RG. Direct measurement of surface forces due to charging of solids immersed in a nonpolar liquid. *Langmuir.* 2002;18(10):3945-3956.
14. Sainis SK, Germain V, Mejean CO, Dufresne ER. Electrostatic interactions of colloidal particles in nonpolar solvents: Role of surface chemistry and charge control agents. *Langmuir.* 2008;24(4):1160-1164.
15. Espinosa CE, Guo Q, Singh V, Behrens SH. Particle charging and charge screening in nonpolar dispersions with nonionic surfactants. *Langmuir.* 2010;26(22):16941-16948.
16. Gacek M, Bergsman D, Michor E, Berg JC. Effects of trace water on charging of silica particles dispersed in a nonpolar medium. *Langmuir.* 2012;28(31):11633-11638.

17. Strubbe F, Verschueren ARM, Schlangen LJM, Beunis F, Neyts K. Generation current of charged micelles in nonaqueous liquids: Measurements and simulations. *J Colloid Interface Sci.* 2006;300(1):396-403.
18. Prieve DC, Hoggard JD, Fu R, Sides PJ, Bethea R. Two independent measurements of debye lengths in doped nonpolar liquids. *Langmuir.* 2008;24(4):1120-1132.
19. Guo Q, Singh V, Behrens SH. Electric charging in nonpolar liquids because of nonionizable surfactants. *Langmuir.* 2010;26(5):3203-3207.
20. Karvar M, Strubbe F, Beunis F, Kemp R, Smith N, Goulding M. Investigation of various types of inverse micelles in nonpolar liquids using transient current measurements. *Langmuir.* 2014;30:12138-12143.
21. Yezer BA, Khair AS, Sides PJ, Prieve DC. Use of electrochemical impedance spectroscopy to determine double-layer capacitance in doped nonpolar liquids. *J Colloid Interface Sci.* 2015;449:2-12.
22. Beunis F, Strubbe F, Karvar M, Drobchak O, Brans T, Neyts K. Inverse micelles as charge carriers in nonpolar liquids: Characterization with current measurements. *Curr Opin Colloid Interface Sci.* 2013;18(2):129-136.
23. Poovarodom S, Berg JC. Effect of particle and surfactant acid-base properties on charging of colloids in apolar media. *J Colloid Interface Sci.* 2010;346(2):370-377.
24. Roberts GS, Sanchez R, Kemp R, Wood T, Bartlett P. Electrostatic charging of nonpolar colloids by reverse micelles. *Langmuir.* 2008;24(13):6530-6541.
25. Dukhin AS, Goetz PJ. How non-ionic “electrically neutral” surfactants enhance electrical conductivity and ion stability in non-polar liquids. *J Electroanal Chem.* 2006;588:44-50.
26. Karvar M, Strubbe F, Beunis F, et al. Charging dynamics of aerosol OT inverse micelles. *Langmuir.* 2015;31:10939-10945.
27. Kemp R, Sanchez R, Mutch KJ, Bartlett P. Nanoparticle charge control in nonpolar liquids : Insights from small-angle neutron scattering and microelectrophoresis. *Langmuir.* 2010;26(10):6967-6976.
28. Sainis SK, Germain V, Dufresne ER. Statistics of particle trajectories at short time intervals reveal fN-scale colloidal forces. *Phys Rev Lett.* 2007;18303(1):1-4.
29. Pugh, R J; Matasunaga, T; Fowkes FM. The dispersibility and stability of carbon black in media of low dielectric constant. 1. Electrostatic and steric contributions to colloidal stability. *Colloids and Surfaces.* 1983;7:183-207.
30. Pugh, Robert J; Fowkes FM. The dispersibility and stability of carbon black in media of low dielectric constant. 2. Sedimentation volume of concentrated dispersions, adsorption and surface calorimetry studies. 1984;9:33-46.
31. Kim J, Garoff S, Anderson JL, Schlangen LJM. Movement of colloidal particles in two-dimensional electric fields. *Langmuir.* 2005;21(24):10941-10947.

32. Keir RI, Suparno, Thomas JC. Charging Behavior in the Silica/Aerosol OT/Decane System. *Langmuir*. 2002;18(5):1463-1465.
33. Poovarodom S, Poovarodom S, Berg JC. Effect of alkyl functionalization on charging of colloidal silica in apolar media. *J Colloid Interface Sci*. 2010;351(2):415-420. doi:10.1016/j.jcis.2010.07.058.
34. Gacek M, Brooks G, Berg JC. Characterization of mineral oxide charging in apolar media. *Langmuir*. 2012;28:3032-3036.
35. Lyklema J. Principles of the stability non-aqueous media of lyophobic colloidal dispersions in nonaqueous media. *Adv Colloid Interface Sci*. 1968;2:65-114.
36. McGown DNL, Parfitt GD. Stability of non-aqueous dispersions. *Kolloid-Z Z Polym*. 1967;219:48-51.
37. Morrison ID. Criterion for electrostatic stability of dispersions at low ionic strength. *Langmuir*. 1991;7(9):1920-1922.
38. Albers W, Overbeek JG. The correlation between electrokinetic potential and stability. *J Colloid Sci*. 1959;14:501-509.
39. Feat GR, Levine S. The double-layer interaction of two charged colloidal spherical particles of a concentrated dispersion in a medium of low dielectric constant. *J Colloid Interface Sci*. 1976;54(1):34-44.
40. Liu T, Jia S, Kowalewski T, Matyjaszewski K, Casado-portilla R, Belmont J. Grafting poly(n-butyl acrylate) from a functionalized carbon black surface by atom transfer radical polymerization. *Langmuir*. 2003;19:6342-6345.
41. Parent ME, Yang J, Jeon Y, et al. Influence of surfactant structure on reverse micelle size and charge for nonpolar electrophoretic inks. *Langmuir*. 2011;27:11845-11851.
42. Singh BP, Menchavez R, Takai C, Fuji M, Takahashi M. Stability of dispersions of colloidal alumina particles in aqueous suspensions. *J Colloid Interface Sci*. 2005;291:181-186.
43. Lu S, Chung DDL. Viscoelastic behavior of carbon black and its relationship with the aggregate size. *Carbon N Y*. 2013;60:346-355.
44. Kornilovitch P, Jeon Y, Kornilovitch P, Jeon Y. Transient electrophoretic current in a nonpolar solvent. *J Appl Phys*. 2011;109(6).
45. Nisisako T, Torii T, Higuchi T. Droplet formation in a microchannel network. *Lab Chip*. 2002;2:24-26.
46. van der Graaf S, Nisisako T, Schroe CGPH, van der Sman RGM, Boom RM. Lattice boltzmann simulations of droplet formation in a T-shaped microchannel. *Langmuir*. 2006;22(15):4144-4152.
47. Christopher GF, Anna SL. Microfluidic methods for generating continuous droplet streams. *J Phys D Appl Phys*. 2007;40(19):319-336.

48. Garstecki P, Fuerstman MJ, Stone A, Whitesides GM. Formation of droplets and bubbles in a microfluidic T-junction - scaling and mechanism of break-up. *Lab Chip*. 2006;6:437-446.
49. Christopher GF, Noharuddin NN, Taylor JA, Anna SL. Experimental observations of the squeezing-to-dripping transition in T-shaped microfluidic junctions. *Phys Rev E*. 2008;78:1-12.
50. Nelson CW. Probing the phase behavior of complex fluids using microliter droplet reactors. (*Unpublished Dr Diss*. 2016).
51. Engl W, Backov R, Panizza P. Controlled production of emulsions and particles by milli- and microfluidic techniques. *Curr Opin Colloid Interface Sci*. 2008;13:206-216.
52. Trivedi V, Doshi A, Kurup GK, Ereifej E, Vandevord PJ, Basu AS. A modular approach for the generation, storage, mixing, and detection of droplet libraries for high throughput screening. *Lab Chip*. 2010;10(18):2433-2442.
53. Lorber N, Pavageau B, Mignard E, Laboratoire UMR, Schweitzer AA. Droplet-based millifluidics as a new miniaturized tool to investigate polymerization reactions. *Macromolecules*. 2010;43:5524-5529.
54. Lorber N, Sarrazin F, Guillot P, et al. Some recent advances in the design and the use of miniaturized droplet-based continuous process : Applications in chemistry and high-pressure microflows. *Lab Chip*. 2011;11:779-787.
55. Baraban L, Bertholle F, Salverda MLM, et al. Millifluidic droplet analyser for microbiology. *Lab Chip*. 2011;11:4057-4062.
56. Wang WS, Vanapalli SA. Millifluidics as a simple tool to optimize droplet networks : Case study on drop traffic in a bifurcated loop. *Biomicrofluidics*. 2014;8(64111):1-23.
57. Lourdes M, Baños M De, Carrier O, Bouriat P, Broseta D. Droplet-based millifluidics as a new tool to investigate hydrate crystallization : Insights into the memory effect. *Chem Eng Sci*. 2015;123:564-572.
58. Boitard L, Cottinet D, Bremond N, Baudry J, Bibette J. Growing microbes in millifluidic droplets. *Eng Life Sci*. 2015;15:318-326.
59. Feuerborn A, Prastowo A, Cook PR, Walsh E. Merging drops in a Teflon tube, and transferring fluid between them, illustrated by protein crystallization and drug screening. *Lab Chip*. 2015;15:3766-3775.
60. Schultz KM, Furst EM. High-throughput rheology in a microfluidic device. *Lab Chip*. 2011;11:3802-3809.
61. Lee J, Yezer BA, Prieve DC, Behrens SH. Janus particles in a nonpolar solvent. *Langmuir*. 2016;32:3095-3099.
62. Yezer BA, Khair AS, Sides PJ, Prieve DC. Determination of charge carrier concentration in doped nonpolar liquids by impedance spectroscopy in the presence of charge adsorption. *J Colloid Interface Sci*. 2016;469:325-337.

63. Zukoski CF, Saville DA. An experimental test of electrokinetic theory using measurements of electrophoretic mobility and electrical conductivity. *J Colloid Interface Sci.* 1985;107(2):322-333.
64. Bradshaw-Hajek BH, Miklavcic SJ, White LR. Frequency-dependent electrical conductivity of concentrated dispersions of spherical colloidal particles. *Langmuir.* 2008;24(9):4512-4522.
65. Schueler R, Petermann J, Schulte K, Wentzel H. Agglomeration and electrical percolation behavior of carbon black dispersed in epoxy resin. *J Appl Polym Sci.* 1996:1741-1746.

Chapter 8. Small Angle Neutron Scattering on Millifluidic Droplets (SANSDrop) to Characterize Fluid Structure over Large Composition Space

8.1 Introduction

Determining structure and behavior of colloidal suspensions is a fundamental characterization and necessary to fully understand colloidal systems. Characterization of these systems is important for industrial applications including coatings, formulations, personal care products, oil and gas, and pharmaceuticals. Excellent, well-studied classification techniques include non-invasive scattering measurements, specifically neutron scattering and X-ray scattering. These scattering techniques can provide insight and quantification into the size and fluid structure of complex colloidal materials.

Small angle neutron scattering (SANS) is a common neutron scattering experiment typically performed on complex fluids or soft materials to understand structural information. The length scale most appropriate for current SANS capabilities is in the range of singles to hundreds of nanometers. This size range covers most colloidal systems including micellar structures,¹⁻⁴ polymers,⁵⁻⁷ particles,^{8,9} proteins,¹⁰⁻¹³ and surfactant-based systems.^{14,15} The advantages of SANS over small angle X-ray scattering (SAXS) are the ability to contrast match materials, larger penetration depth, and no polarization of electron clouds or electrostatic interaction with sample material. The major drawback of SANS compared with SAXS is the orders of magnitude lower flux intensity, resulting in longer experiment times (minutes to hours) compared with X-rays (seconds). Both techniques provide fluid structure information from scattering results for length scales too small for optical microscopy detection.

Millifluidic droplets provide an excellent tool in combination with scattering experiments to perform high composition resolution scattering measurements with less sample material and more automation. Millifluidic droplets are droplets on the millimeter length scale with $O(\mu\text{L})$ of volume per droplet. Typical path lengths are on the order of several millimeters, similar to bulk SAXS and SANS sample path lengths. Millifluidic experiments have been previously conducted to investigate chemical reactions,^{16–20} biological applications,^{21–28} crystallization,^{29,30} droplet flow behavior,^{31–33} and particle synthesis.^{34–42} In line, non-intrusive measurements have been previously performed on millifluidic devices including optical absorbance measurements,²⁰ fluorescence measurements,²⁸ infrared thermography,¹⁹ and X-ray absorbance spectroscopy⁴³ as well as intrusive methods including microwave heating²⁷ and UV exposure^{36,39} to control reaction initiation in droplets. However, neither SANS nor SAXS have been currently performed on millifluidic droplets to the authors' knowledge.

In this work, we aim to combine droplet-based millifluidic experiments and SANS to obtain full scattering patterns of individual droplets with good signal to noise ratio. Concentration gradients in droplet composition are introduced to produce droplets across boundary lines and monitor scattering peak intensity and structure as phase boundaries are approached. We perform preliminary experiments to verify capabilities of the device and demonstrate collection and registry of unique droplet scattering patterns for a continuous droplet train by performing a droplet-based contrast match experiment of silica nanoparticles in $\text{H}_2\text{O}/\text{D}_2\text{O}$ mixtures. The goal is to optimize droplet scattering time to provide reasonable signal intensity while maximizing number of droplets per time to maximize composition resolution. After preliminary experiments, experiments are expanded to more complex particle-based systems to characterize complete phase behavior in single pre-programmed experiments.

8.2 Materials and Methods

8.2.1 Sample preparation

50 cSt silicone oil is obtained from Gelest Inc. (Morrisville, PA). Deionized water (18.2 M Ω -cm) is used for all H₂O solutions and D₂O (99.9%) is purchased from Cambridge Isotope Laboratories (Tewksbury, MA). 40 wt/wt% Ludox HS-40 and 34 wt/wt% Ludox TMA silica particles are purchased from Sigma-Aldrich (St. Louis, MO) and used as received. Sodium chloride is purchased from Alfa Aesar (Ward Hill, MA), 2-butoxyethanol (C₄E₁, 99%) is purchased from TCI America (Portland, OR) and 600 g/mol PEO is purchased from Sigma-Aldrich.

For contrast match experiments, 40 wt/wt% stock Ludox HS-40 is mixed in 1 part : 10 parts by volume with pure H₂O and pure D₂O resulting in 1.9 vol% Ludox HS-40 suspensions. The H₂O rich sample contains 0% D₂O solvent by volume and the D₂O rich sample contains 92.6% D₂O solvent by volume. Silica samples are sonicated for 20 minutes prior to use.

8.2.2 Neutron scattering conditions

Neutron scattering is performed at the NIST Center for Neutron Research (NCNR) in Gaithersburgh, MD. Experiments are performed on the 10 m NG-B SANS instrument. Results are collected at a neutron wavelength of 5 Å at a detector distance of 1.1 m to collect high q scattering and a neutron wavelength of 8 Å at a 5.2 m or 4.6 m detector distance for low q scattering for the contrast matching and gauntlet experiments respectively. An overall q range of 0.003 to 0.67 1/Å is available with these conditions. A 6.3 mm x 1 mm slit is used to focus neutrons through a 10'' quartz capillary with a 2 mm ID and 3 mm OD.

8.2.3 Device setup

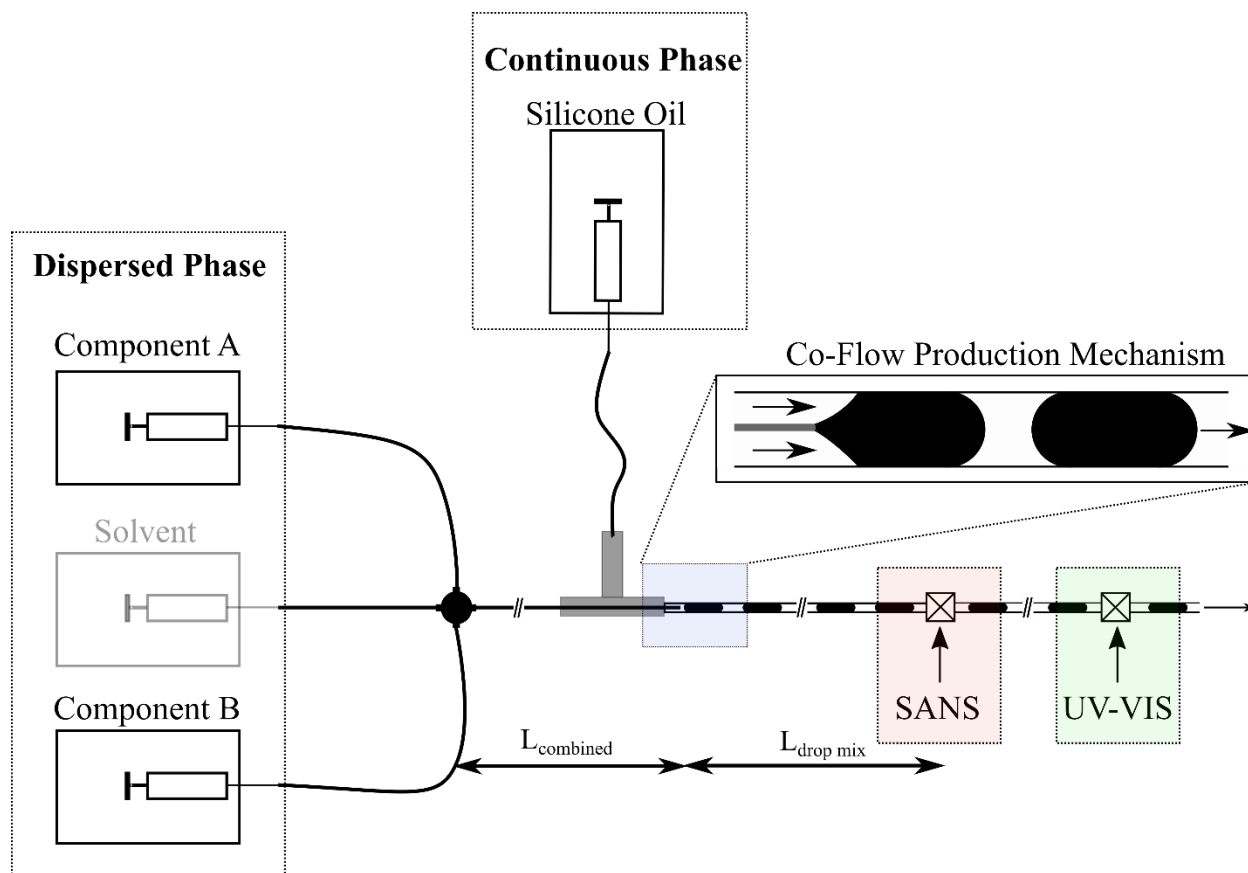


Figure 8.1: Schematic diagram of millifluidic SANSDrop device. Two to three dispersed phase pumps are automatically controlled by preprogrammed commands. A silicone oil continuous phase meets the mixed dispersed phase at the droplet production sites and droplets are produced via a co-flow mechanism. Droplets flow through an in-line neutron beam source followed by a UV-Vis spectrophotometer and scattering and absorbance are continuously measured.

Figure 8.1 shows a schematic representation of the millifluidic neutron scattering device setup.

Droplets are produced using co-flow droplet production, demonstrated in the figure. Between two and three dispersed phase syringes are combined based on the desired experimental composition control. Two syringes provide composition control back and forth along a single gradient line while three syringes provide full three dimensional composition control. The dispersed phase components meet at a 4-point fluidic junction and flow together 10.5 cm

(denoted as L_{combined} in Figure 8.1) towards the droplet production site. Reynolds numbers are low ($O[1]$) leading to controlled, laminar flow in this section.

Simultaneously, a silicone oil continuous phase is flowed through a T-junction and surround the inner capillary containing the dispersed phase mixture. Droplets are pinched at the droplet production site by a dripping production mechanism via co-flow.⁴⁴ Once produced, droplets are flowed at a steady flowrate along the 2mm quartz capillary. Droplets in this region are mixed due to the induced eddy flows during droplet pinching⁴⁵ and the recirculation patterns within a droplet.⁴⁶ Neutron scattering is positioned orthogonally to the capillary approximately 9.0 cm past the droplet production site as shown in Figure 8.1 and a detector is placed behind the neutron beam. After passing through the neutron source, droplets continue to flow for 9.75 cm where a UV-Vis optical absorbance measurement is recorded, measuring absorbance at $\lambda = 525$ nm every second to determine droplet quality. Droplets at the end of the capillary are flowed directly into a waste collection bin.

8.2.4 Contrast match experiment

For the contrast match experiment, three pumps are used to create a gradient in H_2O/D_2O ratio across droplet samples. One pump (Braintree Scientific Single Syringe Pump) is used to flow a continuous 50 cSt silicone oil outer phase fluid from a 10 mL syringe at a constant flow rate of 5 $\mu\text{L}/\text{min}$. The remaining two pumps (Harvard Apparatus PHD2000) contain the H_2O rich and D_2O rich 1.9 vol% Ludox suspensions from 5 mL syringes with a constant combined flow rate of 30 $\mu\text{L}/\text{min}$. Aqueous droplets of the Ludox system are produced in the continuous silicone oil outer phase via co-flow.⁴⁴ A 2 mm inner diameter quartz capillary is used for droplet production.

The maximum flow rate ratio between the H₂O rich and D₂O rich pumps is a value of 5, chosen to avoid issues with incorrect droplet concentrations at high flow rate ratios discussed in Chapter 3. This flow rate ratio creates a range of D₂O concentration in droplets from 15% to 77 vol% D₂O. Droplets are initially produced at a constant concentration of 15% D₂O for 20 minutes to achieve steady state. Once steady state is reached, a linear gradient in D₂O composition is performed across the droplet train. Pump flow rates are programmed to vary from 5:1 to 1:5 for the H₂O rich: D₂O rich flow rate ratio for a 30 µL/min constant combined flow rate. Finally, droplets are produced for 20 minutes at a constant composition of 77 vol% D₂O to allow time for the droplets to reach the beam while maintaining a constant flow rate. This procedure is described more in depth in Chapter 3.

8.2.5 Gauntlet experiment

With three independently controlled inlet pumps, precise composition control within the droplets is possible in any direction and a three component phase diagram can be fully explored. Figure 8.2 describes one possible approach to mapping large composition space with a single pre-programmed droplet experiment. Further details on the experimental procedure can be found in Chapter 3.

In this experiment, three independently controlled inlet syringe pumps combine to produce droplets at a fixed total flow rate. A gradient in concentration for a single component is introduced across a droplet train while a secondary component concentration is held fixed. This is possible by decreasing the flow rate of a third pure solvent component and proportionally increasing the flow rate of the varying component. The combined flow rate remains fixed at 20 µL/min and at any instance only two flow rates are varying while one remains constant. Figure 8.2a-c shows programmed flow rates of the three independently controlled syringes.

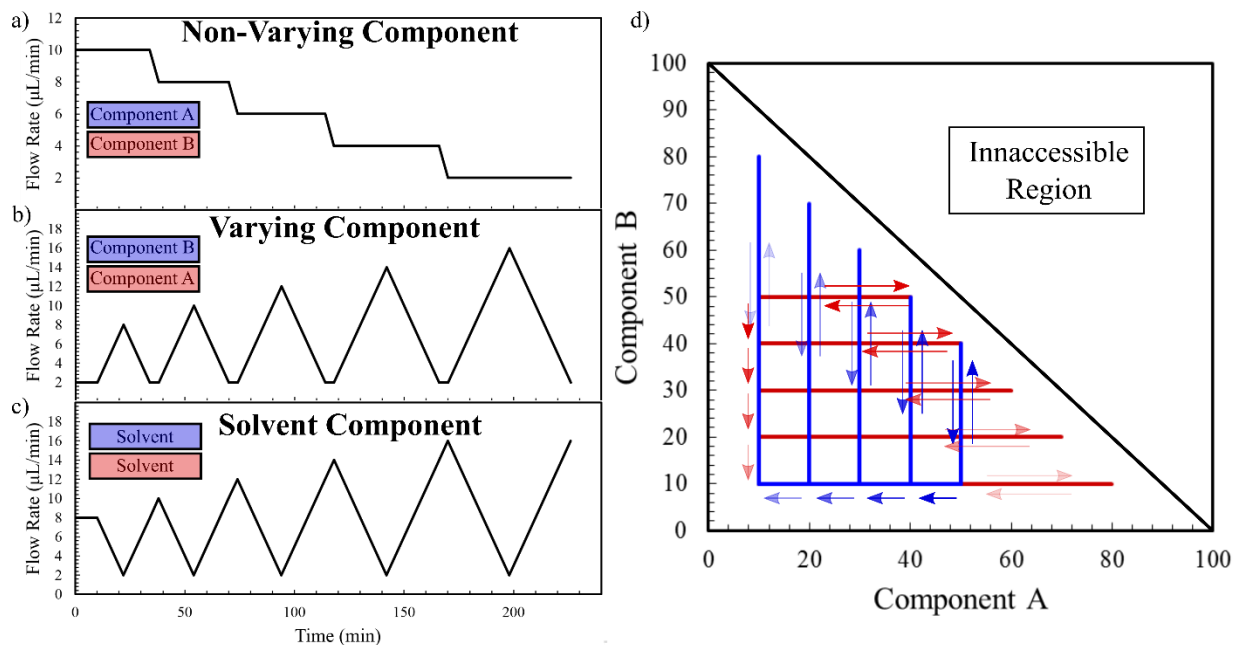


Figure 8.2: (a-c) Programmed pump flow rates for three independently controlled syringe pumps corresponding to a (a) non-varying component, (b) varying component, (c) and solvent component. (d) Results of combined flow rate in Component A-Component B phase space. Blue lines correspond to a vertical gauntlet with fixed Component A concentration and gradients in Component B concentration. Red lines correspond to a horizontal gauntlet with fixed Component B concentration and gradients in Component A concentration.

Figure 8.2a corresponds to the flow rates for syringe A, considered the non-varying component, while Figure 8.2b corresponds to flow rates for syringe B, considered the varying component.

Figure 8.2c depicts the flow rates for the third syringe which always contains pure solvent. The flow rates are programmed to have an initial 10 minute constant flow rate to achieve steady state droplet production. After 10 minutes a linear gradient is introduced between the varying component pump (syringe B) and the solvent pump (syringe C). Once the gradient is complete, the gradient is reversed until the initial composition is recovered. The non-varying component flow rate (syringe A) is then changed to a new concentration over 4 minutes to probe new phase space. Once complete, a second gradient is introduced between the varying component and the solvent component syringes. This process is repeated for a total of 5 times to create 5 individual gradient arms, with a constant rate of change of $0.5 (\mu\text{L}/\text{min})/\text{min}$.

The compositional paths in Component A-Component B phase space resulting from the pump programs from Figure 8.2a-c are shown in Figure 8.2d. The blue and red lines in Figure 8.2d denote paths dependent on varying and non-varying component choice. If component A is the non-varying component and component B is the varying component, then droplets are initially produced at a concentration of 50% Component A and 10% Component B. The first gradient from the pump program results in an increase in Component B concentration while maintaining Component A concentration. Once the gradient reaches its maximum, the flow rates are reversed and droplets are produced down the gradient path until the initial concentration is recovered, as denoted by the solid blue arrows. Once the first uphill and downhill gradient is complete, component A concentration is changed from 50% to 40% and the process is repeated. Through the entire process, droplets are produced along 5 unique gradient lines with constant Component A concentrations of 50%, 40%, 30%, 20%, and 10% while varying in Component B concentration. This is considered a vertical gauntlet program. Reversing the pump programs corresponding to Component A and Component B will switch the orientation of the process and change the vertical gradient lines in component B concentration to horizontal gradient lines in component A concentration, demonstrated as the red lines in Figure 8.2d. This is considered a horizontal gauntlet. Throughout this paper, syringes with pump programs corresponding to Figure 8.2a are referred to as the non-varying component and syringes with pump programs corresponding to Figure 8.2b are referred to as the varying component. Programs with vertical lines in phase space are referred to as vertical gauntlets and programs with horizontal lines in phase space are referred to as horizontal gauntlets. The individual gradient lines are referred to as gradient fingers.

The gauntlet program is only one example of the type of phase space sampling that can be achieved using this technique. It is possible to program all 3 pumps to vary at the same time which will create composition paths that travel diagonally in Component A-Component B phase space. However, it is important to note that pumps must be programmed such that all three syringes account for at least 10% of the dispersed phase flow rate each. It has been shown in Chapter 3 that using flow rate ratios lower than this ratio can lead to inconsistent droplet production.

8.2.6 Droplet-spacer detection

D₂O droplets containing 1.9 vol% Ludox HS-40 are produced and flowed past a neutron source while the scattered neutrons are continuously collected on a two dimensional detector perpendicular to the beam direction. Droplets pass the neutron beam at a rate of approximately 1 droplet every 90 seconds. Scattered neutrons are collected on a detector at a distance of 5.2m and a registry of the time and location of each neutron that hits the detector is continuously recorded for 7.5 minutes. The registry of neutron hits is grouped into different sized bins for further analysis.

Figure 8.3 shows the neutron hits/bin results for the Ludox HS-40 in D₂O droplet experiment for different bin sizes. The black circles correspond to a bin time of 20 seconds, the red squares correspond to 5 seconds, and the blue hexagons correspond to 1 second bins. The total number of bins in each data set is 22, 90, and 450 bins respectively. As the bin size decreases, the number of bins will increase but the number of neutrons/bin will decrease. This is clearly demonstrated in Figure 8.3. As the bin time decreases, the neutrons/bin curves shift downward but increase in number of data points. The smaller the bin time, the noisier the data.

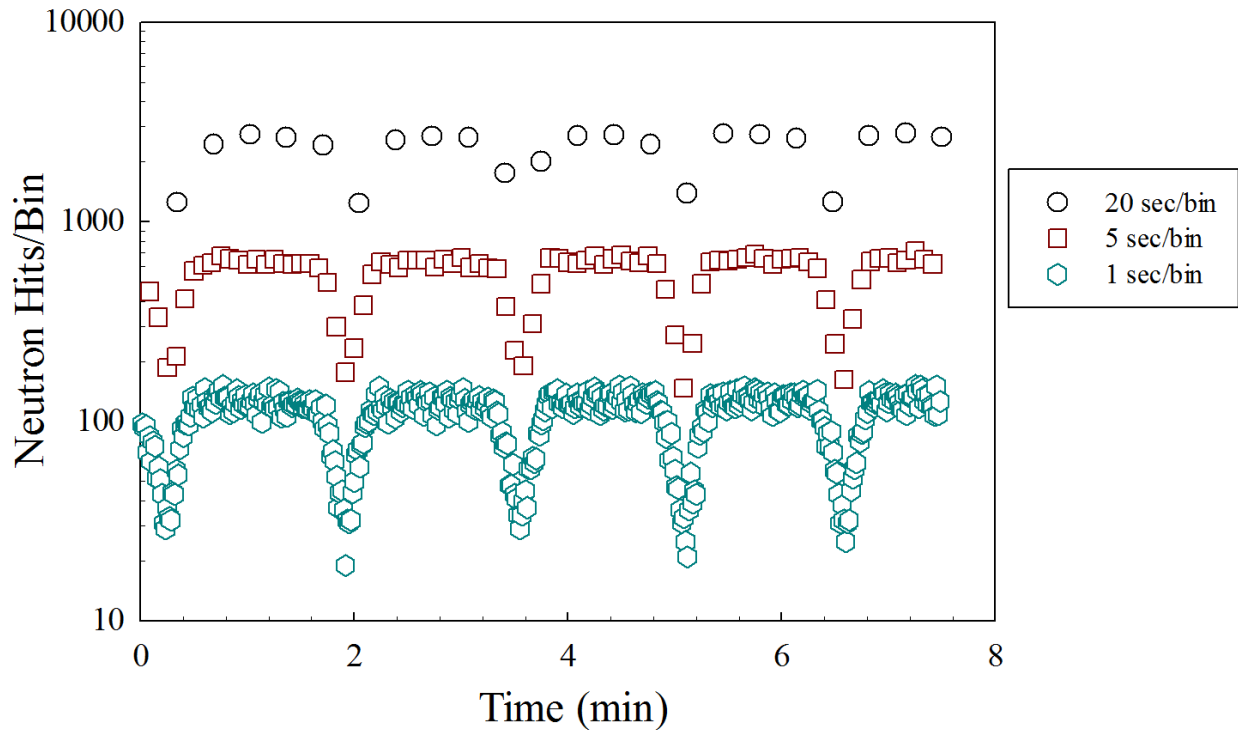


Figure 8.3: Neutron scattering results for 1.9 vol% Ludox HS-40 in pure D₂O droplets at a dispersed phase flow rate of 30 $\mu\text{L}/\text{min}$ and continuous silicone oil outer phase flow rate of 5 $\mu\text{L}/\text{min}$. Black circles correspond to a bin size of 20 seconds, red squares a bin size of 5 seconds, and blue hexagons a bin size of 1 second. Flat plateaus denote droplets and sharp valleys denote spacers.

Droplets that flow past the neutron beam are separated by a small continuous oil spacer. The droplets contain 1.9 vol% Ludox HS-40 silica particles and will scatter strongly, but the spacers are 50 cSt silicone oil and should not scatter as much as the droplets. This difference can be used to separate the droplet regions and the spacer regions using only the neutron scattering results. In Figure 8.3, the flat plateaus with high scattering values are scattering measurements taken within a droplet while the low scattering troughs between droplets are scattering measurements taken in the oil spacer. Using this information, relative positions of droplets and spacers can be defined and used to separate the scattering information from individual droplets. Ideally, binning returns the most neutron scattering per bin while maintaining clear distinction between droplet and spacer. A bin size of 5 seconds is chosen for analysis because of the clear distinction between droplet and spacer while maximizing neutron hits/bin. Additional bin sizes

of 40, 10, 2.5, and 0.5 seconds were investigated. Larger bin sizes may be necessary for more weakly scattering systems.

The technique described in Figure 8.3 is used during gauntlet experiments to determine droplet registry and allow for binning and characterization of individual droplets. Figure 8.4 shows characteristic binned neutron scattering results for droplets containing Ludox TMA silica particles and C_4E_1 in a mixture of H_2O/D_2O as concentrations are varied. Neutron count rate is binned into 5 second intervals as determined from Figure 8.3 and shown as the black lines for a one hour experiment. Spacer identification is determined by the location of a valley between droplet scattering plateaus and shown as open blue circles. This technique is used to determine the start and end time of each droplet for binning of neutron scattering results and correlation with droplets.

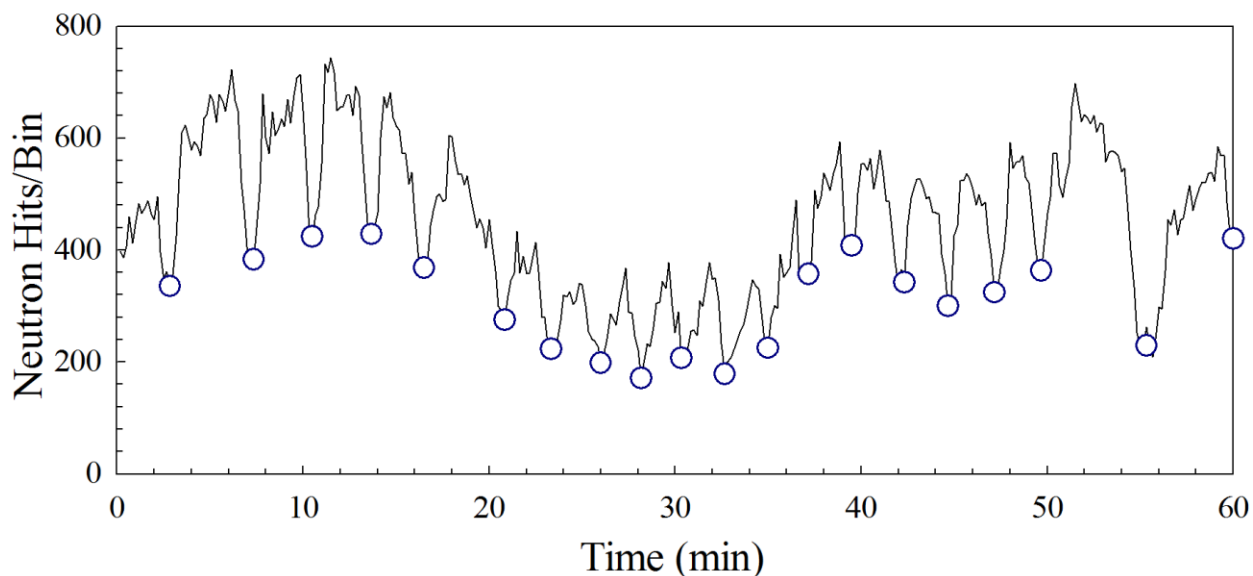


Figure 8.4: Characteristic neutron scattering results from a gauntlet experiment binned into 5 second bins to determine droplet-spacer location. The black curve is binned neutron scattering results and the open blue circles denote separation points between droplets. The time between two points is used to distinguish individual droplet scattering curves.

UV-Vis absorption measurements are performed in-line with neutron scattering experiments 9.75 cm past the neutron beam. With a combined flow rate of 35 $\mu\text{L}/\text{min}$ and 2 mm ID capillary size, droplets require approximately 8.75 minutes to travel from the neutron beam to the UV-Vis source. Transmission of a 1 mm diameter laser ($\lambda = 525 \text{ nm}$) is measured with a photodiode. Future experiments are being designed to obtain UV-Vis and neutron scattering measurements simultaneously at the same point.

UV-Vis provides a more precise measurement of droplet location and quality due to the significant increase in measurement resolution due to the smaller probe area and faster measurement time. Neutron scattering of a droplet spacer may capture scattering from the end caps of the neighboring droplets as well as some of the material in one or both of the separated droplets. UV-Vis, however, has a 1 mm circular spot size and measures absorbance every second. This resolution allows for the detection of distinct droplet and spacer regions.

Figure 8.5 shows UV-Vis absorption measurements of a droplet train with droplets containing 1.9 vol% Ludox HS-40. Similar analysis is performed to differentiate the flat droplet plateaus with the droplet spacer troughs. The absorbance of the droplet plateaus are averaged and displayed as red circles while the absorbance of the spacers are averaged and displayed as the blue diamonds. Large spikes in absorbance occur when the droplet-spacer interface causes significant scattering. The inset in Figure 8.5 shows absorbance measurements for the same droplets over 1 hr to demonstrate monodisperse droplet production. This analysis is used to ensure droplet quality throughout an experiment and to find the relative time and length of each droplet. Droplets are separated by an average of 70 seconds with a standard deviation of 15 seconds, or about 20% variation.

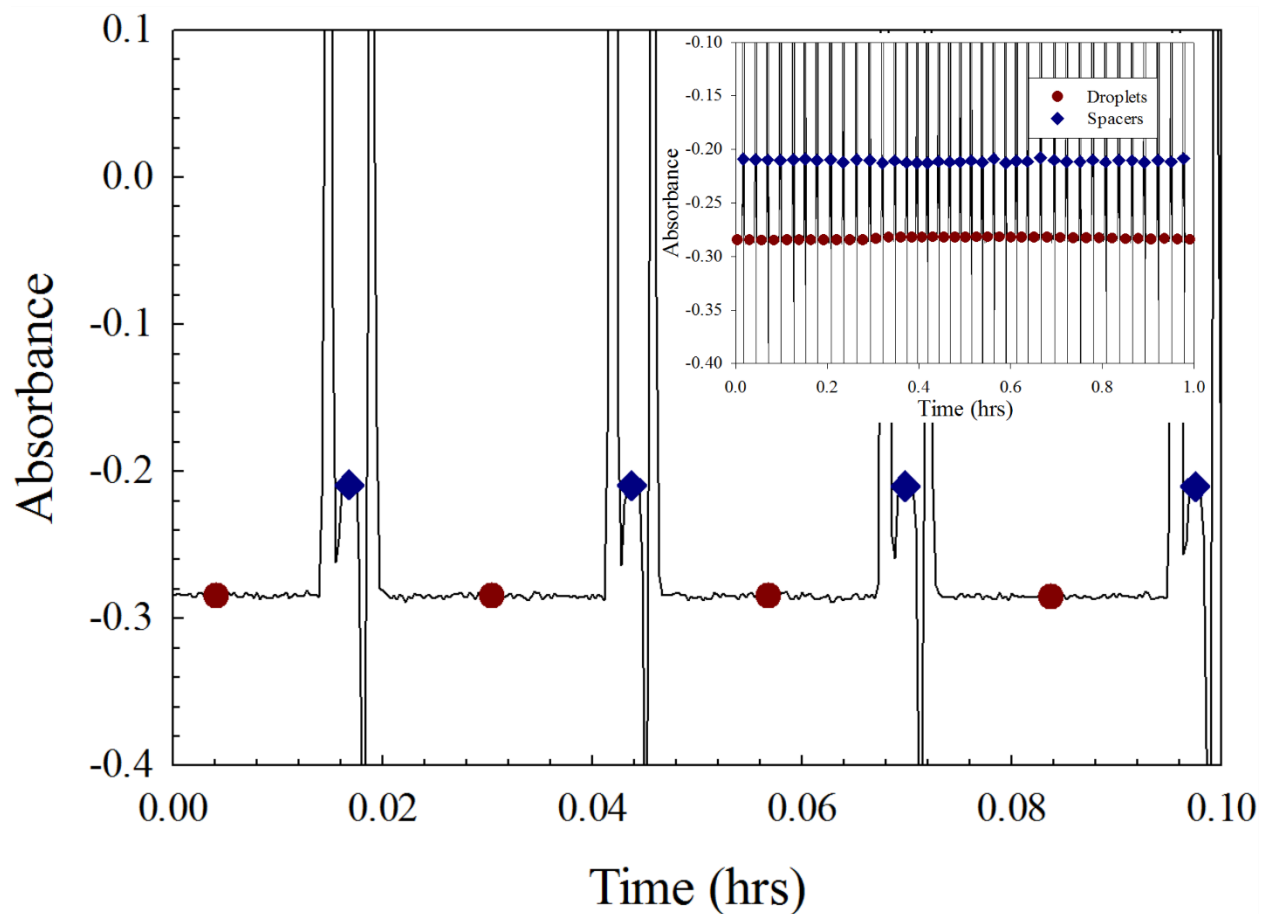


Figure 8.5: UV-Vis absorbance measurements performed during a contrast match experiment. Black line denotes absorbance results at $\lambda = 525$ nm recorded every second. Long plateau sections denote droplets and higher plateau values denote spacers. Red circles correspond to average absorbance measurements of each droplet and blue diamonds correspond to average absorbance measurements of spacers. Sharp spikes in absorbance are measurements performed through a curved droplet-spacer interface. Inset displays identical results for 1 hr to demonstrate monodispersity of droplet production.

8.2.7 Macroscopic phase behavior

Macroscopic jar experiments are performed on all multi-component systems used in droplet experiments. 4mL of sample are produced in 7 mL scintillation vials and observed for phase separation behavior. Results are shown in Figure 8.6 with closed points corresponding to 1-phase fluids and open circles corresponding to phase separated or gelled systems. Figure 8.6a shows results for Ludox TMA silica particles and C_4E_1 . Silica particles and C_4E_1 are known to phase separate at high particle and surfactant concentrations with low concentrations of salt.⁴⁷

However, no phase separation is observed in any macroscopic samples with Ludox TMA.

Ludox TMA is the salt-free version of Ludox TM-40. Mixtures of Ludox TM-40 and C₄E₁ show clear phase separation, suggesting that salt is necessary to induce the liquid-liquid phase separation.

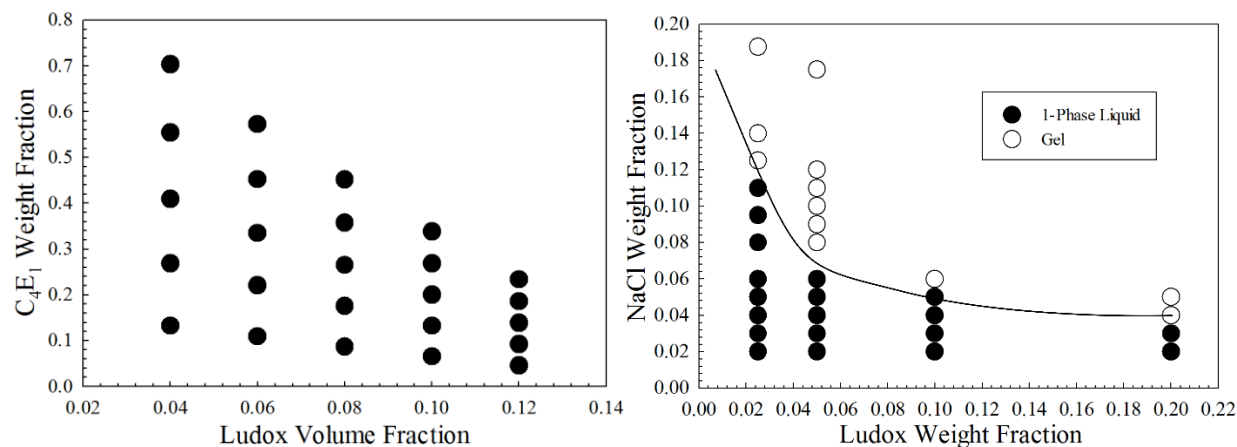


Figure 8.6: Macroscopic phase diagrams for Ludox systems used in millifluidic experiments. (a) Ludox TMA and C₄E₁, (b) Ludox TMA and NaCl, (c) Ludox TMA and 600 g/mol PEO.

Figure 8.6b shows macroscopic phase behavior results for Ludox TMA and NaCl mixtures.

NaCl is known to induce aggregation and gelation in electrostatically stabilized particulate systems.⁴⁸ Signs of gelation are recorded after 10 minutes by inverting scintillation vials and observing which samples flow and which do not.

8.3 Results

8.3.1 Contrast matching of silica nanoparticles in H₂O/D₂O mixtures

A contrast match experiment with pre-programmed syringe pumps is performed to produce a continuous aqueous droplet train of 1.9 vol% Ludox HS-40 (silica) droplets ranging from 15% to 77 vol% D₂O. A continuous phase flow rate of 5 μL/min and a combined dispersed phase flowrate of 30 μL/min is used. The pumps are programmed into 3 different sections. Droplets are first produced at a fixed ratio of 15 vol% D₂O for 20 minutes. Then the droplet D₂O

composition relative to H₂O begins to increase at a rate of approximately 3 vol% D₂O/min until a final D₂O concentration of 77 vol% over 20 minutes. The particle concentration remains fixed at 1.9 vol% silica particles. Once a 77 vol% D₂O droplet composition is reached, droplets are produced at this fixed ratio for 20 minutes to allow time for droplets to reach the neutron source. Two identical experiments are performed – one collecting neutron scattering measurements and the other collecting neutron transmission measurements.

Figure 8.7 shows neutron scattering data for the complete scattering and transmission contrast match experiments divided into 5 second bins. The top plot in Figure 8.7 corresponds to scattering results (integrated over the detector) and the bottom plot corresponds to transmission results (zero scattering angle). In the scattering results, the detection and separation of droplets and spacers is evident. Similar to Figure 8.3, the plateaus are indicative of droplet locations and the troughs indicate the oil spacers between droplets. The red points are the averages of the plateaus (droplet) sections. The thick dotted black lines define the region where the 20 minute H₂O/D₂O gradient is performed and the dot-dash red line is the position within the gradient where the droplets are expected to contrast match (58 vol% D₂O).⁴

The first droplet does not have the same scattering intensity as the following droplets because the droplet composition is recovering from a previous experiment and the droplet composition must reach 15 vol% D₂O. Once steady state is achieved, the average droplet intensity is relatively flat indicating droplets containing a constant H₂O/D₂O ratio (programmed to be 15 vol% D₂O). At the 20 minute timepoint, the gradient is initiated and droplet composition varies from H₂O rich to D₂O rich, crossing through the contrast match point of silica particles (expected to be 58 vol% D₂O). Within this region, the results in Figure 8.7 show a steady decline in average neutrons scattered per droplet to a minimum at approximately 34

minutes. Droplets beyond this time point show an increase in scattered neutron counts per droplet until the end of the gradient at $t = 40$ min. After 40 minutes the droplets recover flat scattered neutron intensity within droplets, again indicating a constant $\text{H}_2\text{O}/\text{D}_2\text{O}$ droplet production ratio, as is preset in the pump program. There is good agreement between the minimum of the neutron scattering curve and the predicted contrast match point.

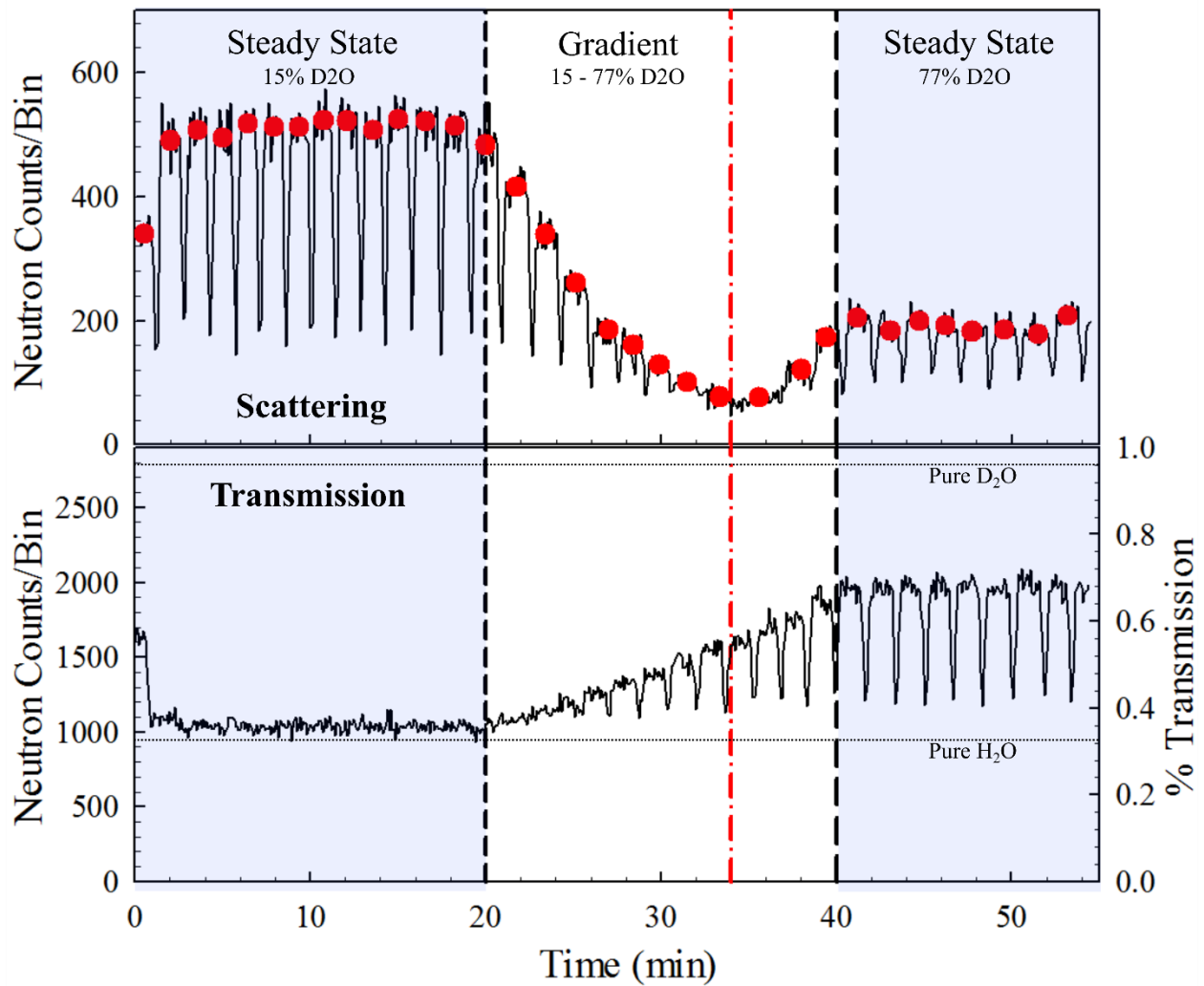


Figure 8.7: Neutron scattering and transmission results for an $\text{H}_2\text{O}/\text{D}_2\text{O}$ contrast match experiment with 1.9 vol% Ludox HS-40 binned into 5 second bins. The black curve denotes binned neutron scattering data and red points denote average scattering for each droplet. For $t = 0$ -20 min, pumps are programmed to produce steady state droplets at 15 vol% D_2O . For $t = 20$ -40 min, a linear gradient from 15-77 vol% D_2O is introduced. For $t = 40$ -60 min, droplets are produced at a constant 77 vol% D_2O . Dot-dashed red line denotes the predicted contrast match point based on the position of the gradient. Particle concentration remains constant throughout experiment.

In the transmission results, droplet-spacer detection is blurred for the first 20 minute steady state. When the gradient is initiated at $t = 20$, min neutron counts per bin begin a linear increase and droplet-spacer detection becomes feasible. The increase in neutron counts per bin continues until the gradient ends at $t = 40$ min, after which transmission of droplets remains flat. The percent transmission relative to the open beam during the experiment is shown on the right axis of the transmission plot. From the NIST Center for Neutron Research (NCNR) online scattering length density (SLD) calculator, H_2O has a reported 32% transmission for a 2 mm path length and a 77% D_2O solution has a reported 74% transmission.

Neutron scattering on macroscopic samples is performed on identical Ludox HS-40 samples used during the microfluidic experiments to confirm agreement between millifluidic, macroscopic, and literature contrast match results. The standard practice to determine a contrast match point for a given system is to measure scattering on at least 5 samples with varying $\text{H}_2\text{O}/\text{D}_2\text{O}$ composition and extrapolate to find the minimum. Low q scattering is typically coherent scattering caused by the suspended material and high q scattering is dominated by incoherent scattering caused by the hydrogenated solvent. To determine the contribution solely from the Ludox HS-40, the high q value is subtracted from the low q value to determine an intensity difference. This results in a parabolic shape, so the square root of the intensity difference is quantified to transform the trend into a linear relationship.

Figure 8.8 compares the droplet based millifluidic contrast match experiment with a classical macroscopic based approach. The square root of the droplet neutron intensity results are plotted as the closed diamond points. This intensity value has not been reduced nor has the high q incoherent scattering been subtracted. These are the raw intensity values, thus the point of minimum intensity corresponds to a contrast match point, but will not reach a value of 0 as the

solvent and quartz cell contribute to scattering. The open red circles correspond to the square root of the reduced macroscopic neutron scattering results. The macroscopic results have been appropriately reduced, thus the contrast match point can be deduced by determining the concentration at which the linear trend through the macroscopic results intersects the x-axis.

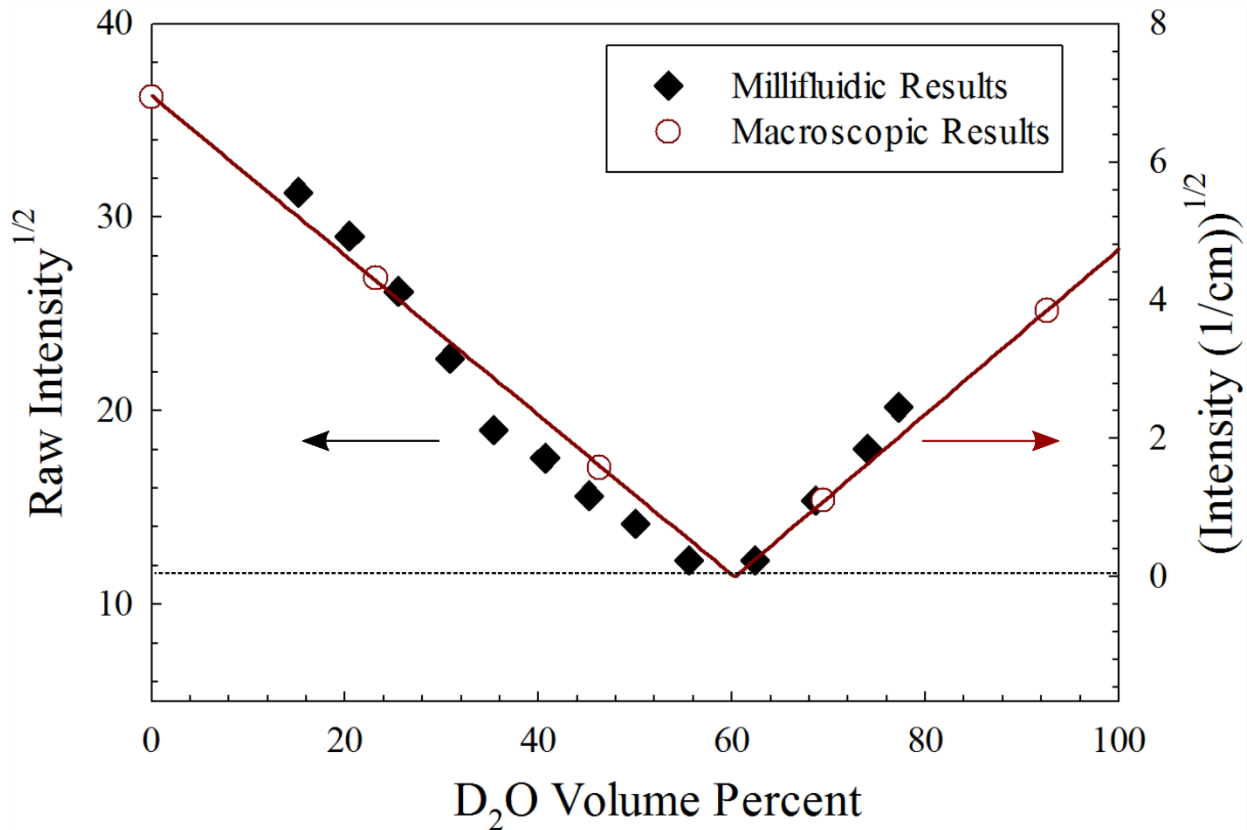


Figure 8.8: Comparison between macroscopic and millifluidic contrast match results. Black diamonds correspond to the raw scattering intensity of individual droplets from Figure 8.7. The y-axis is the square root of the raw scattering intensity average. Open red circles correspond to reduced scattering results from macroscopic samples of identical particle concentration. The magnitude is shown on the right Y-axis as the square root of the reduced scattering intensity. The solid red line denotes a linear fit of macroscopic results to find point of minimum intensity.

The macroscopic results provide a match point of 60% D₂O, while the millifluidic results provide a minimum between 57% and 64% D₂O with a midpoint of 61% D₂O. There is good agreement for the contrast match point between the traditional measurements and the millifluidic experiments.

Once the position of each droplet is obtained from the scattering data in Figure 8.7a, the full 2-D neutron scattering profile for each individual droplet can be isolated and further analyzed. Figure 8.9 shows the 1-D radially averaged scattering curves for 4 different droplets at varying H₂O/D₂O ratios as droplet concentration passes through the contrast match point. The x-axis is the scattering vector Q from a Q range of .0065 to 0.056 and the y-axis is the nonreduced scattering intensity. The individual curves correspond to 15 % D₂O, 46% D₂O, 64 % D₂O, and 77 vol% D₂O respectively.

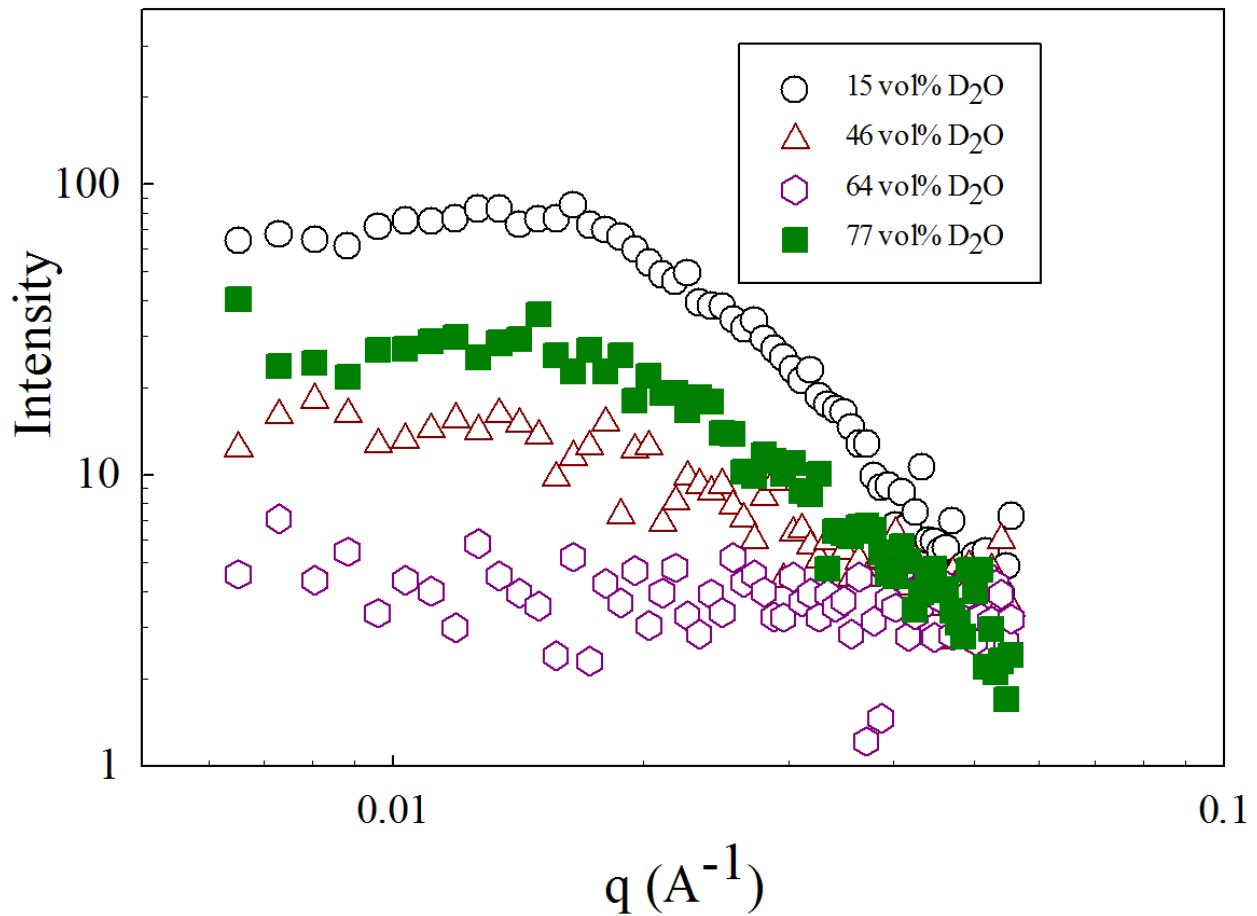


Figure 8.9: Neutron scattering profiles for individual droplets containing 1.9 vol% Ludox HS-40 at various H₂O/D₂O compositions from the contrast match experiment. The D₂O concentration of each droplet are 15.4, 46.1, 63.6, and 77 vol% D₂O described by circles, triangles, hexagons, and squares respectively. Droplet samples pass through the contrast match point for silica particles of 58 vol% D₂O.

Silica particles have a reported contrast match point of 58 vol% D₂O.⁴ As the D₂O concentration in the droplets increases towards 58 vol%, the overall scattering is observed to decrease until the signal becomes mostly noise. As the D₂O concentration continues to increase above the contrast match point, scattering signal similarly increases as shown by the 77 vol% D₂O scattering profile. This demonstrates the capability of the droplet-based experiment to collect enough neutrons to examine scattering curves of individual samples and detect changes among them.

These results provide proof of principle of the millifluidic droplet-based setup for particulate systems. Droplets are produced at discrete, controllable concentrations and neutron scattering is continuously collected across a droplet train. Neutron scattering results are binned into individual droplet compositions for comparison between samples. Silica particle contrast match results are consistent between millifluidic results, macroscopic results, and literature. This experimental setup is applied to more complex phase separating particulate systems to gain insight into interparticle interactions near phase boundaries.

8.3.2 Phase separating silica nanoparticle systems

The results provided in section 8.3.1 demonstrate the feasibility and capability of the SANSDrop technique. With proof of principle established, the goal becomes to investigate more complex colloidal systems and probe interparticle interactions with high composition resolution, specifically as phase boundaries are approached. The particulate systems tested in this work consist of silica nanoparticles and either surfactant, salt, or polymer. Gauntlet experiments from Figure 8.2 are performed on each system to cover large regions of available phase space. Neutron scattering is collected, separated into individual droplets, and paired with the appropriate droplet concentration based on flow conditions. We observe droplet quality and

scattering intensity information to detect changes in particle interaction and characterize microscale system behavior.

In the contrast match experiment, only the ratio of H₂O:D₂O is varied causing no change in interparticle interactions. Phase separation of droplets during production, however, can lead to abnormal droplet breakup and inaccurate droplet concentrations. A classification between well produced and poorly-produced droplets is necessary to avoid analysis on droplets with potentially incorrect droplet concentrations.

When droplet production is performed in a simple non-phase separating system, monodisperse droplets have a standard deviation in size of approximately 20 percent as observed by analyzing droplet lengths from optical analysis of the contrast match experiment. Twice the standard deviation from the controlled experiment is chosen as a baseline to define the quality of droplet production. Droplets with lengths greater than two standard deviations (40%) from the average are considered poorly-produced droplets. This prevents droplets with incorrectly calculated concentrations from being considered in further analysis. To determine droplet quality during an experiment, we define

$$\left| \frac{L - L_{avg}}{L_{avg}} \right| < 0.4, \quad (8.1)$$

where L is the droplet length and L_{avg} is the average droplet length for the experiment. Length is measured either in time or distance for constant velocity experiments. Droplets that meet this criteria are considered good droplets and droplets with lengths outside the boundary criteria are considered poor droplets.

8.3.2.1 Ludox TMA and C₄E₁

A gauntlet experiment is performed on a system containing Ludox TMA silica particles and C₄E₁, known to liquid-liquid phase separate at high particle and surfactant concentrations.⁴⁷ In the vertical gauntlet, the non-varying component is a 34 wt% Ludox TMA particle suspension in pure H₂O, the varying component is pure C₄E₁, and the solvent component is pure D₂O. The experiment is designed to produce droplets that increase then decrease in C₄E₁ concentration at a fixed particle concentration. For this system, the tested particle concentrations are $\phi_{\text{Ludox}} = 0.085, 0.068, 0.051, 0.034, \text{ and } 0.017$. The complete experiment is performed over 4 hours with a total of 75 droplets (samples). Once completed, the same experiment is repeated, but the pump programs for varying and non-varying components are reversed. This creates a horizontal gauntlet with droplet production along fixed C₄E₁ concentrations that increase and decrease in Ludox TMA concentration. The C₄E₁ concentrations are $\phi_{\text{C}_4\text{E}_1} = 0.5, 0.4, 0.3, 0.2, \text{ and } 0.1$. Binned neutron scattering results similar to Figure 8.4 for the Ludox TMA and C₄E₁ system are used to determine the time and location of each droplet and to differentiate between well-produced and poorly-produced droplets. Droplet size is determined by calculating the difference between each oil spacer. Performing this analysis on the full eight hour data set returns an average droplet size of 2.9 ± 1.0 minute ($23 \text{ mm} \pm 8 \text{ mm}$ at $25 \mu\text{L}/\text{min}$).

Figure 8.10 shows the results from the drop quality analysis for the Ludox TMA and C₄E₁ system for both the vertical and horizontal gauntlet experiments. The x-axis in both figures is the experimental time in minutes and the y-axis is concentration of the varying component for each respective experiment. In Figure 8.10a, the non-varying component is 34wt% Ludox TMA in H₂O and the varying component is pure C₄E₁ and in Figure 8.10b, the non-varying component is pure C₄E₁ and varying component is 34 wt% Ludox TMA in H₂O. The dotted black lines in

Figure 8.10 separate the regions of constant concentration of non-varying component samples. The fixed non-varying component concentration for each experiment is displayed on the figures and varied in the small 4 minute gaps between two adjacent dotted black lines.

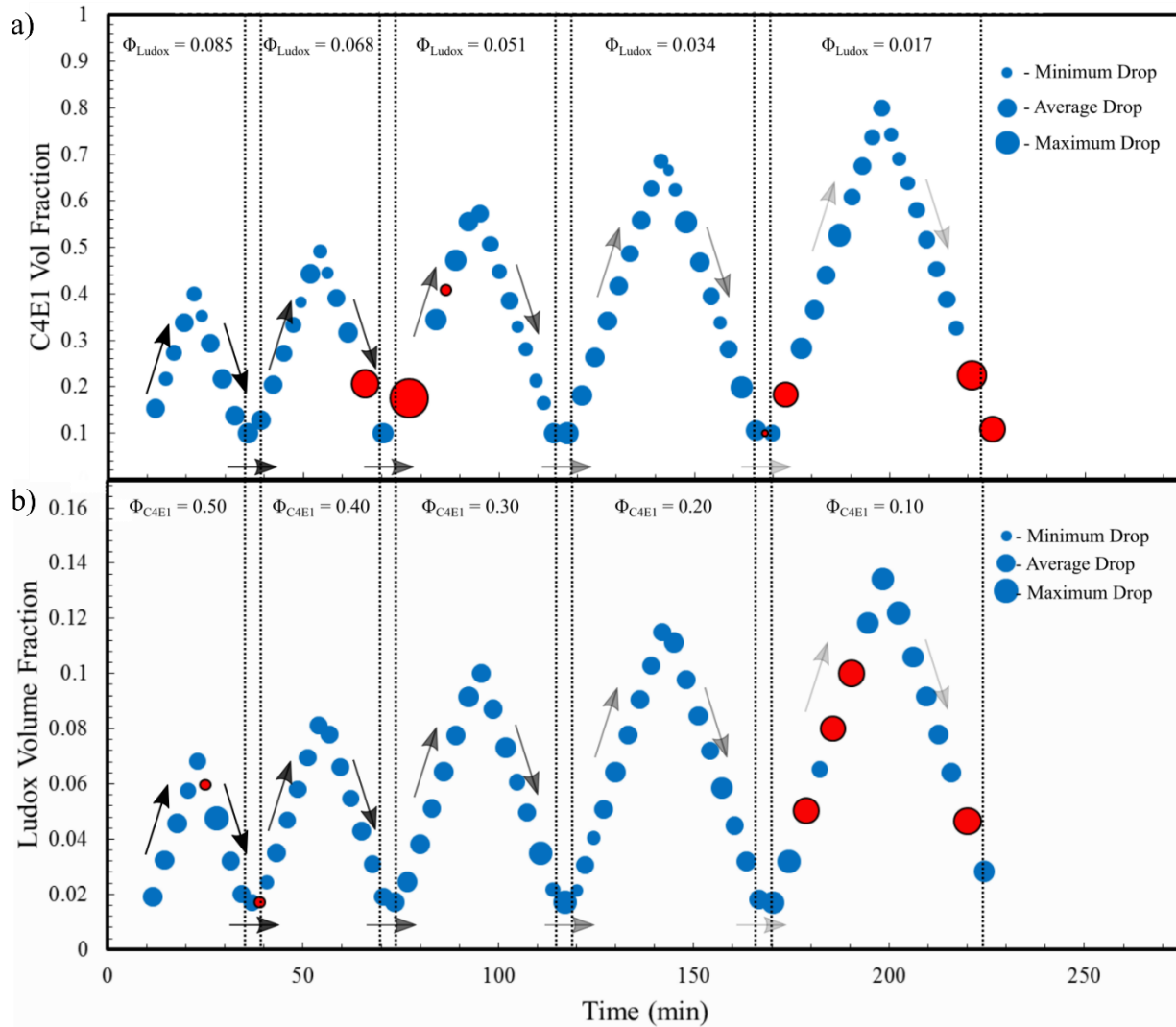


Figure 8.10: Droplet quality results for droplets of a Ludox TMA, C₄E₁, and water system. Dotted black lines denote sections of constant non-varying component. Circles correspond to individual droplet varying component concentration and time. Circle size corresponds proportionally to droplet length. Example minimum, average, and maximum circle sizes are shown in the top right. Droplets within the minimum-maximum limit are blue and considered well produced. Droplets outside the limit are red and considered poorly produced. Droplet production follows direction of black arrows. (a) Denotes results for vertical gauntlet and (b) displays results for horizontal gauntlet.

Each blue or red circle denotes the time and concentration of a droplet determined through the method described from Figure 8.4. The size of the circle proportionally corresponds to the size of the droplet length. A legend is shown in the top right corner of each figure describing the circle diameter that corresponds to an average droplet as well circle diameters at the 40% criteria limit. Droplets that satisfy this criteria are considered good droplets and are displayed as blue circles. Droplets that are either too small or too large are considered poor droplets and are displayed as red circles with a black outline. These results allow for characterization of droplet quality at any point in the experiment. Overall, there are 13 droplets out of 145 droplets in both experiments that are considered poorly-produced droplets. Poor droplet production is likely due to changes during droplet pinch off due to rapid phase separation and changes in fluid properties. It is important to note droplet quality of regions near the top of each peak, which correspond to the end of each gradient where system concentration is highest, in order to make definitive statements about system structure.

Droplet quality can be replotted in Ludox TMA and C₄E₁ phase space coordinates, as the concentration in each droplet is known. In addition, results from Figure 8.4 provide the location of each individual droplet and allow for isolation of the 2-D neutron scattering pattern corresponding to each droplet. The area under the radially averaged scattering curve from $1 = 0.0047$ to 0.0394 1/Å is integrated numerically for each droplet to determine the average scattering intensity for every droplet. This invariant analysis allows the scattering of each droplet to be simultaneously compared with the droplet quality results.

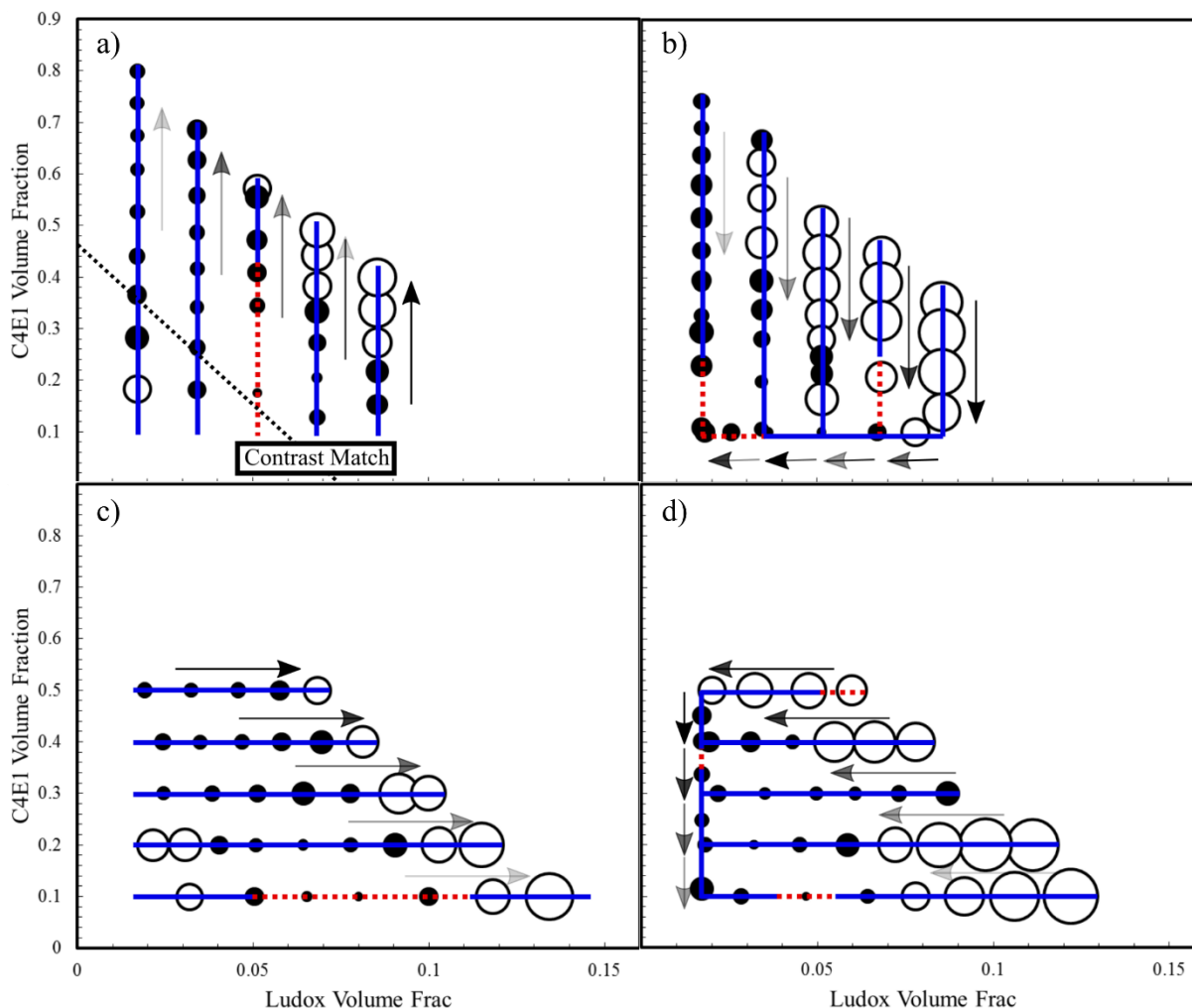


Figure 8.11: Neutron scattering intensity results for individual droplets in Ludox TMA-C4E1 phase space. (a-b) Results from vertical gauntlet and (c-d) results from horizontal gauntlet. (a&c) Uphill sections of each gauntlet and (b&d) downhill sections of each gauntlet. Circles denote droplet composition with circle size corresponding to average scattering intensity. Closed circles denote droplets with lower scattering and open circles denote droplets with higher scattering. Solid blue and dotted red lines depict droplet quality results from Figure 8.10 with blue denoting regions of well-produced droplets and red denoting regions of poorly-produced droplets.

Figure 8.11 shows droplet scattering intensities for all droplets in the Ludox TMA and C4E1 system with corresponding droplet quality results overlaid. Separate figures are shown for each gauntlet. In addition, figures are separated by droplet compositions from the upward and downward portion of each gradient. Figure 8.11a-b corresponds to a vertical gauntlet (lines of constant Ludox TMA concentration) and Figure 8.11c-d corresponds to a horizontal gauntlet

(lines of constant C_4E_1 concentration). Figure 8.11a&c denote results from the upward portion of each gradient and Figure 8.11b&d denote results from the downward portion of each gradient. The droplet quality results from Figure 8.10 are shown as lines through the circles with solid blue corresponding to regions with good droplet production and dotted red corresponding to regions with poor droplet production.

Each circle characterizes the scattering intensity of a single droplet with the diameter of the circle proportional to the magnitude of scattering. A value of twice the average scattering from the contrast match experiment is chosen to mark droplets with significant scattering. The closed black circles denote droplets within this criteria while the open circles denote droplets with scattering larger than the limit. Regions of interest correspond to sections where droplet production remains good (blue lines) and the scattering intensity size varies consistently as droplet concentration changes.

In both the vertical and horizontal gauntlets, droplet scattering is consistent and low at the beginning of each gradient (small, evenly spaced circles). When the end of the upward gradient fingers are reached, most droplets display an increase in scattering, demonstrated by the large open circles. These are the concentrations at which the system is expected to phase separate. On the corresponding downward sections of each gradient finger in Figure 8.11b&d, droplets typically require time to recover back to low scattering systems. This may be due to induced phase separation at the droplet production site that must recover before 1-phase droplets are produced. This is the rationale for producing droplets both up and down each gradient, to give the system time to recover before the next gradient is initiated.

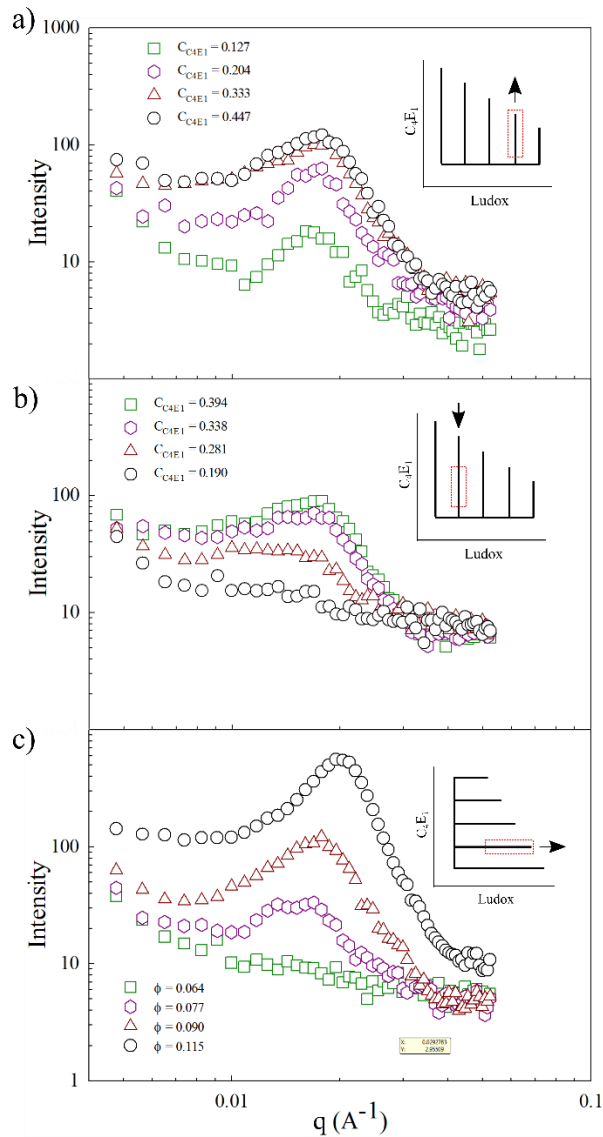


Figure 8.12: Neutron scattering profiles for individual droplets from the Ludox TMA and C₄E₁ gauntlet experiments. Insets show the measured region for each figure with the arrow depicting uphill or downhill direction. (a) Droplets along an uphill gradient in the vertical gauntlet (b) droplets along a downhill gradient in the vertical gauntlet (c) droplets along an uphill gradient in the horizontal gauntlet. Droplet concentrations are denoted in respective legends.

As mentioned previously, 2-D droplet scattering patterns are isolated and collected for each droplet in an experiment. The full 2-D scattering pattern can be radially averaged to produce intensity as a function of q results where I is scattering intensity and q is scattering vector. Figure 8.12 shows examples of intensity curves for droplets approaching phase separation. Scattering profiles for all droplets are collected, but for ease of demonstration three

representative sections among the vertical and horizontal gauntlets are shown in Figure 8.12. In all three plots, the inset in the top right depicts the probed gradient region of each respective gauntlet. Figure 8.12a shows scattering patterns for droplets at a fixed Ludox TMA concentration and varying C₄E₁ concentration along the second upward gradient finger. Referring back to Figure 8.11a, individual droplet concentrations and integrated scattering intensities can be observed. As C₄E₁ concentration is increased, scattering intensity increases to a maximum, after which it remains constant

Figure 8.12b shows neutron scattering patterns for droplets in the downward fourth gradient finger of the vertical gauntlet, as shown in the inset. As C₄E₁ concentration is decreased, scattering is observed to decrease towards a nearly q independent background scattering. Figure 8.12c shows neutron scattering patterns for the horizontally oriented gradient finger where C₄E₁ concentration is fixed and Ludox TMA concentration varies. In these results, scattering curves are observed to increase as Ludox TMA concentration is increased, with a strong peak forming near $q = 0.0195 \text{ 1/Å}$.

8.3.2.2 Ludox TMA and NaCl

Droplet based neutron scattering experiments are performed on a second system consisting of Ludox TMA silica particles and NaCl salt. Ludox TMA is electrostatically stabilized silica particles with a zeta potential of $\zeta = -25 \text{ mV}$.⁴⁹ Addition of NaCl will screen the surface charge groups and induce aggregation and flocculation at high salt concentrations. This flocculation can lead to gelling and jamming of structures at the droplet production site, causing significant issues with droplet production until aggregates are cleared. In addition, time becomes an important factor. The presence of salt will increase the rate of flocculation, but the total degree of flocculation will depend on the time since salt is introduced to the system.

Measurement time can be varied by changing the flow rate or length of the capillary before the neutron source.

Two complete 4-hour gauntlet series are performed identical to those from the Ludox TMA and C₄E₁ system. The first gauntlet experiment contains 34wt% Ludox TMA in H₂O as non-varying component and 650 mM NaCl in D₂O as with varying component with pure D₂O as solvent component. The second gauntlet reverses the non-varying and varying component such that 650 mM NaCl in D₂O is the non-varying component and 34 wt% Ludox TMA in H₂O is the varying component. In this experiment, UV-Vis absorbance measurements are simultaneously captured 9.75 cm past the position of the neutron probe. Absorbance results are used to determine droplet length instead of neutron scattering results due to increased measurement resolution

Figure 8.13 shows the droplet quality results from the optical absorbance measurements using the droplet criteria. The results are displayed in an identical method to those in Figure 8.10. There are a many regions of red points in these results. This denotes sections where droplet production is poor and droplet concentration may be compromised. In most cases, droplet production becomes poor at the end of an uphill section or the beginning of a downhill section (where concentration is the highest). Inconsistent droplet production persists for a short time before droplet production recovers and similar size, blue points are measured. This suggests that although the aggregating particle-salt mixture may disrupt droplet production at high concentrations, the system can recover once low concentrations are reached as long as the capillary does not clog with solid material.

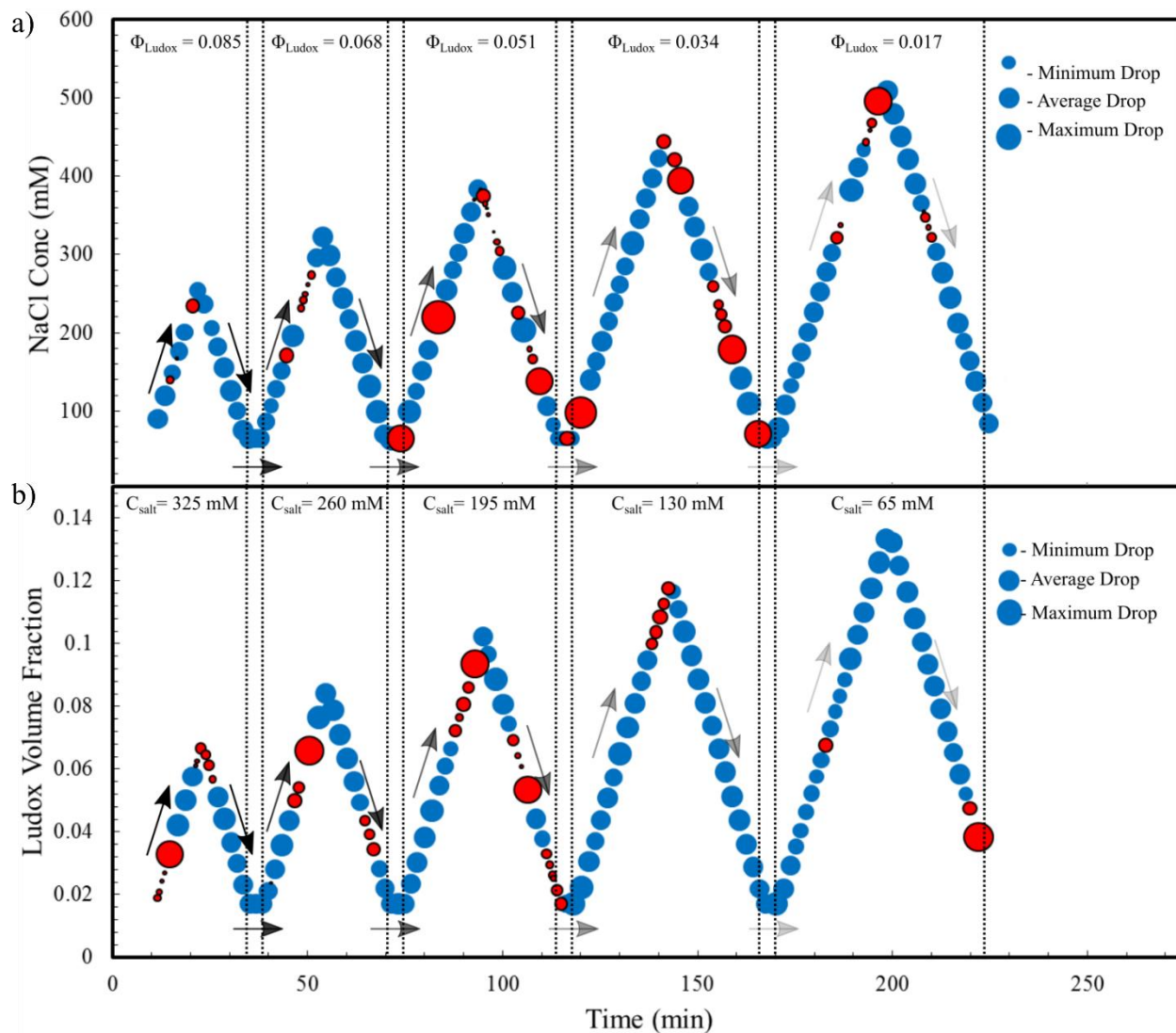


Figure 8.13: Droplet quality results for Ludox TMA, NaCl, and water system. Dotted black lines denote sections of constant non-varying component. Circles correspond to individual droplet varying component concentration and time. Circle size correspond proportionally to droplet length. Example minimum, average, and maximum circle sizes are shown in the top right. Droplets within the minimum-maximum limit are blue and considered well produced. Droplets outside the limit are red and considered poorly produced. Droplet production follows direction of black arrows. (a) Denotes results for vertical gauntlet and (b) displays results for horizontal gauntlet.

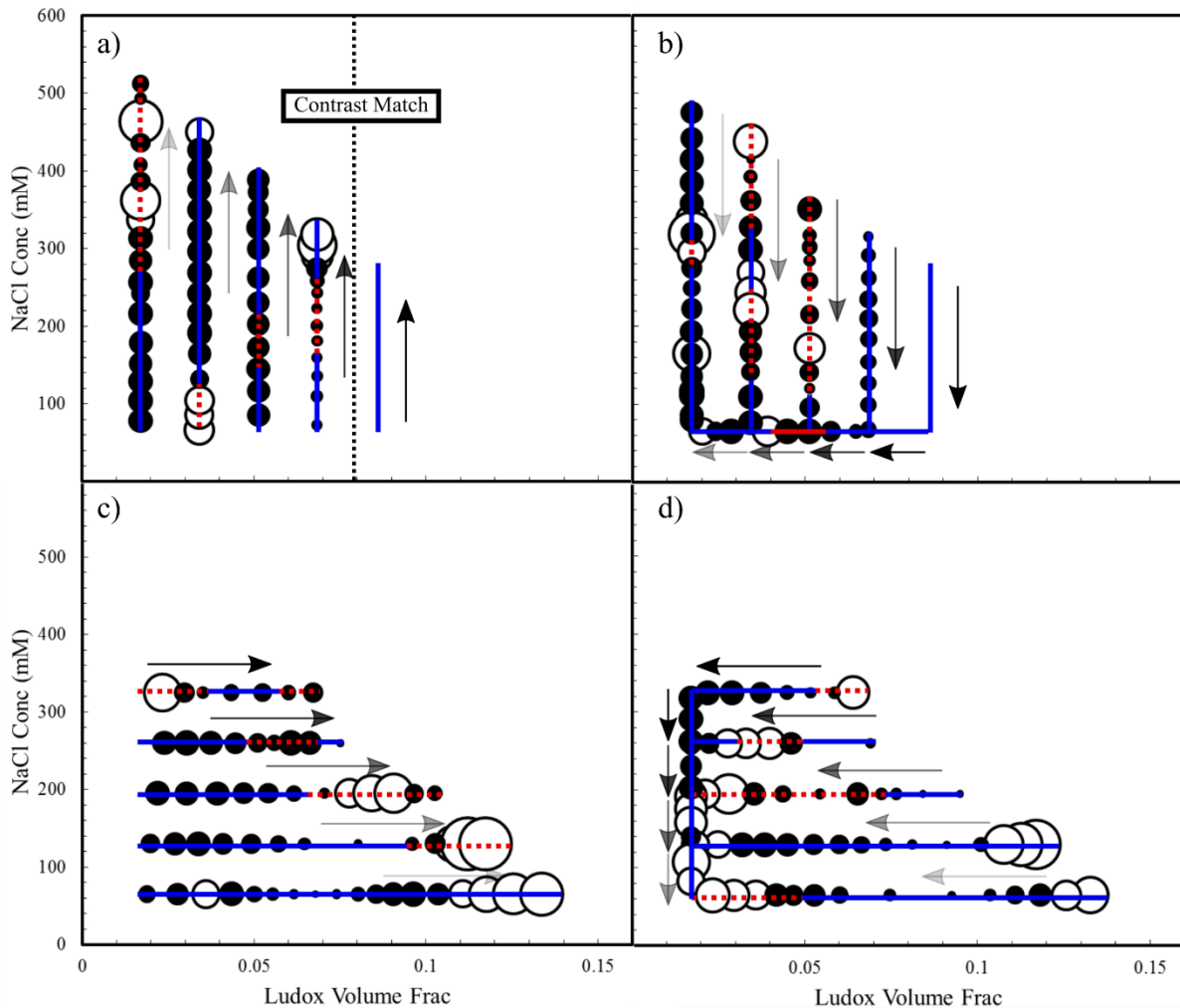


Figure 8.14: Neutron scattering intensity results for individual droplets in Ludox TMA-NaCl phase space. (a-b) Results from vertical gauntlet and (c-d) results from horizontal gauntlet. (a&c) Uphill sections of each gauntlet and (b&d) downhill sections of each gauntlet. Circles denote droplet composition with circle size corresponding to average scattering intensity. Closed circles denote droplets with lower scattering and open circles denote droplets with higher scattering. Solid blue and dotted red lines depict droplet quality results from Figure 8.13 with blue denoting regions of well-produced droplets and red denoting regions of poorly-produced droplets.

Figure 8.14 shows the droplet quality results from Figure 8.13 overlaid on neutron scattering intensity results. Results are displayed similarly to Figure 8.11 with Figure 8.14a-b corresponding to the vertical gauntlet and Figure 8.14c-d corresponding the horizontal gauntlet.

The first gradient for the vertical gauntlet has no results for neutron scattering intensity due to a contrast match between the particles and solvent at this concentration and a difficulty in separating droplet and spacer. The droplets along this gradient contain 55 vol% D₂O compared with the contrast match point of 58 vol% D₂O. In this experiment, contrast matching occurs at a Ludox TMA concentration $\phi = 0.079$ and is shown by the dotted black line in Figure 8.14a.

For the vertical gauntlet, upward gradient fingers shown in Figure 8.14a generally result in consistent, low scattering droplets until the peaks of the gradients are reached. The downward gradient fingers in Figure 8.14b show inconsistent droplet scattering with poor droplet production as the system likely recovers from a flocculation event.

Figure 8.15 shows radially averaged neutron scattering results for unique droplets from the Ludox TMA and NaCl experiment corresponding to gradient sections highlighted in each inset. Figure 8.15a shows droplets along the last gradient finger from the horizontal gauntlet increasing in Ludox TMA concentration for a fixed salt concentration of 65 mM NaCl. Neutron scattering is observed to increase as Ludox concentration increases with a peak near $q = 0.0178$ 1/Å. Figure 8.15b-c show neutron scattering results from droplets along the same downhill gradient finger. Figure 8.15b shows droplets at the high particle concentrations where scattering is initially constant, but decreases as particle concentration decreases. Figure 8.15c shows droplets at lower concentrations where scattering is relatively constant as particle concentration decreases from $\phi = 0.060$ to $\phi = 0.017$.

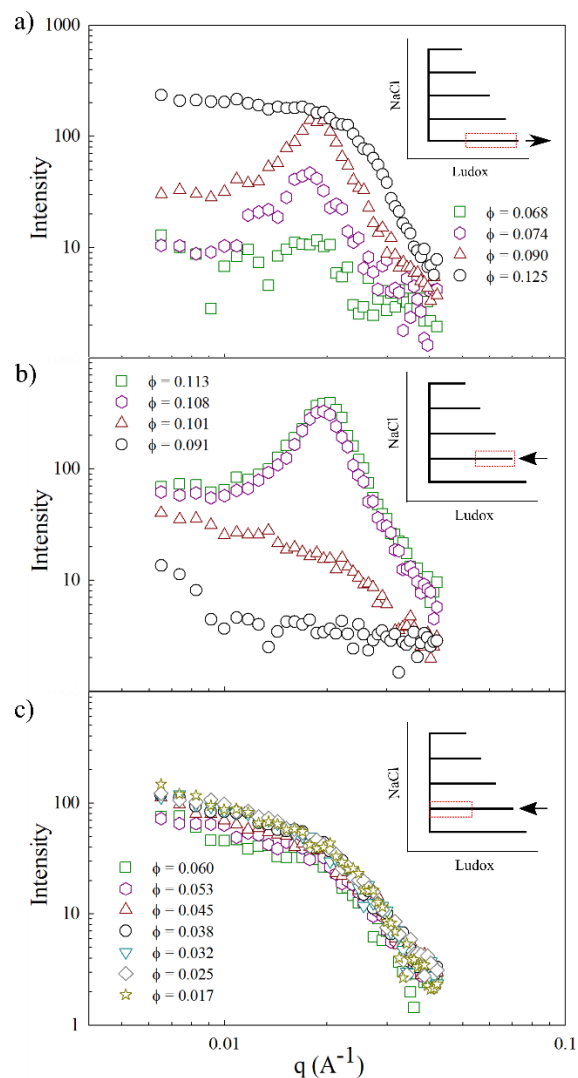


Figure 8.15: Neutron scattering profiles for individual droplets from the Ludox TMA and NaCl gauntlet experiments. Insets show probed gradient region for each figure with the arrow depicting uphill or downhill direction. (a) Droplets along an uphill gradient in the horizontal gauntlet (b) droplets along the first half of a downhill gradient in the horizontal gauntlet (c) droplets along the second half of a downhill gradient in the horizontal gauntlet. Droplet concentrations are denoted in respective legends.

It is important to note that the system passes through the contrast match point as the droplets change in Ludox TMA concentration. Droplets from Figure 8.15b passing through the contrast match point which may be the reason for the large decrease in scattering. However, there is also a structural change in the peak at $q = 0.0195 \text{ 1/\AA}$ which disappears as particle concentration decreases, suggesting that the decrease in scattering may be due to both a contrast match between the particles and solvent and a change in the interparticle interactions. Once the

droplets recover from changes in interparticle interactions and the composition becomes distant from the contrast match point, droplet scattering remains relatively constant as shown in Figure 8.15c.

8.3.2.3 Ludox TMA and 600 g/mol PEO

A third system containing Ludox TMA and 600 g/mol PEO is characterized using similar experimental parameters. For this system, only one gauntlet is tested, where the non-varying component is 34 wt% Ludox TMA in H₂O and the varying component is 80 wt% 600 g/mol PEO in D₂O. The experimental time for the entire gauntlet is halved from 4 hrs to 2 hrs with each section being proportionally decreased in time. UV-Vis absorbance measurements are simultaneously recorded and used for droplet quality analysis.

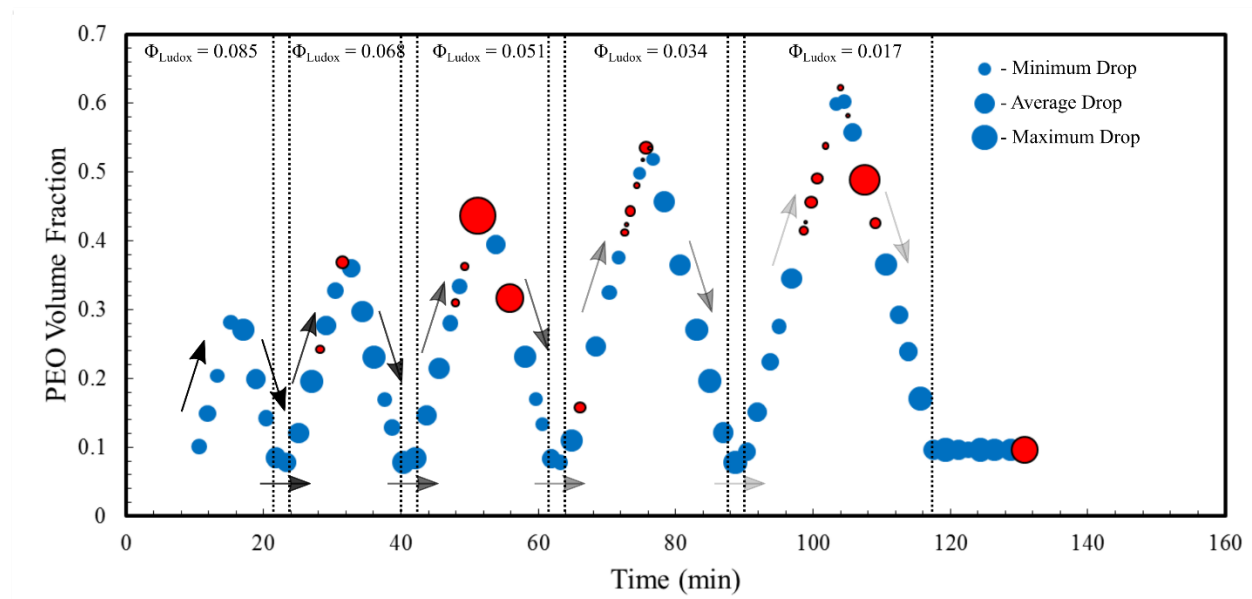


Figure 8.16: Droplet quality results for Ludox TMA, 600 g/mol PEO, and water system. Dotted black lines denote regions of constant particle concentration. Circles correspond to individual droplet PEO concentration and time. Circle size correspond proportionally to droplet length. Example minimum, average, and maximum circle sizes are shown in the top right. Droplets within the minimum-maximum limit are blue and considered well produced. Droplets outside the limit are red and considered poorly produced. Droplet production follows direction of black arrows. Overall experiment is half the time of original gauntlet experiment.

Figure 8.16 shows droplet quality results for the Ludox TMA and 600 g/mol PEO system, shown similarly to Figure 8.10. Droplet production becomes inconsistent at the peak of all gradient fingers except the first one, indicating an issue with droplet production at high polymer concentrations. Droplet production is observed to recover after each inconsistency.

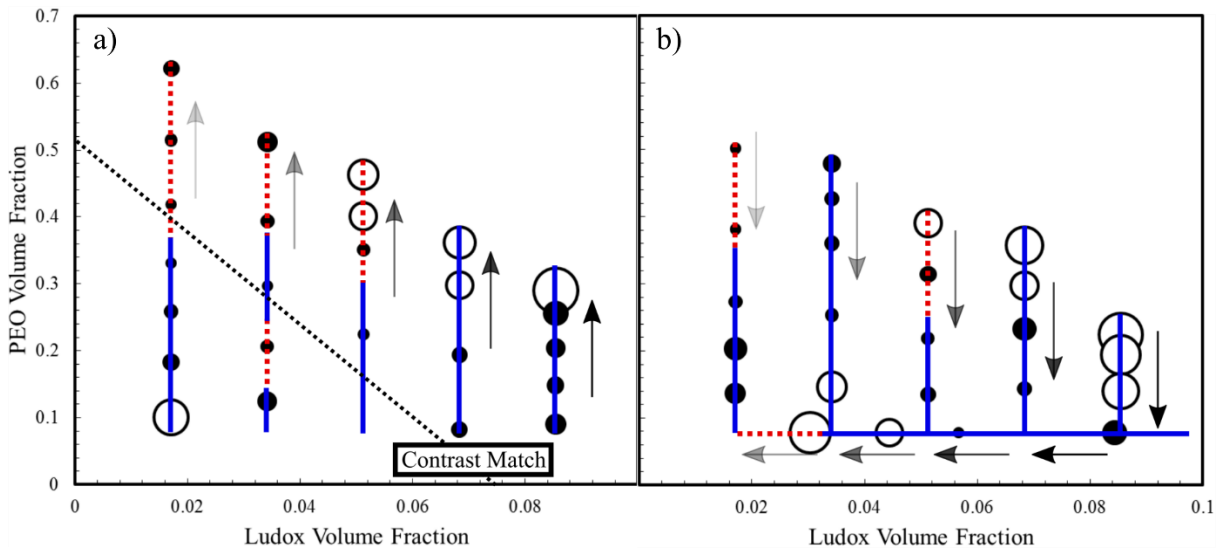


Figure 8.17: Neutron scattering intensity results for individual droplets in Ludox TMA-PEO phase space. (a-b) Results from vertical gauntlet with (a) describing uphill sections the gauntlet and (b) describing downhill sections of the gauntlet. Circles denote droplet composition with circle size corresponding to average scattering intensity. Closed circles denote droplets with lower scattering and open circles denote droplets with higher scattering. Solid blue and dotted red lines depict droplet quality results from Figure 8.16 with blue denoting regions of well-produced droplets and red denoting regions of poorly-produced droplets. Dotted black line denotes a line of constant SLD equal to the SLD of silica.

The droplet quality results from Figure 8.16 are overlaid on neutron scattering intensity results in Figure 8.17. The dotted black line shows in Figure 8.17a shows a line of constant SLD equal to the SLD of silica particles ($3.4 \times 10^{10} \text{ cm}^{-2}$). There are 50 droplets total, less than previous experiments due to the experiment time being only half as long.

In this system, poor droplet production occurs near the peaks of each finger, resulting in loss of reliability of those droplets. Only two uphill fingers provide structural information on well-produced droplets. This may be a result of system choice or reducing experimental time by

a factor of two. In addition, droplet scattering intensity becomes small at concentrations close to the dotted contrast match line and large at concentrations far from the contrast match line, suggesting a large impact on scattering intensity from contrast differences.

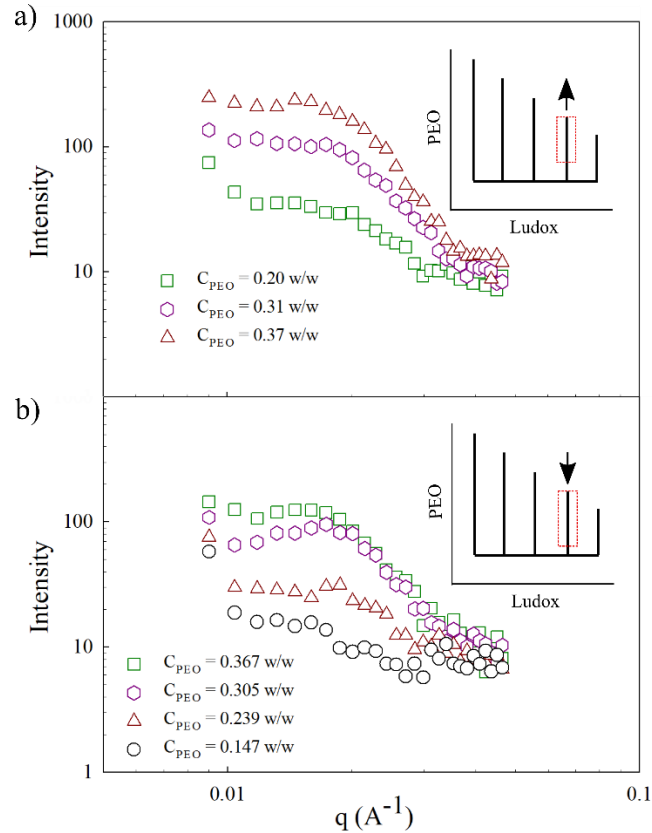


Figure 8.18: Neutron scattering profiles for individual droplets from the Ludox TMA and 600 g/mol PEO gauntlet experiment. Insets show probed gradient region for each figure with the arrow depicting uphill or downhill direction. (a) Droplets along an uphill gradient and (b) droplets along the same downhill gradient in the vertical gauntlet. Droplet concentrations are denoted in respective legends.

Figure 8.18 shows the radially averaged neutron scattering profiles for unique droplets from the Ludox TMA and 600 g/mol PEO system. The curves correspond to scattering of droplets from regions highlighted in the inset of each figure with a constant particle volume fraction = 0.068 and varying PEO concentrations. Figure 8.18a shows results for the uphill portion of the second gradient finger where PEO concentration is increasing. Scattering is observed to increase as concentration increases. Figure 8.18b shows results for the downhill

portion of the same gradient finger, continuing with the next droplet in the gradient after Figure 8.18a. Droplet scattering remains relatively constant before decreasing monotonically as PEO concentration decreases.

Scattering magnitude is observed to increase with increase in polymer concentration, but no structural scattering peaks arise. The increase in scattering magnitude is consistent with an increase in the contrast between particles and solvent. This suggests that variation in droplet scattering results may only be due to changes in contrast.

8.4 Discussion

Performing neutron scattering experiments on continuous droplet samples has numerous advantages over traditional macroscopic scattering experiments as well as continuous flow experiments. Droplets allow for isolation of unique, individual samples that achieve good mixing due to the recirculation patterns that occur during droplet pinch off and flow.^{45,46} This technique produces many more samples per experiment, achieving high composition resolution with an automated setup. Significant portions of phase space can be experimentally probed with a single, continuous experiment, providing high quality scattering information throughout an entire region of phase separation. In addition, phase separating droplets do not permanently disrupt future droplet production. Instead, there is a short period of recovery after which a new gradient can begin.

Figure 8.2 describes one possible approach to mapping large composition space with a single pre-programmed droplet experiment. Five gradients in component concentration are introduced at different non-varying component concentrations. This technique is used to monitor droplet neutron scattering and system structure as droplet compositions are pushed toward phase

boundaries. Systems containing Ludox TMA particles and either C_4E_1 , 600 g/mol PEO, or NaCl are examined in this work.

UV-Vis absorbance and neutron scattering measurements are simultaneously recorded, each contributing part of the necessary droplet information. Absorbance measurements provide droplet quality information by comparing the relative droplet lengths during an experiment and detecting if abnormal droplet production occurs. Neutron scattering results provide scattering intensity and structural information. Together, the UV-Vis and neutron scattering results provide a detailed description of the complex structural information of each droplet with verification of regions where droplet production is normal and consistent. It is important to note that droplet quality can still be determined solely from the neutron scattering information as shown in Figure 8.4, but resolution is lower than with optical absorbance measurements.

8.4.1 Ludox TMA and C_4E_1

The first system tested consists of Ludox TMA silica particles, C_4E_1 , and water, known to phase separate at high particle or C_4E_1 concentrations.⁴⁷ Addition of C_4E_1 changes the Hamaker constant and dielectric constant of the system and adsorbs to particle surfaces, modifying surface properties and interparticle interactions. There are a few locations in both the vertical and horizontal gauntlet experiments where droplet quality behaves poorly and droplets do not fit the normal droplet criteria, but for the majority of the experiments, good quality droplet production is achieved. This allows for reliable scattering quality analysis on most droplets in the experiment.

Figure 8.12 shows the 1-D radially averaged scattering curves for droplets both approaching and receding from the phase boundary line. Uphill gradient fingers in both the horizontal and vertical direction demonstrate significant increase in scattering as concentration is

increased, with a peak forming around a similar q value of $Q = 0.0195$. This peak structure is characteristic of a developing fluid structural peak. In addition, Figure 8.12b shows that a downhill gradient results in a recovery in scattering consistent with particles becoming stable and minimizing interparticle interactions. This is an important result, suggesting that if droplet production goes awry or produces complex, phase separating systems, then monodisperse droplet production can be recovered by lowering system concentrations and allowing equilibration time.

8.4.2 Ludox TMA and NaCl

A second system containing Ludox TMA, NaCl, and water is tested. This system contains the most issues with droplet production at distances far along each gradient finger. Figure 8.13 shows the droplet quality results for this experiment using UV-Vis absorbance results to quantify droplet size. It is important to note the clusters of small drops that are discernable using the UV-Vis technique. Poor droplet quality in this experiment tends to appear at the peaks of the gradients where concentration is highest.

In both uphill and downhill experiments, droplet scattering is observed to decrease to a minimum at approximately $\phi = 0.09$ followed by an increase in scattering. In the vertical gauntlet, all droplets along a particular gradient finger are at the same $\text{H}_2\text{O}/\text{D}_2\text{O}$ composition, but in the horizontal gauntlet, the $\text{H}_2\text{O}/\text{D}_2\text{O}$ composition varies based on particle concentration. The contrast match point will occur at a particle volume fraction $\phi = 0.079$. The results suggest that the characteristic decrease then increase in scattering intensity with particle volume fraction may be due to the contrast matching of the particles in the solvent. In addition, Figure 8.15a-b demonstrates that heading towards or away from the contrast match point decreases or increases the scattering respectively. However in both plots, a strong scattering peak forms near $Q = 0.0195$ as droplet $\text{H}_2\text{O}/\text{D}_2\text{O}$ ratio diverges from the contrast match point, suggesting a structural

change in interparticle interactions along with an increase in scattering due to an increase in scattering length density difference. In addition, Figure 8.15c shows that droplets far from the contrast match point in a region of good droplet production behave similarly, further suggesting that the structural peak at $Q = 0.0195$ is a change in interparticle behavior and not an artifact of contrast matching differences.

Similarly to the Ludox TMA and PEO system, D_2O is used for the salt solution and solvent component syringe to minimize incoherent scattering when possible. However, it has been shown in this work that particle based systems in droplets provide enough coherent scattering to be detectable even at high H_2O concentration (large background scattering). Therefore, H_2O can be used as the only solvent to entirely avoid contrast match issues. This will increase the background scattering of the system due to a difference in incoherent scattering between H_2O and D_2O , but solve the nuisance of unintended contrast matching along droplet composition paths.

8.4.3 Ludox TMA and 600 g/mol PEO

The third system tested with this technique is a system containing Ludox TMA particles, 600 g/mol PEO, and water. Figure 8.17 shows the uphill and downhill gradient neutron scattering results for Ludox TMA and 600 g/mol PEO. Because the experiment was programmed for half the time, there are fewer droplets in the experiment, although not half as many. System choice is known to affect droplet size by changing the viscosity and interfacial tension between the droplet phase and immiscible outer phase oil.⁵⁰ In the first three gradients, neutron scattering is low for droplets at the beginning of each gradient and large for droplets at the end of each gradient, similar to the Ludox TMA and C_4E_1 system.

However, there are some high scattering droplets at the beginning of the final two gradient fingers. It is possible that running the experiment twice as quickly does not provide enough time for the system to recover before a new gradient is introduced. In addition, contrast matching of the particles to the solvent is likely playing a role. Table 8.1 shows the scattering length densities (SLD) for the four components in the system. H₂O enters into the system through the particle source while D₂O enters in the polymer solution and the solvent component syringe. This creates a contrast match point relationship between the particle and polymer concentration shown in Figure 8.17a. The large open points in Figure 8.17 are far from the contrast match point, suggesting that the increase in scattering may be a factor of scattering length density differences and not interparticle interactions or phase separation.

Table 8.1: Scattering length density parameters for components in the silica particle and PEO system.^{4,47}

Material	Scattering Length Density (cm ⁻²)
Silica	3.4×10^{10}
PEO	0.57×10^{10}
Light Water (H ₂ O)	-0.56×10^{10}
Heavy Water (D ₂ O)	6.38×10^{10}

Figure 8.18 shows the radially averaged scattering curves for droplets at fixed particle concentration while PEO concentration is increased. In this system, a strong structural peak is not as prevalent as the Ludox TMA and C₄E₁ or NaCl results. But a similar trend of increasing scattering distance along the gradient is observed. As previously mentioned, it is difficult to distinguish between contrast match effects and changes in interparticle interaction. The results from the Ludox TMA and PEO work suggest that contrast match point must be taken into larger consideration during experimental design to avoid this issue. In future experiments, H₂O can be used as the only solvent since the scattering length density of silica lies outside those of H₂O and PEO.

8.5 Design Implications

Experimental design is a major consideration when a new system is to be introduced to the SANSDrop technique. Design conditions should be tailored for each system to determine experimental feasibility and maximize quality of results. Numerous parameters affect potential results including inherent system properties (viscosity, interfacial tension, density), wetting conditions, contrast matching, flow rate ratios, exposure time, and stock solution concentrations. Steps must be taken to properly consider the effects of each experimental handle.

8.5.1 Concentration dependence

Arguably the most important consideration when designing SANSDrop experiments is determining the concentrations at which droplets will be produced and if they will fall within a potential region of interest (phase boundary or structure change). As discussed in the materials section, there are three dispersed phase syringes for a gauntlet experiment: a non-varying syringe containing component A solution, a varying syringe containing component B solution, and a solvent syringe containing pure solvent. To maintain consistent droplet production, all syringes must maintain a minimum of 10% of the total dispersed phase flow rate. Therefore the highest concentration of any droplet is 80% of the stock solution. However, this significantly limits the variable concentration of the second component

For example, if component A is 20 vol% particles and component B is 20 vol% polymer, the droplet with the highest achievable particle concentration is 16 vol% particles with 2 vol% polymer. However, there is only one possible polymer concentration of 2 vol% available at this particle concentration since both the polymer and solvent syringe pumps are already at their minimum 10% total flow rate values. In order to create variation in polymer concentration, the particle concentration must be reduced. If the particle syringe flow rate is reduced to 60% of the

total dispersed phase flow rate, the droplet particle concentration will be 12 vol% particles with a variable polymer concentration from 2-6 vol%. As particle concentration decreases, the possible range of polymer concentration increases. However, certain phenomena may only occur at high enough polymer or particle (component A or component B) concentrations. Therefore, it is important to consider the phase space where interesting behavior is expected and determine the stock solution concentrations necessary to achieve droplet production at those concentrations. This is especially applicable when precious material at low concentrations is being considered.

A major advantage of the droplet-based technique is the recoverability of droplet production after a phase separating phenomena. In all three gauntlet experiments, regions of high concentration where droplet production becomes abnormal are reached. In each case, droplet composition recovers on the downhill section of the gradients, eventually returning to standard, monodisperse droplet production before the next gradient. As long as the phase separation does not entirely block or clog the capillary, the setup has shown the ability to recover. However, the potential for clogging should still be taken into consideration for fast flocculating systems.

8.5.2 Contrast matching

Contrast matching is an extremely powerful aspect of small angle neutron scattering and is often a major benefit in experiments. It can be a potential benefit of the SANSDrop approach as well, as shown in the contrast match experiments in Figure 8.7, but can also be an experimental issue if unintended contrast matching occurs during a droplet gradient. In the gauntlet experiments performed in this work, all three systems contrast matched at certain concentrations during the droplet experiment. This occurred because the SLD of silica particles is between the SLD of D₂O and either H₂O, PEO, or C₄E₁. D₂O is used as the solvent in all three

systems because it has lower incoherent scattering than H₂O and we attempted to avoid unnecessary solvent scattering to increase particle scattering signal. However, this lead to a contrast match point in all three systems, causing difficulties in separating system structural changes from contrast matching changes. In future experiments, it is recommended to investigate a solute with a SLD outside of the other two components to avoid any contrast matching.

8.5.3 Fluid properties

Experimental properties including viscosity of the continuous and dispersed phases, the interfacial tension between the droplets and the oil, and the density of each phase play a role in droplet production using a co-flow setup. There are two dimensionless groups that control the drop pinching mechanism: the capillary number and the Weber number. The capillary number is defined as the balance between the viscous forces on a drop and the interfacial tension and the Weber number is defined as the balance between the inertial forces on the drop and interfacial tension described by Equations 8.2 and 8.3

$$Ca = \frac{u\mu}{\gamma}, \quad (8.2)$$

$$We = \frac{\rho u^2 D}{\gamma}, \quad (8.3)$$

where u is fluid velocity, μ is outer phase viscosity, γ is interfacial tension, ρ is fluid density, and D is capillary diameter. Utada *et al.* demonstrate the relationship between capillary and Weber number on the droplet pinching mechanism.⁴⁴ When capillary number is large ($>O(1)$), the droplets will be produced by a jetting droplet production mechanism regardless of the Weber number. When capillary number is small ($<O(1)$), the droplet mechanism depends solely on

Weber number. At Weber numbers larger than $O(1)$, droplet will be produced via jetting and when Weber number is smaller than $O(1)$, droplets will be produced via dripping. In the SANSDrop setup, it is preferable and more consistent to produce droplets via the dripping mechanism. Therefore, both the capillary number and Weber number should be tuned to stay well below a value of 1.

There is no real limit on how slowly droplets can be produced, but the upper limit on how quickly they can be produced will depend on the viscosity of the fluid, the pump flow rates, the capillary of the device, and the interfacial tension. It is important to note that the interfacial tension can decrease 1-2 orders of magnitude if a highly surface active component is introduced to the system, potentially unfavorably switching the droplet production technique from dripping to jetting.

8.5.4 Adsorption to interface

A difference between performing experiments in a droplet versus a macroscopic jar sample is the presence of a fluid-fluid interface between the two liquid phases as opposed to a fluid-solid interface between the sample and the container. This leads to different adsorption behavior and, more importantly, a higher surface area to volume ratio in droplets compared with macroscale samples. An important design constraint to consider for dilute solutions is the depletion of solute to the fluid-fluid interface. If enough solute adsorbs to the interface, it can affect the droplet bulk concentration.

Assuming a millifluidic droplet with spherical end caps that is 10 mm in length and 2 mm in diameter (typical of these experiments), the droplet will be approximately 30 μL in volume with 0.6 cm^2 of interface. Assuming an adsorption of 1 mg/m^2 , an initial concentration of 1 wt/vol or 10 mg/mL solute will result in 0.02% of the solute at the interface. At this

concentration, the amount of adsorbed material is negligible compared to the amount of material in the bulk. In order to have 1% of the solute material adsorb at the interface, the initial concentration needs to be approximately 0.2 mg/mL. As long as initial droplet concentration is greater than 0.2 mg/mL, depletion to the interface is not an issue. This will likely only become a concern if the phase behavior of a precious, expensive material at very dilute concentrations is of interest.

8.5.5 *Wetting*

Wetting conditions between the droplet phase, the oil phase, and the capillary material largely impact droplet production capabilities. Ideally, the outer phase will strongly wet the capillary material (strong intermolecular attractions) while the droplet phase will not wet the capillary (strong intermolecular repulsion). These conditions create dispersed phase droplets completely engulfed in a continuous outer phase fluid, isolating droplet material from both the walls of the capillary and neighboring droplets. However, if wetting favorability of the capillary is similar between droplet and continuous phase fluids, droplet production will become irregular and difficult to control.

In this thesis, three outer phase fluid choices are considered and investigated as potential continuous phase fluids: silicone oil, mineral oil, and fluorinated oil. Each fluid has advantages and disadvantages of droplet production and work best with different capillary material. Mineral oil performs best as an outer phase with polyethylene (PE) tubing and can easily dissolve many oil-soluble surfactants to aid in wetting conditions. Silicone oil works best with borosilicate or quartz capillaries, but few commercial surfactants are soluble in PDMS. In addition, water and silicone oil have relatively similar wetting on quartz. When highly surface active material is added to the droplet phase, wetting conditions can switch causing the aqueous phase to become

the outer phase and silicone oil to become the droplet phase. This is a serious issue if one is interested in investigating the phase behavior of surface active material, and should be one of the first problems solved in future work. Fluorinated oil (FC-70) is the best outer phase fluid choice when PTFE (Teflon) tubing is available as a capillary material. The wetting behavior of fluorinated oil on PTFE tubing is highly favorable, allowing for droplet production of samples containing polymer, biomolecules, and surfactant. In addition, most oils are insoluble in fluorinated oil. Therefore, droplets of oil-based systems can be produced with a fluorinated oil outer phase as well as aqueous droplets.

In the context of neutron scattering, fluorinated (PTFE) tubing is a strong scatterer of neutrons. In fact, it is the material used to align the beam due to its strong scattering properties. This poses an issue when attempting to find small changes in sample scattering as is performed in SANSDrop experiments. Quartz capillaries provide minimal scattering and are therefore used as a capillary material for neutron scattering experiments. Fluorinated oil with quartz capillaries result in poor wetting conditions, necessitating the use of silicone oil in all SANSDrop experiments. However, we are currently investigating the potential use of a fluorinated silane (1H,1H,2H,2H-Perfluorodecyltriethoxysilane) as a capillary coating material to change wetting conditions and create a more fluorinated friendly surface. Preliminary experiments show increased wetting between the fluorinated oil and quartz capillary allowing for production of 2 wt% PEO droplets. Continued research will attempt to find a long term wetting solution to create a versatile fluorinated oil outer phase and quartz capillary setup.

8.5.6 Flow rates and exposure time

Another factor to consider is the amount of exposure/scattering time for each droplet in the experiment. If droplets flow past the neutron source too quickly, many samples will be

tested, but poor scattering resolution will be collected on each sample. If droplets flow too slowly, good scattering resolution is achieved, but the number of samples per experiment is minimized. It is an optimization problem that depends on the desired composition resolution, the scattering intensity of the material, and the path length of the capillary.

In these experiments, droplets are designed to spend at least 1 minute each in the neutron beam. The time spent in the beam is most easily controlled by the continuous and dispersed phase flow rates. If the continuous phase flow rate is halved while maintaining dispersed phase flow rate, droplets will be formed at approximately twice the length while flowing at close to the same speed, leading to a nearly 2-fold increase in exposure time. If both the continuous and dispersed phase flow rates are halved simultaneously, then droplets will be produced at the same size but flow half as quickly, again resulting in a 2-fold increase in exposure time. Based on the results in the paper, 1-2 minutes of scattering per droplet is sufficient to achieve good scattering resolution when a strong neutron scatterer like silica particles is present. If a more weakly scattering material like polymers or surfactant are to be investigated, it is recommended to increase exposure time of each droplet.

8.5.7 Alternative designs

Performing a gauntlet experiment using a single co-flow quartz capillary with a silicone oil outer phase has proven to be an excellent proof-of-principle experiment as shown by the three tested systems in this work. Nevertheless, there are many alternative designs that can be utilized to create more robust, versatile techniques.

Varying composition path is the simplest adaptation to integrate since only the pump programming needs to be changed. Instead of creating five fingers along a gauntlet, more unique and tailored designs can be implemented. For example, if the location of a phase boundary is

known, a saw-tooth cloud point method can be created to vary back and forth across a phase boundary line similar to macroscopic experiments.⁵¹ In addition, a single region can be examined with much finer detail compared with a broad gauntlet experiment. Gradients can also be independently controlled to create slow droplet production up a gradient, but quick droplet production down a gradient to decrease time spent in the recovery phase. The simplicity of pump programming offers a range of potential composition paths to be explored.

Capillary choice is another handle that can be changed to make improvements to the experimental design. If the fluorinated coating proves to be functional, a capillary set up can be designed such that a long stretch of Teflon tubing connects to a short section (1-2") of quartz capillary followed by another stretch of Teflon tubing. Teflon tubing is easy to pinch at the ends and arrest droplet motion after droplets are produced. This allows for droplets to be produced beforehand and stored in a sealed, immobile container. Droplets can then be flowed and stopped in front of the neutron source for an extended exposure time before flowing the next droplet into position. In addition, droplet production can be made more complex by creating emulsion droplets within droplets.⁴⁴

8.6 Conclusions

A novel droplet-based neutron scattering experimental design (entitled SANSDrop) is developed and provides a new technique to probe colloidal structure of complex fluid systems with high composition resolution. Flow rates and capillary size are optimized to provide maximum neutron scattering while maintaining minimum sample size and analytical procedures are developed based on preliminary results. SANSDrop accuracy is demonstrated through an H₂O/D₂O contrast match experiment of Ludox HS-40 silica particles. The measured contrast

match point is 61 vol% D₂O using the millifluidic technique compared with 60 vol% D₂O from classical experiments and 58 vol% from literature.⁴

Gauntlet experiments are designed and performed to investigate phase behavior of three unique systems containing Ludox TMA silica particles with C₄E₁, NaCl, or 600 g/mol PEO. Droplet quality is classified via UV-Vis absorbance measurements to determine regions of consistent droplet production. 2-D neutron scattering patterns are characterized for all individual droplets to examine trends in scattering structure with changes in concentration. Results show structural peaks consistent with developing fluid structure forming at high concentrations of C₄E₁ and NaCl. Droplet production can become inconsistent at high system concentrations, but recovers as concentration becomes more dilute, allowing for experiments to probe beyond phase boundary lines.

8.7 References

- (1) Kotlarchyk, M.; Huang, J. S.; Chen, S. H. Structure of AOT Reversed Micelles Determined by Small-Angle Neutron Scattering. *J. Phys. Chem.* **1985**, *89* (20), 4382–4386.
- (2) Chen, S. H. Small Angle Neutron Scattering Studies of the Structure and Interaction in Micellar and Microemulsion Systems. *Annu. Rev. Phys. Chem.* **1986**, *37*, 351–399.
- (3) Mortensen, K. Structural Studies of Aqueous Solutions of PEO-PPO-PEO Triblock Copolymers, Their Micellar Aggregates and Mesophases; a Small-Angle Neutron Scattering Study. *J. Phys. Condens. Matter* **1996**, *8*, A103–A124.
- (4) Pozzo, D. C.; Walker, L. M. Small-Angle Neutron Scattering of Silica Nanoparticles Templated in PEO-PPO-PEO Cubic Crystals. *Colloids Surfaces A Physicochem. Eng. Asp.* **2007**, *294* (1–3), 117–129.
- (5) King, J. S. Neutron Scattering from Polymers. *J. Macromol. Sci. Part B* **1976**, *12* (1), 13–25.
- (6) Bates, F. S.; IUCr. Small-Angle Neutron Scattering from Amorphous Polymers. *J. Appl. Crystallogr.* **1988**, *21* (6), 681–691.
- (7) Frick, B.; Richter, D. The Microscopic Basis of the Glass Transition in Polymers from Neutron Scattering Studies. *Science* (80-.). **1995**, *267* (5206), 1939–1945.
- (8) Freltoft, T.; Kjems, J. K.; Sinha, S. K. Power-Law Correlations and Finite-Size Effects in Silica Particle Aggregates Studied by Small-Angle Neutron Scattering. *Phys. Rev. B* **1986**, *33* (1), 269–275.
- (9) Hasmy, A.; Anglaret, E.; Foret, M.; Pelous, J.; Remi, J. Small-Angle Neutron-Scattering Investigation of Long-Range Correlations in Silica Aerogels: Simulations and Experiments. *Phys. Rev. B* **1994**, *50* (9), 6006–6016.
- (10) Guo, X. H.; Zhao, N. M.; Chen, S. H.; Teixeira, J. Small-Angle Neutron Scattering Study of the Structure of Protein/detergent Complexes. *Biopolymers* **1990**, *29* (2), 335–346.
- (11) Svergun, D. I.; Richard, S.; Koch, M. H.; Sayers, Z.; Kuprin, S.; Zaccai, G. Protein Hydration in Solution: Experimental Observation by X-Ray and Neutron Scattering. *Proc. Natl. Acad. Sci. U. S. A.* **1998**, *95* (5), 2267–2272.
- (12) Zaccai, G. How Soft Is a Protein? A Protein Dynamics Force Constant Measured by Neutron Scattering. *Science* (80-.). **2000**, *288* (5471), 1604–1607.
- (13) Yong, W.; Lomakin, A.; Kirkitadze, M. D.; Teplow, D. B.; Chen, S.-H.; Benedek, G. B. Structure Determination of Micelle-like Intermediates in Amyloid -Protein Fibril Assembly by Using Small Angle Neutron Scattering. *Proc. Natl. Acad. Sci.* **2002**, *99* (1), 150–154.
- (14) Sottmann, T.; Strey, R.; Chen, S.-H. A Small-Angle Neutron Scattering Study of Nonionic Surfactant Molecules at the Water–oil Interface: Area per Molecule, Microemulsion Domain Size, and Rigidity. *J. Chem. Phys.* **1997**, *106* (15), 6483–6491.

- (15) Bergström, M.; Pedersen, J. S.; Schurtenberger, P.; Egelhaaf, S. U. Small-Angle Neutron Scattering (SANS) Study of Vesicles and Lamellar Sheets Formed from Mixtures of an Anionic and a Cationic Surfactant. *J. Phys. Chem. B* **1999**, *103* (45), 9888–9897.
- (16) Cygan, Z. T.; Cabral, J. T.; Beers, K. L.; Amis, E. J. Microfluidic Platform for the Generation of Organic-Phase Microreactors. *Langmuir* **2005**, *21* (8), 3629–3634.
- (17) Krishna, K. S.; Biswas, S.; Navin, C. V.; Yamane, D. G.; Miller, J. T.; Kumar, C. S. S. R. Millifluidics for Chemical Synthesis and Time-Resolved Mechanistic Studies. *J. Vis. Exp.* **2013**, No. 81, 1–9.
- (18) Olivon, K.; Sarrazin, F. Heterogeneous Reaction with Solid Catalyst in Droplet-Flow Millifluidic Device. *Chem. Eng. J.* **2013**, *227*, 97–102.
- (19) Romano, M.; Pradere, C.; Sarrazin, F.; Toutain, J.; Batsale, J. C. Enthalpy, Kinetics and Mixing Characterization in Droplet-Flow Millifluidic Device by Infrared Thermography. *Chem. Eng. J.* **2015**, *273*, 325–332.
- (20) Pinsolle, A.; Charmantray, F.; Hecquet, L.; Sarrazin, F. Droplet Millifluidics for Kinetic Study of Transketolase. *Biomicrofluidics* **2016**, *10* (6), 1–10.
- (21) Trivedi, V.; Doshi, A.; Kurup, G. K.; Ereifej, E.; Vandevord, P. J.; Basu, A. S. A Modular Approach for the Generation, Storage, Mixing, and Detection of Droplet Libraries for High Throughput Screening. *Lab Chip* **2010**, *10* (18), 2433.
- (22) Baraban, L.; Bertholle, F.; Salverda, M. L. M.; Bremond, N.; Panizza, P.; Baudry, J.; de Visser, J. A. G. M.; Bibette, J. Millifluidic Droplet Analyser for Microbiology. *Lab Chip* **2011**, *11* (23), 4057.
- (23) Boitard, L.; Cottinet, D.; Bremond, N.; Baudry, J.; Bibette, J. Growing Microbes in Millifluidic Droplets. *Eng. Life Sci.* **2015**, *15*, 318–326.
- (24) Lalanne-Aulet, D.; Piacentini, A.; Guillot, P.; Marchal, P.; Moreau, G.; Colin, A. Multiscale Study of Bacterial Growth: Experiments and Model to Understand the Impact of Gas Exchange on Global Growth. *Phys. Rev. E - Stat. Nonlinear, Soft Matter Phys.* **2015**, *92* (5), 1–11.
- (25) Amine, C.; Boire, A.; Davy, J.; Marquis, M.; Renard, D. Droplets-Based Millifluidic for the Rapid Determination of Biopolymers Phase Diagrams. *Food Hydrocoll.* **2017**, *70*, 134–142.
- (26) Martins, E.; Poncelet, D.; Marquis, M.; Davy, J.; Renard, D. Monodisperse Core-Shell Alginate (Micro)-Capsules with Oil Core Generated from Droplets Millifluidic. *Food Hydrocoll.* **2017**, *63*, 447–456.
- (27) Garagalza, O.; Petit, C.; Mignard, E.; Sarrazin, F.; Reynaud, S.; Grassl, B. Droplet-Based Millifluidic Device under Microwave Irradiation: Temperature Measurement and Polymer Particle Synthesis. *Chem. Eng. J.* **2017**, *308*, 1105–1111.
- (28) Illing, R.; Burkart, C.; Pfitzner, D.; Jungmann, D.; Baraban, L.; Cuniberti, G. Ecotoxicity Assessment Using Ciliate Cells in Millifluidic Droplets. *Biomicrofluidics* **2016**, *10* (2), 1–10.

- (29) Ildefonso, M.; Candoni, N.; Veessler, S. A Cheap, Easy Microfluidic Crystallization Device Ensuring Universal Solvent Compatibility. *Org. Process Res. Dev.* **2012**, *16*, 556–560.
- (30) Lourdes, M.; Baños, M. De; Carrier, O.; Bouriat, P.; Broseta, D. Droplet-Based Millifluidics as a New Tool to Investigate Hydrate Crystallization : Insights into the Memory Effect. *Chem. Eng. Sci.* **2015**, *123*, 564–572.
- (31) Engl, W.; Roche, M.; Colin, A.; Panizza, P.; Ajdari, A. Droplet Traffic at a Simple Junction at Low Capillary Numbers. *Phys. Rev. Lett.* **2005**, *95* (20), 2–6.
- (32) Wang, W. S.; Vanapalli, S. A. Millifluidics as a Simple Tool to Optimize Droplet Networks : Case Study on Drop Traffic in a Bifurcated Loop. *Biomicrofluidics* **2014**, *8* (64111), 1–23.
- (33) Feuerborn, A.; Prastowo, A.; Cook, P. R.; Walsh, E. Merging Drops in a Teflon Tube, and Transferring Fluid between Them, Illustrated by Protein Crystallization and Drug Screening. *Lab Chip* **2015**, *15*, 3766–3775.
- (34) Barnes, S. E.; Cygan, Z. T.; Yates, J. K.; Beers, K. L.; Amis, E. J. Raman Spectroscopic Monitoring of Droplet Polymerization in a Microfluidic Device. *Analyst* **2006**, *131* (9), 1027.
- (35) Salazar-Alvarez, G.; Muhammed, M.; Zagorodni, A. A. Novel Flow Injection Synthesis of Iron Oxide Nanoparticles with Narrow Size Distribution. *Chem. Eng. Sci.* **2006**, *61* (14), 4625–4633.
- (36) Bouquey, M.; Serra, C.; Berton, N.; Prat, L.; Hadziioannou, G. Microfluidic Synthesis and Assembly of Reactive Polymer Beads to Form New Structured Polymer Materials. *Chem. Eng. J.* **2007**, *135* (SUPPL. 1), 93–98.
- (37) Serra, C.; Berton, N.; Bouquey, M.; Prat, L.; Hadziioannou, G. A Predictive Approach of the Influence of the Operating Parameters on the Size of Polymer Particles Synthesized in a Simplified Microfluidic System. *Langmuir* **2007**, *23* (14), 7745–7750.
- (38) Abou Hassan, A.; Sandre, O.; Cabuil, V.; Tabeling, P. Synthesis of Iron Oxide Nanoparticles in a Microfluidic Device: Preliminary Results in a Coaxial Flow Millichannel. *Chem. Commun.* **2008**, No. 15, 1783.
- (39) Engl, W.; Backov, R.; Panizza, P. Controlled Production of Emulsions and Particles by Milli- and Microfluidic Techniques. *Curr. Opin. Colloid Interface Sci.* **2008**, *13*, 206–216.
- (40) Tachibana, M.; Engl, W.; Panizza, P.; Deleuze, H.; Lecommandoux, S.; Ushiki, H.; Backov, R. Combining Sol-Gel Chemistry and Millifluidic toward Engineering Microporous Silica Ceramic Final Sizes and Shapes: An Integrative Chemistry Approach. *Chem. Eng. Process. Process Intensif.* **2008**, *47* (8), 1323–1328.
- (41) Gokmen, M. T.; Van Camp, W.; Colver, P. J.; Bon, S. A. F.; Du Prez, F. E. Fabrication of Porous Clickable Polymer Beads and Rods through Generation of High Internal Phase Emulsion (HIPE) Droplets in a Simple Microfluidic Device. *Macromolecules* **2009**, *42* (23), 9289–9294.

- (42) Chang, Z.; Serra, C. A.; Bouquey, M.; Kraus, I.; Li, S.; Michael Köhler, J. Multiscale Materials from Microcontinuous-Flow Synthesis: ZnO and Au Nanoparticle-Filled Uniform and Homogeneous Polymer Microbeads. *Nanotechnology* **2010**, *21* (1).
- (43) Sai Krishna, K.; Navin, C. V.; Biswas, S.; Singh, V.; Ham, K.; Bovenkamp, G. L.; Theegala, C. S.; Miller, J. T.; Spivey, J. J.; Kumar, C. S. S. R. Millifluidics for Time-Resolved Mapping of the Growth of Gold Nanostructures. *J. Am. Chem. Soc.* **2013**, *135* (14), 5450–5456.
- (44) Utada, A. S.; Chu, L. Y.; Fernandez-Nieves, A.; Link, D. R.; Holtze, C.; Weitz, D. A. Dripping, Jetting, Drops, and Wetting: The Magic of Microfluidics. *MRS Bull.* **2007**, *32* (9), 702–708.
- (45) Tice, J. D.; Song, H.; Lyon, A. D.; Ismagilov, R. F. Formation of Droplets and Mixing in Multiphase Microfluidics at Low Values of the Reynolds and the Capillary Numbers. *Langmuir* **2003**, *19* (22), 9127–9133.
- (46) Tice, J. D.; Lyon, A. D.; Ismagilov, R. F. Effects of Viscosity on Droplet Formation and Mixing in Microfluidic Channels. *Anal. Chim. Acta* **2004**, *507* (1), 73–77.
- (47) Kline, S. R.; Kaler, E. W. Colloidal Interactions in Water/2-Butoxyethanol Solvents. *Langmuir* **1994**, *12*, 412–417.
- (48) Trompette, J. L.; Meireles, M. Ion-Specific Effect on the Gelation Kinetics of Concentrated Colloidal Silica Suspensions. *J. Colloid Interface Sci.* **2003**, *263* (2), 522–527.
- (49) Kirby, S. M.; Anna, S.; Walker, L. Effect of Surfactant Tail Length and Ionic Strength on the Interfacial Properties of Nanoparticle-Surfactant Complexes. *Soft Matter* **2017**, *14*, 112–123.
- (50) Christopher, G. F.; Anna, S. L. Microfluidic Methods for Generating Continuous Droplet Streams. *J. Phys. D. Appl. Phys.* **2007**, *40* (19), 319–336.
- (51) Glyk, A.; Scheper, T.; Beutel, S. Influence of Different Phase-Forming Parameters on the Phase Diagram of Several PEG–salt Aqueous Two-Phase Systems. *J. Chem. Eng. Data* **2014**, *59*, 850–859.

Chapter 9. Conclusions

In this thesis, droplet based approaches are merged with classical colloidal characterization techniques to investigate complex fluid behavior with low sample sizes while maintaining high composition resolution. Both microfluidic and millifluidic droplets are employed to achieve the same high composition resolution goal through different approaches. The microfluidic droplet technique produces single droplets that dehydrate with time while being continuously recorded. Time is used to vary concentration as water partitions out of the droplet, producing 100's to 1000's of unique measurements per experiment. Millifluidic droplets utilize concentration gradients to vary droplet composition. Each droplet in the millifluidic experiments is a unique sample, as opposed to time measurements in the microfluidic experiment. Microfluidic experiments are best suited for optical microscopy applications where the phenomena can be observed visually. Millifluidic droplets are best suited for in-line, non-intrusive measurements such as optical absorbance, neutron scattering (SANS), X-ray scattering (SAXS), and Raman spectroscopy measurements.

Chapters 4-6 utilize the microfluidic dehydrating droplet technique. In Chapter 4, the microfluidic droplet trap device is characterized through investigation of phase behavior of a dehydrating salt-polymer (PEO-ammonium sulfate) system. System composition traverses the single phase dilute regime to the two phase concentrated regime during the course of an experiment. With this common organic-inorganic system, phase separation is observed in droplet form at high concentrations, yielding a phase diagram with high compositional resolution that agrees well with macroscopic results. In addition, the phase separation can be observed *in situ* leading to valuable information about the phase separation process.

In Chapter 5, the microfluidic device is used to dehydrate non-phase separating colloid-polymer suspensions containing silica particles and PEO. It is found that final particle volume fraction largely decreases at dilute polymer concentrations (low polymer/particle mass ratios). A colloidal bridging flocculation theory is proposed to explain the variation in final particle volume fraction as a function of polymer/particle mass ratio (ξ). The data suggests that at low polymer/particle mass ratios, the system undergoes bridging flocculation caused by the polymer-particle interactions.

In Chapter 6, a phase separating colloid-polymer system is studied with the same microfluidic device. A system containing 20 nm PS particles and 90k g/mol HEC polymer is found to display significant and reproducible optical darkening (phase separation) as droplets dehydrate, with results suggesting a depletion induced flocculation aggregation mechanism. Interparticle potential is varied by changing polymer molecular weight, particle size, and polymer type. Increasing particle size suppressed optical darkening for an identical particle-polymer system, suggesting a transition from reaction-limited (RLCA) to diffusion-limited (DLCA) aggregation with an increase in particle size.

In Chapters 7-8, the millifluidic droplet technique is used to map composition space with gradients instead of dehydration. In Chapter 7, stability of carbon black particles in nonpolar solvents with the addition of a nonionic surfactant (OLOA 11000) is examined. Droplets are produced and arrested vertically for optical detection of sedimentation behavior. This work provides affirmation of the assumed steric to electrostatic transition and further insight into the slow degree by which the transition occurs, suggesting that electrostatic interactions in the system arise gradually as opposed to an “on-off” effect.

In Chapter 8, the millifluidic droplet technique is expanded to more complex colloidal systems and small angle neutron scattering (SANS) is used as a measurement technique. Flow rates and capillary size are optimized to provide maximum neutron scattering while maintaining minimum sample size and analytical procedures are developed based on preliminary results. SANSDrop accuracy is demonstrated through an H₂O/D₂O contrast match experiment of Ludox HS-40 silica particles. Gauntlet experiments are designed and performed to investigate phase behavior of 3 unique systems containing Ludox TMA silica particles with C₄E₁, NaCl, or 600 g/mol PEO. Droplet quality and scattering intensity are paired to allow for definitive statements about system structure and interparticle behavior.

In conclusion, this thesis demonstrates novel microfluidic and millifluidic droplet-based techniques to study complex fluid systems with small sample volume while maintaining high composition resolution. Both time and composition gradients are used to control droplet concentration with precise and discrete variations. Model systems are chosen to demonstrate feasibility and accuracy of the methods and optical microscopy, optical absorbance measurements, and neutron scattering are used to as measurement techniques. The resulting coupling of droplet-based experiments and classical colloidal measurements provides new, useful classification techniques for industrial colloidal systems.

Appendix A. Phase Behavior of Concentrating Particle-Polymer-Salt Systems

Differences in phase behavior of concentrating particle-polymer suspensions from Chapter 5 for different particle sources are investigated. Droplets are produced on the microfluidic dehydrating droplet device and concentrated under observation. Phase behavior is characterized optically. Ludox TMA and Ludox TM-40 silica particles are tested as particle sources and 7500 g/mol PEO is used as the polymer. The only differences between Ludox TMA and Ludox TM-40 are the pH of the system and the presence of a low concentration of Na_2SO_4 . Ludox TM-40 stock particles have an initial concentration of 40 wt%, a pH of 8.7, and a Na_2SO_4 concentration of 0.1 wt%.¹ Ludox TMA stock particles have an initial concentration of 34 wt%, a pH of 6.1, and are reported as salt free.

Figure A.1 is the same as Figure 5.4 from Chapter 5 revisited for a different analysis. In this scope, phase behavior is of interest as opposed to final particle volume fraction. Figure A.1 shows the microfluidic results of the 22 nm in diameter Ludox TMA and 7500 g/mol PEO system. The x-axis is particle concentration in particle volume fraction and the y-axis is polymer concentration in g/mL. Each thin dotted black line represents the compositional path of a tested droplet for a given polymer/particle ratio. The closed red circles denote droplet samples at their initial dilute concentration, the open circles correspond to the final concentration of droplets once they stop dehydrating, and the single closed black circle represents the only concentration at which phase separation is observed. The dotted black lines show the maximum possible concentration of polymer (1.13 g/mL)³ and particles (random close packed limit, $\phi = 0.63$).⁴ The solid black line denotes the concentration of the system where all the water leaves the droplets,

and the dotted red line shows the mass ratio that corresponds to the adsorption limit for PEO on silica particles ($\Gamma = 1.2 \text{ mg/m}^2$).²

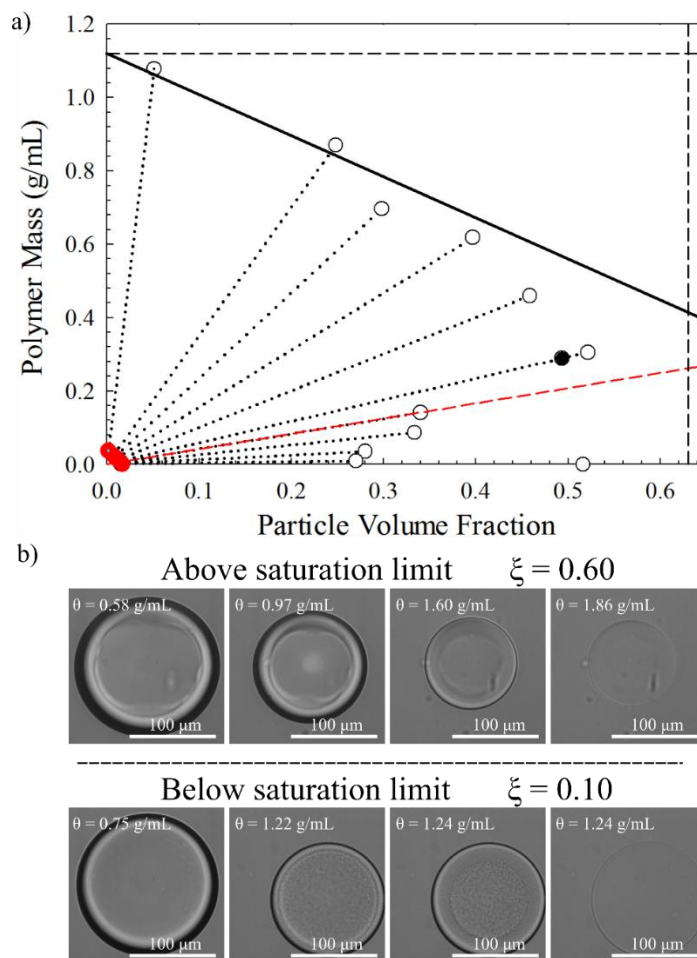


Figure A. 1: Phase diagram of Ludox TMA particles and 7500 g/mol PEO mapped using microfluidic droplet drying. (a) The red circles denote initial droplet concentrations, open circles denote the final droplet concentration, and the single closed black circle denotes the only system that displays phase separation. The thin dotted black lines depict the composition paths of each experiment, the thick dotted black lines represent maximum concentration of particles and polymer, and the solid black line shows the system composition when no water remains in the droplet. The dotted red line denotes the saturation line (1.2 mg/m^2 , $\xi = 0.17$).² (b) Images of droplet behavior at the final stages of the drying experiment. First row of images is characteristic of droplets above the saturation limit and the second row is characteristic of droplets below the saturation limit.

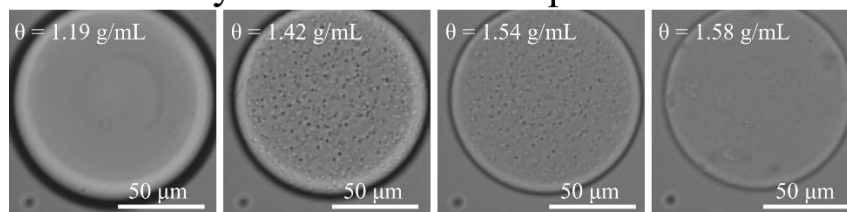
For all experiments except one, droplets remain clear through the entire dehydration process and do not show any signs of the optical darkening that is observed in the PS system.

The single point that does show phase separation is at mass ratio $\xi = 0.23$. However, this phase

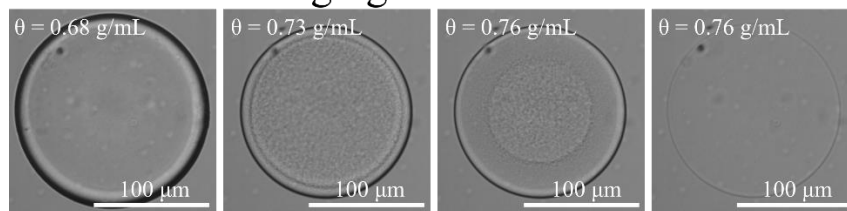
separation looks consistent with polymer-salt phase separation observed in Chapter 4 and not with the darkening phase separation observed in Chapter 6. This result suggests that a small doping of salt contaminant can lead to phase separation in a complex particle-polymer system. To further examine this observation, Ludox TM-40 is used as a replacement for Ludox TMA to test how slight changes in particle source affects phase behavior. As previously mentioned, the only differences between Ludox TMA and Ludox TM-40 are the pH and salt concentration.

Numerous polymer/particle mass ratios are tested to fully map the phase behavior of the Ludox TM-40 and 7500 g/mol PEO system. Three types of optical changes are observed based on the polymer-particle mass ratio shown in Figure A.2a. In the first type of optical change, dark black dots appear across the entire droplet at a particular concentration and remain until the droplet completely dehydrates. The black specks disappear at the end of the dehydration process. Images of this transition are shown in the first row of images in Figure A.2a. In the second type of optical change, a ring forms at the edge of the droplet and moves concentrically towards the center of the droplet. Once the ring reaches the middle of the droplet, the droplet no longer concentrates. This observation is identical to that seen in the bridging flocculation section of Chapter 5, and images of the behavior can be seen in the second row of images in Figure A.2a. The third type of optical change is a combination of the first two. Larger gray/white dots appear instead of black dots. As the droplet continues to dehydrate, a less pronounced ring forms as the gray/white specs disappear. The ring moves towards the center of the droplet and no longer concentrates after it reaches the middle. This third type of optical change is effectively a transition between the first and second type, shown in image form in the third row of images in Figure A.2a.

Polymer-Salt Phase Separation



Bridging Flocculation



Transition Regime

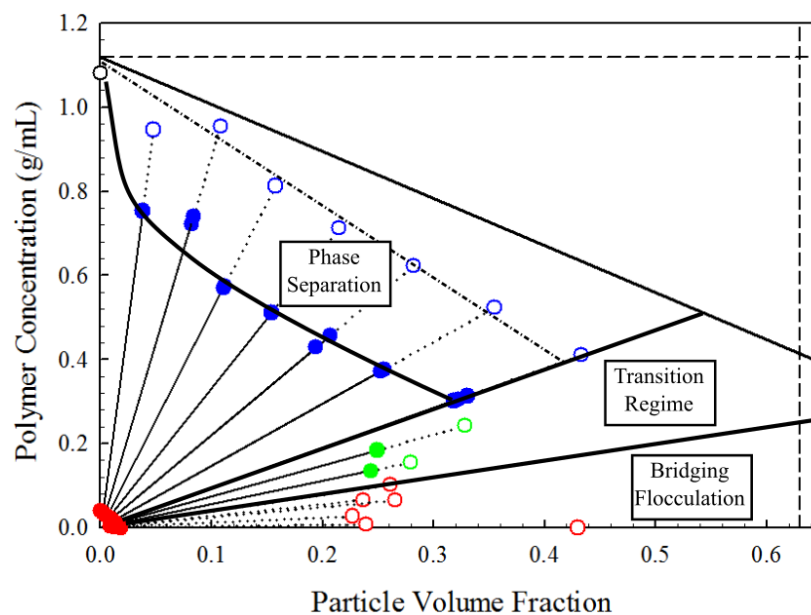
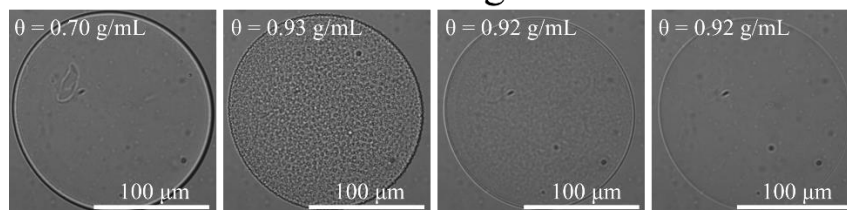


Figure A. 2: Phase behavior of concentrating Ludox TM-40 and 7500 g/mol PEO droplets. (a) Images of droplet dehydration in separate regimes. (b) Phase diagram of the dehydration results. Closed red circles denote initial droplet concentrations and closed blue and green points denote phase separation concentration. Open points denote final droplet concentrations with blue, green, and red corresponding to sections of phase separation, transition, and bridging flocculation respectively.

Figure A.2b shows phase separation results from microfluidic droplet experiments of Ludox TM-40 and 7500 g/mol PEO. The closed red circles denote the initial droplet concentrations, the closed circles correspond to the phase separation points, and the open circles denote final droplet concentrations. The different colors correspond to different optical changes characterized as phase separation, particle drying, and transition regime and are color coded in Figure A.2a as blue points, red points, and green points respectively. The line c_{\max} corresponds to a concentration at which all water leaves the droplet and only particles and polymer remain. Therefore, any composition above the c_{\max} line is infeasible and is denoted as an inaccessible region. The dotted black lines correspond to a maximum concentration of polymer and particles.

As discussed in Chapter 5, there is a section low polymer/particle mass ratios where the droplets stop concentrating much earlier than expected. This is the region where we suggest bridging flocculation leads to early particle aggregation. In this region, no phase separation is observed in any droplets and only a ring is seen at the final particle concentration. In the transition regime, brief polymer-salt phase separation occurs before particle becomes aggregated and halt the dehydration process. In the phase separation region, all droplets are observed to phase separate similar to the first row of images in Figure A.2a. Droplets continue dehydration until they reach a stable final concentration.

The trend in final particle volume fraction between the Ludox TMA and Ludox TM-40 systems is similar, but the phase separation behavior between the two is different. All compositions above the bridging flocculation region for Ludox TM-40 show phase separation, but only 1 composition for Ludox TMA was seen to phase separate. As mentioned earlier, the only difference between the particle sources are the pH of the system and the added Na_2SO_4 .

Experiments are performed to elucidate which system parameter causes a difference in phase behavior.

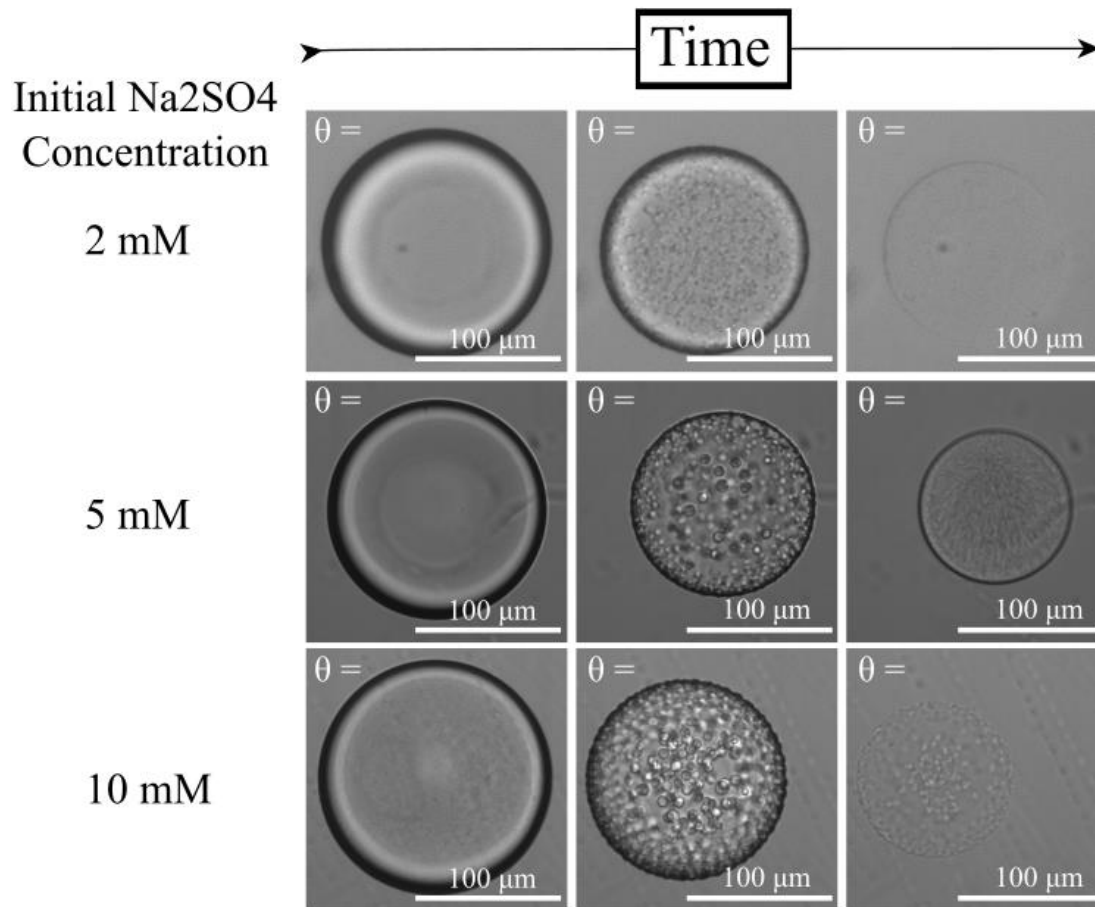


Figure A. 3: Images of dehydrating Ludox TMA and 7500 g/mol PEO droplets with different concentrations of added Na₂SO₄.

Experiments are performed along a single compositional track to determine the cause for differences in phase behavior between the Ludox TMA and TM-40 systems. A system composition of $\xi = 0.63$ with an initial concentration of $\theta = 0.05$ g/mL is chosen. A pH based experiment is performed by varying the pH of the Ludox TMA suspension from 6.1 to 8.7 with the addition of sodium hydroxide (NaOH). The change in pH had no effect on the optical

behavior of the system and the final particle concentration of the pH adjusted droplet is $\phi = 0.36$ as opposed to $\phi = 0.39$ for the unadjusted system.

Figure A.3 shows the results of adding different concentrations of Na_2SO_4 to the Ludox TMA system. Adding an amount of salt equivalent to that of Ludox TM-40 (1-2 mM Na_2SO_4 for a 4 wt% suspension) resulted in similar phase separation compared with the Ludox TM-40 system shown in Figure A.3. Continuing to add salt (5-10 mM Na_2SO_4) resulted in phase separation that occurs at systematically more dilute θ (total mass/volume) concentrations. In addition, the phase separation shows different visual characteristics when high salt concentrations are added. At these higher salt concentrations, the two phases separate more rapidly and distinctly than the lower salt experiments. In addition, when the droplets completely dehydrate, the phase separated microstructure becomes encapsulated in the dried droplet.

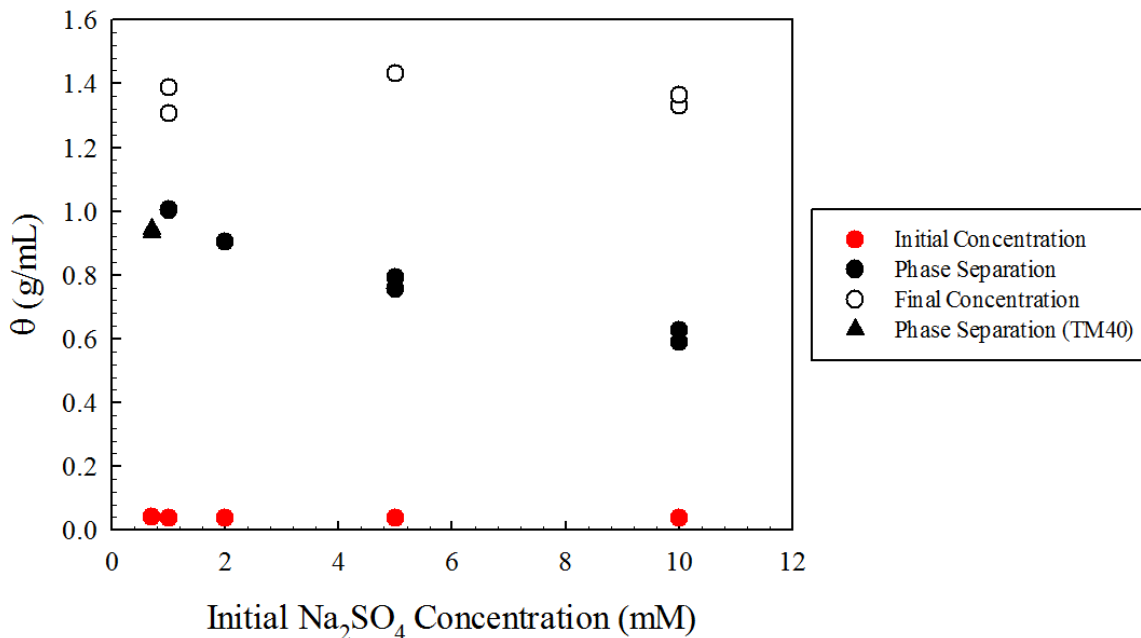


Figure A. 4: Effect of Na_2SO_4 concentration on the phase separation concentration for Ludox TMA and 7500 g/mol PEO. Red circles denote initial concentrations, black circles denote phase separation concentration with Ludox TMA particles, black triangles denote phase separation concentration with Ludox TM-40 particles, and open circles denote final droplet concentration.

Figure A.4 shows the effect of initial salt concentration (mM Na₂SO₄) on the phase separation concentration (θ) for a mass ratio of $\xi = 0.63$. The closed red circles denote initial concentrations of each droplet. The closed black circles denote the θ values at which phase separation occurs in the Ludox TMA and 7500 g/mol PEO system doped with small amounts of Na₂SO₄. The single closed square point corresponds to the phase separation concentration for Ludox TM-40 and 7500 g/mol PEO at the same mass ratio. This assumes a 7mM Na₂SO₄ concentration in the 40 wt% Ludox TM-40 stock suspension. The open circle points denote the final concentrations of each droplet.

An overall trend of decreasing phase separation concentrations with increasing initial salt concentration is observed. The phase separation point of the single Ludox TM-40 experiment falls in line with the Ludox TMA trend. In addition, the final particle-polymer droplet concentration does not change as the salt concentration and phase separation varies. This demonstrates that adding salt to the particle-polymer system alters the phase separation behavior of the droplets but does not change the final droplet compositions. It will, however, change the microstructure of the final droplets as the phase separated structure becomes immobilized.

References

- (1) *Ludox Technical Information Document*; Columbia, MD, 2008.
- (2) Bjelopavlicl, M.; Zaman, A. A.; Moudgi, B. M. Adsorption of Poly (Ethylene Oxide) Onto Silica at Different Solids Loadings. *KONA Powder Part. J.* **2000**, *18* (18), 60–65.
- (3) *Polyethylene Oxide Product Specification Document*; St. Louis, MO.
- (4) Hunter, G.; Weeks, E. The Physics of the Colloidal Glass Transition. *Rep. Prog. Phys.* **2012**, *75* (6), 66501.